Western&Graduate&PostdoctoralStudies

4-20-2020 10:00 AM

Physical Dispersions of Meteor Showers Through High Precision Optical Observations

Denis Vida
The University of Western Ontario

Supervisor
Brown, Peter G.
The University of Western Ontario Co-Supervisor
Campbell-Brown, Margaret D.
The University of Western Ontario

Graduate Program in Geophysics
A thesis submitted in partial fulfillment of the requirements for the degree in Doctor of Philosophy
© Denis Vida 2020

Abstract

Meteoroids ejected from comets form meteoroid streams which disperse over time due to gravitational perturbations and non-gravitational forces. When stream meteoroids collide with the Earth's atmosphere, they are visible as meteors emanating from a common point-like area (radiant) in the sky. Measuring the size of meteor shower radiant areas can provide insight into stream formation and age. The tight radiant dispersion of young streams are difficult to determine due to measurement error, but if successfully measured, the dispersion could be used to constrain meteoroid ejection velocities from their parent comets. The estimated ejection velocity is an uncertain, model-dependent value with significant influence on the prediction accuracy of meteor shower models which are operationally used by space agencies to mitigate the meteoroid impact risk.

The first part of this work consists of a theoretical investigation of achievable meteor radiant and velocity measurement accuracy using optical observation systems. From dynamical meteoroid stream modelling it has been estimated that a minimum radiant measurement accuracy of 0.1° is needed to begin to resolve the radiant structure of young meteor showers. Using a novel meteor trajectory simulator, it was found that this accuracy can be achieved using narrow field of view optical systems and a newly developed method of meteor trajectory estimation. The measurement accuracy of pre-atmosphere meteoroid velocities remains model-dependent because meteoroids may decelerate up to $750\,\mathrm{m\,s^{-1}}$ prior to becoming visible.

The second part of the work was observational and done using the Canadian Automated Meteor Observatory (CAMO). Four Electron Multiplying CCD cameras were used to observe the 2018 outburst of the Draconid meteor shower which had a radiant dispersion of 0.25°, consistent with simulations and previous high-precision measurements. A mass index of $s = 1.74 \pm 0.18$ during the peak was estimated using a novel method. The CAMO mir-

ror tracking system was used to observe the 2019 Orionids. For the first time, the Orionid radiant structure was accurately measured, showing indications of two stream branches. As part of the meteoroid modelling work to improve radiant and orbit measurements the compressive strengths of meteoroids were estimated through direct observations of fragmentation. The measured values were a good match to in-situ Rosetta measurements from comet 67P.

Summary for Lay Audience

When comets come close to the Sun, dust particles called meteoroids are ejected from the comet's surface and form meteoroid streams which initially closely follow the comet's orbit. Meteoroids within a stream drift away (disperse) from each other over time because they are pushed by Sun's radiation and pulled by the gravity of nearby planets. When stream meteoroids collide with the Earth's atmosphere, they are visible as meteor showers ("shooting stars") emanating from a common point-like area in the sky called the radiant. Observing meteors using video cameras from several locations enables us to compute their radiant and 3D trajectory in the atmosphere. Young streams (10s-100s years old) have tight radiant areas which are difficult to resolve because the measurements are usually not accurate enough. Knowing the true radiant dispersion can help to directly calculate the speed at which meteoroids were ejected from comets. Right now, the ejection speed is calculated from different theoretical models which do not agree with each other. The ejection speed is one of the most important parameters in meteor shower prediction models which are used by space agencies. During times of high meteor activity, space walks are suspended and satellites are reoriented to minimize the chance of impact. Historically, predicting the true activity of meteor showers has been challenging and several major meteor shower outbursts were not predicted because of unknown ejection speeds.

In this work, it was determined through meteoroid stream modelling that radiants should be measured with an accuracy of at least $0.1°$ to reveal the true radiant dispersion of young meteor showers. Using a new meteor shower simulator developed here, it was shown that the required accuracy can be achieved by existing optical meteor observation systems if our new method of computing meteor trajectories is used. Using very precise optical instruments that are a part of the Canadian Automated Meteor Observatory, real radiant dispersions of the Draconid and Orionid meteor showers were measured. The observed Draconid radiant positions match theoretical radiants well, and the structure of the Orionid radiant was revealed for the first time.

Co-Authorship Statement

This thesis is based on five chapters that have either been previously published, or accepted for publication.

Chapter 2: Vida, D., Brown, P.G., and Campbell-Brown, M. 2018. "Modelling the measurement accuracy of pre-atmosphere velocities of meteoroids." *Monthly Notices of the Royal Astronomical Society*, 479, 4307.

Chapter 3: Vida, D., Gural, P.S., Brown, P.G., Campbell-Brown, M., and Wiegert, P. 2020. "Estimating trajectories of meteors: an observational Monte Carlo approach – I. Theory." *Monthly Notices of the Royal Astronomical Society*, 491, 2688.

Chapter 4: Vida, D., Brown, P.G., Campbell-Brown, M., Wiegert, P., and Gural, P.S. 2020. "Estimating trajectories of meteors: an observational Monte Carlo approach – II. Results". *Monthly Notices of the Royal Astronomical Society*, 491, 3996.

Chapter 5: Vida, D., Campbell-Brown, M., Brown, P.G., Egal, A., and Mazur, M. 2020. "A new method for measuring the meteor mass index: application to the 2018 Draconid meteor shower outburst". *Astronomy & Astrophysics*, accepted for publication

Chapter 6: Vida, D., Brown, P.G., Campbell-Brown, M., Weryk, R.J., Stober, G., and McCormack, J.P. 2020. "High precision meteor observations with the Canadian Automated Meteor Observatory: Data reduction pipeline and application to meteoroid mechanical strength measurements". *Icarus*, submitted

I performed the theoretical development, code implementation, and data analysis for each chapter and wrote each of the five manuscripts. My supervisors Dr. Peter Brown and Dr. Margaret Campbell-Brown provided guidance at all stages of my research, and gave advice and suggestions for each manuscript. Peter S. Gural kindly shared the code for his Multi Parameter Fit

meteor trajectory estimation method using in Chapters 3 and 4, and provided invaluable insight into the minute details of optical meteor observation. Dr. Paul Wiegert performed numerical integrations of the 2011 Draconid outburst used in Chapter 4, and Dr. Auriane Egal did the same for the 2018 outburst discussed in Chapter 5. Dr. Margaret Campbell-Brown computed the flux of the 2018 Draconid outburst in Chapter 5. Dr. Gunter Stober computed the variations in neutral air densities using NAVGEM data which was used in Chapter 6. Dr. Auriane Egal processed orbital elements of the comet Halley from B1950.0 to J2000.0 that were used in Chapter 7.

Optical meteor observations were done with the Canadian Automated Meteor Observatory, a system operated by the Meteor Physics Group at the University of Western Ontario, and built by Zbigniew Krzeminski and Robert Weryk. Robert Weryk and Jason Gill wrote and maintained the automation code, as well as computer programs used for data calibration and reduction.

Acknowlegements

I wholeheartedly thank my supervisors Dr. Peter Brown and Dr. Margaret Campbell-Brown for their support and guidance. Your kindness will never be forgotten.

I also thank Damir Šegon and Pete Gural for instilling a passion for meteors in me through their relentless thirst for knowledge. Furthermore, I would like to thank many other passionate amateur astronomers who encouraged me to pursue astronomy as a profession.

Many thanks to all past and present members of the Western Meteor Physics Groups for sharing their expertise and friendship.

Finally, I thank my friends and family for their undivided support and kindness, as well as the employees of the restaurant Babylon for their friendliness and amazing food which kept me going.

Contents

List of Figures

List of Tables

Chapter 1

Introduction

1.1 Motivation

The goal of this thesis is to measure true physical radiant dispersion of meteor showers through optical observations. *Meteoroids* are defined by the International Astronomical Union (Koschny & Borovicka, 2017) as 30 μm to 1 m solid objects moving in interplanetary space. When they collide with a gaseous atmosphere they start *ablating* and produce light, ionisation, and other phenomena which are collectively called *meteors*. The point on the sky from which a meteor appears to originate is called the *radiant*.

If meteors have a common origin and hence similar heliocentric orbits, they will appear to an observer on the Earth's surface to have similar radiants and velocities forming a *meteor shower*. Meteor showers are caused when Earth encounters *meteoroid streams* – groups of meteoroids on similar orbits. The origins of meteoroids are from either cometary or asteroidal *parent bodies* (Ceplecha et al., 1998).

Meteoroids are released from cometary parent bodies when comets approach the Sun. In this case, the volatiles near the surface start to sublimate and this leaves a trail of meteoroids behind the comet (Vaubaillon et al., 2019). Meteoroids of asteroidal origin are released through asteroid collisions, tidal/spin-up disruptions, or ejection due to thermal stresses (Lauretta et al.,

2019; Agarwal, 2019).

Meteoroids initially closely follow the orbit of the parent body, as ejection speeds are a small fraction of the parent orbital velocity (Jenniskens, 1998). Over time, meteoroid orbits become dispersed due to gravitational perturbations and non-gravitational forces such as Solar radiation pressure (Egal et al., 2019). Thus, the orbits in a meteoroid stream vary slightly and this is reflected in the apparent angular *dispersion* of their radiant locations in the sky (radiant areas).

Young meteor showers most often have tighter (smaller) angular radiants and sharp (temporal) peaks of activity, while older showers are more dispersed and last longer. Very old meteoroid streams lose the orbital memory of the parent body and become part of the sporadic background (Jenniskens, 2006). Figure 1.1 shows the different stages of life of an average meteoroid. In contrast to meteor showers, which occur annually for a period of several hours up to several weeks, *sporadic* meteors have a steady flux which varies about ±30% throughout the year (Campbell-Brown & Jones, 2006).

In practical terms, being able to measure true physical radiant dispersions can help to constrain ages of meteor showers and models of their formation. These models are used by satellite operators to estimate the meteoroid impact risk and undertake action to minimize it (Drolshagen & Moorhead, 2019). Finally, these models are used to predict annual shower activity by NASA (Moorhead et al., 2019) and schedule spacewalks on the International Space Station during periods of lowest meteoroid activity to mitigate the impact risk to astronauts (Hoffman et al., 2020).

1.2   Meteor Physics

When meteoroids hit the Earth's atmosphere they undergo rapid heating caused by collisions with air particles and become visible to the human eye at altitudes between $70 - 120$ km. Meteoroids that orbit the Sun enter the atmosphere at hypervelocity speeds. The slowest me-
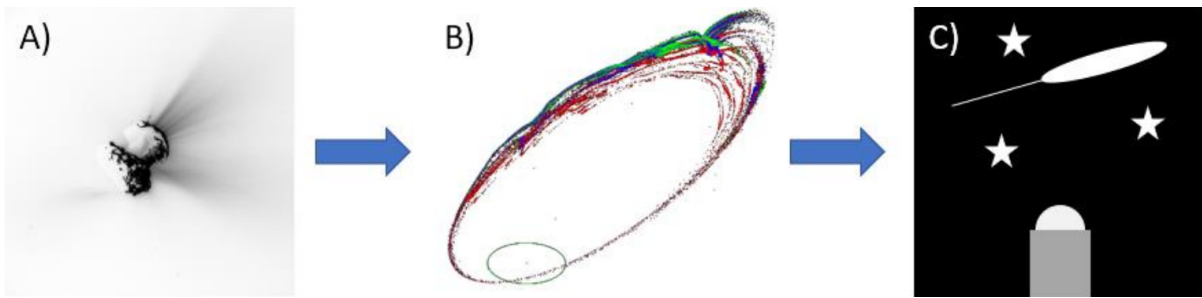
Figure 1.1: (A) Meteoroid ejection from a comet (Source: ESA), B) Meteoroid stream evolution (Source: Dr. Peter Brown), C) Meteor observed in the atmosphere after an encounter with the Earth.

teors are those whose relative velocities with respect to the Earth are near net zero, thus they enter the atmosphere with a speed equivalent to the escape velocity from Earth's surface $\sqrt{\frac{2GM_E}{r}} = 11.2\,\mathrm{km\,s^{-1}}$, where M_E is the mass of the Earth and r is the Earth's radius. The fastest observed meteors are those that are close to escaping the Solar System with heliocentric velocities at Earth's orbit $\sqrt{\frac{2GM_S}{r_E}} = 42.1\,\mathrm{km\,s^{-1}}$, and they collide with the Earth head on, adding Earth's orbital velocity $\sqrt{\frac{GM_S}{r_E}} = 29.8\,\mathrm{km\,s^{-1}}$ to the total of $71.9(5)\,\mathrm{km\,s^{-1}}$ (it varies due to the changing Earth-Sun distance r_E; M_S is the mass of the Sun). Temporary captured meteoroids in an orbit around the Earth (Shober et al., 2019) may have even lower geocentric velocities (i.e. velocities relative to the centre of the Earth), and interstellar objects may have velocities far exceeding the upper limit (Taylor et al., 1996).

Meteors observed by the human eye are usually produced by meteoroids smaller than a millimetre. These small meteoroids almost completely ablate away in the atmosphere, turning into disassociated ions (Popova et al., 2019). Objects smaller than 30 μm do not ablate and are known as interplanetary dust particles (IDPs) which slowly settle down in the atmosphere and may be collected in the stratosphere (Brownlee, 1985). Refractory meteoroid components that survive the entry and IDPs that arrive to the surface are known as micrometeorites, and are usually collected in areas where they concentrate over time, such as ice sheets in the Arctic and ocean sediments (Genge et al., 2008).

On the other hand, meteorite-dropping fireballs are caused by larger >20 cm meteoroids (Ceplecha et al., 1998), and are rare events that only occur several times a year on regional

scales (Brown et al., 2002). An average of ~40 t of extraterrestrial material of all sizes falls to the Earth's surface every day, but estimates vary by an order of magnitude (Plane, 2012).

Millimetre-size meteoroids can generally be divided into several groups by their physical properties derived from optical and spectral observations (Borovička, 2005): low-density ($\rho_m = 100 - 1000 \, \mathrm{kg \, m^{-3}}$) cometary meteoroids with high porosity (Borovička et al., 2007, 2014), asteroidal meteoroids with stony composition ($\rho_m = 2500 - 4000 \, \mathrm{kg \, m^{-3}}$), and high density iron meteoroids (Vojáček et al., 2019). Meteoroid bulk density is still a contentious issue due to measurement and model limitations - for example, Kikwaya et al. (2011) proposed a correlation between bulk density and orbital characteristics, but Vojáček et al. (2019) showed that meteoroids on asteroidal orbits can also have low bulk densities.

Figure 1.2 shows the distribution of geocentric velocities of meteors observed by the Global Meteor Network (GMN), a world-wide network of video cameras (Vida et al., 2019). The distribution is bimodal and the different peaks correspond to different meteor sources on the sky. To illustrate, Figure 1.3 shows the distribution of GMN meteor radiants in Sun-centered ecliptic (SCE) coordinates - the observed geocentric velocities are colour coded. Note that the local peaks in the velocity distribution correspond to certain meteor showers which are also labeled in Figure 1.3.

Figure 1.4 shows an SCE radiant plot of combined North and South hemisphere radar observations (Brown et al., 2005; Pokorný et al., 2017). We will use the two plots to illustrate observational biases and explain observed meteoroid sources. In contrast to optical observations, radar observations can be performed 24/7 under all weather conditions. Radars also typically observe meteoroids smaller than optical systems; at such sizes (< mm) sporadic meteors are more prevalent than shower meteors (Campbell-Brown, 2007).

The centre of SCE plots is aligned with the Earth's direction of motion around the Sun, i.e. the apex, and corresponds to meteoroid geocentric velocities above ~41 $\mathrm{km \, s^{-1}}$ (minimum geocentric velocity of 11.2 $\mathrm{km \, s^{-1}}$ + mean orbital velocity of Earth of 29.8 $\mathrm{km \, s^{-1}}$). These meteoroids hit the Earth "head on", and are mainly produced by Halley-type comets (Campbell-
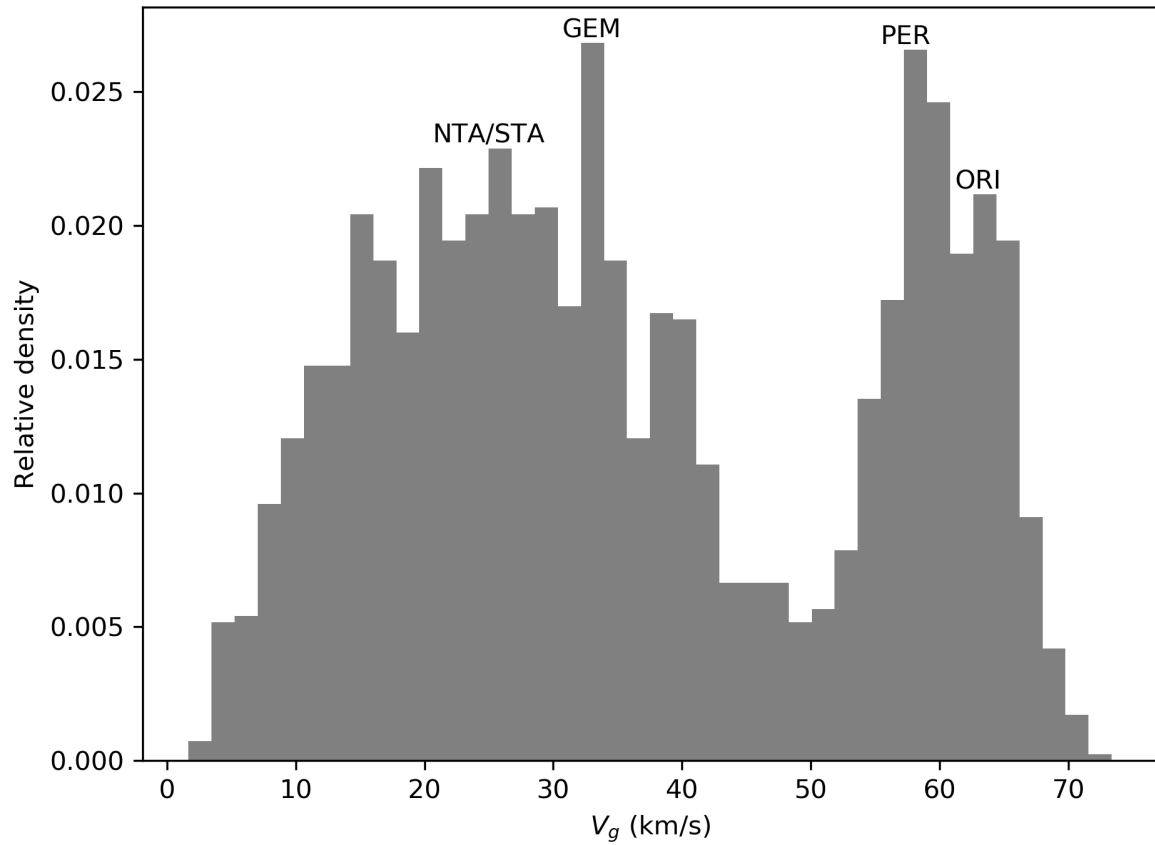
Figure 1.2: Distribution of meteoroid geocentric velocities of $\sim 100,000$ meteors observed in 2019 by the Global Meteor Network (Vida et al., 2019). Full names of meteor showers are given in Table 1.1.
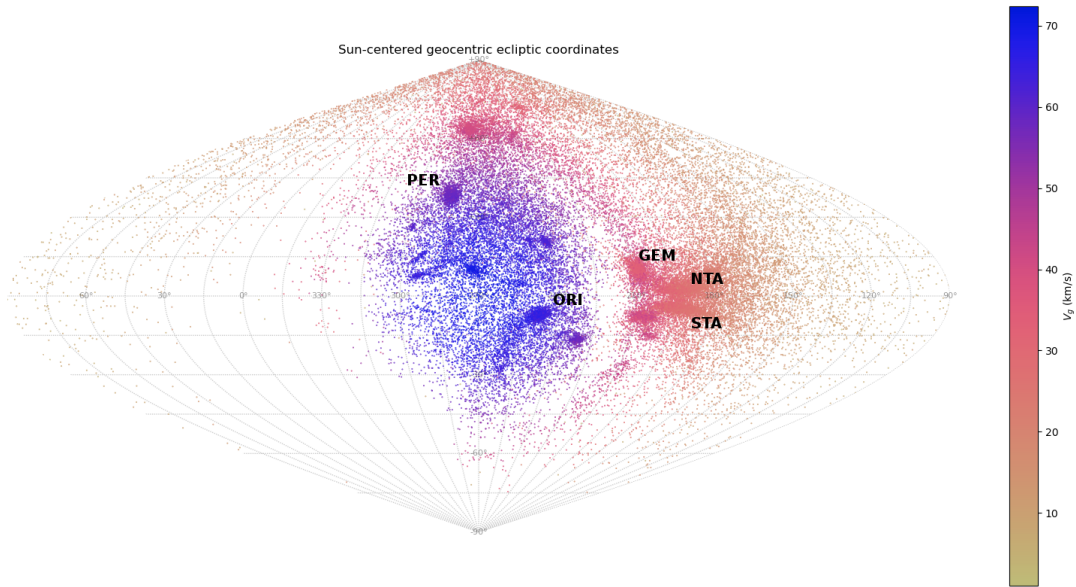
Figure 1.3: Meteor radiants in Sun-centred ecliptic coordinates collected in 2019 by the Global Meteor Network. The geocentric velocity is colour coded.
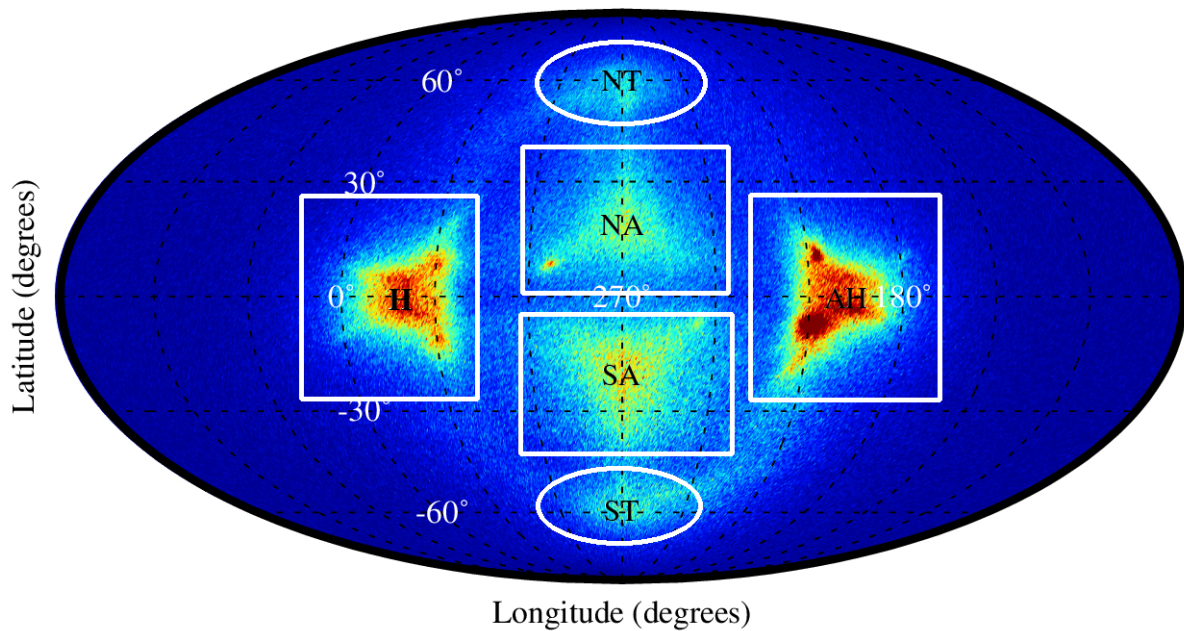
Figure 1.4: Sporadic meteoroid sources as seen by the Canadian Meteor Orbit Radar (CMOR; Brown et al., 2005) and the Southern Argentina Agile MEteor Radar (SAAMER; Janches et al., 2015). The relative areal density of meteoroid radiants is colour coded. H is the helion source, AH is the anti-helion source, NA and SA are the North and the South apex source, and NT and ST are the North and the South Toroidal source. Courtesy of Dr. Petr Pokorny.

Brown & Wiegert, 2009). 90° to the right of the centre is the anti-helion ("anti-Sun") sporadic source. These meteoroids have smaller velocities ($20 - 40 \, \mathrm{km \, s^{-1}}$) and are mainly produced by short-period comets, such as 2P/Encke (Wiegert et al., 2009).

On the opposite side of the plot, 90° to the left of centre, is the apparent location of the Sun. Because the GMN data was obtained using optical systems that only work during the night, Figure 1.3 shows no observed radiants close to that direction. On the other hand, Figure 1.4 comprising radar radiants clearly shows the helion source. Meteoroids coming from the helion source are on the post-perihelion leg (after *perihelion*, the closest point to the Sun) of the same family of orbits as those from the anti-helion source, which represents the pre-perihelion portion. Finally, the radiant concentrations at the top and bottom of the ring around the apex source (with speeds around $35 \, \mathrm{km \, s^{-1}}$) are known as the Toroidal sources (North and South) which are fed by short and long period comets, as well as near-Earth asteroids (Wiegert et al., 2009; Pokornỳ et al., 2014).

On a clear night when no major meteor showers are active, a human observer may see 1-2 meteors an hour. This number can increase dramatically if a major meteor shower is active, to about 100 meteors an hour. In rare occurrences, thousands of meteors an hour can be seen during meteor shower outbursts (Jenniskens, 2006). Figure 1.5 shows a meteor shower activity forecast for 2019 from (Moorhead et al., 2018).

The Zenithal Hourly Rate (ZHR) is the number of meteors a human observer would see in an hour of observation under ideal conditions, assuming that the shower radiant is at the zenith. Note that this is only an approximate upper limit to the number that can actually be seen - the observed number decreases by $1/\cos z_c$ where z_c is the angle between the shower radiant and the zenith (Arlt et al., 2008). For example, if the radiant was only 30° above the horizon ($z_c = 60$), one would only see half the number of meteors given by the ZHR.

Table 1.1 lists some major meteor showers that were predicted to be active in 2019. Most showers have an activity peak that only lasts on the order of hours to days. Note the Southern and Northern Taurids have small activity, but they last more than 2 months. The shower dura-
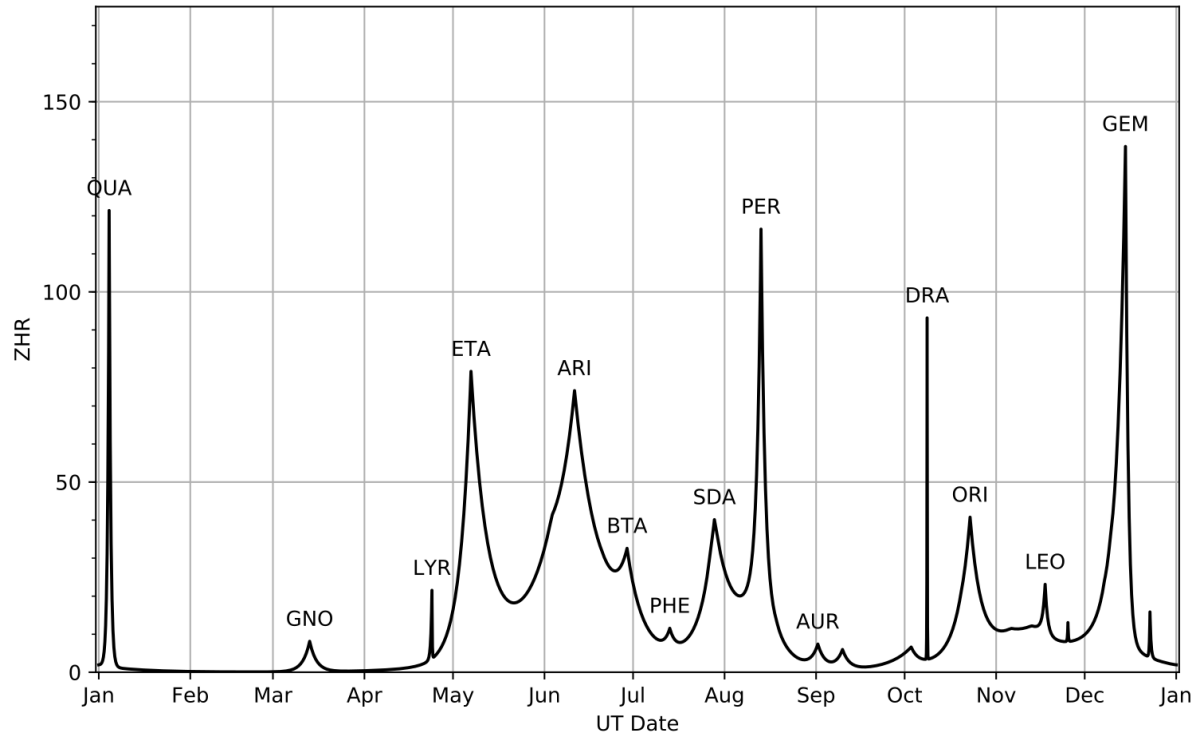
Figure 1.5: 2019 meteor shower activity forecast plot. Reproduced from Moorhead et al. (2018). The Zenithal Hourly Rate (ZHR) is the number of meteors a human observer would see in an hour if the meteor shower radiant was in the zenith.

tion and level of activity are determined in part by its age and evolution. For example, in 2019 there was a predicted Draconid outburst that was supposed to last only a matter of hours, but the predicted activity did not materialize. Models show that meteoroids causing the outburst were less than 100 years old (Egal et al., 2019), thus if they did collide with the Earth, the activity enhancement would have been substantial (the shower usually has a small ZHR in most years). But because the meteoroid stream was young and spatially narrow, uncertainties in the model made the prediction uncertain as well.

In contrast, the Taurid complex (NTA and STA) is likely tens of thousands of years old (Valsecchi et al., 1995), based on its long duration, low activity and broad radiant. The Taurid meteoroid stream is thus very spread out and tends to have consistently low inter-annual activity.

Meteoroids present a danger to satellites and astronauts in orbit. For an 8-hour low Earth

Table 1.1: Major meteor shower activity predictions for 2019 by Moorhead et al. (2018).

IAU code	Name	Peak date	Parent body	Speed (km/s)	ZHR (meteors/h)
QUA	Quadrantids	Jan 4	96P/Machholz	41	110
PER	Perseids	Aug 13	109P/Swift-Tuttle	59	110
DRA	Draconids	Oct 8	21P/Giacobini–Zinner	20	10-100
STA	Southern Taurids	Nov 05	2P/Encke	27	5
ORI	Orionids	Oct 23	1P/Halley	66	20
NTA	Northern Taurids	Nov 12	2P/Encke	29	5
GEM	Geminids	Dec 14	3200 Phaethon	35	140

orbit spacewalk, there is a 1 in 5000 probability of impact induced leakage leading to end of a space walk due to either an orbital debris or a meteoroid impact (Pate-Cornell & Sachon, 2001). Although the time-integrated flux of the sporadic background over the whole year is about a factor of 10 times higher than that of meteor showers (Jones & Brown, 1993), the main contributor to the increase of spacecraft impact risk from natural sources are young meteoroid streams which have not been perturbed, and whose activity can be order of magnitude higher than that of regular meteor showers. Such meteor showers are called meteor storms and their activity can reach up to several thousand meteors visible per hour to a ground-based observer (~ 1 meteor every second that can be seen by human eye; Jenniskens, 2006).

Beech & Brown (1993) estimated the impact probability of a Perseid meteoroid during the 1993 Perseid meteor outburst with an object the size of the Space Shuttle to be about 0.1%. During the outburst, the European Space Agency's (ESA) satellite Olympus lost an on-board gyroscope and spun out of control. Subsequent analysis has shown that the most probable explanation was a high-speed impact ($\sim 58\,\mathrm{km\,s^{-1}}$) of a Perseid meteoroid which produced impact generated plasma and short-circuited sensitive electronics (Caswell et al., 1995). Another

ESA satellite, the XMM-Newton X-ray space observatory lost two CCD imaging arrays while observing an object located in the direction of the south Toroidal sporadic source (Drolshagen, 2008; Cooke, 2014).

1.2.1 Meteoroid genesis and orbital evolution

Comets were first established as being meteor shower parent bodies in the nineteenth century. Schiaparelli (1867) measured the radiant locations of the Perseid and Leonid meteor showers, and demonstrated that these showers had orbits with striking similarity to comets 109P/Swift-Tuttle and 55P/Tempel-Tuttle, respectively. Comets are small Solar System bodies composed of a mixture of rock, dust, and different ices. The most abundant are water, carbon dioxide, carbon monoxide, methane, and ammonia ice (Greenberg et al., 1998). Although described as "dirty snowballs" in the past, recent findings indicate that their dust-to-ices ratio is in fact a factor of two (or more) larger (Fulle et al., 2017), making them more akin to icy dirtballs (Keller, 1989).

Comets are among the most primitive remnants of the formation of the Solar System. After initially forming in the inner Solar System, they were ejected during encounters with the growing giant planets far from the Sun early in Solar System history (Tsiganis et al., 2005; Levison et al., 2008). Most of the time, comets reside in a low-temperature environment far from the Sun and remain dormant. When they are flung into an orbit that brings them closer to the Sun by gravitational interactions with passing stars or the tides of the galaxy (Duncan et al., 1987), the ices start to sublimate and the comet develops a coma.

The most significant volatile sublimation is due to water ice sublimation which starts at 152 K, a temperature which cometary nuclei reach when around 3 au from the Sun (1 au is the average distance from the Sun to the Earth). Other ices start sublimating at larger distances due to a much lower sublimation temperature (e.g. 25 K for carbon monoxide), but they are not the main drivers of cometary activity (Womack et al., 2017).

Sublimating ices form jets of gas that lift dust particles from the comet surface. As the

height from the surface increases, the gas drag becomes smaller and the particles are decel-
erated by the comet's gravity. They achieve a terminal ejection velocity in the range from
$1 - 1000 \, \mathrm{m \, s^{-1}}$, depending on the size and density of the particle, as well as the comet distance
from the Sun (Vaubaillon et al., 2005). Several authors have developed hydrodynamical models
describing the dust-gas interaction, but the predicted ejection velocities may differ significantly
between models (Whipple, 1951; Jones, 1995; Crifo & Rodionov, 1997). Another important
physical process is the distributed coma production, i.e. sublimation of embedded ices occur-
ring on the lifted meteoroids themselves. Including this effect reduces the resulting ejection
velocities compared to surface-only production (Brown & Jones, 1998).

Meteor shower outbursts can be predicted in time and approximately in expected strength
by numerically modeling orbits of meteoroids after ejection from their parent comets (Vaubail-
lon et al., 2005). In these cases, actions can be taken to minimize the impact risk from outbursts
to both satellites and astronauts in orbit.

As an example, Vaubaillon et al. (2011) and Maslov (2011) predicted the 2011 outburst of
the Draconid meteor shower which was subsequently well observed using optical (Koten et al.,
2014; Šegon et al., 2014) and radar methods (Kero et al., 2012; Ye et al., 2013a). A year later
an unpredicted Draconid outburst was observed which reached meteor storm levels of ~ 9000
meteors per hour (Ye et al., 2013b) for smaller radar meteoroid sizes (the visual rate was an
order of magnitude lower). Such cases demonstrate that existing models do not always match
the observations: either there is a meteor shower outburst that was not predicted, or a predicted
outburst which did not happen. Egal et al. (2019) predicted an enhanced concentration of Dra-
conid meteoroids in 2018 close to ESA's GAIA spacecraft which was re-oriented in response
to minimize the exposed satellite area to the incoming meteoroid stream.

To perform numerical modelling of meteoroid streams, hundreds of thousands to millions
of test particles with different ejection velocities, masses, and densities are ejected from the
sunlit side of the parent comet and their motion is integrated in time. It is often assumed
that there is no interaction with the parent body. Because the comet size (kilometer scale) is

negligible compared to total integrated distances, the particles are created at the position of the parent body with the velocity equal to the sum of the parent motion and ejection velocity vectors. It is also assumed that the particles do not interact with one another (Vaubaillon et al., 2005). The motion can be described by a fundamental specific force equation which is solved numerically

$$\vec{x}'' = \frac{d\vec{v}}{dt} = F(\vec{x}', \vec{x}, t) = F_g(\vec{v}, \vec{x}, t) + F_r(\vec{v}, \vec{x}, t), \qquad (1.1)$$

where $\vec{x}$ is the particle position vector with respect to the Sun, $\vec{v}$ its velocity vector, and t is the simulation time. The gravitational (F_g) and non-gravitational (F_r) specific forces are considered separately (Klačka & Kocifaj, 2008). High order integrators (usually 15th order) are used to integrate the meteoroid motion in time, taking care to account for machine precision and numerical artifacts (Everhart, 1985; Rein & Spiegel, 2014). Gravitational interactions with the Sun, all eight planets, and the Moon are included by using the classical law of universal gravitation

$$F_g(\vec{v}, \vec{x}, t) = -\frac{Gm_\odot}{|\vec{x}|^3}\vec{x} - \sum_{p=1}^{9} Gm_p \left(\frac{\vec{x} - \vec{x_p}}{|\vec{x} - \vec{x_p}|^3} + \frac{\vec{x_p}}{|\vec{x_p}|^3} \right), \qquad (1.2)$$

where G is the gravitational constant, $m_\odot$ is the mass of the Sun, m_p are masses of individual planets and the Moon, and $\vec{x_p}$ is the position vector of the planet with respect to the Sun.

Non-gravitational forces acting on the test particle are related to solar radiation, but usually just the Poynting–Robertson effect is included. It can be described as a relativistic effect which causes the particle to lose angular momentum and over time spiral into the Sun. As the particles are moving at tens of kilometers a second ($\sim 10^{-4}c$), from the reference frame of individual particles it appears that that the solar radiation is coming from a slightly forward direction due to the aberration of light, thus the radiation absorption causes a drag force. This effect depends on the particle size. To characterize this behaviour, we can consider the ratio β between the solar radiation pressure F_r and the force of gravity $F_{g\odot}$ between the particle and the Sun (Burns

et al., 1979)

$$\beta = \frac{F_r}{F_{g\odot}} = \frac{L_\odot \pi R^2}{4\pi G M_\odot m} \frac{\bar{Q}'_{pr}}{c}, \tag{1.3}$$

where $L_\odot$ is the solar luminosity, R the particle radius, $\bar{Q}'_{pr}$ the radiation pressure efficiency factor averaged over all wavelengths and weighted by the solar spectrum, and m is the particle mass. Particles with $\beta \geq 0.5$ will be blown out of the Solar System on hyperbolic orbits because the radiation pressure exceeds the force of gravity. They are called β-meteoroids and typically have 1 μm scale diameters, i.e. they are too small to be considered in meteoroid ejection models (Grün & Zook, 1980). On the other hand, particles with $\beta < 0.1$ (larger than ~ 10 μm) will spiral into the Sun approximately after

$$\tau = \frac{1}{4} \left(\beta \frac{G m_\odot}{c} \right)^{-1} a_0^2, \tag{1.4}$$

where a_0 is the particle's initial semi-major axis (Leinert & Grün, 1990; Krivov et al., 2006). Assuming a $\beta = 0.1$ particle was ejected at $a = 1$ au, it will take it abound 10,000 years to spiral into the Sun.

Particles with $0.1 < \beta < 0.5$ may spiral in or be ejected, depending on their physical properties. Particles >1 mm are largely unaffected because they have large mass to surface areas and the radiation pressure is a second order effect. However, we still consider it for all meteoroids even on shorter time scales because it plays a role in meteoroid stream dispersion and can slightly alter orbital paths, an important consideration for some meteor outbursts with orbits near the Earth. The radiation pressure force expression is

$$F_r(\vec{v}, \vec{x}, t) = \beta \frac{G M_\odot}{|\vec{x}|^2} \left[\left(1 - \frac{\vec{v} \cdot \hat{e}_x}{c} \right) \hat{e}_x - \frac{\vec{v}}{c} \right],$$
$$\hat{e}_x = \frac{\vec{x}}{|\vec{x}|}. \tag{1.5}$$

The motions of test particles are integrated until they make a close encounter with the

Earth. Usually particles that approach the Earth within $\Delta x = |\vec{v}|\Delta T$ are considered as potential impactors, where ΔT is the expected time of the shower (Egal et al., 2019). Major sources of uncertainty related to shower predictions are the unknown true orbit and the activity of the parent body (i.e. total dust production) at the time of meteoroid ejection.

In many cases the ejection may have happened thousands of years ago, and no reliable comet observations exist at that time. For older showers, the influence of non-gravitational forces on meteoroids and perturbations of meteoroid orbits after close encounters with Jupiter is particularly important to their future motion (Vaubaillon, 2017). Jupiter's gravity scatters compact streams and increases the prediction uncertainty. For younger showers, where the dynamical evolution has not had enough time to disperse the stream and the influence of non-gravitational forces is negligible, the main causes of prediction uncertainty are the unknown ejection velocities of meteoroids from comet surfaces.

Measuring the real dispersion of the radiant (the angular spread in the radiant) in a young meteor shower could give an independent estimate of the ejection velocities, potentially enabling more accurate predictions of the future activity of a particular shower. During modelling, one also has to assume a comet size, density, and the ejected dust mass range and mass distribution. The mass distribution is usually described as a power-law, i.e. a line in a number vs mass log-log plot. The cumulative mass distribution index is the slope of that line.

In-situ observations of the comet 67P/Churyumov–Gerasimenko by the Rosetta probe show that at sizes >1 mm the particles follow a power-law and the cumulative mass index is constant at around $s = 2$ (i.e. the number of particles increases ten times for every order of magnitude decrease in mass). At sizes <1 mm the mass index varies from $s = 1.3$ beyond 2 au (i.e. more larger particles) to $s = 1.9$ at perihelion (i.e. the closest point to the Sun, at around 1.2 au) (Fulle et al., 2016).

The observed mass distribution became dramatically different after the comet passed the closest point to the Sun – the mass ejected prior to perihelion was dominated by particles of 1×10^{-6} kg, while much smaller 1×10^{-9} kg particles dominated the mass output in post-

perihelion ejection. This observation may suggest that the meteoroids that produced the 2012 Draconid outburst might have been ejected after the perihelion of the parent comet, as the outburst was dominated by smaller meteoroids visible only by radar (Ye et al., 2013b). In all the preceding cases, activity profiles of the shower are known (which helps constrain models) but the radiant dispersion has never been reliably measured; the latter would provide direct estimates of meteoroid ejection speeds and hence improve models.

1.2.2 Atmospheric entry

Individual meteoroids are too small to be detected in space; hence we use the atmosphere as a detector. Through collision with air molecules, the meteoroid rapidly loses kinetic energy. The resulting light, heat, and ionization are used as proxies to estimate the meteoroid mass and pre-atmospheric orbit.

The interaction between the meteoroid and the atmosphere can be described by mass loss equations which use conservation of momentum and energy. Assuming a non-fragmenting solid spherical particle, the received thermal energy flux from air particles hitting the meteoroid is balanced by radiative losses, temperature increase, and mass loss (Jones & Kaiser, 1966), which can be formulated as

$$\pi R^2 \Lambda \frac{\rho_a v^3}{2} = 4\pi R^2 \epsilon \sigma_b (T_s^4 - T_0^4) + \frac{4}{3}\pi R^3 \rho_m c \frac{dT_s}{dt} - L\frac{dm}{dt}, \qquad (1.6)$$

where R is the particle radius, Λ the heat transfer coefficient (usually unity if there is no shielding), ρ_a the atmosphere density, v the instantaneous velocity, ϵ the emissivity coefficient, σ_b the Stefan-Boltzman constant, T_s the meteoroid surface and T_0 the atmosphere temperature, ρ_m the meteoroid density, and L is the energy needed to ablate a unit of mass. The constants in this equation are Λ, ϵ, σ_b, ρ_m, and L.

For particles in the meteoroid size range, the altitude at which the received energy flux is larger than radiative and heating losses is around $110 - 130$ km, which corresponds to the be-

ginning heights of most meteors (Popova et al., 2019). In this regime the mass loss dominates, so the radiation and heating can be disregarded, and the expression can be simplified to

$$\frac{dm}{dt} = -\Lambda \frac{\pi R^2 \rho_a v^3}{2L} \, . \tag{1.7}$$

The momentum a spherical meteoroid loses in time Δt through interaction with an encountered column of atmosphere is

$$\Delta p = -\rho_a S v^2 \Gamma \Delta t \, , \tag{1.8}$$

where S the meteoroid's cross-sectional area, and Γ the drag coefficient. Deceleration can be simply found if we know that $F = m\frac{dv}{dt}$ and $F = \frac{\Delta p}{\Delta t}$

$$\frac{dv}{dt} = -\frac{\rho_a S v^2 \Gamma}{m} \, . \tag{1.9}$$

Equations 1.7 and 1.9 can be connected by introducing the ablation coefficient σ, which describes the mass loss rate and hence the instantaneous total meteoroid mass as a function of velocity (Ceplecha et al., 1998)

$$\sigma = \frac{\Lambda}{2L\Gamma} \, . \tag{1.10}$$

The equations above assume that the meteoroid's only source of energy is its kinetic energy. It is usually assumed that at any instant in time a portion of the meteoroid kinetic energy is radiated away as light in the form

$$I = -\tau \frac{dE_k}{dt} = -\tau \left(\frac{v^2}{2} \frac{dm}{dt} + mv \frac{dv}{dt} \right) \, , \tag{1.11}$$

where I is the luminous intensity in watts and τ is the (dimensionless) luminous efficiency. The exact value of luminous efficiency is uncertain, but it is around 1%, plus or minus an order of magnitude (Subasinghe & Campbell-Brown, 2018), and likely depends on height, speed,

intensity, and mass. Equations 1.7 and 1.9 can be integrated analytically (Pecina & Ceplecha, 1983), although they are often numerically fit to observations to invert physical properties of meteoroids (Borovička et al., 2007; Kikwaya et al., 2011).

Optical meteor observations measure the meteor brightness in the units of apparent stellar magnitude, so to compare meteor observations to the simulated brightness, one needs to convert I to an apparent magnitude. In short, the brighter an observed object is, the lower its magnitude. A difference of 1 magnitudes from some defined zero point in the spectral bandpass of an instrument corresponds to a difference in brightness of ~ 2.5 times. Thus the magnitude M of a meteor at a given point in time can be calculated as

$$M = -2.5 \log_{10} \frac{I}{P_{0m}} , \qquad (1.12)$$

where P_{0m} is a power of a zero magnitude meteor in a given instrumental spectral bandpass. For example, Weryk & Brown (2013) computed $P_{0m} = 1210\,\text{W}$ assuming a black body meteor with a temperature of $T = 4500\,\text{K}$ and a spectral bandpass appropriate to Sony HAD CCD cameras. Note that spectral observations indicate that there are several spectral classes of meteors (classified by sodium and iron abundance) and no "average" spectrum exists (Vojáček et al., 2019). Using the black body distribution is just a rough approximation to the actual spectral energy distribution. Meteors observed by the human eye are usually in the range of magnitudes from $+2^M$ to $+4^M$; meteors brighter than $+2^M$ are small in number, while meteors fainter than $+4^M$ are mostly below the sensitivity of the human eye (Millman & Burland, 1961). Meteorite dropping fireballs are brighter events, with magnitudes typically brighter than -4^M.

One important phenomenon that classical single-body equations do not capture is fragmentation. From photographic observations in the 1950s and 60s it was discovered that meteors are shorter and decelerate more rapidly than predicted by the classical single-body equations (Verniani, 1969). Furthermore, it was noticed that meteors often show long wakes of dust behind the leading body. These observations can be best explained by assuming fragmentation is present.

Generally, two types of fragmentation are considered (Borovička et al., 2007): The first is erosion (continuous fragmentation), in which grains of dust in the 10s to 100s micron range are constantly released from the meteoroid. The second is disruption (gross fragmentation) in which the main body fissions into several parts of comparable size at one point in time.

Based on high-resolution observations, Subasinghe et al. (2016) has shown that 85% of mm-sized meteors show long wakes which are consistent with continuous fragmentation, and about 5% show gross fragmentation. The remaining 10% appear to be single bodies, but Campbell-Brown (2017) was only able to explain their observed light production by assuming a small amount of continuous fragmentation. This indicates that fragmentation is a common phenomenon that must be included in models, but accounting for fragmentation is difficult and it tremendously increases the complexity of ablation models.

1.3   Optical meteor observations

Meteoroid ejection speeds and other physical simulation parameters can be constrained by observations, but the expected physical radiant dispersion of a young stream is very small and beyond the detection limits of most regular meteor detection systems. Brown & Jones (1998) have shown that the true radiant dispersion of a meteor shower, if it could be measured with a precision of ~0.1°, would allow a direct estimate of the true age of the encountered stream and could also be used to measure ejection speeds. The accuracy of the ejection velocity and age estimation would have to be investigates on a case-by-case basis for every meteor shower.

Optical meteor observations historically have been done photographically or using a low-light video camera. With the advent of highly sensitive and low-cost CCD cameras in the early 1990s, video meteor observations became one of the preferred way to optically observe meteors (Molau & Nitschke, 1996). These video cameras are usually operated at 25 to 30 frames per second (FPS), have all-sky to moderate fields of view (180° to 20°), and can detect meteors down to magnitudes from $+2^M$ to $+5^M$ (Molau & Gural, 2005; Jenniskens et al., 2011).
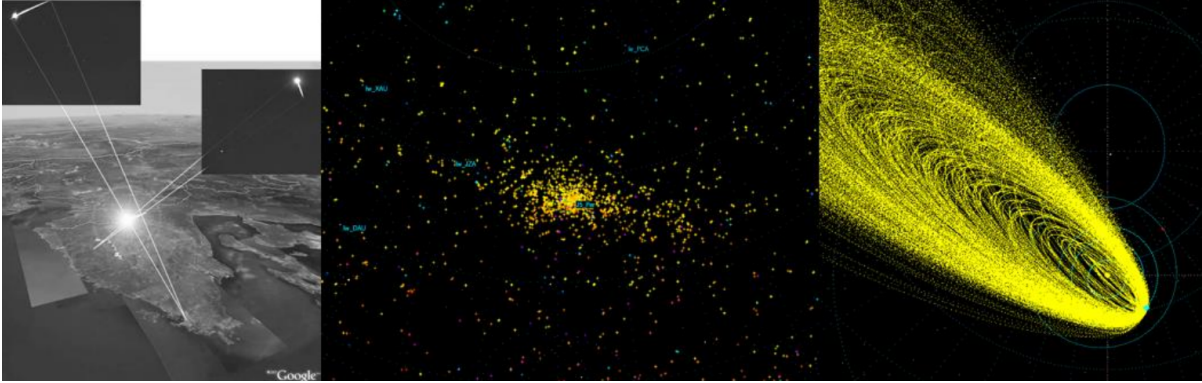
Figure 1.6: Left: Geometry of a meteor observed from 2 stations allowing a three dimensional trajectory to be computed; Middle: Radiants of 2009 Perseids projected on a celestial sphere. Right: Orbits of Perseid meteoroids in the Solar System (courtesy of the Croatian Meteor Network).

Meteors are detected using one of several available automated algorithms which provides measurements of meteor position and brightness in time. A minimum of four frames are required to reliably estimate the meteor velocity (Albin et al., 2016), which puts an effective lower limit for observed meteor duration to around 0.15 s. By observing a meteor from multiple locations it is possible to triangulate its trajectory in 3D space, and by measuring the initial velocity it is possible to estimate its orbit in the Solar System (see Figure 1.6). Most optical systems can measure positions of meteors with a precision on the order of 1 arc minute ($\sim$50 m at 100 km, the typical meteor height), yielding a radiant and velocity precision of $0.5°$ and $1\,\mathrm{km\,s^{-1}}$, respectively (Jenniskens et al., 2011), while radar trajectories derived from transverse scattering detections are generally less precise (Weryk & Brown, 2012). Optical observations have historically been a critical resource for studies of meteoroid fragmentation and physical properties (Jacchia et al., 1967), including recovery of meteorites produced by meteorite-dropping fireballs (Spurnỳ, 2015).

Accurately measuring pre-atmospheric velocities of meteors (i.e. the velocity before any atmospheric deceleration) is essential in estimating the velocity distribution inside the stream. This also is key to precisely estimating radiant dispersion, as well the influence of non-gravitational forces on meteoroids which reduce the size of their orbits relative to purely Kep-

lerian orbits.

For this thesis, the highest resolution optical system for meteor observations developed to date are used, namely the Canadian Automated Meteor Observatory (CAMO) tracking system (Weryk et al., 2013). The system uses a wide-field high speed camera ($30° \times 30°$ field of view) which detects meteors in real time and then cues a pair of mirrors which track the meteor and redirect its light through a telescope ($1.5° \times 1.5°$ field of view). The light is amplified using an image intensifier and the video is captured using a high-resolution camera operated at 100 frames per second. This setup gives a spatial resolution of about 1 arc second (~0.5 m at 100 km) and is capable of routinely detecting individual meteor fragments, a unique capability among optical systems. The tracking system has a meteor limiting magnitude (i.e. sensitivity threshold) of about $+5.5^M$. The system is described in more detail in Chapter 6.

1.3.1   Computing meteor trajectories

In this section we give a brief overview of methods for meteor trajectory estimation. See Chapter 3 for a more detailed discussion and quantitative development.

Given a set of observations of the same meteor from different locations (the distance between the observers should usually be at least 50 km for typical optical systems), one may use several approaches to compute the meteor trajectory. Historically, the first method that was developed consists of fitting planes through observations from every location - this can be done as meteors should follow a great circle on the celestial sphere (Ceplecha, 1987). The trajectory is assumed to be a straight line in space and is found as the intersection of these planes.

Another approach is to consider individual measurements from all observers as lines of sight and fit a 3D trajectory directly to measurements as a line which minimizes the distance between all lines of sight (Borovička, 1990).

The second important measurement in reconstructing the meteoroid's orbit is its pre-atmosphere velocity. Conventionally, this velocity is estimated by projecting observations to the trajectory line and either computing the average velocity of the whole meteor (which will surely include

some deceleration), or by computing the average velocity of the first half of the observed flight to minimize the effects of deceleration. Alternatively, one may fit an empirical or physical deceleration model to reconstruct the pre-atmosphere velocity (Whipple & Jacchia, 1957).

In recent years, new methods have been developed which couple the trajectory and velocity estimation by modelling the meteoroid flight dynamics. In this approach, the model is tuned to minimize the difference between modelled and observed positions on the sky and produce a best fit. The flight models may be empirical and described by simple analytical expressions (Gural, 2012), or full physical ablation models described by differential equations (see section 1.2.2) requiring integration (Sansom et al., 2019).

Generally, these approaches provide improved trajectory accuracy, but are model-dependent and such models may be hard to fit to data, potentially introducing biases (Egal et al., 2017). Hajduková et al. (2017) have shown that orbits of the annual Geminid meteor shower published by different authors show large variability in the mean geocentric velocity, an indication of inconsistency in the methods used for data reduction (the geocentric velocity is the pre-atmospheric velocity corrected for Earth's gravity and rotation). The reduction methods are usually not transparent; their details are either unpublished or described in insufficient details. Hajduková et al. (2017) have also shown a systematic underestimation of the observed geocentric velocity compared to modelled values, either indicating a problem with the methods, or existence of a physical process modifying the meteoroid orbits.

1.3.2 Meteor shower dispersions

Hajduková et al. (2017) have also shown a large variation in the observed Geminid meteor shower dispersion between observations from different authors. A part of the problem may also be the meteor shower association algorithm - as shown in Figure 1.3, meteor showers are surrounded by sporadic meteors and it may be hard to avoid sporadic contamination. As no formal, quantitative definition of a meteor shower exists, the separation of shower meteors from the background is often done manually (Jenniskens et al., 2016).

Borovička et al. (2014) have also shown differences between radiant dispersions - the high-precision manual radiant measurements of the 2011 Draconid outburst by Ondrejov Observatory cameras all fall within a radius of about 0.5°, while the measurements by Toth et al. (2012) and Trigo-Rodríguez et al. (2013) lie within a radius of 1°-2°. This strongly suggests that in many cases the measurement error dominates dispersion measurement, obscuring the true age of meteor showers.

Šegon et al. (2017) confirmed the connection between seven parent bodies and newly discovered meteor showers by performing dynamical modelling of meteoroid ejection from said parent bodies. The most striking parts of their paper were plots comparing simulated and observed radiant distribution, reproduced in Figure 1.7. The observed radiants have an order of magnitude larger dispersion than the simulated radiants, indicating that either the observations are not precise enough (Kresák, 1992), or the simulation assumptions are incorrect (Jenniskens, 1998). A rigorous observational error analysis is rarely done and the true radiant and velocity accuracy remains unknown. Finally, very little research into dispersions of meteor shower radiants was done since Kresák & Porubcan (1970) and this thesis aims to make further progress in this regard.

1.4 Thesis Goals

The primary goal of this thesis is to accurately measure radiants and velocities of meteors through high-precision optical measurements with the goal of providing constraints which may be used in meteor shower prediction models. Improved prediction accuracy is essential for mitigating the risk meteoroids from young unperturbed meteor streams pose to astronauts and spacecraft.

The thesis is highly focused on understanding the measurement accuracy and errors associated with meteor trajectory estimation. The specific objectives of this work are:

1. To determine the accuracy and limits to measurements of the pre-atmosphere velocities
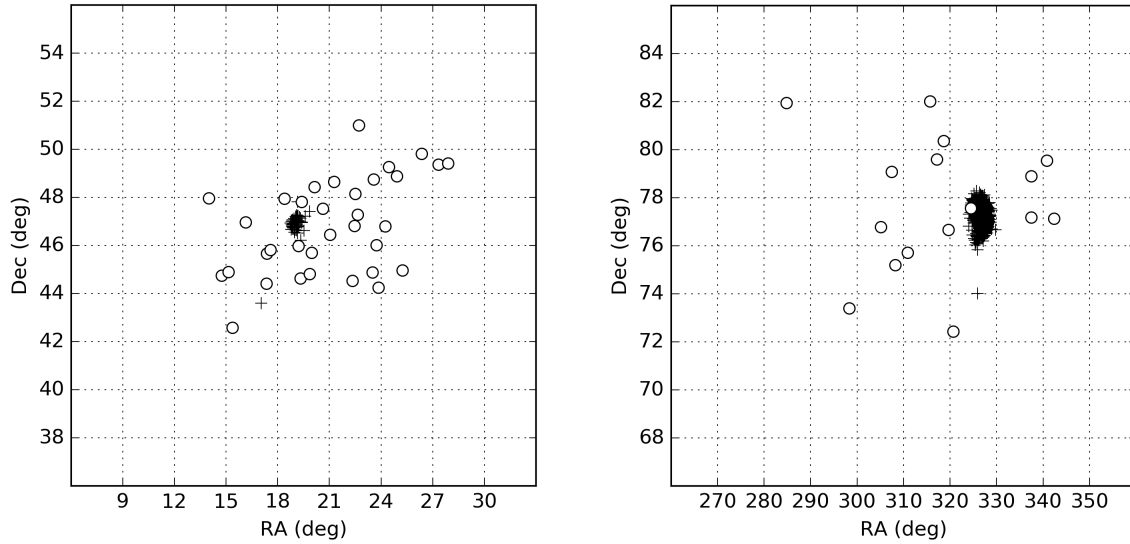
Figure 1.7: Left: Observed (circles) and simulated radiants (crosses) of 49 Andromedids. Right: κ Cepheids. Credit: Šegon et al. (2017), A&A, 598, A15, 2017, reproduced with permission, ©ESO.

of meteors.

2. To determine the minimum radiant accuracy needed to measure the dispersion of meteor showers with the smallest radiant areas.

3. To investigate different methods of meteor trajectory estimation and what meteor radiant accuracy one may expect for a particular optical observation system.

4. To investigate the influence of meteor physical properties and morphology on the measurement accuracy.

5. To apply the procedures developed in this thesis to measure the true physical dispersion of at least one meteor shower.

In Chapter 2 (published as Vida et al., 2018) I investigate the amount of deceleration experienced by meteors before they become detectable by three representative optical systems. This shows that the pre-atmosphere velocity accuracy is model dependent. In Chapter 3 (published as Vida et al., 2020d) I develop a novel method of meteor trajectory estimation and a novel meteor trajectory simulator which is used to investigate the performance of different methods

of meteor trajectory estimation and provides rigorous error estimates. In Chapter 4 (published as Vida et al., 2020b) I give the results of the theoretical development done in Chapter 3.

In Chapter 5 (published as Vida et al., 2020c) I develop a novel method of meteor shower mass index estimation and apply it, together with the meteor trajectory estimation method developed in Chapter 3, on high-precision observations of the 2018 Draconid outburst.

In Chapter 6 (published as Vida et al., 2020a) I describe the upgraded CAMO hardware, data calibration, and reduction pipeline. Next, I demonstrate that the trajectory measurement accuracy is heavily dependent on meteor morphology, the type, and amount of fragmentation. In this Chapter I also show the first meteoroid compressive strengths measurements derived from direct observations of meteoroid gross fragmentation.

Finally, in Chapter 7 I measure the dispersion of the 2019 Orionid meteors showers using high-precision CAMO data. The overall thesis work is summarised in Chapter 8.

Bibliography

Agarwal, J. 2019, Science, 366, 1192

Albin, T., Koschny, D., Soja, R., Srama, R., & Poppe, B. 2016, in International Meteor Conference Egmond, the Netherlands, 2-5 June 2016, 20–25

Arlt, R., Asher, D. J., Brown, P. G., et al. 2008, Handbook for meteor observers (International Meteor Organization)

Beech, M., & Brown, P. 1993, Monthly Notices of the Royal Astronomical Society, 262, L35

Borovička, J. 1990, Bulletin of the Astronomical Institutes of Czechoslovakia, 41, 391

—. 2005, Proceedings of the International Astronomical Union, 1, 249

Borovička, J., Koten, P., Shrbenỳ, L., Štork, R., & Hornoch, K. 2014, Earth, Moon, and Planets, 113, 15

Borovička, J., Spurnỳ, P., & Koten, P. 2007, Astronomy & Astrophysics, 473, 661

Brown, P., & Jones, J. 1998, Icarus, 133, 36

Brown, P., Jones, J., Weryk, R., & Campbell-Brown, M. 2005, in Modern Meteor Science An Interdisciplinary View (Springer), 617–626

Brown, P., Spalding, R., ReVelle, D. O., Tagliaferri, E., & Worden, S. 2002, Nature, 420, 294

Brownlee, D. E. 1985, Annual Review of Earth and Planetary Sciences, 13, 147

Burns, J. A., Lamy, P. L., & Soter, S. 1979, Icarus, 40, 1

Campbell-Brown, M. 2007, Dust in Planetary Systems, 643, 11

—. 2017, Planetary and Space Science, 143, 34

Campbell-Brown, M., & Jones, J. 2006, Monthly Notices of the Royal Astronomical Society, 367, 709

Campbell-Brown, M., & Wiegert, P. 2009, Meteoritics & Planetary Science, 44, 1837

Caswell, R. D., McBride, N., & Taylor, A. 1995, International Journal of Impact Engineering, 17, 139

Ceplecha, Z. 1987, Bulletin of the Astronomical Institutes of Czechoslovakia, 38, 222

Ceplecha, Z., Borovička, J., Elford, W. G., et al. 1998, Space Science Reviews, 84, 327

Cooke, W. J. 2014

Crifo, J., & Rodionov, A. 1997, Icarus, 127, 319

Drolshagen, G. 2008, Advances in space Research, 41, 1123

Drolshagen, G., & Moorhead, A. V. 2019, The Meteoroid Impact Hazard for Spacecraft, ed. G. O. Ryabova, D. J. Asher, & M. J. Campbell-Brown, 255

Duncan, M., Quinn, T., & Tremaine, S. 1987, The Astronomical Journal, 94, 1330

Egal, A., Gural, P., Vaubaillon, J., Colas, F., & Thuillot, W. 2017, Icarus, 294, 43

Egal, A., Wiegert, P., Brown, P., et al. 2019, Icarus, 330, 123

Everhart, E. 1985, in International Astronomical Union Colloquium, Vol. 83, Cambridge University Press, 185–202

Fulle, M., Marzari, F., Della Corte, V., et al. 2016, The Astrophysical Journal, 821, 19

Fulle, M., Della Corte, V., Rotundi, A., et al. 2017, Monthly Notices of the Royal Astronomical Society, 469, S45

Genge, M. J., Engrand, C., Gounelle, M., & Taylor, S. 2008, Meteoritics & Planetary Science, 43, 497

Greenberg, J. M., et al. 1998, Astronomy and Astrophysics, 330, 375

Grün, E., & Zook, H. 1980, in Symposium-International Astronomical Union, Vol. 90, Cambridge University Press, 293–298

Gural, P. S. 2012, Meteoritics & Planetary Science, 47, 1405

Hajduková, M., Koten, P., Kornoš, L., & Tóth, J. 2017, Planetary and Space Science, 143, 89

Hoffman, K., Hyde, J., Christiansen, E., & Lear, D. 2020, in First International Orbital Debris Conference, 1–14

Jacchia, L., Verniani, F., & Briggs, R. E. 1967, Smithsonian Contributions to Astrophysics, 10, 1

Janches, D., Close, S., Hormaechea, J. L., et al. 2015, The Astrophysical Journal, 809, 36

Jenniskens, P. 1998, Earth, planets and space, 50, 555

—. 2006, Meteor showers and their parent comets (Cambridge University Press)

Jenniskens, P., Gural, P., Dynneson, L., et al. 2011, Icarus, 216, 40

Jenniskens, P., Nénon, Q., Albers, J., et al. 2016, Icarus, 266, 331

Jones, J. 1995, Monthly Notices of the Royal Astronomical Society, 275, 773

Jones, J., & Brown, P. 1993, Monthly Notices of the Royal Astronomical Society, 265, 524

Jones, J., & Kaiser, T. 1966, Monthly Notices of the Royal Astronomical Society, 133, 411

Keller, H. 1989, in Physics and Mechanics of Cometary Materials, Vol. 302

Kero, J., Fujiwara, Y., Abo, M., Szasz, C., & Nakamura, T. 2012, Monthly Notices of the Royal Astronomical Society, 424, 1799

Kikwaya, J.-B., Campbell-Brown, M., & Brown, P. 2011, Astronomy & Astrophysics, 530, A113

Klačka, J., & Kocifaj, M. 2008, Monthly Notices of the Royal Astronomical Society, 390, 1491

Koschny, D., & Borovicka, J. 2017, WGN, Journal of the International Meteor Organization, 45, 91

Koten, P., Vaubaillon, J., Tóth, J., Margonis, A., & Ďuriš, F. 2014, Earth, Moon, and Planets, 112, 15

Kresák, L. 1992, Contributions of the Astronomical Observatory Skalnate Pleso, 22, 123

Kresák, L., & Porubcan, V. 1970, Bulletin of the Astronomical Institutes of Czechoslovakia, 21, 153

Krivov, A., Löhne, T., & Sremčević, M. 2006, Astronomy & Astrophysics, 455, 509

Lauretta, D., Hergenrother, C., Chesley, S., et al. 2019, Science, 366

Leinert, C., & Grün, E. 1990, in Physics of the inner heliosphere I (Springer), 207–275

Levison, H. F., Morbidelli, A., VanLaerhoven, C., Gomes, R., & Tsiganis, K. 2008, Icarus, 196, 258

Maslov, M. 2011, WGN, Journal of the IMO, 39, 3

Millman, P. M., & Burland, M. S. 1961, The Astronomical Journal, 66, 291

Molau, S., & Gural, P. 2005, WGN, Journal of the International Meteor Organization, 33, 15

Molau, S., & Nitschke, M. 1996, WGN, Journal of the International Meteor Organization, 24, 119

Moorhead, A., Cooke, B., & Moser, D. 2018

—. 2019

Pate-Cornell, E., & Sachon, M. 2001, IEEE Transactions on Aerospace and Electronic Systems, 37, 134

Pecina, P., & Ceplecha, Z. 1983, Bulletin of the Astronomical Institutes of Czechoslovakia, 34, 102

Plane, J. M. 2012, Chemical Society Reviews, 41, 6507

Pokornỳ, P., Janches, D., Brown, P., & Hormaechea, J. L. 2017, Icarus, 290, 162

Pokornỳ, P., Vokrouhlickỳ, D., Nesvornỳ, D., Campbell-Brown, M., & Brown, P. 2014, The Astrophysical Journal, 789, 25

Popova, O., Borovička, J., & Campbell-Brown, M. D. 2019, Modelling the Entry of Meteoroids, ed. G. O. Ryabova, D. J. Asher, & M. J. Campbell-Brown, 9

Rein, H., & Spiegel, D. S. 2014, Monthly Notices of the Royal Astronomical Society, 446, 1424

Sansom, E. K., Jansen-Sturgeon, T., Rutten, M. G., et al. 2019, Icarus, 321, 388

Schiaparelli, M. 1867, Astronomische Nachrichten, 68, 331

Šegon, D., Andreić, Ž., Gural, P. S., et al. 2014, Earth, Moon, and Planets, 112, 33

Šegon, D., Vaubaillon, J., Gural, P. S., et al. 2017, Astronomy & Astrophysics, 598, A15

Shober, P., Jansen-Sturgeon, T., Sansom, E., et al. 2019, The Astronomical Journal, 158, 183

Spurnỳ, P. 2015, Proceedings of the International Astronomical Union, 10, 69

Subasinghe, D., & Campbell-Brown, M. 2018, The Astronomical Journal, 155, 88

Subasinghe, D., Campbell-Brown, M. D., & Stokan, E. 2016, Monthly Notices of the Royal Astronomical Society, 457, 1289

Taylor, A., Baggaley, W., & Steel, D. 1996, Nature, 380, 323

Toth, J., Piffl, R., Koukal, J., et al. 2012, WGN, Journal of the International Meteor Organization, 40, 117

Trigo-Rodríguez, J. M., Madiedo, J. M., Williams, I. P., et al. 2013, Monthly Notices of the Royal Astronomical Society, 433, 560

Tsiganis, K., Gomes, R., Morbidelli, A., & Levison, H. F. 2005, Nature, 435, 459

Valsecchi, G., Morbidelli, A., Gonczi, R., et al. 1995, Icarus, 118, 169

Vaubaillon, J. 2017, Planetary and Space Science, 143, 78

Vaubaillon, J., Colas, F., & Jorda, L. 2005, Astronomy & Astrophysics, 439, 751

Vaubaillon, J., Neslušan, L., Sekhar, A., Rudawska, R., & Ryabova, G. O. 2019, From Parent Body to Meteor Shower: The Dynamics of Meteoroid Streams, ed. G. O. Ryabova, D. J. Asher, & M. J. Campbell-Brown, 161

Vaubaillon, J., Watanabe, J., Sato, M., Horii, S., & Koten, P. 2011, WGN, Journal of the IMO, 39, 3

Verniani, F. 1969, Space Science Reviews, 10, 230

Vida, D., Brown, P. G., & Campbell-Brown, M. 2018, Monthly Notices of the Royal Astronomical Society, 479, 4307

Vida, D., Brown, P. G., Campbell-Brown, M., et al. 2020a, Icarus, submitted, ?

Vida, D., Brown, P. G., Campbell-Brown, M., Wiegert, P., & Gural, P. S. 2020b, Monthly Notices of the Royal Astronomical Society, 491, 3996

Vida, D., Campbell-Brown, M., Brown, P. G., Egal, A., & Mazur, M. J. 2020c, Astronomy & Astrophysics, 635, A153

Vida, D., Gural, P. S., Brown, P. G., Campbell-Brown, M., & Wiegert, P. 2020d, Monthly Notices of the Royal Astronomical Society, 491, 2688

Vida, D., Šegon, D., & Merlak, A. 2019, e-Zine for meteor observers meteornews. net, 22

Vojáček, V., Borovička, J., Koten, P., Spurnỳ, P., & Štork, R. 2019, Astronomy & Astrophysics, 621, A68

Weryk, R., Campbell-Brown, M., Wiegert, P., et al. 2013, Icarus, 225, 614

Weryk, R. J., & Brown, P. G. 2012, Planetary and Space Science, 62, 132

—. 2013, Planetary and Space Science, 81, 32

Whipple, F. L. 1951, The Astrophysical Journal, 113, 464

Whipple, F. L., & Jacchia, L. G. 1957, Smithsonian Contributions to Astrophysics, 1, 183

Wiegert, P., Vaubaillon, J., & Campbell-Brown, M. 2009, Icarus, 201, 295

Womack, M., Sarid, G., & Wierzchos, K. 2017, Publications of the Astronomical Society of the Pacific, 129, 031001

Ye, Q., Brown, P. G., Campbell-Brown, M. D., & Weryk, R. J. 2013a, Monthly Notices of the Royal Astronomical Society, 436, 675

Ye, Q., Wiegert, P. A., Brown, P. G., Campbell-Brown, M. D., & Weryk, R. J. 2013b, Monthly Notices of the Royal Astronomical Society, 437, 3812

Chapter 2

Measurement accuracy of initial velocities of meteors

A version of this chapter has been published as:

Vida, D., Brown, P.G., & Campbell-Brown, M. (2018). *Modelling the measurement accuracy of pre-atmosphere velocities of meteoroids.* Monthly Notices of the Royal Astronomical Society, 479, 4307.

2.1   Introduction

Understanding the linkage of meteor showers to their parent bodies over time requires starting conditions for backward orbital integration, namely the contemporary osculating orbits of both the parent and stream meteoroids (Abedin et al., 2018). However, calculation of precise heliocentric orbits of meteoroids from ground-based optical observations is difficult as atmospheric deceleration affects all measurements to some extent. Ultimately, one has to know the pre-atmosphere position and the velocity vector of the meteoroid to a high degree of accuracy, prior to the meteoroid's interaction with the atmosphere if long-term backward integrations are to be meaningful for timescales comparable to the lifetime of a meteoroid stream.

With the increasing precision of optical meteor observing systems, various authors have examined the probable initial velocity of meteors and performed uncertainty estimates. For example, Egal et al. (2017) used "CAmera for BEtter Resolution" (CABERNET) network data, a system which achieves a spatial precision of 3.24 arc seconds, and found that it is possible to determine meteoroid initial velocities with a precision of 1.25% by using the trajectory estimation method of Gural (2012).

However, the question of true velocity accuracy is quite complex, as the velocity of the meteoroid at the beginning of its luminous phase is often equated with its pre-atmospheric velocity (Jenniskens et al., 2011; Trigo-Rodríguez et al., 2013; Šegon et al., 2014), but this is not strictly true. Ceplecha (1987) advises estimating the pre-atmosphere velocity from time vs. length along the track using the method of Pecina & Ceplecha (1983, 1984) and assumes the velocity after the correction for Earth's rotation (equation 35 in Ceplecha, 1987) to be equal to the no-atmospheric velocity, which may be a valid assumption for fireball-sized meteoroids, although this was never validated for fainter meteors.

For meteoroids corresponding to fireball sizes, this approach has recently been validated by Spurnỳ et al. (2017) who reduced 144 Taurid fireballs and modelled their trajectories using the Ceplecha et al. (1993) ablation model, which corresponds to the Pecina & Ceplecha (1983, 1984) model if no fragmentation is assumed. Using an atmosphere mass density model, they assumed that the velocity at the height of $150\,\mathrm{km}$ corresponds to the pre-atmosphere velocity (private communication, Dr. Borovička). They found a new branch (a separate group in the meteorid stream) of the Taurid meteor shower, with fireball-sized meteoroids having tightly clustered radiants/speeds as independently predicted for the Taurid resonant swarm (Asher & Izumi, 1998). The authors quote the initial velocity of fireballs (all with initial masses higher than $10^{-4}\,\mathrm{kg}$) to within several tens of meters per second, the most precise ones approaching $\pm 7\,\mathrm{m\,s^{-1}}$. As the Ceplecha et al. (1993) method models the full trajectory of the meteoroid, it is possible to estimate (within model assumptions) its real pre-atmosphere velocity (velocity at $t = -\infty$); indeed the authors attribute the discovery of the new Taurid branch to the high

precision of their data reduction, a fact validated by the tight statistical clustering of the resonant swarm radiants. In contrast, much smaller meteoroids measured by backscatter radars Brown et al. (2005, 2008) need a deceleration correction which can be as much as $6\,\mathrm{km\,s^{-1}}$ (up to 50%) for meteors with beginning heights of $80\,\mathrm{km}$.

Hajdukova Jr et al. (2017) have recently shown that most orbits of video meteors suffer from a significant bias in semi-major axis due to underestimated initial velocities. They point out that initial velocities of the Geminids are usually underestimated as much as $200\,\mathrm{m\,s^{-1}}$ to $500\,\mathrm{m\,s^{-1}}$ compared to values derived from dynamical simulations and high-precision manual reduction done by Koten et al. (2004).

These examples motivate the general question of how accurately one can in practice measure the initial velocity of a meteoroid (i.e. the velocity at the beginning of the luminous phase) and the closely associated question of how this velocity differs from the real pre-atmosphere velocity of a meteoroid? Here we define the real pre-atmosphere velocity as the velocity prior to any sensible deceleration by the atmosphere; operationally this occurs for most meteoroids at heights above 180km.

This paper seeks to address two specific questions:

1. How does the true meteoroid velocity far out of the atmosphere differ from the often adopted initial velocity measured at the beginning height (i.e. height of first detection) as a function of mass and meteoroid type?

2. What are the effective limits to the achievable accuracy of pre-atmospheric velocities for different optical systems and are these primarily model-related limitations or equipment limitations?

To determine the difference between a meteoroid's velocity before it enters the atmosphere and the instrumentally measured velocity at the beginning of the luminous phase, we employ a modified single-body meteor ablation model from Campbell-Brown & Koschny (2004) for fainter meteors, and the FM model by Ceplecha & Revelle (2005) for fireballs.

In what follows, we compare simulated meteor velocities at the beginning of their modelled trajectory (at 180 km height) and their velocity at the height where they would first be detected by a given optical system. We then model three real-world, but quite different, optical meteor observation systems which cover the meteoroid mass range from 5×10^{-7} kg to ~ 10 kg. The details of the modelled systems are given in section 2.3.

For each system we have modelled three populations of meteoroids ranging in bulk density from $180 \, \text{kg} \, \text{m}^{-3}$ to $5425 \, \text{kg} \, \text{m}^{-3}$. The details of the adopted material properties for each population are given in section 2.4. A major uncertainty in this model approach is the effect of fragmentation. Approximately 90% of faint meteors fragment during flight (Subasinghe et al., 2016), although Hawkes & Jones (1975) point out that release of $\sim 10^{-9}$ kg grains may begin even before the luminous phase of the flight. Stokan & Campbell-Brown (2014) inspected 1800 high-resolution videos recorded by the Canadian Automated Meteor Observatory of masses $\sim 10^{-4}$ kg (Weryk et al., 2013) and found only 3 meteors which exhibited complex gross fragmentation which occurred before the event was recorded by the system. In what follows, we use this observation to justify use of a single-body meteor ablation model up to the point of detection, while using an appropriate (larger) apparent ablation coefficient to simulate continuous fragmentation into finer grains. We note that ignoring fragmentation prior to luminous onset will make our speed corrections lower limits; the true difference may be larger.

2.2 Ablation models and simulation details

2.2.1 Faint meteor ablation model

To perform our simulations for fainter meteors, we have modified the dustball model of Campbell-Brown & Koschny (2004) so that there is no fragmentation due to thermal disruption. The model assumes that the initial kinetic energy of a meteoroid is carried away by three types of energy losses: loss through heat transfer due to collisions with air molecules, black-body radiation, and heat lost with evaporating meteoroid material

$$\frac{dT_m}{dt} = \frac{1}{cm} \left[\frac{\Lambda \rho_a v^3}{2} A \left(\frac{m}{\rho_m} \right)^{2/3} \right.$$
$$\left. -4\sigma_B \epsilon \left(T_m^4 - T_a^4 \right) A \left(\frac{m}{\rho_m} \right)^{2/3} - L \frac{dm}{dt} \right],$$

$$(2.1)$$

where T_m is the temperature of the meteoroid (initial value is assumed to be 280 K), c is the specific heat of meteoroid ($c = 1000\,\mathrm{J\,kg^{-1}\,K^{-1}}$), m the meteoroid mass, Λ the heat transfer coefficient ($\Lambda = 0.5$), ρ_a the atmospheric density, which we take from the NRLMSISE-00 model (the geographical coordinates used were 45° N, 0° E on January 1, 2000 at 12:00 UTC) (Picone et al., 2002), v the meteoroid velocity, A the shape factor ($A = 1.21$, sphere), ρ_m the meteoroid density, σ_B the Stefan-Boltzmann constant, ϵ the meteoroid emissivity ($\epsilon = 0.9$), T_a the atmospheric temperature (constant at $T_a = 280\,\mathrm{K}$) and L is energy needed to ablate a unit mass (heat of ablation).

Compared to classical single-body ablation models, our model assumes that the ablation starts as the meteoroid heats high in the atmosphere, and combines the Clausius-Clapeyron partial vapour pressure equation with the additional incorporation of the Knudsen-Langmuir evaporation rate formula for calculating the mass loss

$$\frac{dm}{dt} = A \left(\frac{m}{\rho_m} \right)^{2/3} \psi \frac{P_a exp\left(\frac{L\mu}{k_B T_B} \right) exp\left(-\frac{L\mu}{k_B T_M} \right) - p_v}{\sqrt{\frac{2\pi k_B T_m}{\mu}}},$$

$$(2.2)$$

where ψ is the condensation coefficient ($\psi = 0.5$), μ is the molar mass ($\mu = 36\,\mathrm{u}$), k_B is the Boltzman constant, P_a is the standard atmospheric pressure at sea level, T_B the boiling temperature of the meteoroid material at P_a ($T_B = 1850\,\mathrm{K}$), and p_v is the vapour pressure of meteoroid material at its surface (we assume $p_v = 0$ for free molecular flow, in which the meteoroids are at high altitudes).

The change in speed is calculated through conservation of momentum, when air molecules collide with the meteoroid

$$\frac{dv}{dt} = \frac{\Gamma \rho_a v^2}{m} A \left(\frac{m}{\rho_m} \right)^{2/3} , \qquad (2.3)$$

here Γ is the drag coefficient, which is assumed to be unity. Acceleration due to Earth's gravity is also taken into account.

The energy going into light production is assumed to be some fraction of the kinetic energy loss, including the deceleration term

$$I = \tau \left(\frac{dm}{dt} \frac{v^2}{2} + mv \frac{dv}{dt} \right) , \qquad (2.4)$$

where I is the luminous intensity and τ is the non-dimensional luminous efficiency.

In what follows, all numerical integrations are performed using the fourth order Runge-Kutta method with a fixed time step of 0.001 s, until the whole mass of the meteoroid is ablated which we identify to be equivalent to the residual mass falling below 10^{-14} kg.

2.2.2 Fireball ablation model

For masses of meteoroids in the fireball range, we apply the fragmentation model (FM) by Ceplecha & Revelle (2005) which is based on classical single-body ablation equations with explicit addition of fragmentation. Modelling assumptions for faint meteors are not valid for larger masses, primarily because these meteoroids are no longer in free molecular flow as fireballs penetrate deeper into the atmosphere and are larger, entering the continuum flow regime (Campbell-Brown & Koschny, 2004). The FM was developed in part to explain the discrepancies between measured photometric and dynamic masses of fireballs. In the original work it was successfully applied to 15 fireballs, and later further validated through application to meteorite-dropping fireballs (Borovička et al., 2013).

As the FM code produces magnitudes in the photographic bandpass, we convert them to the bandpass of Sony HAD CCD based systems (see section 2.3.3), by applying a color index derived by Silber (2014) where $M_{HAD} = M_{ph} + 1.2$.

2.3   Optical system parameters

To explore speed corrections using representative optical meteor observation systems in use today, we model three "typical" optical meteor systems: an image intensified system lens coupled to a CCD video camera with a narrow field of view, a moderate field of view CCD video system, and an all-sky CCD video fireball system. Each system is sensitive to a different range of meteoroid masses, peak magnitudes (i.e. the magnitude when the meteor is the brightest), and beginning heights. To simulate the detectability of meteors for each system we estimate the following parameters:

- The magnitude at which the system typically detects the beginning of the meteor.

- The bolometric power of a zero-magnitude meteor P_{0m} in each system bandpass. We assume a black-body meteor with peak temperature at $T = 4500\,\text{K}$ (Borovička, 2005) and we use Table 3 from Weryk & Brown (2013) for determining P_{0m} per bandpass.

- The typical mass of a meteoroid most commonly detected by a system is a strong function of velocity, which is determined from the observations. Mass is typically the most uncertain characteristic for a meteoroid so we appeal to the known invariance of beginning heights with meteoroid mass for smaller meteoroids (Hawkes & Jones, 1975; Koten et al., 2004), and assume that for a range of peak magnitudes for a given optical system the corresponding meteoroid mass is purely a function of velocity.

- We assume a linear correlation between meteoroid velocity and peak magnitude, physical quantities which are strongly correlated (e.g. Jacchia et al. (1967)). Operationally, we then produce a functional fit of peak magnitude and velocity using real observations as measured by real-world examples of each type of system.

- For faint meteors (image intensified and moderate field of view CCD video systems) we use the Campbell-Brown & Koschny (2004) meteor ablation model with a fixed luminous

Table 2.1: Meteor limiting magnitude (MLM), equivalent bolometric power for a 0 magnitude meteor (P_{0m}), the expected peak magnitude (Mpeak) for meteors with a particular initial speed (V_{init}), estimated initial mass of a meteoroid m[kg], and assumed luminous efficiency. Models of the Canadian Automated Meteor Observatory (CAMO), Cameras for All-sky Meteor Surveillance (CAMS), and Southern Ontario Meteor Network (SOMN) are given.

System	Based on	MLM	P_{0m} [W]	M_{peak}	$\log m[kg]$	τ
Image intensified	CAMO influx system, 1*	$+7.5^M$	840	$-0.035 V_{init} + 4.623$	$\frac{-0.4 M_{peak}}{V_{init}^2} \log 0.098$	0.7 %
Moderate field of view	CAMS, 2*	$+5.0^M$	1210	$-0.022 V_{init} + 2.244$	4*, modified	0.7 %
All-sky	SOMN, 3*	-0.5^M	1210	$-0.009 V_{init} - 4.033$	$1.8 - 3.5 \log V_{init} - 0.413 M_{peak}$	5*

References: 1* - Weryk et al. (2013), 2* - Jenniskens et al. (2011), 3* - Brown et al. (2010), 4* - Jacchia et al. (1967), 5* - Ceplecha & Revelle (2005)

efficiency of 0.7 %. For fireballs (all-sky system) we use the Ceplecha & Revelle (2005) luminous efficiency model.

The details of the model parameters for each optical system are given in Table 2.1 and described briefly in the following sections.

2.3.1 Image intensified system

The model we adopt for a narrow-field image intensified system is the Canadian Automated Meteor Observatory (CAMO) influx system as employed by the Western Meteor Physics Group (Campbell-Brown et al., 2013; Weryk et al., 2013). These systems use a high sensitivity CCD camera running at 20 frames per second with a chip of 1600×1200 pixels and 14-bit optical depth. The lens is a 50 mm $f/0.95$ Navitar, which gives a field of view of 20×20 degrees. The camera is lens coupled to a 25 mm Generation 3 ITT model FS9925 image intensifier. The stellar limiting magnitude is $+8.5^M$, while the limiting magnitude for meteors is $+7.5^M$.

There are two identical influx systems separated by a baseline of 45 km, one at Elginfield (43.193° N, 81.315° W) and the other at Tavistock (43.264° N, 80.772° W) in Southwestern Ontario, Canada.

The photometric calibration was done in the R band for which the total bolometric power output of a zero-magnitude $T = 4500$ K blackbody meteor is $P_{0m} = 840$ W (Weryk & Brown, 2013). The magnitude and mass dependencies were fitted to 4882 manually reduced double

station meteors. The trajectories were calculated using the MILIG software (Borovička, 1990) which employs the least squares line-of-sight fitting method.

The initial velocities are taken to be the average velocity of the first half of the meteor trajectory. We have only taken events with eccentricities $e < 1.0$, velocities within $11.2\,\mathrm{km\,s^{-1}}$ and $71\,\mathrm{km\,s^{-1}}$, and peak magnitudes fainter than -2^M. Photometric meteoroid masses were calculated using a luminous efficiency of $\tau = 0.7\%$ based on the integrated lightcurves.

After performing initial meteoroid ablation simulations with these measured masses, we had to reduce the mass by a factor of 2 to match the simulation results to the observations, effectively using $\tau = 1.4\%$. The original photometric masses were producing events which started at heights well above those observed. When we reduced masses further (by a factor of 3 and more), the meteors with smaller masses were too faint to be detected by the system. We attribute this to the uncertainty in the luminous efficiency τ in particular recent work which indicates that τ might be on the order of several percent for smaller meteoroids (Subasinghe & Campbell-Brown, 2018). For our simulations we wish to adopt simple relations between meteoroid mass, magnitude and velocity. Hence, we performed a linear fit on the peak magnitudes versus velocities (in $\mathrm{km\,s^{-1}}$) and obtained the following relation:

$$M_{peak}(V_{init}) = -0.035 V_{init} + (4.623 \pm 1.25)\,, \qquad (2.5)$$

note that we only characterize the uncertainty in the intercept which we use as an indicator of the physical spread in the data, which will be used later to reconstruct the observed range of masses.

We also generated a simple empirical photometric mass model using this same luminous efficiency, comparing also the peak magnitudes and initial velocities

$$\log m(V_{init}, M_{peak}) = \frac{-0.4 M_{peak}}{V_{init}^2} \log k\,, \qquad (2.6)$$

where photometric mass is given in kilograms and the velocity in $\mathrm{km\,s^{-1}}$. Note that the -0.4
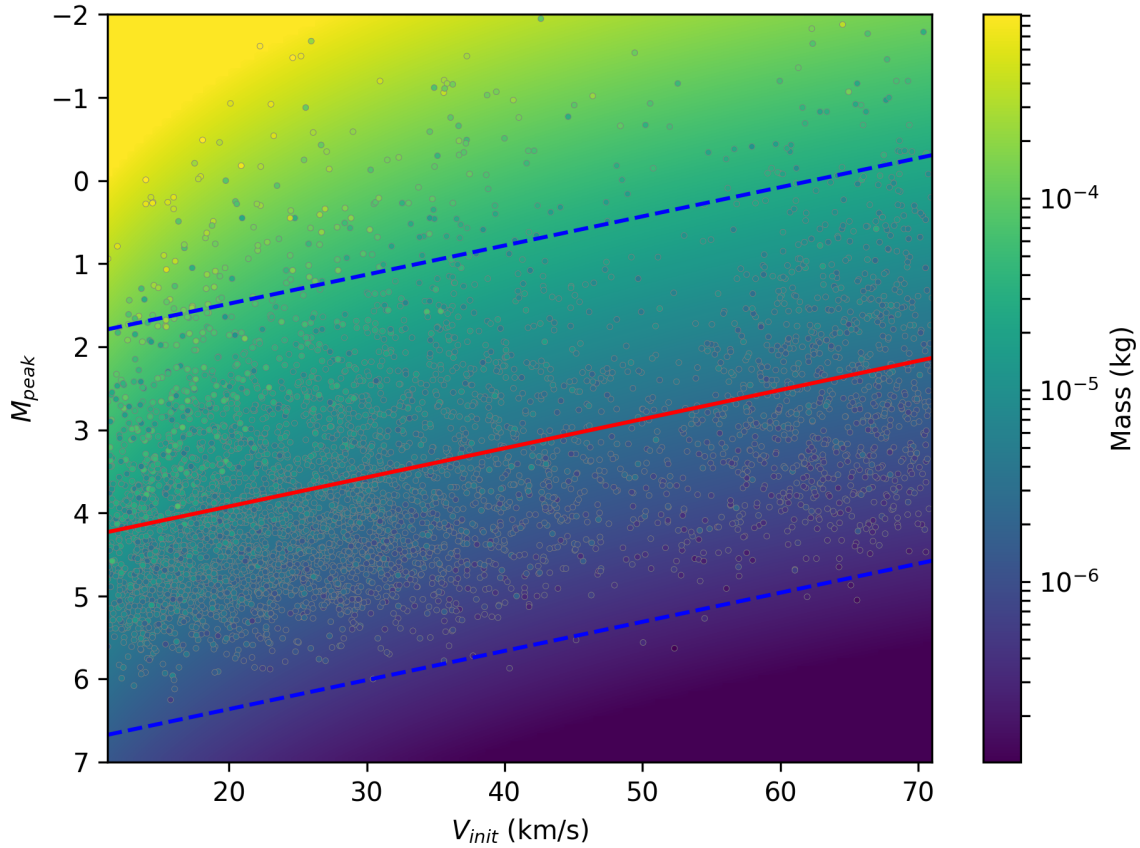
Figure 2.1: The photometric mass dependence as a function of the initial velocity and peak magnitude for the CAMO image intensified influx system. The colored dots represent the measurements, while the background colour represents the fit. The red line is the fit given by equation 2.5, while blue lines represent the 95% confidence interval of the fit.

term comes from the definition of the magnitude (see Chapter 1). After fitting the model, we obtained $k = 0.098$. It is worth mentioning that fitting the logarithm of the photometric mass instead of the mass directly produces a better fit, as this linearizes the differences in the mass across the mass spectrum; otherwise, the fit for smaller masses is not reliable. Figure 2.1 shows the measured masses as colored dots, while the background color represents the model. Note that the model fits the data well, as no major discrepancies in colour between the dots and the background can be seen. Figure 2.2 shows the dependence of the peak magnitude and the mass on the initial velocity.
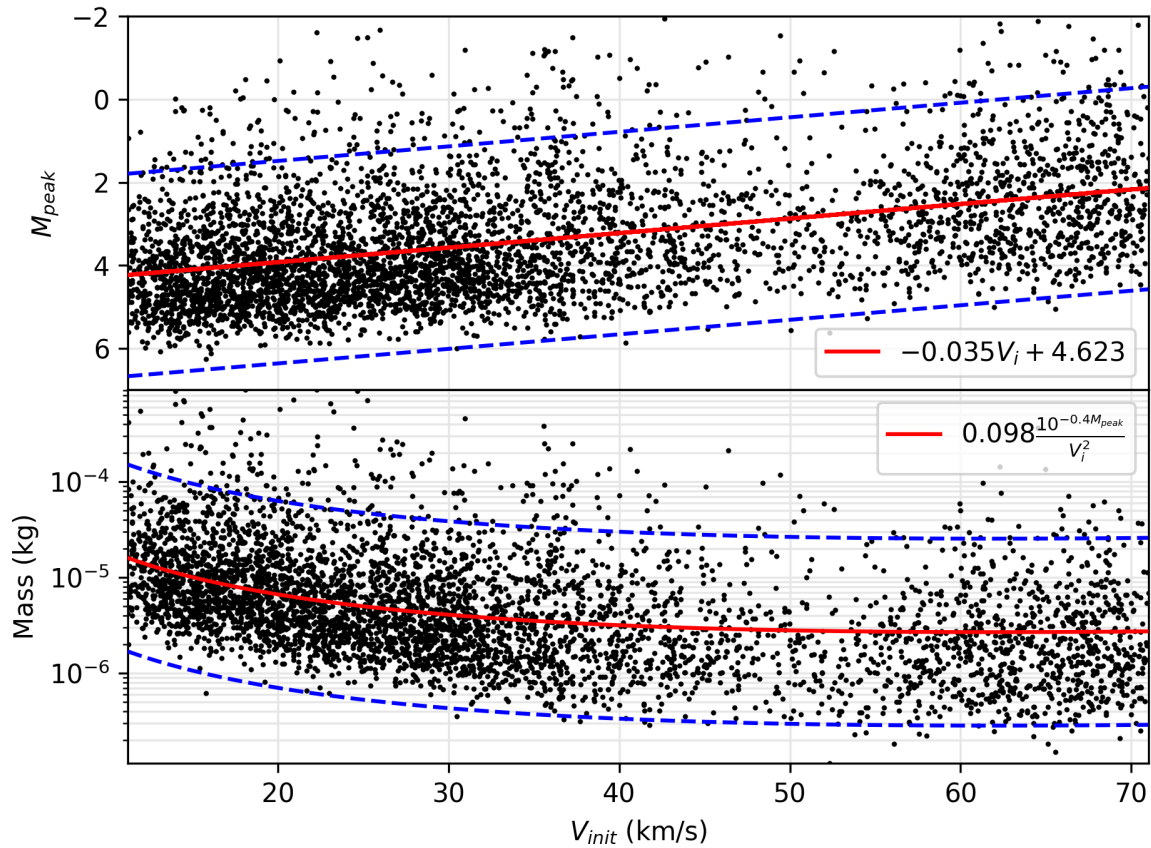
Figure 2.2: The top panel shows the dependence of peak magnitude on initial velocity, and the bottom plot shows the dependence of photometric mass on velocity for the CAMO image intensified influx system. Blue lines represent the 95% confidence interval of the fit. Note that the mass confidence interval is also symmetric around the mean (red) line in the logarithmic mass plot because the $10^{-0.4M_{peak}}$ term.

2.3.2   Moderate field-of-view system

The moderate field-of-view system model is based on the Cameras for Allsky Meteor Surveillance (CAMS) (Jenniskens et al., 2011). For this system we have used P_{0m} = 1210 W appropriate to a Sony HAD CCD chip (Weryk & Brown, 2013), used in the Watec 902 H2 Ultimate cameras operated by CAMS. Although Jenniskens et al. (2011) state that the limiting magnitude of CAMS cameras is $+5.5^M$, they point out that very few meteors that faint are multi-station. In our simulations, we have found the value of $MLM = +5.0^M$ matches the observed beginning heights best, as we have treated the limiting magnitude as a free parameter, compensating for uncertainties in meteor geometry and the luminous efficiency.

In the CAMS orbit database (Jenniskens et al., 2016a), there is no data on photometric meteoroid masses; thus we have followed the work of Jenniskens et al. (2016b) and used the results of Jacchia et al. (1967) to calculate meteoroid masses in grams, which we had to slightly modify as initial the simulations did not match the observations

$$\log m(V_{init}, M_{peak}, Z_G) = \log \frac{\tau_v(V_{init})}{0.03}\Big(5.15 - 3.89 \log V_{init}$$
$$-0.33(M_{peak} + 0.6) - 0.67 \log (\cos Z_G)\Big). \tag{2.7}$$

As suggested by Jenniskens et al. (2016b), in the caption to their Table 5, we applied a color index correction of +0.6 to observed peak magnitudes between the photographic and HAD CCD systems before computing the mass. We also had to change the peak magnitude term from 0.44 to 0.33. This new value was empirically chosen because the original range of masses produced unphysical simulations - more massive meteoroids had very large beginning heights, while smaller meteoroids (fainter than peak magnitude $+3^M$) were too faint to be detected, indications that the range of masses had to be reduced. As equation 2.7 was derived using the luminous efficiency of Verniani (1965), the computed masses were normalized to $\tau = 0.7\%$, a value that produced simulations that were most consistent with observations.

$\tau_v(V_{init})$ is the Verniani (1965) luminous efficiency given as a fraction (not a percent):

$$\tau_v(V_{init}) = 10^{-7} P_{v0m} V_{init}\,, \tag{2.8}$$

where V_{init} is given in km s^{-1} and $P_{v0m} = 1490\,\text{W}$ is the radiated power appropriate to a 4500 K black-body zero magnitude meteor in the visual bandpass, as given by Weryk & Brown (2013).

To obtain an empirical relation between velocities and peak magnitudes for this dataset, we first filtered the CAMS data set by taking only those meteors with a convergence angle $Q_C > 15°$, a reported error in geocentric velocity $\sigma_{V_g} < 10\%$ and eccentricities $e < 1.0$. The total number of remaining meteors was 80232. A linear fit of velocity to peak magnitude produces

$$M_{peak}(V_{init}) = -0.022V_{init} + 2.243 \pm 1.45\,. \tag{2.9}$$

Figure 2.3 shows both the peak magnitude fit and the empirical mass function fit adopted in our simulations for this system.

2.3.3   All-sky system

At the higher end of meteoroid masses, we investigated pre-detection decelerations of meteoroids observed by all-sky video systems. As a representative system we used the Southern Ontario Meteor Network (SOMN) (Weryk et al., 2008; Brown et al., 2010).

The systems use HiCam HB-710E Sony Ex-View HAD CCD cameras equipped with Rainbow L163VDC4 $1.6 - 3.4$mm $f/1.4$ lenses. The cameras have a resolution of 640×480 pixels and are operated at 29.97 frames per second. Meteor trajectories were estimated using the method of Borovička (1990). The automated data reduction pipeline only provides the average velocity of the event, though in most cases little deceleration is evident due to the low resolution of these systems. From examination of the results of the automated detection software, we find that the system most often detects meteors when they reach a visual magnitude between
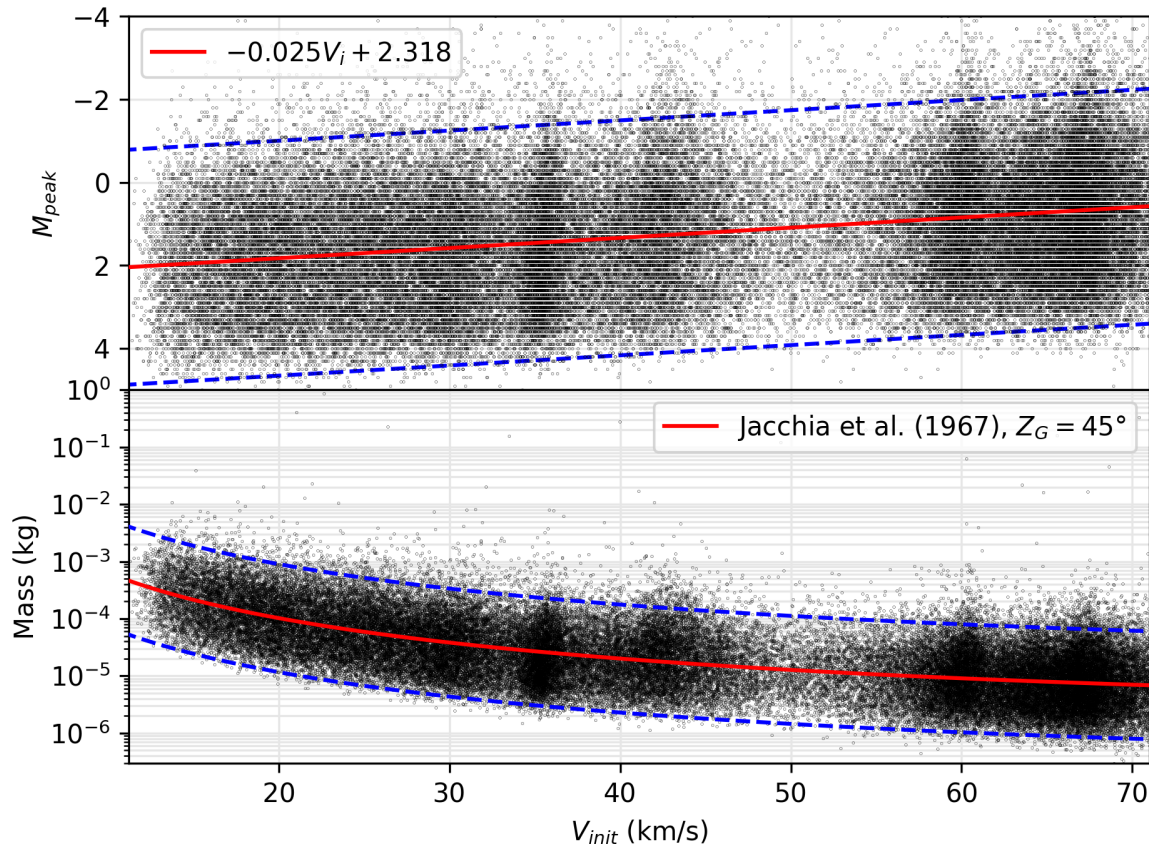
Figure 2.3: The top panel shows the dependence of peak magnitude on initial velocity of CAMS data, and the bottom plot shows the dependence of mass on velocity for a zenith angle $Z_G = 45°$ using equation 2.7. Blue lines represent the 95% confidence interval of the fit. The horizontal banding in the top plot is due to rounding to one decimal place in the magnitude value in the original data set.

0^M and -1^M. Our simulations were most consistent with observations for $MLM = -0.5^M$.

We found the automated photometry to be inconsistent with manual photometric reductions; therefore we fit our empirical relations by using representative mass and peak magnitudes from a subset of 283 manually reduced all-sky events. We have found that the peak magnitude does not show a strong correlation with velocity, probably due to saturation which occurs at higher brightness levels and the larger pixel scale of these systems:

$$M_{peak}(V_{init}) = -0.009 V_{init} - 4.033 \pm 1.53 \,. \tag{2.10}$$

In contrast to the two previous systems, we have found that the simplistic mass model given by equation 2.5 does not fit the computed all-sky masses well, so we used a model similar to Jacchia et al. (1967), but without the zenith angle term. Upon running the simulations with the original estimated photometric masses, we noticed that the smallest meteoroids are not visible to the system. Simulations matched the observations only when we increased all masses by a factor of 4, which we attribute to uncertainties in the luminous efficiency and saturation effects. The resulting mass function was the following:

$$\log m(V_{init}, M_{peak}) = 1.806 - 3.512 \log V_{init} - 0.413 M_{peak} \,, \tag{2.11}$$

where the masses are given in kilograms. Figure 2.4 shows the peak magnitude fit and the corresponding masses for values of initial velocity and peak magnitude for the subset of 283 manually measured SOMN events.

2.4   Types of meteoroids

To cover the range of expected material properties and ablation behaviour in our model, we use three distinct types of meteoroids: cometary, asteroidal, and iron-rich. The detailed physical parameters for each category are given in Table 2.2. These classes were adopted by applying the
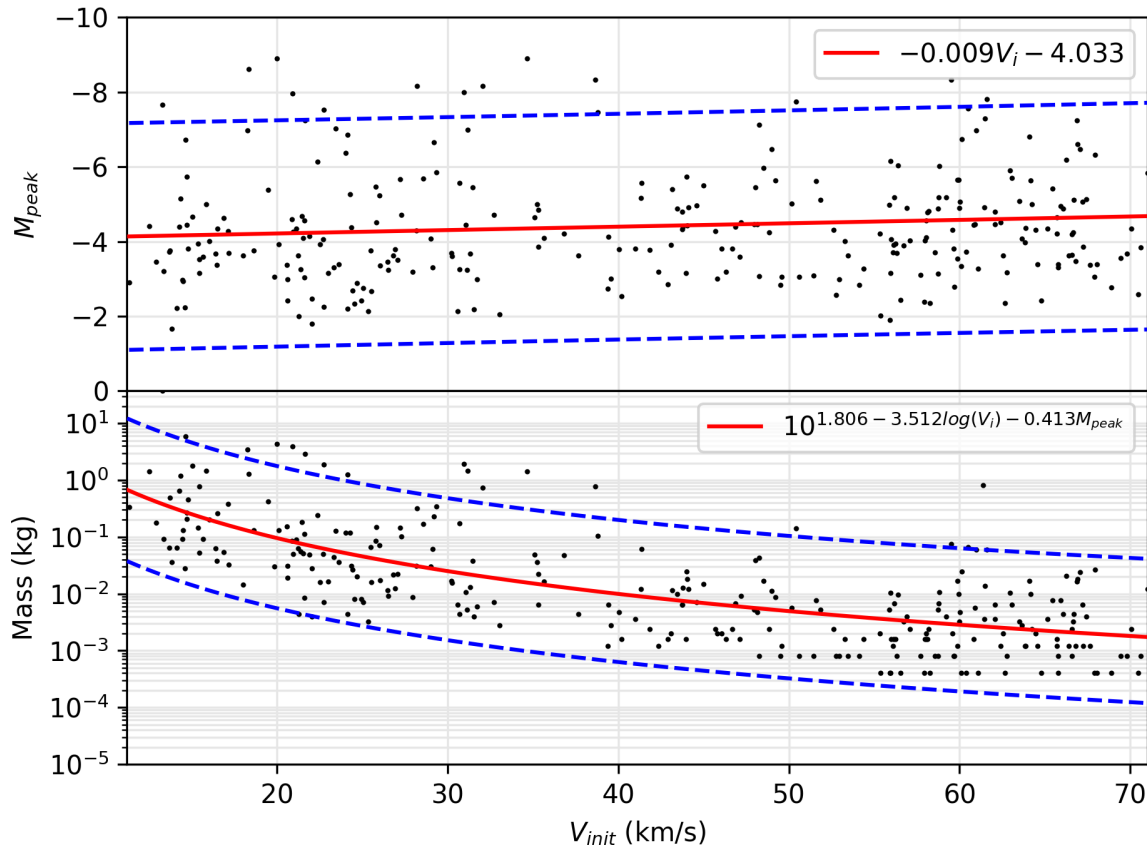
Figure 2.4: The top panel shows the dependence of peak magnitude on initial velocity, and the bottom plot shows the dependence of mass on velocity for the all-sky fireball system. Blue lines represent the 95% confidence interval of the fit. As expected for such a large pixel scale system, the average peak magnitude is a weak function of speed.

Campbell-Brown & Koschny (2004) model in Kikwaya et al. (2011) to 107 optical observations of meteors and from model fits deriving their physical properties. Originally, Kikwaya et al. (2011) divided their meteoroid data into 5 types based on orbit-type, as originally proposed by Borovička et al. (2005). As our simulations are most sensitive to physical structure and not orbital information, we focus on dividing meteoroids into density groups.

This simple density classification scheme was motivated by figure 11 in Kikwaya et al. (2011) which shows a strong correlation between the meteoroid orbit Tisserand parameter with respect to Jupiter T_J and meteoroid bulk density. Three distinct groupings of densities can be identified in that graph. Note that the distinction is purely by density and that meteoroids in JFC-type orbits have densities comparable to our asteroidal category, possibly indicating evolution from Asteroidal-JFC orbits through radiation forces over long timescales. We have also assumed that every meteoroid type has its own characteristic apparent ablation coefficient σ, following the classification first proposed in Ceplecha (1988).

Changing the apparent ablation coefficient is equivalent to adding meteoroid fragmentation, which we have not done explicitly in the model. The apparent ablation coefficient may differ significantly from the intrinsic ablation coefficient, which does not take fragmentation into account. As shown by Ceplecha & Revelle (2005) the average apparent and intrinsic ablation coefficients can differ by as much as two orders of magnitude, meaning that fragmentation is the primary process of meteoroid ablation in most fireball-class (large) meteoroids. High-resolution observations of faint meteors also show a high occurrence rate of visible continuous fragmentation, indicating that the same is probably true for smaller meteoroids as well (Subasinghe et al., 2016).

Ceplecha & Revelle (2005) have also shown that intrinsic ablation coefficients between different types of meteoroids are very similar, indicating that the material composition between meteoroid types is broadly similar; the ablation differences may be in bulk density and mechanical properties which only influence the rate of fragmentation (Borovička et al., 2015). As we use different bulk densities for the different meteoroid classes in our simulations to recreate

the earliest phases of ablation, we adopt the assumptions above for the purposes of this work.

We have assumed fixed drag and heat transfer coefficients $\Gamma = 1.0$ and $\Lambda = 0.5$. The true values are uncertain and different authors have used different values: in Borovička et al. (2007) and Fisher et al. (2000) both values are assumed to be 1.0, while in Campbell-Brown et al. (2013) the values were $\Gamma = 1.0$ and $\Lambda = 0.4$. Kikwaya et al. (2011) searched values from 0.5 to 1.0 in trying to simultaneously match the dynamic and photometric measurements of their meteors. Detailed results presented in Kikwaya (2011) show no strong dependence for these values with meteoroid type. Here we use the values for drag and heat transfer given in Campbell-Brown & Koschny (2004). The apparent ablation coefficient was altered only through changes to the heat of ablation L, thus effectively simulating different ablation rates. L can be computed using the following expression:

$$L = \frac{\Lambda}{2\sigma\Gamma} . \tag{2.12}$$

The values used in our numerical entry modelling for the apparent ablation coefficients were taken from Ceplecha et al. (1998), Table XVII, where meteoroid types are categorized according to Ceplecha (1988) groups: A, B, C, and D.

Comparing that table with Table 10 in Kikwaya et al. (2011), where the authors associate each Ceplecha group to their individual observed meteors, we conclude that the low-density cometary material (group C) with average density of $800\,\mathrm{kg\,m^{-3}}$ has an average apparent ablation coefficient of $\sigma = 0.1\,\mathrm{s^2\,km^{-2}}$, while the carbonaceous chondrite-like material (group A) has an ablation coefficient of $\sigma = 0.042\,\mathrm{s^2\,km^{-2}}$.

The properties for the iron-rich meteoroids are more uncertain; Ceplecha et al. (1998) gives an apparent ablation coefficient of $\sigma \approx 0.07\,\mathrm{s^2\,km^{-2}}$ for higher densities than ours, $7800\,\mathrm{kg\,m^{-3}}$, which were derived from fireball observations in the mass range (from $0.1\,\mathrm{kg}$ to $2 \times 10^3\,\mathrm{kg}$). Due to the lack of other empirical values, we simply use $\sigma = 0.07\,\mathrm{s^2\,km^{-2}}$ for iron-rich meteoroids, noting that for iron bodies melting as opposed to vaporiztion will dominate ablation so these larger ablation coefficients are expected. Finally, Kikwaya et al. (2011) find a

Table 2.2: Physical properties adopted for the three model meteoroid classes. ρ_{min} and ρ_{max} given the range of bulk densities of meteoroids, σ is the apparent ablation coefficient, while L is the energy needed to ablate a unit mass.

Type	ρ_{min} (kg m^{-3})	ρ_{max} (kg m^{-3})	σ (s^2 km^{-2})	L (J kg^{-1})
Cometary	180	1510	0.1	2.5×10^6
Asteroidal	2000	3500	0.042	6.0×10^6
Iron-rich	4150	5425	0.07	3.6×10^6

strong correlation between the density and thermal conductivity, but because we have assumed a non-fragmenting model, thermal conductivity is not used as one of the parameters in our implementation of the Campbell-Brown & Koschny (2004) model.

2.5   Simulation details

The goal of our simulation is to produce estimated brightness, speed and deceleration/mass loss profiles for a suite of meteoroids with different masses entering at a range of speeds and entry angles for all three types of meteoroids. From this simulation "template" we then select only those meteoroids which would be detectable for a particular optical system, based on the empirical system properties summarized in Table 2.1. We then use these simulated events to compare the true initial speeds to speeds at the moment of detection for each type of optical system.

The simulations were done in $1\,\mathrm{km\,s^{-1}}$ steps in initial velocity V_∞, from $11\,\mathrm{km\,s^{-1}}$ to $71\,\mathrm{km\,s^{-1}}$, and across 13 zenith angle bins, from $0°$ to $75°$, distributed uniformly by the cosine of the zenith angle (thus making the phase space denser at high zenith angles). For zenith angles larger than $75°$ very few simulated meteors reached the limiting magnitude of the systems, which is consistent with observations - e.g. in CAMS data only 3% of all orbits have zenith angles larger than $75°$. For very low velocity meteors (below $13\,\mathrm{km\,s^{-1}}$) at high zenith angles almost no ablation occurred until they were gravity accelerated to higher velocities. This often took more than $10\,\mathrm{s}$, which we view as largely unphysical - we chose to discard

these simulation runs.

The suite of model meteor peak magnitudes were then generated by sampling in 20 uniform steps within the 95% confidence interval of the fit, producing 20 simulated masses. Finally, 5 uniform intervals were taken between the minimum and maximum meteoroid densities given in Table 2.2 for each meteoroid type per simulated mass.

After running the meteor ablation simulation with the Campbell-Brown & Koschny (2004) model, luminous intensities were converted to absolute magnitudes, while the implementation of the Ceplecha & Revelle (2005) method provides photographic absolute magnitudes which are converted to absolute magnitudes in our bandpass (see section 2.2.2). To approximate various geometries between the observers and the meteor trajectory, we have assumed that the range to the meteor at any given point corresponds to $\sqrt{(100 \, \text{km})^2 + h^2(t)}$, where $h(t)$ is height above the ground in kilometres. Our simulations ignore atmospheric extinction.

We define the time of the initial meteor detection t_{init} as the time when the meteor's visual magnitude exceeds the system's limiting magnitude. We reject all meteors which spend less than 0.15 s above the detection limit. This time requirement is based on the typical value used in meteor detection algorithms, namely a meteor is detected if it is above the noise level for 4 consecutive video frames for NTSC frame rates of 30 frames per second (Albin et al., 2016). The simulated beginning height h_{BEG} of the meteor is taken as its height at time t_{init}.

Similarly, the simulated measured initial velocity v_{init} is the velocity at t_{init}. This is an upper limit to the initial velocity observed from a real optical meteor observation system, which necessarily uses a larger segment of the trail to find speeds (in most cases) during which the meteoroid will have decelerated.

For the CAMO Influx system, for example, the initial velocity is computed as the average velocity of the first half of the meteor trajectory. For the all-sky SOMN system initial velocity is equated to the average velocity across the entire trail. In both systems, these are always smaller than the real initial velocity, ie. the initial velocity at the moment the system first detects the meteor.

For the CAMS system, the initial velocities are expected to be closer to the real initial values as they are measured with a more advanced trajectory estimation method using a global fit with time information combined with a deceleration model (Gural, 2012), although the real accuracy of this method remains unclear (Egal et al., 2017).

The difference between the starting velocity and the initial velocity is calculated for every simulation run as

$$\Delta v = v_{init} - v_\infty + \Delta v_{grav}, \tag{2.13}$$

where Δv_{grav} is the change in velocity due to gravitational acceleration, which is already taken into account when computing the geocentric radiant (Ceplecha, 1987), and thus must be taken out of the total velocity difference. Δv_{grav} was computed by running an additional no-atmosphere simulation and taking the difference between the pre-atmosphere velocity and the velocity at the height of detection.

Figure 2.5 shows an example simulation for a CAMS-like system. At about $t = 6\,\mathrm{s}$ ablation coupled with increased atmospheric drag causes rapid deceleration. The meteor would be detected at about $t = 6.7\,\mathrm{s}$, when the difference from the starting velocity has reached $-130\,\mathrm{m\,s^{-1}}$.

As our goal is to provide a correction for the initial speed for the entire meteoroid population for a given observation system, we averaged the velocity differences and beginning heights across simulations for all density intervals per meteoroid type. This is justified as density is not a parameter that can be easily determined from the meteor trajectory alone, as it does not correlate strongly with orbital type (Ceplecha, 1988), and hence requires detailed modelling on a per event basis.

2.6   Results

To validate our working assumptions about the representative mass function and the limiting meteor magnitude for our simulated optical systems, we first compare the modelled and
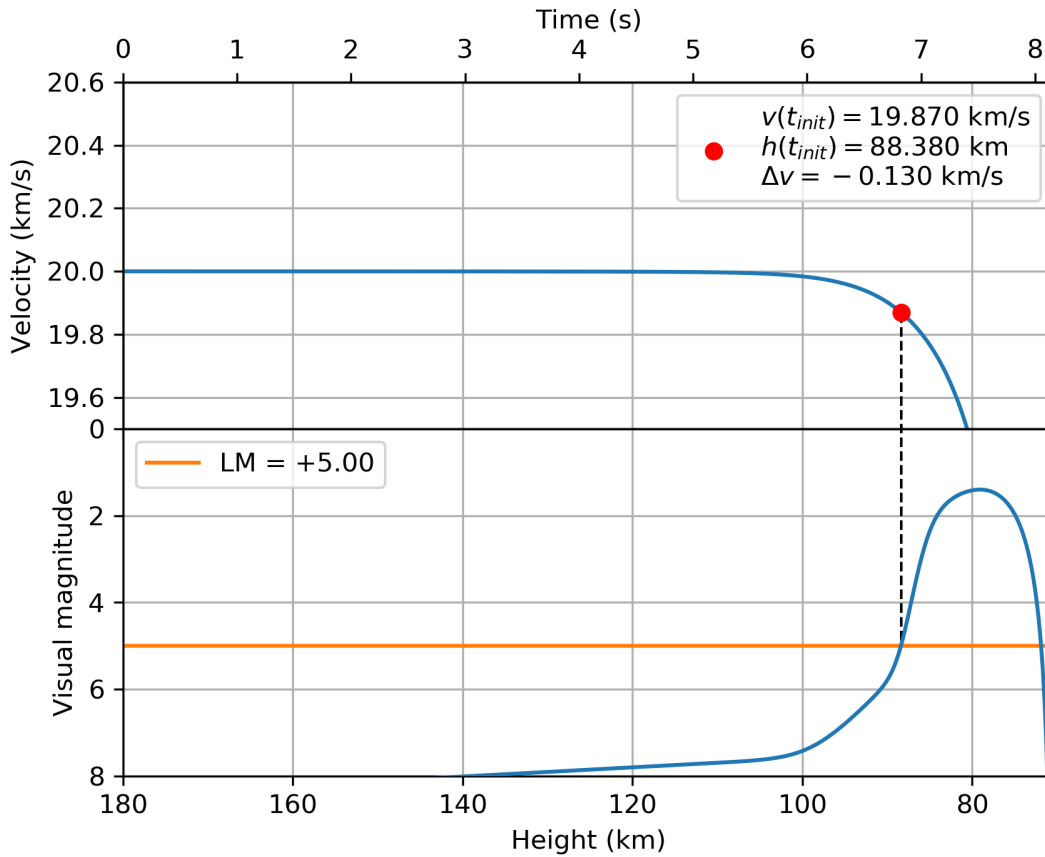
Figure 2.5: Ablation simulation for a $V_\infty = 20\,\text{km s}^{-1}$ cometary meteoroid with mass of $m = 0.1\,\text{g}$, density $\rho_m = 1510\,\text{kg m}^{-3}$ and zenith angle of $Z_G = 45°$. At the limiting CAMS-like system magnitude of $MLM = +5.0^M$, the difference between the original (gravity corrected) and initial velocity was $\Delta v = -130\,\text{m s}^{-1}$. The acceleration due to gravity was removed from the velocity in the top graph.

observed beginning heights for each optical system. We found that our results of beginning heights versus density agree with Kikwaya et al. (2011), an unsurprising result as that study used the same ablation model.

2.6.1   CAMO influx system

Figure 2.6 shows the observed beginning heights of real meteors imaged by the CAMO influx system as a function of speed, and their Tisserand parameters with respect to Jupiter. It can be seen that most meteoroids with $V_{init} > 40\,\mathrm{km\,s^{-1}}$ are of HTC/NIC origin, while the sub-$40\,\mathrm{km\,s^{-1}}$ ones are either JFC or asteroidal in origin. The latter dominate at the lowest velocities ($V_{init} < 13\,\mathrm{km\,s^{-1}}$). This is as expected given the required orbits accessible for a given range of observed speeds at the Earth. Additionally, two branches of beginning heights can be seen, one $\sim 10\,\mathrm{km}$ higher than the other (Ceplecha, 1968). Most of the observed meteors were around magnitude $+5^M$ and a large portion of them were sporadic meteors. Using the showers of the IAU Meteor Data Center for possible association, we found only 13% were potentially from any major shower.

Performing the meteor ablation simulations following the procedure described in section 2.5, the observed and simulated beginning heights are shown in figure 2.7. The simulations generally reproduce the bulk of the observed beginning heights; lower density cometary meteoroids match the upper begin height branch, while denser asteroidal and iron meteoroids match the lower branch. These results are consistent with the findings in Ceplecha (1958) and Ceplecha (1968), where the higher branch was classified as type C (porous material) and the lower branch as type A (stony type). We also note that there is almost no model-predicted difference in beginning heights between asteroidal and iron-rich meteoroids. A small fraction of simulated meteors have beginning heights above the main branches. These were meteoroids with the largest masses. This is consistent with the data which show that meteors with very high beginning heights have peak magnitudes significantly brighter than the rest.

Figures 2.8 through 2.10 show the simulation differences between the initial and pre-
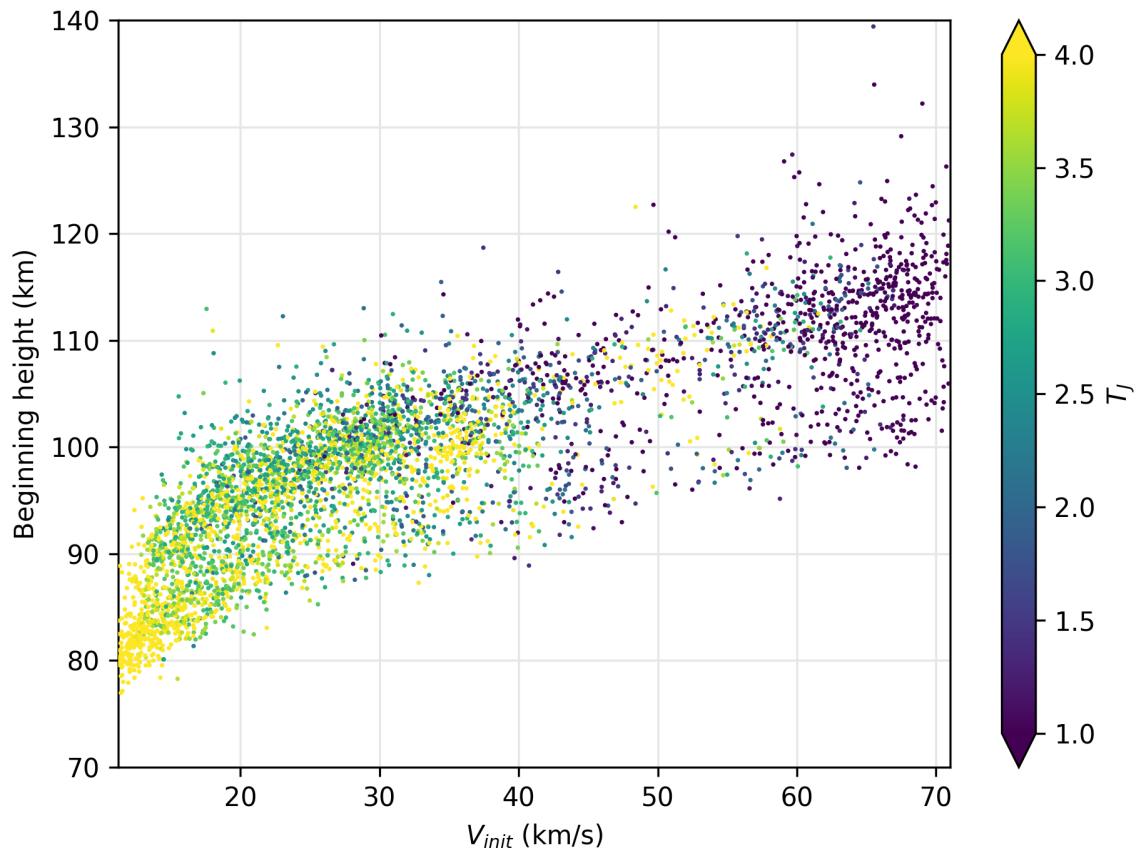
Figure 2.6: The observed dependence of velocity and beginning heights on the Tisserand parameter with respect to Jupiter for meteors detected by the CAMO influx system.
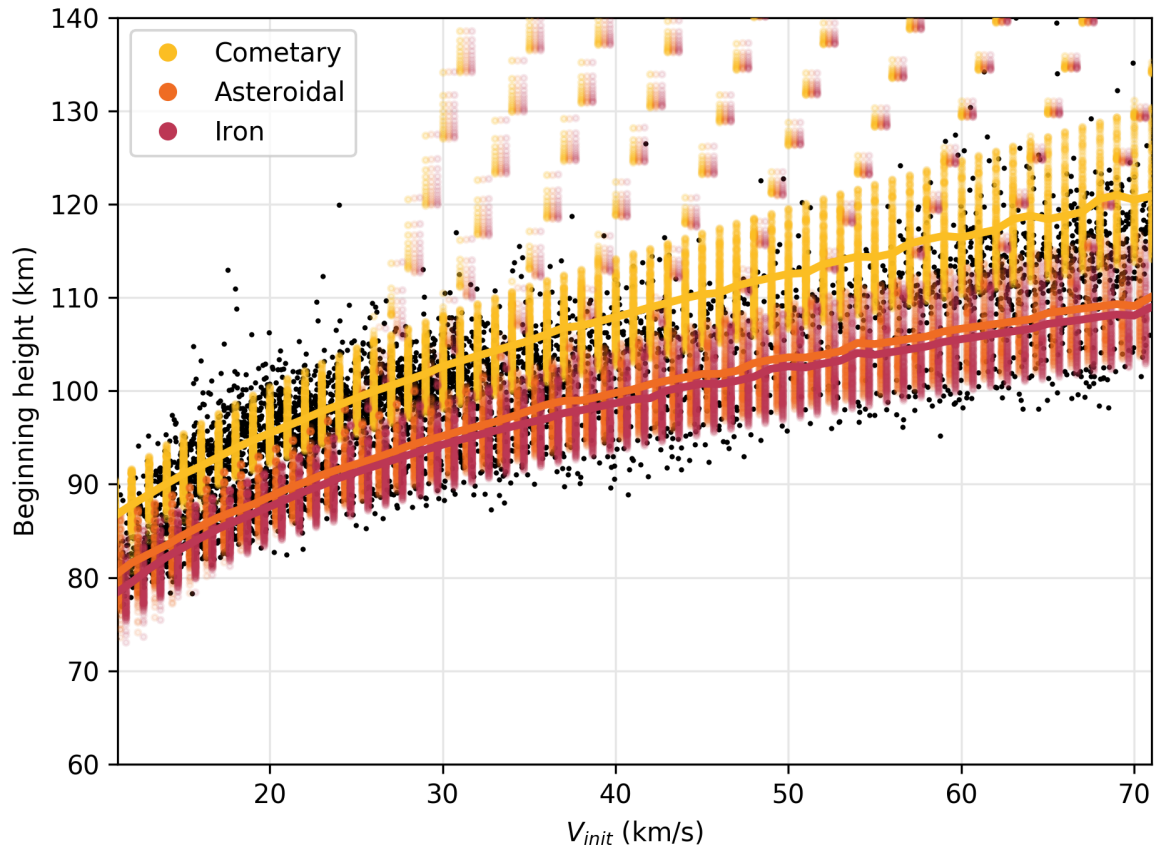
Figure 2.7: Comparison of the observed and simulated beginning heights for the CAMO image intensified influx system. Yellow, orange and brown dots represent cometary, asteroidal and iron meteoroids respectively. Thick lines that follow the branches by the middle are median beginning heights for every branch.

atmosphere velocities for various meteoroid types for the CAMO influx system. Overall, the deceleration at higher velocities and larger masses is only several tens of meters per second, while for lower velocities and smaller masses the velocity difference can reach several hundreds of meters per second. The influence of the zenith angle on the velocity difference is minor and not shown here, but generally Δv increases slightly with increasing zenith angle.

There is a strong dependence of the velocity difference on the type of meteoroid material - cometary meteoroids decelerate less than asteroidal, which we believe is caused by the higher apparent ablation coefficient of cometary meteoroids and their higher beginning heights. In contrast, the velocity differences are higher for asteroidal meteoroids than for iron meteoroids, despite having similar beginning heights. We believe this is a result of higher density of iron-rich meteoroids, which leads to smaller meteoroid cross sections (where the cross section is $A\left(\frac{m}{\rho_m}\right)^{2/3}$ in the ablation equations), as we have assumed the same masses for every meteoroid type, as well as the higher apparent ablation coefficient which causes the iron-rich meteoroids to melt rather than vaporize first.

An operational fit to our results is well represented by a sixth order polynomial such that the velocity difference for any zenith angle is

$$\Delta v = x_0 + x_1 Z_G + x_2 Z_G^2 + x_3 Z_G^3 + x_4 Z_G^4 + x_5 Z_G^5 + x_6 Z_G^6, \tag{2.14}$$

where the zenith angle is in radians, Δv in $\mathrm{m\,s^{-1}}$, and parameters x_0 to x_6 are given in Appendix A of Vida et al. (2018) for increments of $1\,\mathrm{km\,s^{-1}}$ in initial velocity and 20 different peak magnitudes for every meteoroid type. We note that the above relation provides the minimum correction between initial and true pre-atmospheric velocity as we have assumed no fragmentation.
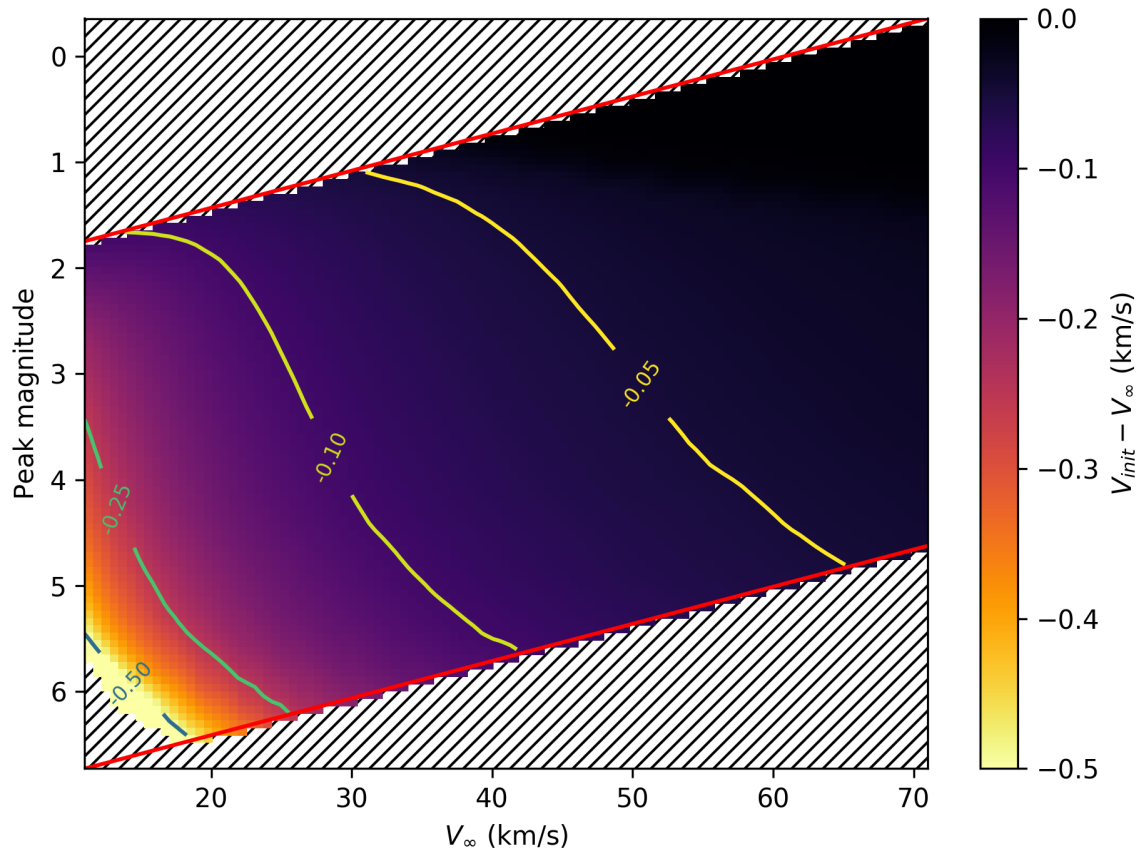
Figure 2.8: Cometary meteoroids - simulations for the CAMO influx image intensified systems. The areas of the parameter space which were outside of the investigated values are hatched using diagonal lines. Red lines represent the range of observed peak magnitudes, and contours $(-0.05, -0.10, -0.25, -0.5,$ and $-0.75\,\mathrm{km\,s^{-1}})$ indicate discrete values of velocity difference. The graph appears tilted due to the dependence of detectable masses on the velocity.
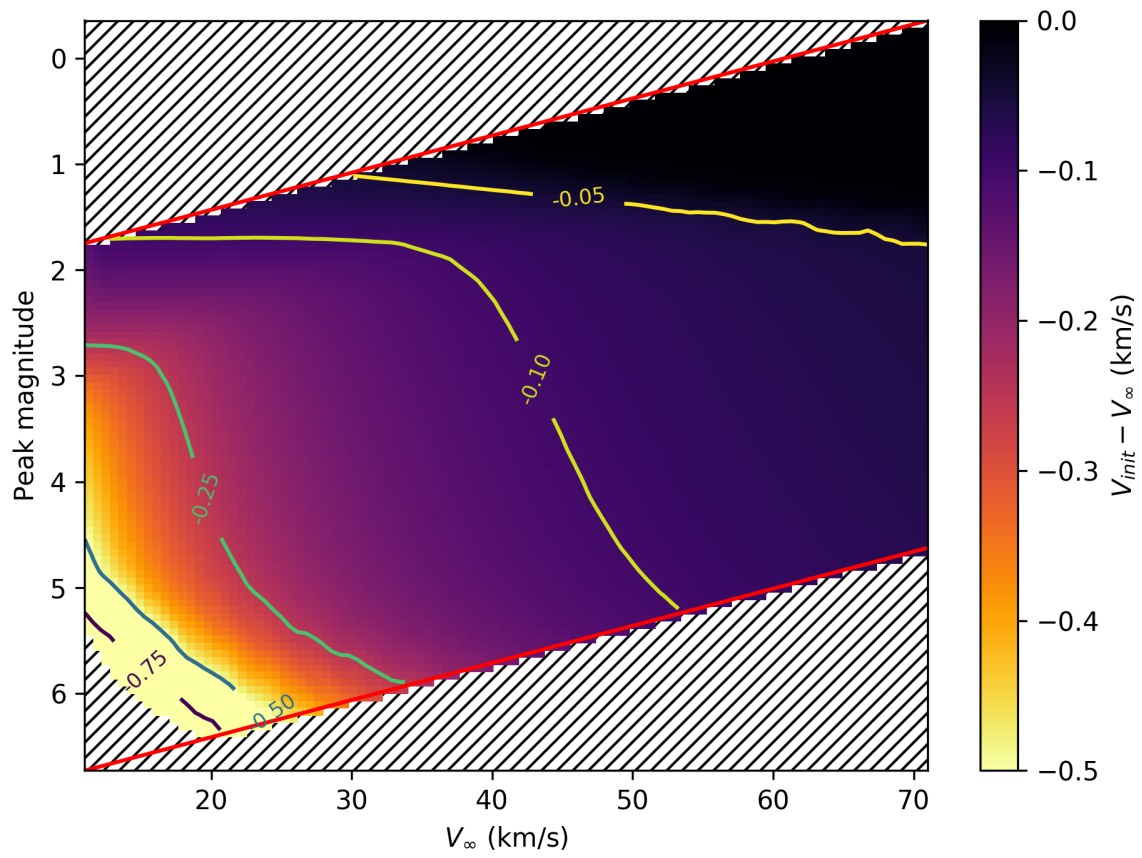
Figure 2.9: Asteroidal meteoroids - simulations for the image intensified systems.
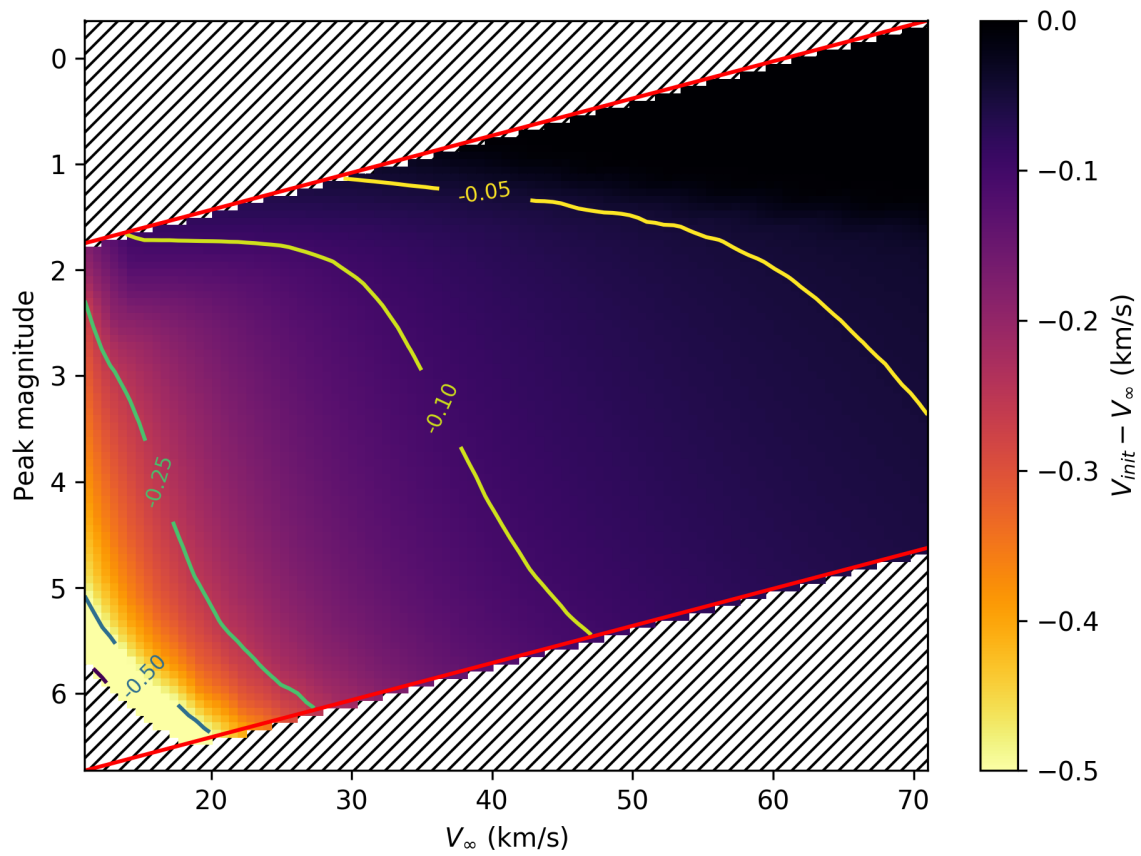
Figure 2.10: Iron-rich meteoroids - simulations for the CAMO influx system.
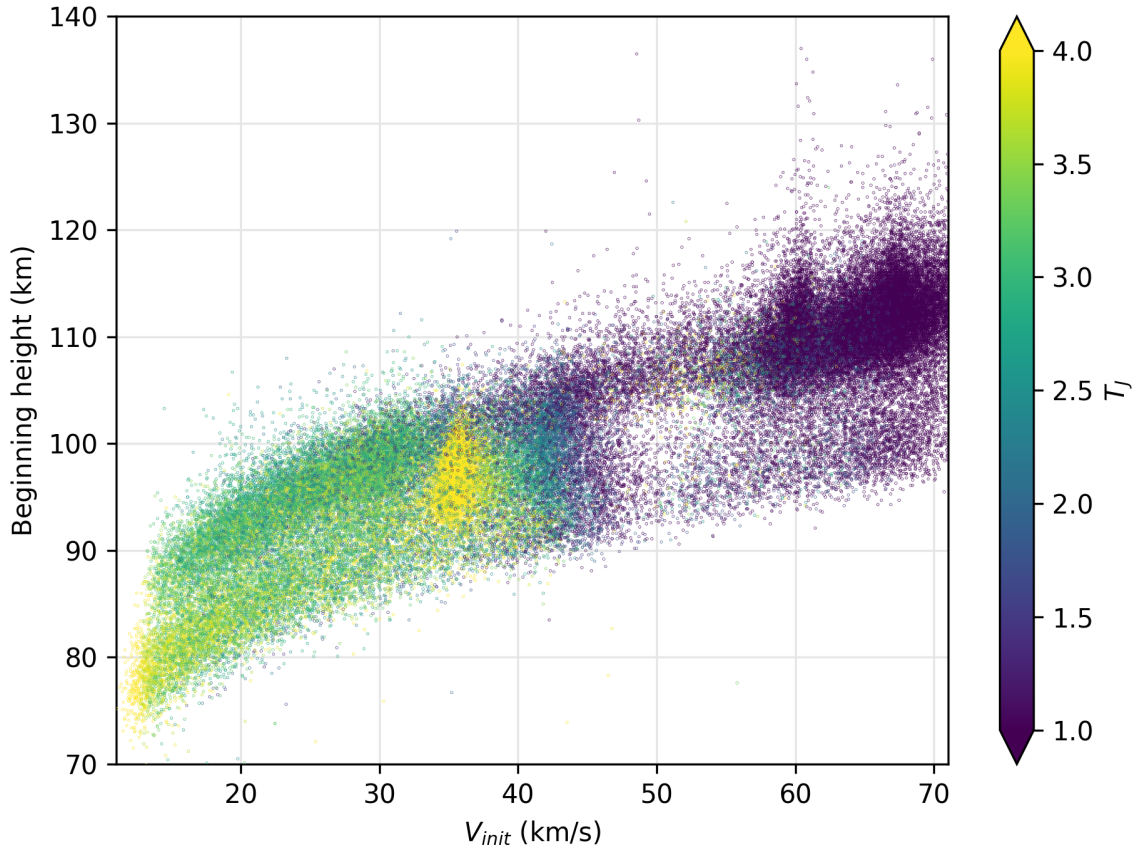
Figure 2.11: The dependence of velocity and beginning heights on the Tisserand parameter with respect to Jupiter for CAMS data.

2.6.2 Moderate field of view system - CAMS

Figure 2.11 shows the observed beginning heights for actual CAMS optical system meteors as a function of speed, and their Tisserand parameters with respect to Jupiter. The same distinction in orbit - types for $V_{init} < 40\,\mathrm{km\,s^{-1}}$ and $V_{init} > 40\,\mathrm{km\,s^{-1}}$ meteors can be seen here as was present with the CAMO influx system, as well as the same separation into two branches of beginning heights. These data contain a substantially larger fraction of shower meteors (27.6 %), notably the Geminids at $V_{init} \approx 35\,\mathrm{km\,s^{-1}}$, and Perseids and Orionids at $V_{init} \approx 60\,\mathrm{km\,s^{-1}}$ and $V_{init} \approx 66\,\mathrm{km\,s^{-1}}$ respectively.

Figure 2.12 compares observed beginning heights with our simulations - the reproduction is satisfactory except for asteroidal and iron-rich material at very low velocities ($V_{init} < 12\,\mathrm{km\,s^{-1}}$)

where only larger meteoroids are visible. These meteoroids are discussed in Jenniskens et al. (2016b) who attribute them to an unexpected population of large and old Poynting-Robertson drag evolved meteoroids at very low semi-major axes ($T_J > 3.2$), indicating collisional lifetimes on the order of 10^6 years and possibly different physical properties than the rest of the population. Alternatively, the luminous efficiency may change dramatically at lower speeds and our mass model may no longer be valid. We also note that a small number have beginning heights above our modelled range, which may be caused by different physical properties of those meteoroids than modelled, seasonal changes in the atmosphere (see section 2.6.4), or simply observational errors.

The beginning heights of the Perseids and Orioinids match those expected for cometary material, consistent with their cometary origin (Borovička, 2005). The Geminids lie between the two discrete branches, suggesting a larger spread in strength/densities and heterogeneity of the meteoroid material, as also suggested by the results of Borovička et al. (2009), who found the densities of Geminid meteoroids to range between $1000 \, \mathrm{kg \, m^{-3}}$ and $3000 \, \mathrm{kg \, m^{-3}}$ for the same mass range. Furthermore, Ceplecha (1977) classified the Geminids as an intermediate type B, between the asteroidal type A and cometary type C, also consistent with our results.

Figures 2.13 to 2.15 show the model differences between the initial and pre-atmosphere velocities for various meteoroid types. Compared to the CAMO influx system, the overall differences in velocities are similar, even though the beginning heights are lower, since the meteoroid masses are larger. At high velocities, cometary meteoroids show velocity differences below $100 \, \mathrm{m \, s^{-1}}$ down to $20 \, \mathrm{km \, s^{-1}}$ when the difference exceeds $200 \, \mathrm{m \, s^{-1}}$. Asteroidal meteoroids show the highest absolute velocity difference, in excess of $500 \, \mathrm{m \, s^{-1}}$ for the faintest meteors at low velocities of $v_\infty \approx 15 \, \mathrm{km \, s^{-1}}$. Finally, as with the CAMO influx system, iron-rich meteoroids exhibit velocity differences that are between the other two types.
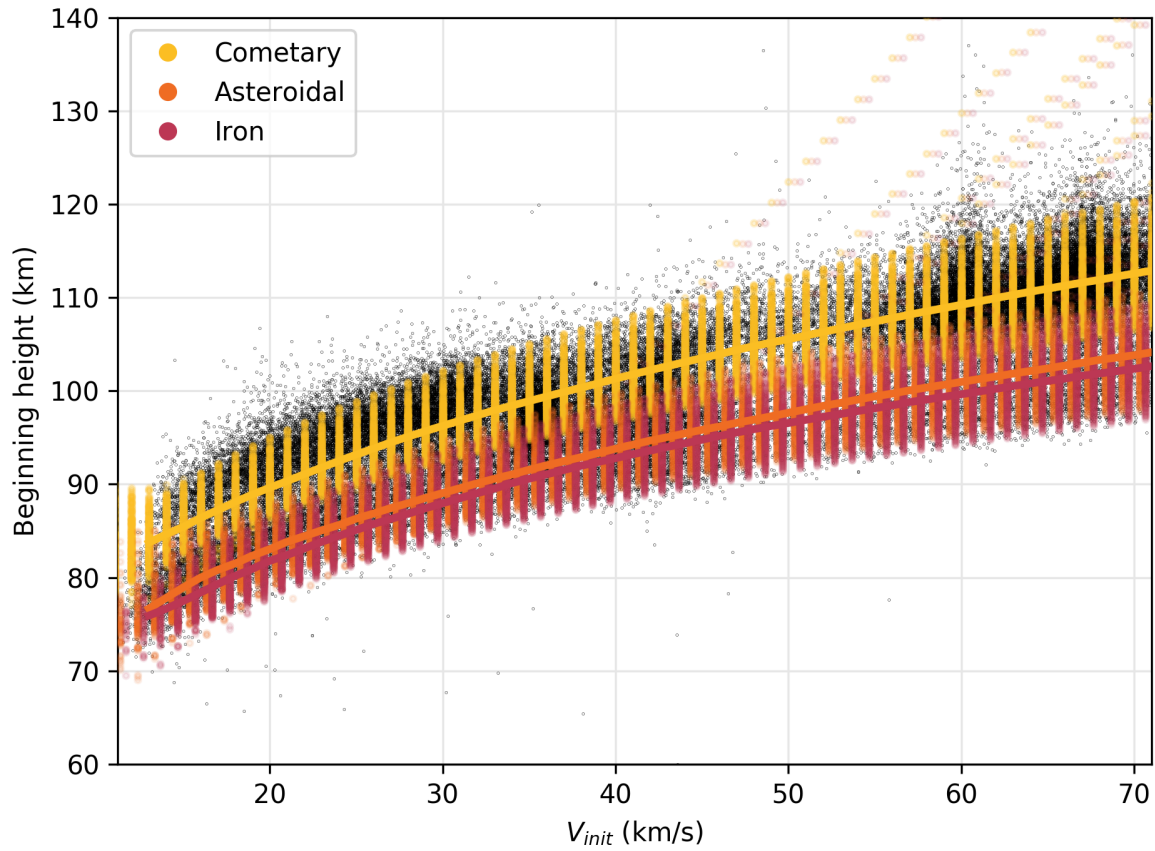
Figure 2.12: Observed and simulated beginning heights for the CAMS-type system. Yellow, orange and brown dots represent cometary, asteroidal and iron meteoroids respectively. Thick lines that follow the branches by the middle are median beginning heights for every branch.
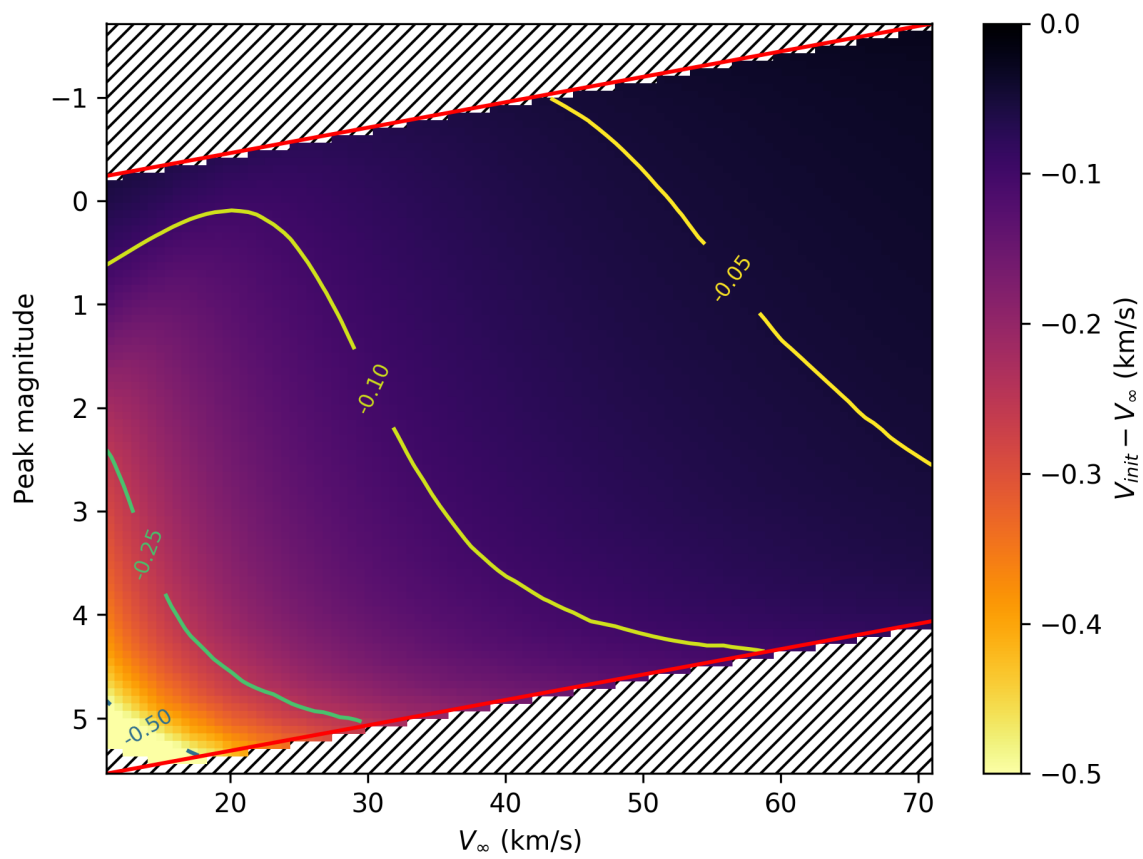
Figure 2.13: Cometary meteoroids - simulations for the CAMS-type system.
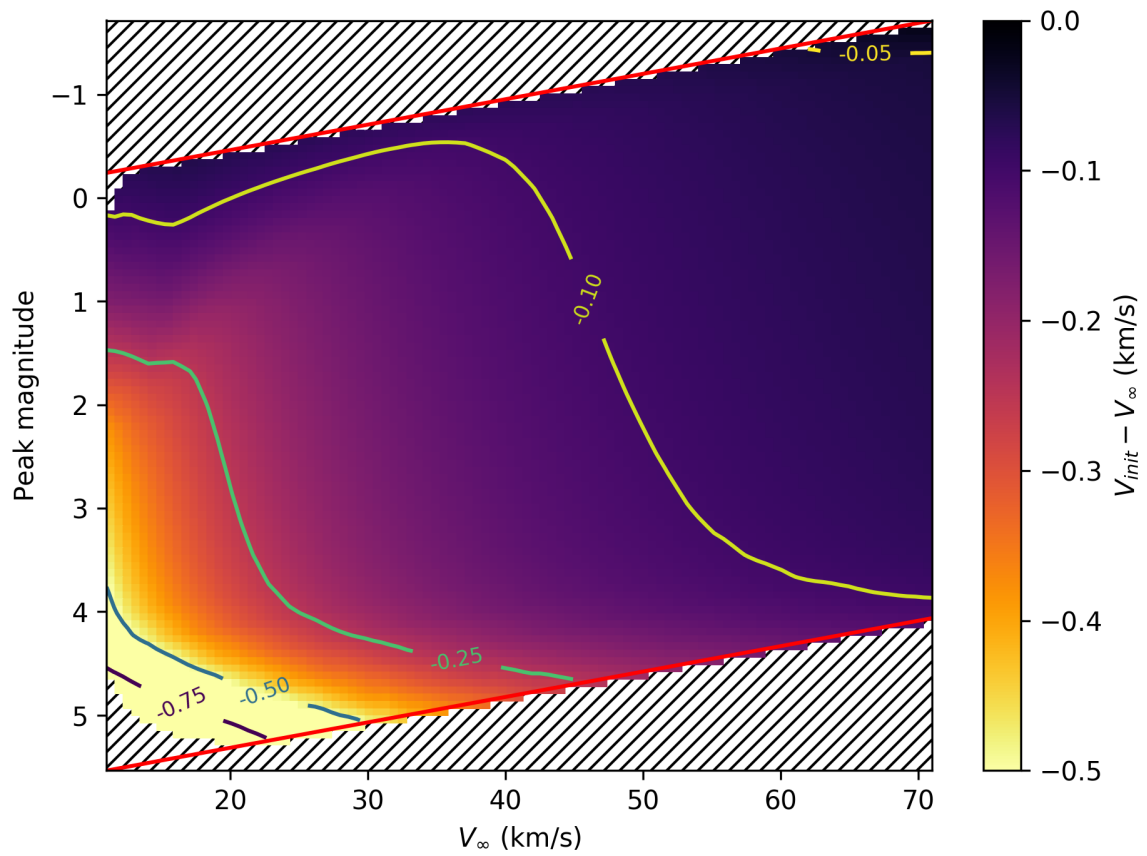
Figure 2.14: Asteroidal meteoroids - simulations for the CAMS-type system.
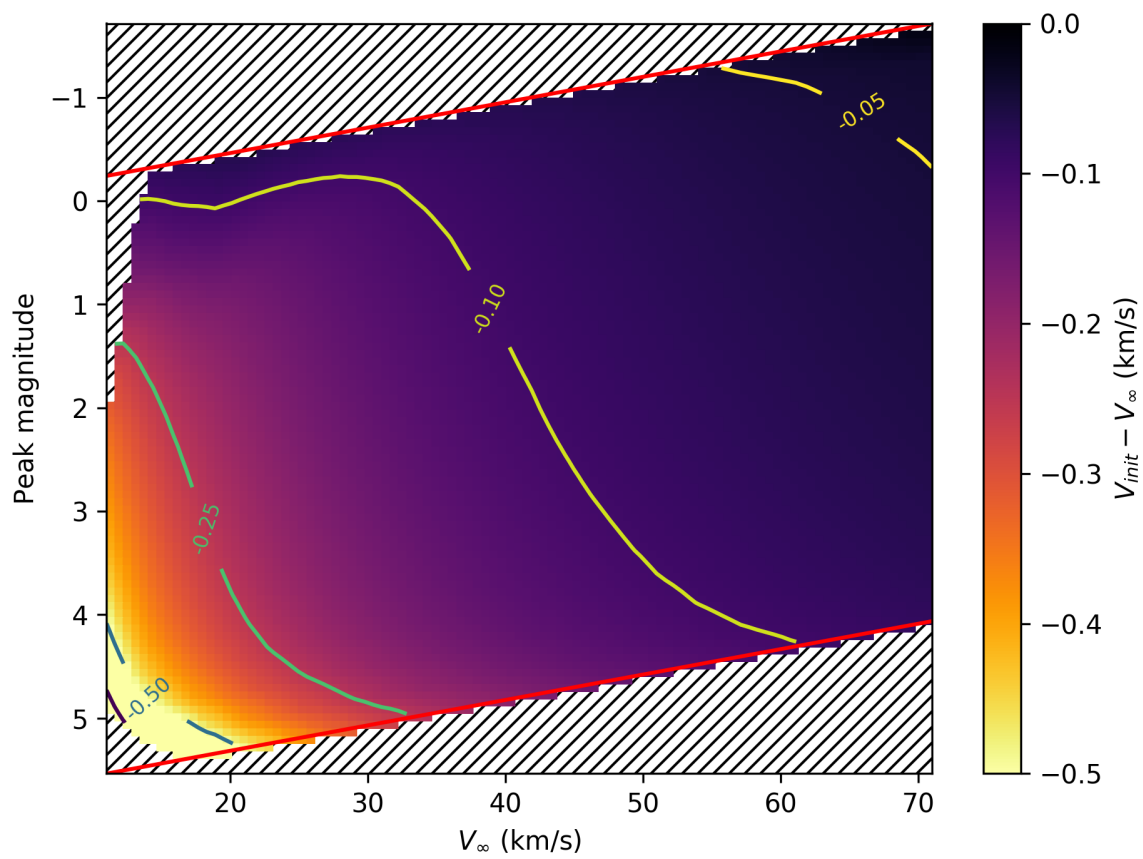
Figure 2.15: Iron-rich meteoroids - simulations for the CAMS-type system.
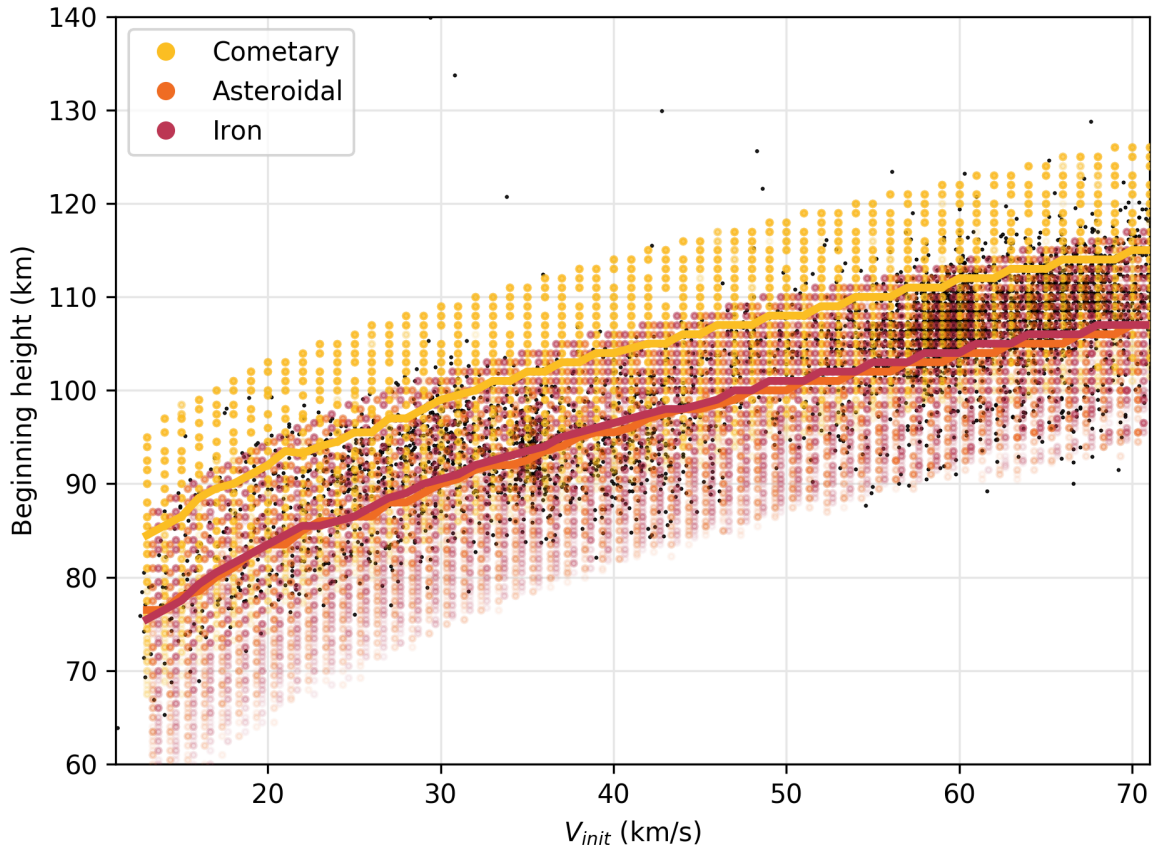
Figure 2.16: Observed and simulated beginning heights for the all-sky system. Yellow, orange and brown dots represent cometary, asteroidal and iron meteoroids respectively. Thick lines that follow the branches by the middle are median beginning heights for every branch.

2.6.3 All-sky (SOMN) system

Figure 2.16 shows the comparison of observed beginning heights and our simulations for an optical system with all-sky video sensitivity. The FM model reproduces the trend of beginning heights well for both branches, across all modelled velocities. The only discrepancy is in the upper regions of the cometary branch - simulations indicate that for the assumed physical parameters cometary meteoroids should start higher. This may indicate that the centimetre-size population lacks low-density cometary material, compared to smaller meteoroids seen by more sensitive systems.

Figures 2.17 through 2.19 show the initial and pre-atmosphere velocity differences. Compared to meteoroids seen by other systems, these have the smallest Δv, indicating the reduction
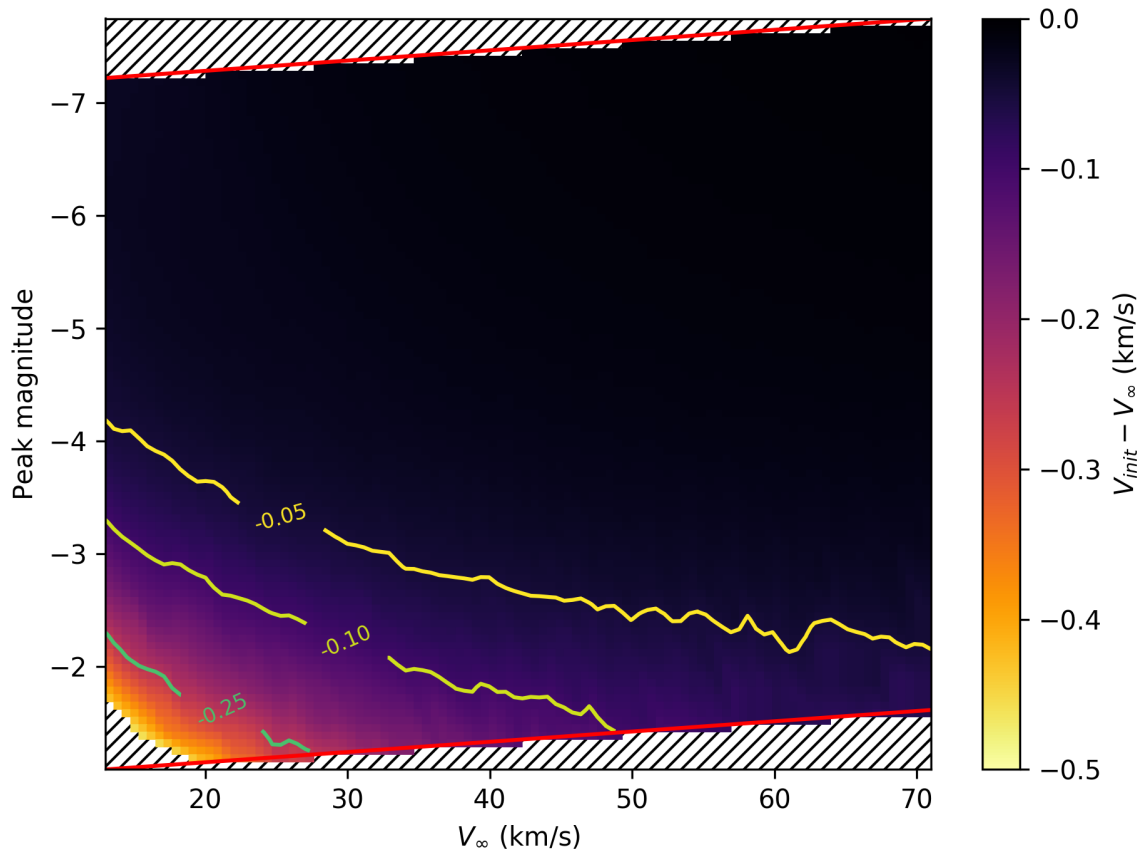
Figure 2.17: Cometary meteoroids - simulations for all-sky systems.

of the velocity difference with the rise in observed meteoroid masses. For all types of mete-oroids with peak magnitudes brighter than -4^M, the difference in velocity is below $50\,\mathrm{m\,s^{-1}}$. The difference in velocity is only significant for very low velocity faint meteors, particularly asteroidal meteoroids. It is close to or in excess of $0.5\,\mathrm{km\,s^{-1}}$ for $v_\infty < 25\,\mathrm{km\,s^{-1}}$ and peak magnitudes below -2^M, which are close to the detection limit of the system.

2.6.4 Dependence of the velocity difference on the varying atmospheric density

Our results may be influenced by latitudinal and seasonal changes in the air mass density at meteor heights, which can vary by up to 50% (Dr. Douglas Drob, personal communication). Unfortunately, no currently available models implement these variances in detail. Thus, we
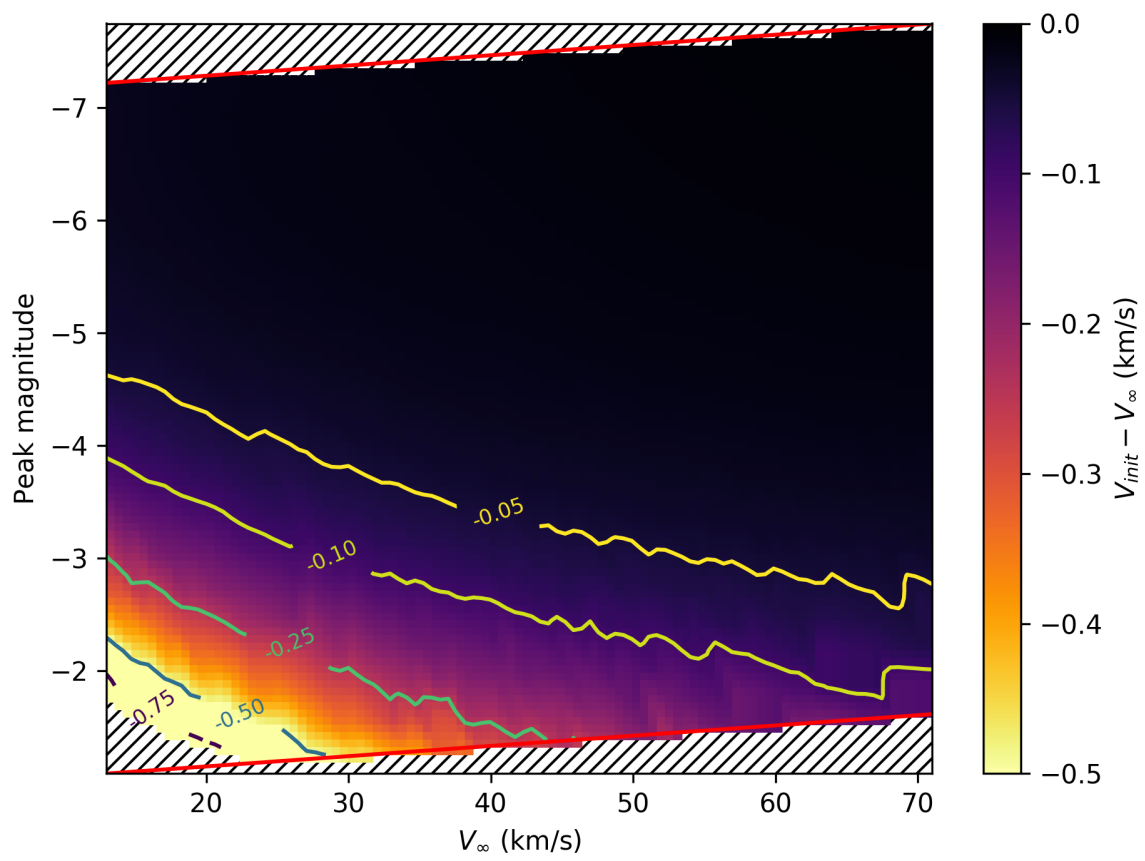
Figure 2.18: Asteroidal meteoroids - simulations for all-sky systems.
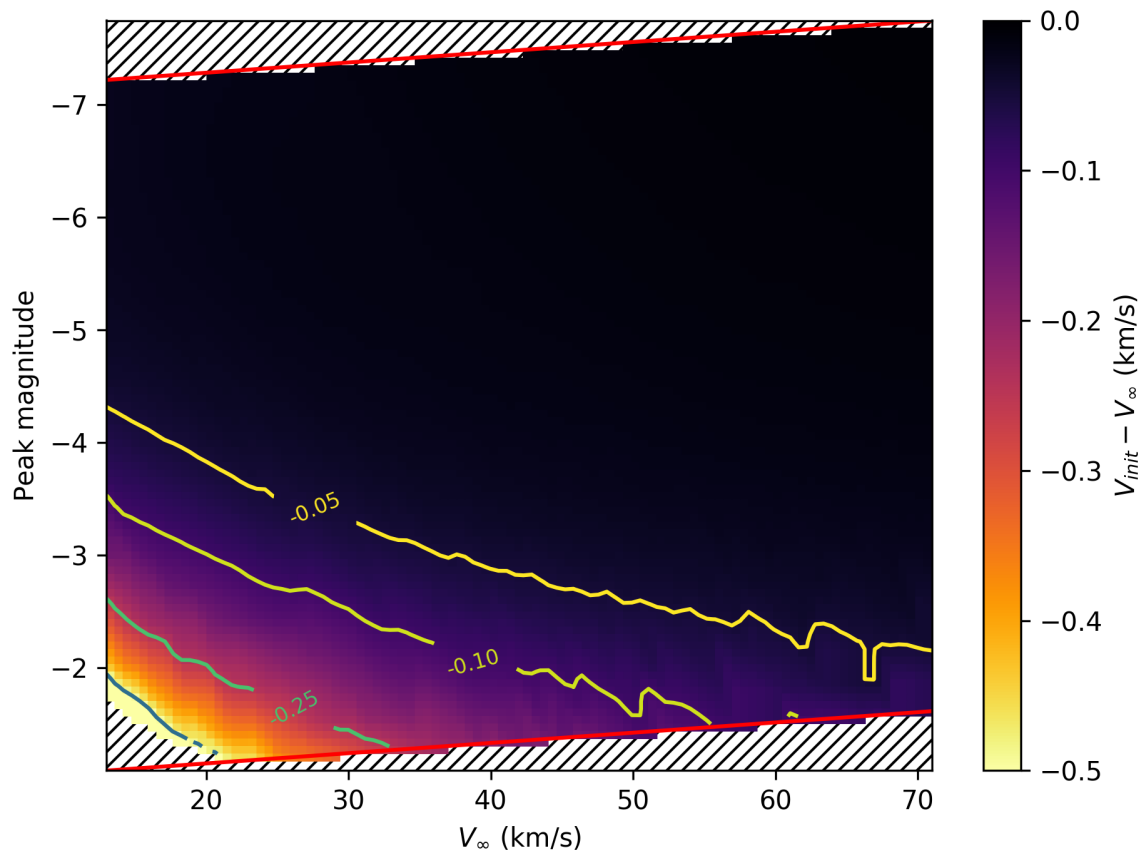
Figure 2.19: Iron-rich meteoroids - simulations for all-sky systems.

investigated the influence of the atmospheric mass density on the velocity difference in two extreme cases, a 50 % increase and a 50 % decrease in atmospheric mass density. Figures 2.20 and 2.21 show simulations of the same meteor as in figure 2.5 but with different values of the atmospheric mass density. Simulations were performed for a $V_\infty = 20\,\mathrm{km\,s^{-1}}$ cometary meteoroid with a mass of $m = 0.1\,\mathrm{g}$, density $\rho_m = 1510\,\mathrm{kg\,m^{-3}}$ and zenith angle of $Z_G = 45°$, as seen by the simulated CAMS-like system. The results show that the beginning heights shift up or down, but Δv remains approximately the same.

Figure 2.22 shows the comparison of beginning heights for meteoroids of different types. As expected, in the case of a denser atmosphere, meteors start several kilometers higher. Similarly, lower assumed atmospheric mass densities lead to meteors having lower starting heights. In contrast to beginning heights, Δv remains virtually unaffected ($< 1\,\mathrm{m\,s^{-1}}$ difference) by atmosphere density changes of order a factor of two across all velocities and for all meteoroid types, as shown in Figure 2.23.

2.7   Model Validation

As older meteoroid streams are expected to have inherent (physical) dispersions of velocities inside the stream of order several kilometers per second (Abedin et al., 2017) it may be difficult to argue that the velocity corrections we are proposing are significant if one considers only the mean velocity of the stream. The largest absolute decelerations before the point of detection are for smaller low-velocity meteoroids, which either do not belong to any meteoroid stream or are very dynamically evolved. Due to these unfavourable circumstances, we are only able to validate our model results for the case of the 2011 Draconid outburst. Maslov (2011) and Vaubaillon et al. (2011) modelled the ejection of meteoroids from comet 21P/Giacobini-Zinner and predicted that a very young stream of material ejected in 1900 and 1907 will produce an outburst in 2011. Both authors predicted a model mean value of meteoroid geocentric velocities of $20.9\,\mathrm{km\,s^{-1}}$ at Earth.
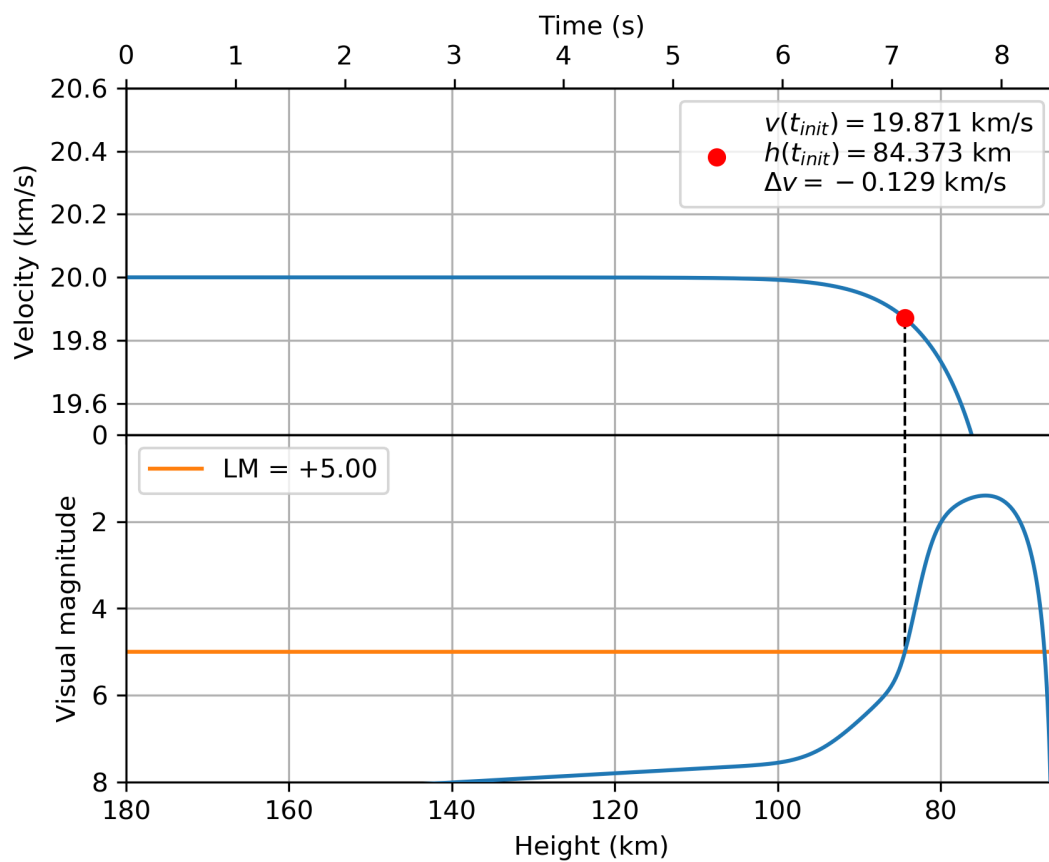
Figure 2.20: Simulation for 50 % lower atmosphere mass density.
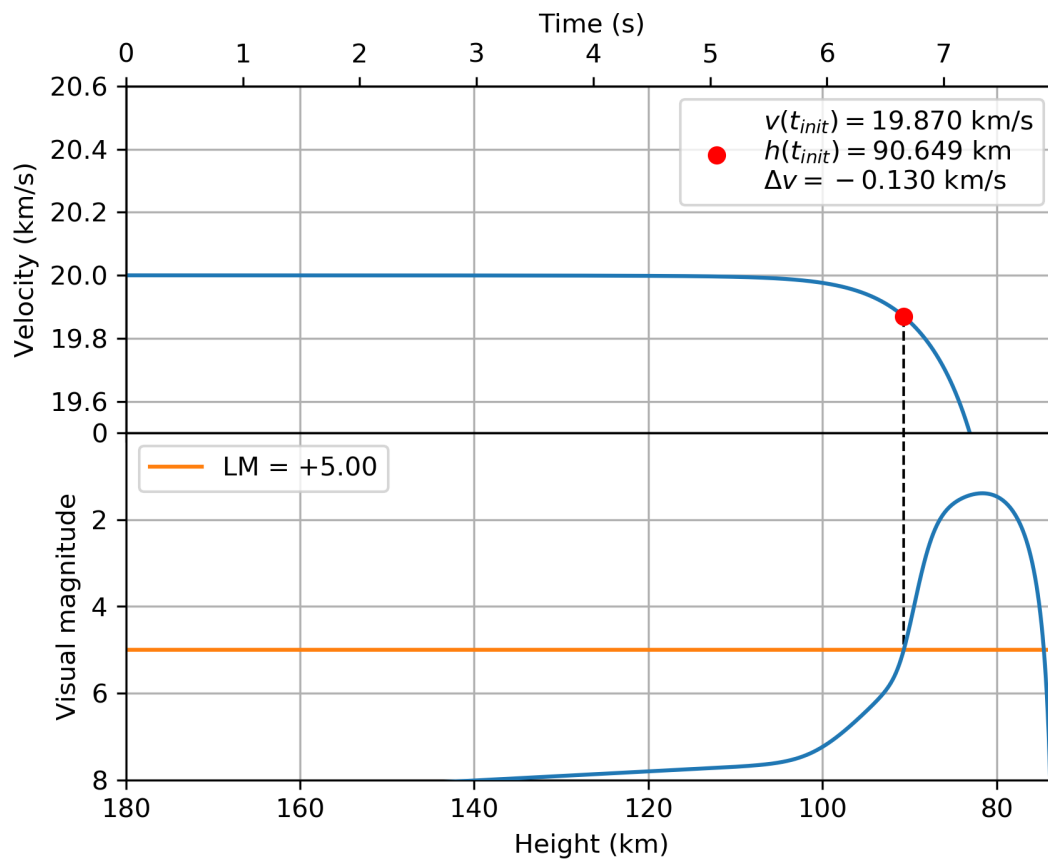
Figure 2.21: Simulation for 50 % higher atmosphere mass density.
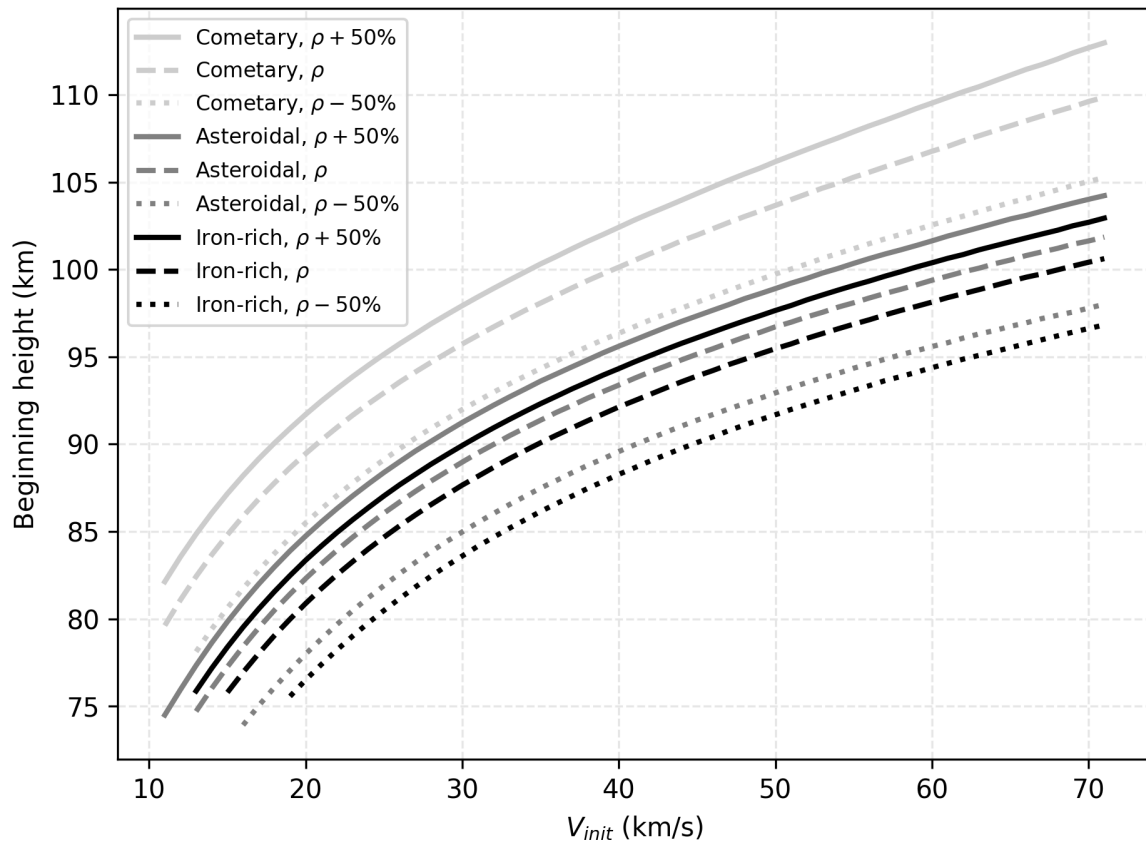
Figure 2.22: Comparison of beginning heights for 3 meteoroid types and ±50% atmosphere mass densities.
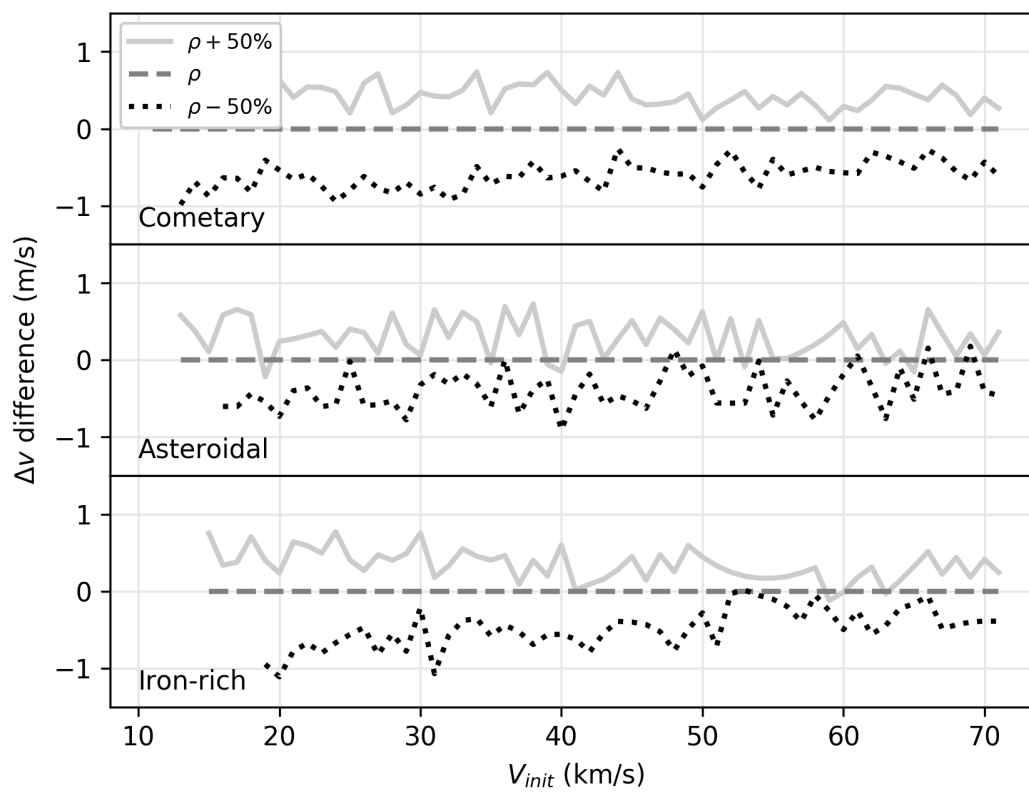
Figure 2.23: Comparison of differences in ΔV for 3 meteoroid types and ±50% atmosphere mass densities.

The outburst was well observed: Toth et al. (2012) observed 62 Draconids from northern Italy, but due to large deceleration they found it difficult to estimate the initial velocity and used a fixed velocity from previous observations by Borovička et al. (2007). Borovička et al. (2014) used the Borovička et al. (2007) meteoroid erosion model which takes deceleration into account and matched it to their observations, which enabled them to more accurately estimate pre-atmosphere initial velocities. They obtained a mean geocentric velocity of $V_g = 20.84 \pm 0.15\,\mathrm{km\,s^{-1}}$, which match the model predictions well. Kero et al. (2012) used meteor head echo data from the MU radar in Japan and showed directly that their meteoroids decelerate significantly before ablation and detection. After applying a deceleration correction they estimated a mean $V_g = 20.9\,\mathrm{km\,s^{-1}}$, also matching the predictions exactly due to the very high velocity precision possible with head echo measurements.

In contrast, optical observations which did not correct for deceleration before detection estimated geocentric velocities which were $150 - 200\,\mathrm{m\,s^{-1}}$ lower than predicted. Šegon et al. (2014) determined the initial velocity of 53 video Draconids using the linear deceleration model of Gural (2012) instead of average velocities. The model assumes that the meteoroid starts with an initial velocity of V_{init} and experiences a constant (fixed) deceleration with time. As there is no information about the deceleration before detection, the initial velocity that was measured was the velocity at the beginning height. They found a mean geocentric velocity of $V_g = 20.74 \pm 0.71\,\mathrm{km\,s^{-1}}$. Trigo-Rodríguez et al. (2013) measured the velocity at the beginning of the meteor trail and found $V_g = 20.76 \pm 0.43\,\mathrm{km\,s^{-1}}$ for 16 manually reduced video Draconids. Jenniskens et al. (2016a) used an exponential deceleration model of Whipple & Jacchia (1957) with the aim of reconstructing true pre-atmopshere velocities and cite a mean geocentric velocity for the 2011 Draconids of $V_g = 20.7\,\mathrm{km\,s^{-1}}$, consistent with other observations measuring only the velocity at the beginning of the visible trail.

The geocentric velocity uncertainty in the three cases above are on the order of hundreds meters per second; however, from our modelling we suggest that they all systematically underestimate the true speeds by $\sim 150\,\mathrm{m\,s^{-1}}$. Systems used by Šegon et al. (2014), Trigo-Rodríguez

et al. (2013), and Jenniskens et al. (2016a) are comparable to our simulated CAMS-like system, for which the predicted velocity difference for cometary meteoroids at $20\,\mathrm{km\,s^{-1}}$ ranges from $\sim 100\,\mathrm{m\,s^{-1}}$ to $\sim 500\,\mathrm{m\,s^{-1}}$, depending on the mass of the meteoroid. This value is a lower boundary as we assume no fragmentation prior to detection, which certainly is not true of the fragile Draconid meteoroids.

Jenniskens et al. (1997) noticed the difference in initial velocities of Quadrantids between photographically determined initial velocities (meteor LM $+0^{M}$, Betlem et al. (1997) data reduction method) and average velocities of image-intensified video meteors (meteor LM $+6^{M}$) to be as much as $0.7\,\mathrm{km\,s^{-1}}$. A large portion of the difference between the two was caused by the overall deceleration of the meteor, but our results suggest that at least $100\,\mathrm{m\,s^{-1}}$ of this difference could be due to the inherent observational biases of both systems. Finally, we note that the $200\,\mathrm{m\,s^{-1}}$ to $500\,\mathrm{m\,s^{-1}}$ initial velocity underestimation for the Geminids described by Hajdukova Jr et al. (2017) is well explained by our analysis.

2.8   Conclusions

We have modeled the velocities of meteoroids at the top of the atmosphere and compared these to expected measured velocities at the moment of first luminous detection, i.e. initial velocities. Our analysis shows that these velocities are expected to differ by a minimum value of order of hundreds of meters per second, the velocity difference being heavily dependent on meteoroid mass, composition, and velocity. In the mass range observed by all-sky fireball networks the difference is almost negligible, while for optical systems detecting typical meteoroid masses smaller than 1 g the difference is significant and can be in excess of $500\,\mathrm{m\,s^{-1}}$. This implies that increasing the precision of measured initial velocities is not the limiting factor for obtaining high accuracy meteoroid orbits. Improving accuracy requires numerical ablation modelling and additional assumptions about the composition of each meteoroid. As a starting point for such corrections, a table providing empirical lookup corrections per optical system and meteoroid

type is given in the supplementary materials of the original paper.

We have reproduced the observed separation of meteoroids by their beginning heights through ablation modeling and determined that it is largely density dependent, thus allowing classification of meteoroids by their beginning heights into rough density groups, confirming the predictions of Ceplecha (1968). Low-density meteoroids of cometary origin always start at higher altitudes, while asteroidal and iron-rich meteoroids start lower, although the latter two do not differ significantly in their beginning heights. Nevertheless, we notice a discrepancy between our findings and those of Kikwaya et al. (2011) for low-density HTC meteors with low beginning heights. Kikwaya et al. (2011) found a range of densities, while our model predicts they should all have asteroidal densities. The similarity of beginning heights between the asteroidal and iron-rich group might indicate that they are in fact the same population in terms of bulk density, as proposed by Moorhead et al. (2017). Notably, that study found that meteoroid densities correlate more strongly with Tisserand parameter than with the Ceplecha (1958) K_B parameter, which is based on beginning heights.

Our findings imply a non-negligible systematic observational bias resulting in underestimation of the semi-major axis of low-velocity meteor showers.

Bibliography

Abedin, A., Wiegert, P., Janches, D., et al. 2018, Icarus, 300, 360 . `http://www.sciencedirect.com/science/article/pii/S0019103516306042`

Abedin, A., Wiegert, P., Pokorný, P., & Brown, P. 2017, Icarus, 281, 417

Albin, T., Koschny, D., Soja, R., Srama, R., & Poppe, B. 2016, in Proceedings of the International Meteor Conference Egmond, the Netherlands, 2-5 June 2016, 20–25

Asher, D. J., & Izumi, K. 1998, Mon. Not. R. Astron. Soc, 297, 23

Betlem, H., Ter Kuile, C., de Lignie, M., et al. 1997, Astronomy and Astrophysics Supplement Series, 128, 179

Borovička, J. 1990, Bulletin of the Astronomical Institutes of Czechoslovakia, 41, 391

—. 2005, Proceedings of the International Astronomical Union, 1, 249

Borovička, J., Koten, P., Shrbený, L., Štork, R., & Hornoch, K. 2014, Earth, Moon, and Planets, 113, 15

Borovička, J., Koten, P., Spurný, P., Boček, J., & Štork, R. 2005, Icarus, 174, 15

Borovička, J., Koten, P., Spurný, P., et al. 2009, Proceedings of the International Astronomical Union, 5, 218

Borovička, J., Spurný, P., & Brown, P. 2015, Asteroids IV, 257

Borovička, J., Spurný, P., & Koten, P. 2007, Astronomy & Astrophysics, 473, 661

Borovička, J., Tóth, J., Igaz, A., et al. 2013, Meteoritics & Planetary Science, 48, 1757

Brown, P., Jones, J., Weryk, R., & Campbell-Brown, M. 2005, in Modern Meteor Science An Interdisciplinary View (Springer), 617–626

Brown, P., Weryk, R., Kohut, S., Edwards, W., & Krzeminski, Z. 2010, WGN, Journal of the International Meteor Organization, 38, 25

Brown, P., Weryk, R., Wong, D., & Jones, J. 2008, Icarus, 195, 317

Campbell-Brown, M., Borovička, J., Brown, P., & Stokan, E. 2013, Astronomy & Astrophysics, 557, A41

Campbell-Brown, M., & Koschny, D. 2004, Astronomy & Astrophysics, 418, 751

Ceplecha, Z. 1958, Bulletin of the Astronomical Institutes of Czechoslovakia, 9, 154

—. 1968, SAO Special report, 279

Ceplecha, Z. 1977, in International Astronomical Union Colloquium, Vol. 39, Cambridge University Press, 143–152

—. 1987, Bulletin of the Astronomical Institutes of Czechoslovakia, 38, 222

—. 1988, Bulletin of the Astronomical Institutes of Czechoslovakia, 39, 221

Ceplecha, Z., Borovička, J., Elford, W. G., et al. 1998, Space Science Reviews, 84, 327

Ceplecha, Z., & Revelle, D. O. 2005, Meteoritics & Planetary Science, 40, 35

Ceplecha, Z., Spurný, P., Borovička, J., & Keclíková, J. 1993, Astronomy and Astrophysics, 279, 615

Egal, A., Gural, P., Vaubaillon, J., Colas, F., & Thuillot, W. 2017, Icarus, 294, 43

Fisher, A., Hawkes, R., Murray, I., Campbell, M., & LeBlanc, A. 2000, Planetary and Space Science, 48, 911

Gural, P. S. 2012, Meteoritics & Planetary Science, 47, 1405

Hajdukova Jr, M., Koten, P., Kornoš, L., & Tóth, J. 2017, Planetary and Space Science, 143, 89

Hawkes, R., & Jones, J. 1975, Monthly Notices of the Royal Astronomical Society, 173, 339

Jacchia, L., Verniani, F., & Briggs, R. E. 1967, Smithsonian Contributions to Astrophysics, 10, 1

Jenniskens, P., Betlem, H., De Lignie, M., Langbroek, M., & Van Vliet, M. 1997, Astronomy and Astrophysics, 327, 1242

Jenniskens, P., Gural, P., Dynneson, L., et al. 2011, Icarus, 216, 40

Jenniskens, P., Nénon, Q., Albers, J., et al. 2016a, Icarus, 266, 331

Jenniskens, P., Nénon, Q., Gural, P., et al. 2016b, Icarus, 266, 384

Kero, J., Fujiwara, Y., Abo, M., Szasz, C., & Nakamura, T. 2012, Monthly Notices of the Royal Astronomical Society, 424, 1799

Kikwaya, J.-B., Campbell-Brown, M., & Brown, P. 2011, Astronomy & Astrophysics, 530, A113

Kikwaya, J.-B. E. 2011, PhD thesis, University of Western Ontario

Koten, P., Borovička, J., Spurný, P., Betlem, H., & Evans, S. 2004, Astronomy & Astrophysics, 428, 683

Maslov, M. 2011, WGN, Journal of the IMO, 39, 3

Moorhead, A. V., Blaauw, R. C., Moser, D. E., et al. 2017, Monthly Notices of the Royal Astronomical Society, 472, 3833

Pecina, P., & Ceplecha, Z. 1983, Bulletin of the Astronomical Institutes of Czechoslovakia, 34, 102

—. 1984, Bulletin of the Astronomical Institutes of Czechoslovakia, 35, 120

Picone, J., Hedin, A., Drob, D. P., & Aikin, A. 2002, Journal of Geophysical Research: Space Physics, 107

Šegon, D., Andreić, Ž., Gural, P. S., et al. 2014, Earth, Moon, and Planets, 112, 33

Silber, E. A. 2014, PhD thesis, University of Western Ontario

Spurnỳ, P., Borovička, J., Mucke, H., & Svoreň, J. 2017, Astronomy & Astrophysics, 605, A68

Stokan, E., & Campbell-Brown, M. 2014, Icarus, 232, 1

Subasinghe, D., & Campbell-Brown, M. D. 2018, Astronomical Journal, accepted

Subasinghe, D., Campbell-Brown, M. D., & Stokan, E. 2016, Monthly Notices of the Royal Astronomical Society, 457, 1289

Toth, J., Piffl, R., Koukal, J., et al. 2012, WGN, Journal of the International Meteor Organization, 40, 117

Trigo-Rodríguez, J. M., Madiedo, J. M., Williams, I., et al. 2013, Monthly Notices of the Royal Astronomical Society, 433, 560

Vaubaillon, J., Sato, M., Moser, D., et al. 2011, Central bureau electronic telegrams, 2819, 2

Verniani, F. 1965, Smithsonian Contributions to Astrophysics, 8, 141

Vida, D., Brown, P. G., & Campbell-Brown, M. 2018, Monthly Notices of the Royal Astronomical Society, 479, 4307

Weryk, R., Brown, P., Domokos, A., et al. 2008, Earth, Moon, and Planets, 102, 241

Weryk, R., Campbell-Brown, M., Wiegert, P., et al. 2013, Icarus, 225, 614

Weryk, R. J., & Brown, P. G. 2013, Planetary and Space Science, 81, 32

Whipple, F. L., & Jacchia, L. G. 1957, Smithsonian Contributions to Astrophysics, 1, 183

Chapter 3

Novel meteor trajectory simulator and solver - I. Theory

A version of this chapter has been published as:

Vida, D., Gural, P.S., Brown, P.G., Campbell-Brown, M., & Wiegert, P. (2020). *Estimating trajectories of meteors: an observational Monte Carlo approach – I. Theory.* Monthly Notices of the Royal Astronomical Society, 491, 2688.

3.1 Introduction

Schiaparelli & von Boguslawski (1871) were the first to show the connection between the orbits of meteor showers and comets (Romig, 1966; Hughes, 1982). This physical connection motivated development of various methods of estimating meteor trajectories, with the first reasonably precise measurements made even earlier with the pioneering work of Brandes and Benzenburg in the late 18th century (Burke, 1986). These techniques typically use optical measurements from multiple sites to estimate atmospheric meteor trajectories. Gural (2012) provides a good historical overview.

In this work we focus on three foundational papers which provide representative descrip-

tions of the three most common modern meteor trajectory estimation methods. These are:

a) the intersecting planes (IP) method as described by Ceplecha (1987)

b) the lines of sight (LoS) method by Borovička (1990)

c) the multi-parameter fit (MPF) method of Gural (2012).

The goal of any trajectory solver is to reconstruct the atmospheric trajectory of a meteor, leading ultimately to an estimate of its pre-atmospheric orbit. The trajectory is defined by a position vector (a reference position in space) and a velocity vector. To compute a reliable heliocentric orbit this should preferably be at a point before any significant deceleration of the meteoroid occurs. A common assumption is that the trajectory is a straight line, a good approximation for shorter meteors. However, longer meteors, particularly those entering at shallow angles, may show significant deviation from a straight-line trajectory due to Earth's gravity (Ceplecha, 1979).

Existing methods usually estimate the geometry of the meteor path separately from the dynamics of the meteoroid (i.e. the time dependent characteristics of the meteor: position, velocity, acceleration). The velocity can be estimated by fitting an empirical model to the observations of time versus path length from the beginning of the meteor. Gural (2012) was the first to note that trajectories can be better constrained by fitting a meteor propagation model to both the meteor trajectory geometry and the meteoroid dynamics at the same time. This assumption makes use of the fact that all observers should see the same dynamical behaviour of a particular meteoroid at the same point in time. A consequence of this approach is that it allows an estimate of the absolute timing offsets between stations. A further recent advance in this area is using a particle filter algorithm to directly fit numerical meteor ablation models to better estimate trajectories of fireballs (Sansom et al., 2017).

The original motivation for this work was earlier analysis of two station meteor data obtained by the Canadian Automated Meteor Observatory (CAMO) mirror tracking system (Weryk et al., 2013). The system achieves an angular precision for meteor positions on the order of a

few arc seconds (limited largely by the system's ability to resolve the physical spreading of the meteor itself (Stokan et al., 2013)), which translates to a spatial precision of a few meters. The temporal precision of the system is 10 ms. This is sufficient to discern individual fragments of fragmenting faint meteors (Subasinghe et al., 2016; Vida et al., 2018a). Similar to Egal et al. (2017), we found that the existing methods of trajectory estimation do not always provide solutions of satisfactory quality. For example, we often found with CAMO measurements that the intersecting planes and the LoS methods produce solutions where the dynamics of the meteor do not match at different stations. The MPF method, in some cases, depending on the velocity model used, had convergence issues. This suggested that in some cases forcing the meteoroid velocity to follow a closed-form empirical model did not result in a physically consistent solution. As a result of this experience we also wanted to objectively quantify the real uncertainties and formally define the true accuracy of individually measured meteor radiants and velocities as estimated using CAMO data, and by extension other optical systems.

This series of papers attempts to answer the following question: For a given type of optical system, what is the best trajectory solver to use, and what quantitative accuracy should one typically expect? We note that this is one step in the process of defining the best estimate for a meteoroid's original heliocentric orbit. The necessary additional step is accounting for deceleration due to atmospheric drag on the earliest measured luminous point of the meteor, a topic addressed in Chapter 2.

In the following sections we discuss in detail the theory behind various methods of trajectory estimation and describe our novel Monte Carlo approach. Finally, for completeness, we summarize the equations for analytically computing meteoroid orbits from trajectory information, as previously published procedures were ambiguous in several crucial steps.

3.2　Overview of trajectory solvers

A set of line-of-sight (angle-angle) measurements of meteor positions from an individual observing station describes a fan of rays when converted into a station-fixed Cartesian coordinate system. By assuming that the position of an observer can be represented by a single point in the same coordinate system (usually at the time of the middle of the meteor's trajectory), a plane can be fit through these points (Ceplecha, 1987). By repeating the procedure for N different stations, one plane for each station is obtained. The intersection of every pair of planes, $\binom{N}{2}$ pairs in total, results in a line which describes the optimal trajectory as measured from two stations. If there are more than two trajectory lines, the average of the trajectories can be computed weighted by the squared sine of the convergence angle between every plane pair. The convergence angle is the angle between a pair of planes.

Borovička (1990) points out a disadvantage of the intersecting planes (IP) method: when the planes are paired using observations from multiple stations, the information about the uncertainty of individual measurements can be lost because only the whole plane is taken into consideration when intersecting it with another to define a trajectory. An outlier line-of-sight measurement can shift the whole plane in a certain direction and influence the resulting trajectory. However the fit residuals will not show the influence from the sole outlier.

Instead of pairing planes from individual stations and producing the trajectory as a secondary product, Borovička (1990) proposes that one can consider every measurement of meteor position as a ray emanating from the observer in the direction of the meteor at a specific point along its linear track. Each ray is usually referred to as a line-of-sight (LoS) measurement of the meteor. The trajectory is then found as the three-dimensional line which results in the minimal distance to all measurement lines-of-sight, with the solution computed using a least squares minimization. Furthermore, Borovička (1990) points out that this method can compensate for Earth's rotation at each LoS observation directly during the trajectory estimation process. In the absence of this compensation, fixed observers on the non-inertial rotating surface of the Earth perceive a virtual force (the Coriolis force) on the apparent meteor trajectory.

Additionally, the Borovička (1990) method makes possible compensation for diurnal aberration, an effect due to the Earth's rotation that occurs because of the changing observer's perspective of the meteor with respect to distant stars. Assuming one knows the absolute time, an Earth-centred Inertial (ECI) reference frame can be adopted in which the observer's coordinates are constantly changing due to Earth's rotation, but the meteor trajectory remains linear. We use the definition of ECI coordinates where the x-axis is aligned with the mean equinox at 12:00 Terrestrial Time on January 1, 2000 (J2000).

In the original LoS paper, Borovička (1990) keeps the observers in the Earth-centred Earth-fixed frame (ECEF), presumably because the timing of each individual measurement (taken on a single photographic film in that era) was unknown. In contrast to the ECI system, which does not rotate with respect to the stars but the coordinates of observers on Earth's surface are changing in time, coordinates of ECEF are fixed with respect to the Earth's surface. Without correcting for the changes in observer positions, Borovička (1990) found the results of the IP and LoS comparable. The reason that it is not possible to account for moving observers in the intersecting planes method is that the motion of the observer and the positions of the meteor are not co-planar (unless all measurements coincide with the observer's zenith, an impossible geometry to have from two different stations).

To provide a concrete estimate of the magnitude of the diurnal aberration correction, let us consider an observer at a latitude of 45° N where the Earth's rotational E-W velocity is about $328 \, \mathrm{m \, s^{-1}}$. For a meteor of 1 s duration, the real position of the observer will change $\pm 164 \, \mathrm{m}$ with respect to the average time of the trajectory determination. There is also a small effect when two observers are not at equal latitudes. A second observer at 46° N (~120 km away) experiences a rotational velocity of $322 \, \mathrm{m \, s^{-1}}$, which causes a differential of 3 m between the first and the last positions of the two observers. This effect is minor if positional errors are orders of magnitude larger, but it has to be taken into account when estimating high precision trajectories where positional measurements are on the order of meters. Figure 3.1 shows a general comparison between the intersecting planes and the LoS method.

Intersecting planes   **Lines of sight**
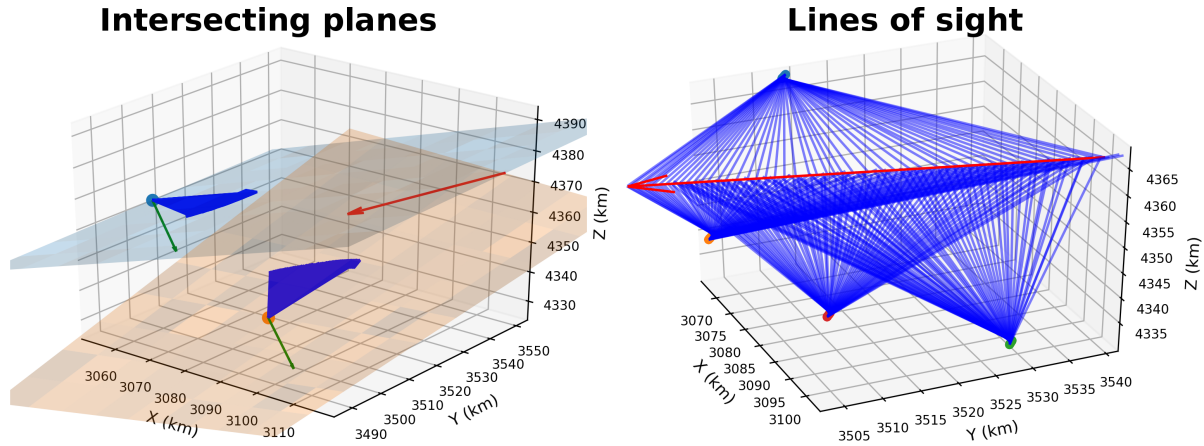
Figure 3.1: Left: The intersecting planes method with only the two stations having the best convergence angle shown. The planes are shown in blue and orange (semi-transparent) and are coplanar with line-of-sight observations (blue arrows emanating from stations). Note that stations are single points in the ECEF (Earth-centered Earth-fixed) frame, but here we show them in the ECI (Earth-centered inertial) frame at a fixed time. The green arrows are plane normals from each station, and the red arrow is the resulting estimated trajectory. Right: Lines of sight method, where coordinates of all four stations are changing due to the Earth's rotation.

The multi-parameter fit method with the underlying algorithmic details was first described in Gural (2012). It had been developed for the Cameras for Allsky Meteor Surveillance (CAMS) project where the full processing pipeline is described in Jenniskens et al. (2011). In contrast to the IP and LoS methods, which are purely geometrical, the multi-parameter fit (MPF) method uses a velocity model (i.e. dynamical information) as well. By assuming an empirical velocity model that may include deceleration terms, the MPF finds a trajectory solution (a line in 3D space) as well as the velocity and deceleration coefficients which bests describes the observed meteor's observations from all stations given the constraints of the empirical dynamical model. Because of the dynamical constraints, the method is also able to estimate relative timing offsets between camera sites, as all observers must see the same velocity at the same time.

To avoid issues of confusion with local minima in the method's cost function, an initial guess for the solution is obtained using the intersecting planes method. This guess is further refined using the LoS method - the latter modified by minimizing the angles between the mea-

sured lines of sight and the model trajectory, instead of minimizing the distances between the two. This refined guess is fed into a simplex-based non-linear equation solver where the angles between the measured lines of sight and the positions predicted by the model are minimized. This effectively ensures that all observers "see" the same dynamics of the meteor in time.

Because observing systems usually do not have absolute synchronized time, the time difference between the observers must be estimated as well in the MPF. In Gural (2012), the MPF was compared to IP and LoS using data from wide-field systems. The results showed that the measured radiant dispersion of meteor showers is significantly smaller if the MPF method with a constant velocity model (ie. no deceleration) is used, especially for cases with small convergence angles. The reduction in the dispersion indicates an improvement in the radiant measurement accuracy. The authors proposed three meteor propagation models:

1) the constant velocity model:

$$d(t) = v_0 t, \qquad (3.1)$$

where $d(t)$ is the distance of the meteor at a particular point in time after the beginning point, and v_0 is the constant velocity of the meteor.

2) the linear deceleration model:

$$d(t) = \begin{cases} v_0 t, & \text{if } t < t_0 \\ v_0 t - \frac{1}{2}a(t - t_0)^2, & \text{otherwise} \end{cases}, \qquad (3.2)$$

where t_0 is the time when meteor begins decelerating with a constant deceleration a.

3) the empirical exponential deceleration model of Whipple & Jacchia (1957):

$$d(t) = v_0 t - |a_1|e^{|a_2|t}, \qquad (3.3)$$

where a_1 and a_2 are deceleration parameters.

The complexities due to the physical properties of the meteoroids and their resulting abla-

tion behavior are not included in these models. The exponential deceleration model is the only one motivated by a physical basis, namely that the meteoroid's deceleration is proportional to the atmospheric density, following classical single-body ablation models (Ceplecha et al., 1998). As the atmospheric density increases exponentially with decreasing height, the velocity should follow a similar functional trend. However, the single-body assumption breaks down when a meteoroid starts fragmenting, a behaviour shown to exist for at least 90% of meteors from high-precision observations (Subasinghe et al., 2016), a phenomenon understood to be ubiquitous across all meteoroid masses (Ceplecha et al., 1998; Hawkes & Jones, 1975). Comparing the performance of different trajectory estimation methods even for single-body ablation has not been rigorously addressed. Gural (2012) performed simulations for a constant velocity model over an extensive range of encounter geometries and speeds. However, the comparison did not examine other functional forms of deceleration.

In recent work by Egal et al. (2017) it was shown that the exponential model is difficult to fit using local cost function minimization methods since it is mathematically ill-conditioned and the associated model coefficients have linear dependencies. The authors showed the advantages of global minimization methods over local techniques. In particular, they applied the particle swarm optimization (PSO) method (Eberhart & Kennedy, 1995) for fitting the exponential deceleration model and showed that it produced superior results, albeit at the expense of higher computational costs. Their work has shown that the fit works well on simulated data produced using the exponential deceleration model. In contrast, the fits were poorer when model data was created using the meteor ablation model of Borovička et al. (2007). They concluded that of all methods tested (IP, LoS and MPF), the multi-parameter fit consistently produced results with the smallest residuals and good radiant solutions even for meteors with very low convergence angles ($Q_c \sim 1°$). They also showed that the initial velocity estimated from all of the trajectory solvers for ablation-simulated meteoroids was not accurately determined. This suggests that a more reliable meteor propagation model is needed for the MPF in particular.

We have directly used all implementations of the three trajectory solvers including the

PSO based implementation of the Gural (2012) method, to test their relative performance on high-precision CAMO data. Given the performance limitations of existing algorithms, it was decided to develop a novel trajectory solver specifically to attempt to improve the accuracy of meteor trajectory solutions where high precision data is available. The details of this trajectory solver are given in section 3.3. To verify the performance of this new method and compare to the three other solvers, we also developed an observational meteor trajectory simulator. This provides synthetic measurement inputs to each solver using known solutions; details are given in section 3.4.

We emphasize that the ultimate limitation to the accuracy in the estimation of a meteoroid orbit based on observations of a meteor in the atmosphere is the amount of deceleration that occurs prior to the luminous phase. We use the term "initial velocity" for the velocity of the meteor at the moment of first detection, and "pre-atmospheric velocity" for the velocity before any significant deceleration has occurred (we assume this to be at a height of 180 km). The difference between the initial velocity and the pre-atmospheric velocity for various types of meteoroids as measured by several typical observation systems was analyzed in Vida et al. (2018b). It was found that low-velocity meteors significantly decelerate (up to $750\,\mathrm{m\,s^{-1}}$ for moderate and narrow field of view optical systems) prior to sensor detection of the visible meteor trail. The proposed correction of Vida et al. (2018b) should be used to reconstruct the real pre-atmosphere velocity from the measured initial velocity. Establishing the latter quantity and its true uncertainty is the focus of this work.

3.3 Monte Carlo trajectory estimation method

Our newly developed method of trajectory estimation builds on the work of Gural (2012) and expands on an earlier similar approach described in Weryk & Brown (2012). This technique uses the intersecting planes and the LoS methods to obtain a first estimate of the trajectory solution, then uses the observed angular residuals between the measurements and the fitted

trajectory as a direct estimate of the angular measurement uncertainty. With these estimates in hand, Monte Carlo runs are then generated by adding Gaussian noise to the observations using the standard deviation of the angular residuals from the initial trajectory estimate and redoing the trajectory solution using noise-added data.

This procedure gives a set of trajectories which are geometrically possible to fit within the measurement uncertainty. We have empirically found that about 250 Monte Carlo runs samples the possible trajectory parameter space well. The lines of sight from individual stations are then projected to the trajectory line and the dynamics of the meteor as seen from every station are computed. Critically in this new technique, the best solution is chosen by comparing the observed dynamics between different stations and choosing the trajectory which has the most consistent dynamics as seen from all stations. This approach constrains the trajectory solution both geometrically and dynamically without limiting the motion to an empirical propagation/ablation model, while simultaneously keeping LoS vectors within measurement uncertainty. Note that unlike in the MPF method, the geometry and dynamics are solved separately; the dynamics is only used as an additional constraint on the geometry.

Here we provide detailed formulations of all the equations used by this trajectory solver, with the exception of well known mathematical and numerical methods. The equations are given in a way that would make their computer implementation unambiguous and thus may slightly deviate from standard mathematical notation. Where the function for the four-quadrant inverse tangent is used, we assume that the order of arguments is $atan2(y, x)$, as in e.g. C, FORTRAN, Python, and MATLAB. This differs from e.g. Mathematica and MS Excel whose implementations have the two arguments reversed. mod is the modulo operator, the integer division remainder operation. The Python implementation of both the simulator and the solver is open source and publicly available at `https://github.com/wmpg/WesternMeteorPyLib`.

3.3.1 Inputs and conversions to rectangular coordinates

For every station $k \in \{1, ...N_{stations}\}$, we have measurements $j \in \{1, ..., N_{meas(k)}\}$, producing inputs to the trajectory solver:

a) Relative time t_{kj} in seconds of each measurement from every station, relative to the reference Julian date JD_{ref}.

b) Angular measurements of meteor positions in the horizontal coordinate system: azimuth measured eastward from the north A_{kj}, and altitude above the horizon a_{kj} for the epoch of date from each station. Equivalently, right ascension α and declination δ may be used which can be converted to azimuth and altitude using equations given in Appendix A.7. If the equatorial coordinates are given in the J2000 epoch, care must be taken to first precess them to the epoch of date (see Appendix A.8). The epoch of date is assumed to be at JD_{ref}.

c) Geographical coordinates of every station: geodetic latitude φ_k, longitude λ_k, and height above a WGS84 Earth ellipsoid h_k (note that this height is not the same as the Mean Sea Level height reported by Google Earth and newer GPS devices - the difference can be up to 100 meters).

The first step in the process is to compute the Julian date of every individual measurement

$$JD_{kj} = JD_{ref} + t_{kj}/86400 . \tag{3.4}$$

These times get updated in the second stage of the iteration when the trajectory is recomputed after the timing offset estimation. Next, measurements are converted to equatorial coordinates for the epoch of date using equations given in Appendix A.6. Two sets of equatorial coordinates are obtained: the first assumes the stations are fixed at JD_{ref} and are used for the intersecting planes method while the second one takes into account the movement of the stations at each measurement time step. Thus, When computing values for the intersecting plane

method, the JD_{ref} reference time should be used for all measurement points. When computing values for the lines of sight method, the Julian date JD_{kj} of the individual measurements should be used. The measurements are then converted to Cartesian unit vectors using equation 3.5. These vectors define the direction of the line of sight from a given station at each measurement point in time.

$$\xi = \cos \delta \cos \alpha,$$
$$\eta = \cos \delta \sin \alpha, \tag{3.5}$$
$$\zeta = \sin \delta.$$

The geographical positions of the stations are converted to Earth-Centered Inertial (ECI) coordinates relative to the center of the Earth using equations given in Appendix A.4.1. Two sets of coordinates are calculated: X_{kj}, Y_{kj}, Z_{kj} for the position of each station at every point in time JD_{kj}, and X'_k, Y'_k, Z'_k for stations fixed at JD_{ref}. ECI coordinates fixed at JD_{ref} are needed for the intersecting planes method, as this method implicitly assumes that the station is a point and its coordinates cannot move in time.

3.3.2 Plane fits

The best fit plane for observations from one station can be defined as

$$a\vec{x} + b\vec{y} + d = -\vec{z}, \tag{3.6}$$

where $\vec{x}, \vec{y}, \vec{z}$ are data vectors containing Cartesian unit vectors of direction ξ, η, ζ, and a zero, which represents the position of the station, taken to be the origin of the direction vector's coordinate system:

$$\vec{x} = [0, \xi_{k1}, ..., \xi_{kN_{meas(k)}}],$$

$$\vec{y} = [0, \eta_{k1}, ..., \eta_{kN_{meas(k)}}], \tag{3.7}$$

$$\vec{z} = [0, \zeta_{k1}, ..., \zeta_{kN_{meas(k)}}].$$

The problem can be written in data matrix form as

$$\begin{bmatrix} x_1 & y_1 & 1 \\ x_2 & y_2 & 1 \\ & ... & \\ x_n & y_n & 1 \end{bmatrix} \begin{bmatrix} a \\ b \\ d \end{bmatrix} = - \begin{bmatrix} z_1 \\ z_2 \\ ... \\ z_n \end{bmatrix}. \tag{3.8}$$

If we take the data matrix and pre-multiply both sides of the equation by its transpose, and invert to solve for the unknowns, we perform the equivalent of a linear least squares fit. One should normalize the points to be relative to their mean, $\bar{x}, \bar{y}, \bar{z}$, in which case d can be excluded and one dimension can be dropped. Thus, the matrix equation solution can be written as

$$\begin{bmatrix} a \\ b \end{bmatrix} = - \begin{bmatrix} \sum_{i=1}^{n}(x_i - \bar{x})^2 & \sum_{i=1}^{n}(x_i - \bar{x})(y_i - \bar{y}) \\ \sum_{i=1}^{n}(x_i - \bar{x})(y_i - \bar{y}) & \sum_{i=1}^{n}(y_i - \bar{y})^2 \end{bmatrix}^{-1}$$

$$\times \begin{bmatrix} \sum_{i=1}^{n}(x_i - \bar{x})(z_i - \bar{z}) \\ \sum_{i=1}^{n}(y_i - \bar{y})(z_i - \bar{z}) \end{bmatrix}. \tag{3.9}$$

After solving the matrix, the direction normal to the fit plane is

$$\vec{n} = [a, b, 1]^T. \tag{3.10}$$

3.3.3 Plane intersections

We now consider planes in point-normal form. After finding the unit plane normal $\hat{n}_k$ for observations from every station, we make use of the additional constraint that each normal vector must go through the position of the station in ECI coordinates (X'_k, Y'_k, Z'_k). For N stations,

there is a total of $\binom{N}{2}$ combinations of different plane intersections. Although Ceplecha (1987) shows how to compute the weighted average trajectory for all combinations of planes, we follow the approach of Gural (2012), where only the solution with the pair of planes that have the highest convergence angle is taken. This solution is usually satisfactory to estimate the initial estimate of the trajectory for the lines of sight method which is then refined numerically.

For every pair of planes we have their normals, $\hat{n}_A$ and $\hat{n}_B$, and position vectors for every station, $\vec{p_A} = [X'_A, Y'_A, Z'_A]$ and $\vec{p_B} = [X'_B, Y'_B, Z'_B]$. The convergence angle Q_{AB} between the two planes is

$$\cos Q_{AB} = \hat{n}_A \cdot \hat{n}_B . \tag{3.11}$$

The apparent radiant unit vector based on these two stations is

$$\vec{R} = \hat{n}_A \times \hat{n}_B ,$$
$$\hat{R} = \frac{\vec{R}}{|\vec{R}|} . \tag{3.12}$$

We also make sure that the radiant vector is pointing in the correct direction:

$$\hat{R} = \begin{cases} -\hat{R}, & \text{if } [\xi_{A1}, \eta_{A1}, \zeta_{A1}] \cdot \hat{R} < [\xi_{An}, \eta_{An}, \zeta_{An}] \cdot \hat{R} \\ \hat{R}, & \text{otherwise} \end{cases} , \tag{3.13}$$

where $[\xi_{A1}, \eta_{A1}, \zeta_{A1}]$ is the vector pointing to the first observed point on the meteor trajectory from station A, and $[\xi_{An}, \eta_{An}, \zeta_{An}]$ is the vector pointing to the last observed point from station A. This condition follows from the fact that the radiant is always closer to the first observed point.

The equatorial coordinates of the radiant are given by

$$\delta = \arcsin \hat{R}_z ,$$
$$\alpha = \text{atan2}(\hat{R}_y, \hat{R}_x) \bmod 2\pi , \tag{3.14}$$

where the $\mathrm{mod}\, 2\pi$ operation wraps the right ascension to the $[0, 2\pi]$ range.

The intersection of the planes from each station forming the radiant line in three-dimensional space is now known and unit vectors from each station to the closest point on the radiant line to the respective station can be calculated as

$$
\begin{aligned}
\vec{w} &= \hat{R} \times \hat{n}, \\
\hat{w} &= \frac{\vec{w}}{|\vec{w}|}, \\
\hat{w} &= \begin{cases} -\hat{w}, & \text{if } \hat{w} \cdot [\xi_1, \eta_1, \zeta_1] < 0 \\ \hat{w}, & \text{otherwise} \end{cases}.
\end{aligned}
\tag{3.15}
$$

The last equation ensures the vector is pointing from the station towards the radiant line. These vectors, $\hat{w}_A$ and $\hat{w}_B$, are calculated for both stations.

The range vectors from each station to the radiant line can be found as

$$
\begin{aligned}
\Delta\vec{p} &= \vec{p_A} - \vec{p_b}, \\
\cos\omega &= \hat{w}_A \cdot \hat{w}_B, \\
\vec{r_A} &= \frac{\cos\omega(\Delta\vec{p} \cdot \hat{w}_B) - \Delta\vec{p} \cdot \hat{w}_A}{1 - \cos^2\omega} \hat{w}_A, \\
\vec{r_B} &= \frac{\Delta\vec{p} \cdot \hat{w}_B - \cos\omega(\Delta\vec{p} \cdot \hat{w}_A)}{1 - \cos^2\omega} \hat{w}_B,
\end{aligned}
\tag{3.16}
$$

where $\vec{r_A}$ and $\vec{r_B}$ are vectors pointing from the stations to the respective point on the radiant line closest in range to the station.

The ECI coordinates of the position portion of the state vector are calculated by adding the ECI position of one of the stations to the appropriate range vector. We choose the station A

$$
\vec{S} = \vec{p_A} + \vec{r_A}.
\tag{3.17}
$$

The trajectory solution from these two stations alone is thus represented by the apparent radiant unit vector $\hat{R}$ and the reference position vector $\vec{S}$.

For the case with more than two stations we also compute weights W_k for every station k as

$$P_a = \arccos\left(\hat{R} \cdot \hat{w}_k\right),$$

$$W_k = \sin^2 P_a.$$

(3.18)

where w_k is computed from equation 3.15, and P_a is the perspective angle of the trajectory, namely the angle made between the observer, the state vector, and the radiant line. In this approach the station which observes the meteor closest to perpendicular to the trajectory is given the highest weight, while stations observing the meteor "head on" have the lowest weights. If the perspective angle is low, small errors in meteor position measurement will propagate into large errors on the trajectory when they get projected, thus the weight of those observations needs to be reduced. The weights are kept at unity if only 2 stations are used in the solution. The $\sin^2$ weighting scheme follows Ceplecha (1987), with the difference of using the perspective angle instead of the convergence angle. The weighting is only used for the lines of sight method described below.

3.3.4   Line of sight method

After pairing all planes and finding the solution with the best convergence angle, the resulting vectors $\hat{R}$ and $\vec{S}$ are taken as the starting solution for the line of sight method. This method seeks to find a radiant line (a line in 3D space) that minimizes the angular differences between all observation sight lines and the radiant line.

Let $\overrightarrow{d_{obs_{kj}}} = [\xi_{kj}, \eta_{kj}, \zeta_{kj}]$ be the direction vector of every measurement from station k, and $\overrightarrow{d_{mod_{kj}}}$ be the direction of the modelled radiant line as seen from that station. The trajectory solution is then $\hat{R}$ and $\vec{S}$ for which

$$min \frac{\sum_{k=1}^{N_{stations}} \sum_{j=1}^{N_{meas(k)}} W_k \angle(\hat{d}_{obs_{kj}}, \hat{d}_{mod_{kj}})}{\sum_{k=1}^{N_{stations}} W_k}.$$

(3.19)

This sum is minimized numerically using the Nelder-Mead method. $\hat{d}_{mod_{kj}}$ can be calculated

using

$$\overrightarrow{d_{mod_{kj}}} = \overrightarrow{T'_{kj}} - \overrightarrow{p_{kj}},$$

$$\hat{d}_{mod_{kj}} = \frac{\overrightarrow{d_{mod_{kj}}}}{|\overrightarrow{d_{mod_{kj}}}|}, \tag{3.20}$$

where $\overrightarrow{T'_{kj}}$ is the gravity-corrected point on the radiant line which is the closest to the measured line of sight, and $\overrightarrow{p_{kj}}$ are the ECI coordinates of station k at time j. $\overrightarrow{T'_{kj}}$ can be computed as

$$\overrightarrow{T'_{kj}} = \overrightarrow{T_{kj}} - \Delta h(t_{kj})\frac{\overrightarrow{T_{kj}}}{|\overrightarrow{T_{kj}}|}, \tag{3.21}$$

where $\overrightarrow{T_{kj}}$ is a point on the radiant line which is the closest to the measured line of sight that can be computed using equations given in Appendix A.2. Δh is the height drop due to gravity computed using the equations in Appendix A.1; adding this term effectively simulates the curvature of the trajectory due to gravity. t_{kj} here is the time the meteor is at point j as seen from station k relative to JD_{ref}.

The angle between the closest point on the 3D radiant line and the observed line of sight is calculated as (note that unit vectors must be used)

$$\angle(\hat{d}_{obs_{kj}}, \hat{d}_{mod_{kj}}) = \arccos\left(\hat{d}_{obs_{kj}} \cdot \hat{d}_{mod_{kj}}\right). \tag{3.22}$$

3.3.5 Computing meteor length, velocity and lag

Once a trajectory solution is found, the location of the estimated reference state vector position $\overrightarrow{S}$ along the radiant line is moved to the beginning of the meteor. This is done by setting $\overrightarrow{S}$ to the ECI coordinates on the radiant line with the largest observed height, implicitly assuming that a meteor is always descending downward (not necessarily true for Earth-grazers).

The length along the track is found by projecting the observations on the radiant line using the equations given in Appendix A.2, producing $\overrightarrow{d_{mod_{kj}}}$. The meteor length is defined as the distance from the reference state vector position $\overrightarrow{S}$ to every projected measurement ray along

the radiant line,

$$l_{kj} = |\overrightarrow{d_{mod_{kj}}} - \vec{S}|. \tag{3.23}$$

The time variation of velocity defines deceleration, but since it is the second derivative of the length versus time, deceleration itself tends to have large point-to-point variances. As a proxy for overall deceleration, we use lag. Following Subasinghe et al. (2017), we define lag as "the distance that the meteoroid falls behind an object with a constant velocity that is equal to the initial meteoroid velocity". In that work, the authors use the first half of the meteor's trajectory to estimate the initial velocity. The limitation of this approach is that the time offsets between observations from different stations can cause errors if all observations from all sites are simultaneously used for velocity estimation. Thus, the time offsets have to be estimated first.

3.3.6   Estimating timing offsets and the initial velocity

To estimate timing offsets we use the fact that the computed length is insensitive to offsets in time. The timing offset estimation is performed by using the station that first recorded the meteor as the station with reference time for all other stations, i.e. it has absolute time ($\Delta t = 0$). The time offsets for all stations are then numerically estimated by minimizing the sum of time differences for all combinations of station pairs. The minimization cost function $f_{\Delta t}$ is defined as

$$f_{\Delta t} = \frac{t_{sum}}{W_{sum} c_{sum}} \, ,$$

$$t_{sum} = \sum_{k=1}^{N_{stations}} \sum_{r=1}^{N_{stations}} \sum_{j=1}^{N_{meas(r)}} W_k W_r \left(t_k(l_{rj}) - t_{rj} \right)^2 \, ,$$

$$W_{sum} = \sum_{k=1}^{N_{stations}} \sum_{r=1}^{N_{stations}} W_k W_r \, ,$$

$$c_{sum} = \sum_{k=1}^{N_{stations}} \sum_{r=1}^{N_{stations}} N_{overlap} \, ,$$

(3.24)

where k is the station index, r the index of all other stations (iterations where $k = r$ are skipped), t_{rj} is the time from station r, and $t_k(l_{rj})$ is the time from station k at length from station r. $t_k(l_{rj})$ is obtained by linear interpolation of time vs. length. W_k and W_r are weights for the respective stations as defined in Eq. 3.18, and $N_{overlap}$ is the number of points that overlap in length between stations k and r. Thus, only overlapping segments of the meteor path for stations k and r are used. This requirement is the main limitation of the method: for the approach to work an overlap of at least 4 points between stations is needed. If there is no overlap (e.g. one station observed only the beginning, and the other only the end of a meteor) the approach will not work and one has to assume a velocity model. For those cases we found the MPF method of Gural (2012) worked well.

This approach of estimating time offsets is not sensitive to the functional form of the deceleration, it relies on that fact that a truly accurate trajectory solution must show the same dynamics from all stations. If the observed dynamics differ, that indicates the trajectory was not well estimated. This is the central foundation of our novel approach.

After an initial estimate is made of the timing offsets, the entire trajectory solution is repeated with updated timing offsets. JD_{ref} is shifted to correspond to the new value of t = 0. Because the state vector $\vec{S}$ is kept at the beginning of the meteor, this means that the position of the meteor at time JD_{ref} corresponds to $\vec{S}$.

The initial velocity is then estimated by progressively fitting a line to the solution time vs. length. This is done starting from the first 25% of points from all stations (at least 4 points for

short events) up to 80% of all points. The best estimate of the initial velocity is the fit with the smallest standard deviation.

This modification mitigates the influence of deceleration on the initial velocity estimate, although at best it is the average velocity of the first 25% of the trajectory. In practice we found that this approach works well. This approach was adopted because the standard deviation of the fit done on the first quarter of the trajectory is usually high due to the measurement uncertainty as meteors tend to be faint at the beginning of the trail and thus the initial velocity may be uncertain as well. As more points get included, the standard deviation tends to go down, but it will rise again if significant deceleration is present. The approach is thus a balance between choosing a fit that trades the effects of measurement uncertainty and deceleration.

To demonstrate the accuracy of the method we have simulated a Draconid as it would be observed by a hypothetical network in Southern Ontario consisting of three stations with fields of view of $64° \times 48°$ which form an equilateral triangle with sides of 100 km and observe the same volume of the sky (maximum overlap at height of 100 km, see the second paper for more simulation details). The accuracy of measurements was $\sigma = 0.5$ arc minutes.

Figure 3.2 shows the map of these model stations and the trail of the meteor. The left inset of figure 3.3 shows time vs. length prior to the timing correction. One can see that all observations show the same trend (i.e. dynamics), but they are only offset in time. The right inset shows the lengths after estimating timing offsets and the final fitted initial velocity. Note that the observations start deviating slightly from the fitted velocity line at the end, indicating significant deceleration.

The effect is more visible in figure 3.4 which shows the computed lag. Ideally, the lag would remain zero (a vertical line) until the meteor starts decelerating, and that straight portion would be used for initial velocity estimation. This may not always be the case if the deceleration started prior to detection, as shown in the aforementioned figure. In that case, the initial velocity will be underestimated and ablation modelling is needed to reconstruct the true initial velocity (Vida et al., 2018b). Also, notice the larger scatter in lag and fit residuals (figure 3.5) from
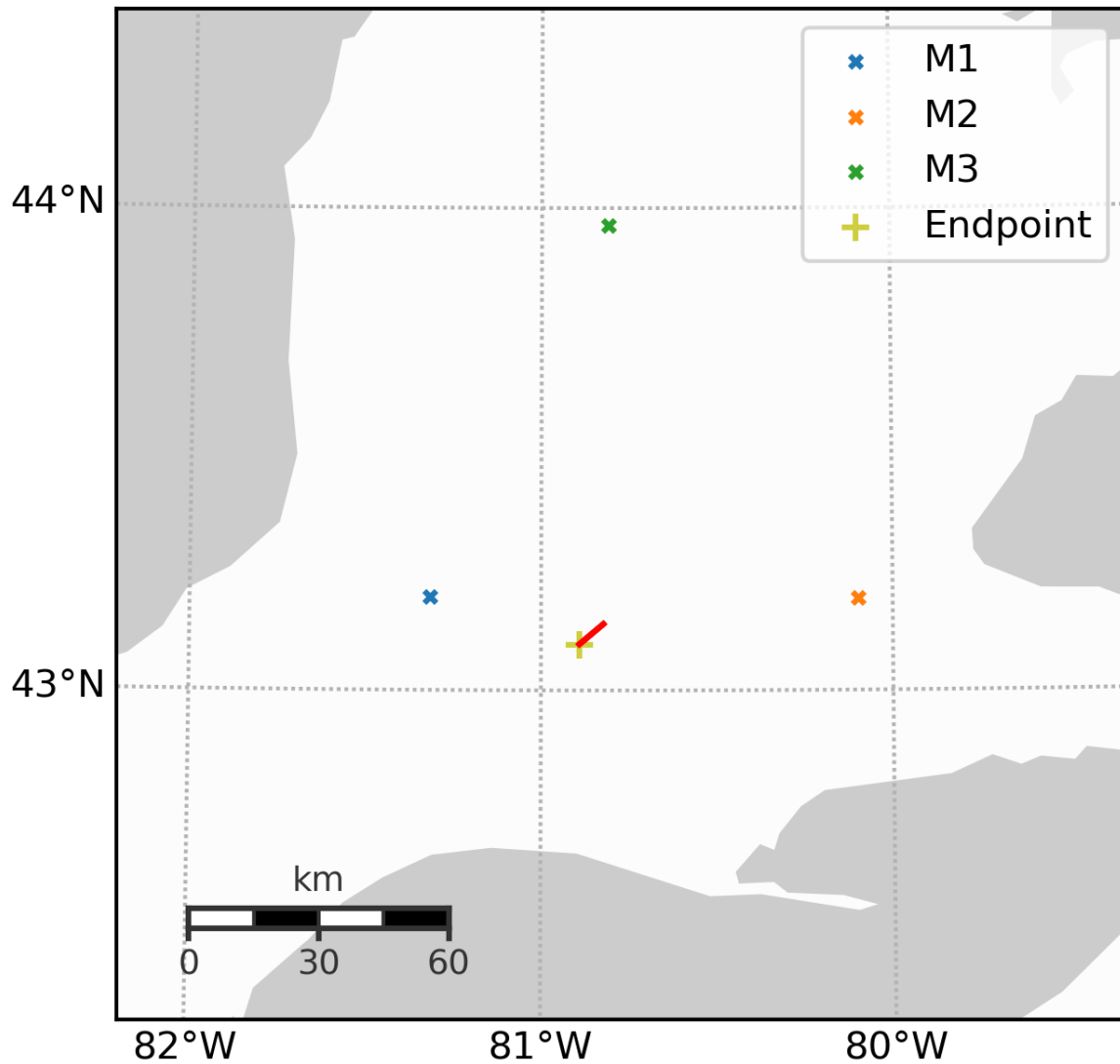
Figure 3.2: Map of the hypothetical moderate FOV network and the simulated Draconid of mass 6.45×10^{-5} kg, density 211 kg m^{-3} and initial velocity of 23.7 km s^{-1}. The meteor had an entry angle of $65°$. Perspective angles for stations M1, M2 and M3 were $19°$, $53°$ and $61°$ respectively. The red line represents the ground track of the meteor.
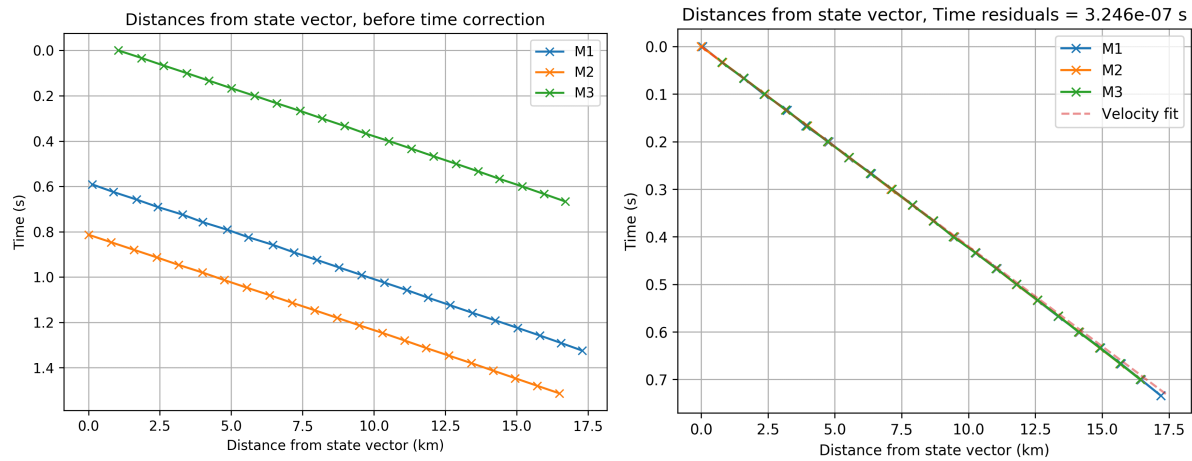
Figure 3.3: Left: Time vs. length before correction. Right: After time offset estimation, all curves are one on top of the other. The cited residual is the average residuals between all lines in seconds.

station M1 due to the low perspective angle of only 19°. The perspective angles of the other two stations M2 and M3 are 53° and 61° respectively.

Finally, after the reference state vector, the apparent radiant, and the initial velocity are known, the orbit is computed using equations given in Appendix A.3.

3.3.7   Refining the trajectory solution - a Monte Carlo approach

With a nominal trajectory solution now available, the next goal is to define uncertainties in the solution and further optimize the solution using time vs. length consistency as the cost function metric.

After estimating the initial "best" solution as described above, the angular residuals of observations from all stations relative to this solution are computed using equation 3.22, as well as the value of the root-mean-square deviation (RMSD). We assume that the computed RMSD represents the standard deviation of the real (random) measurement uncertainty of individual stations.

Figure 3.5 shows the computed angular residuals for the example meteor in figure 3.4. Note that station M1 has the highest RMSD, again due to its low perspective angle. In this
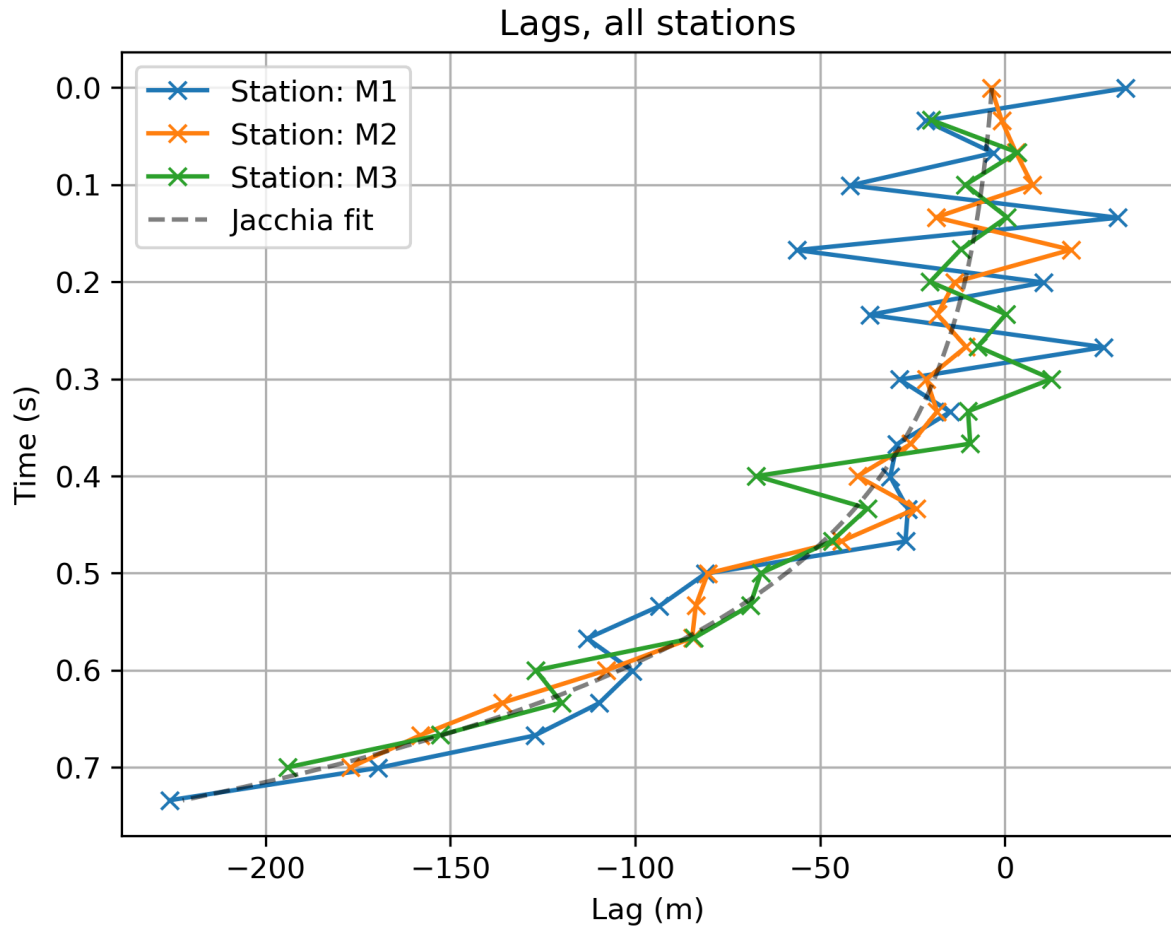
Figure 3.4: A lag of a simulated Draconid observed by a moderate FOV system from 3 stations. "Jacchia fit" is a fit of equation 3.3 to the computed lag.
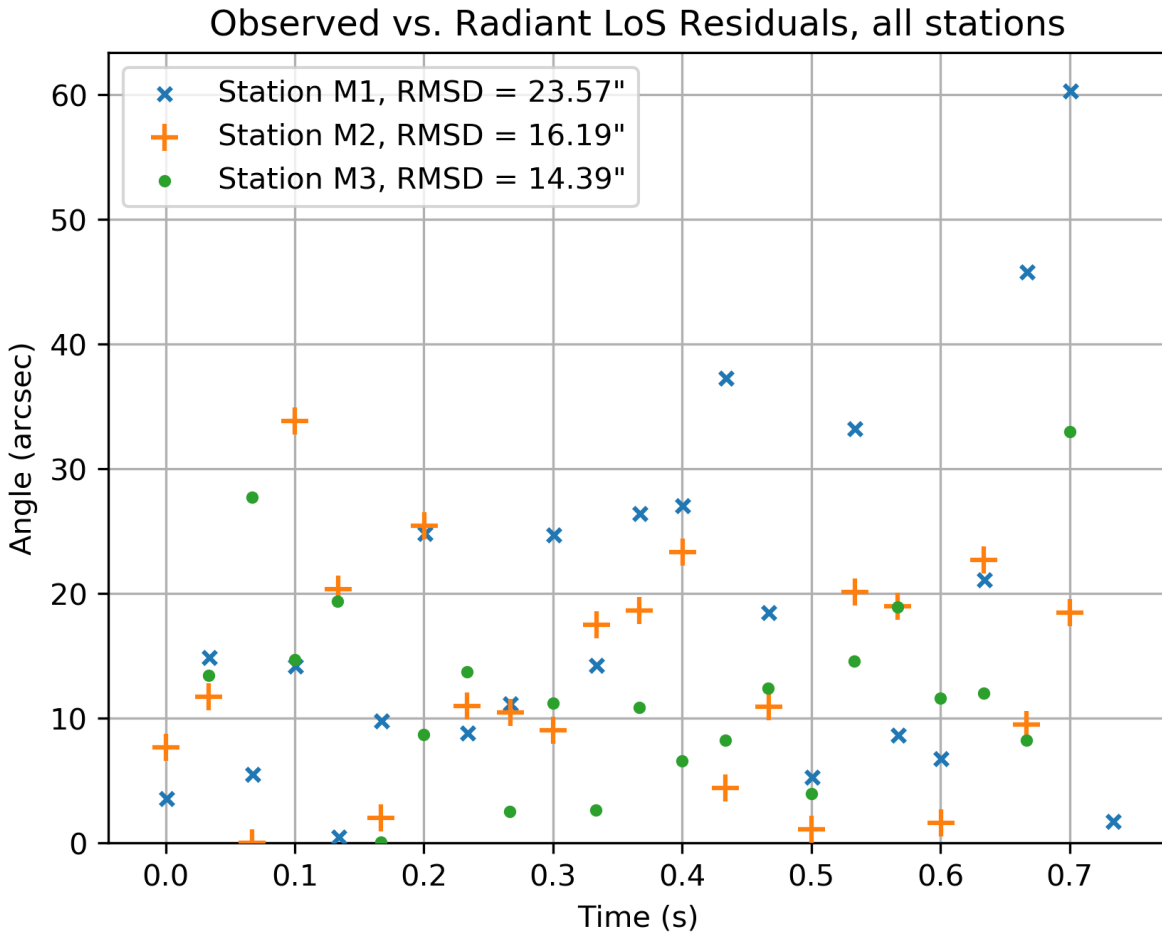
Figure 3.5: Angular residuals of a simulated Draconid. RMSD is the root-mean-square deviation in arc seconds.

case, a low station weight will prevent these measurements from significantly influencing the trajectory solution.

Next, Gaussian noise is added to the original measurements from every station (using equation 3.36), with an a standard deviation estimated from the measured station residuals. The entire trajectory is then recomputed from the beginning and a new positional state vector and radiant are computed using the noise-added data. All dynamical parameters (velocity, lag) and residuals are computed using the original data. Time offsets are independently recomputed in every run. This procedure is repeated hundreds of times with randomized noise.

The best solution is chosen as the one with the smallest value of the $f_{\Delta t}$ function (equation

3.24). This solution is the one where the most consistent dynamics of a meteor have been observed across all stations and which is simultaneously consistent within measurement uncertainty from all stations. This produces the best dynamical solution within the geometrical uncertainty.

In many cases when the geometry is good and the measurements are reasonably precise, the Monte Carlo refinement will not provide additional improvement beyond the initial solution. The comparison of the performance of the Monte Carlo solver to other trajectory solvers on simulated data is given in the second paper in this series.

The measurement uncertainty of every estimated parameter (including the orbital parameters) is computed using the subset of Monte Carlo trajectories which have values of the $f_{\Delta t}$ function smaller than that of the initial purely geometrical solution. If all solutions were to be used for uncertainty estimation, then the uncertainties would be completely driven by geometric uncertainties. This culling removes all solutions which have worse fits to the dynamics between stations than the geometrical solution, thus the dynamical constraints are included. Note that this approach does not estimate possible systematic errors arising from the astrometric calibration and position picks, which are system-dependent and should be handled separately.

Figure 3.6 shows the geocentric radiants of all Monte Carlo solutions (the value of the square root of the $f_{\Delta t}$ function is color-coded), and figure 3.7 shows how the geocentric velocity varies with the radiant position for the example model Draconid meteor. Figure 3.8 shows the spread in orbital elements, in particular the strong dependence of individual orbital elements on one another. This behaviour is not captured simply by describing independently computing standard deviations of every orbital element.

To more realistically convey trajectory and orbital uncertainties, we compute covariance matrices of both the orbit and the initial state vector. Note that the uncertainty in the geocentric radiant is not properly represented by considering standard deviations in the right ascension and declination separately. Most two station meteor events, particularly those with a low convergence angle, show an elongated radiant uncertainty. Using a different model Draconid, just

such an example is shown in figure 3.9.

Note that figure 3.6 shows a clear correlation of the timing residuals (the $f_{\Delta t}$ function) relative to radiant position and a clear global minimum. In experimentation with model fits, we have found this behaviour to be a strong indicator of an improvement in the trajectory solution relative to the geometrical best solution, showing that the best Monte Carlo trajectory should be taken as the solution with lowest lag residuals.

We note that for some model geometries, there are cases when no consistent gradient in the residuals with radiant location is present. In these cases the values of the $f_{\Delta t}$ function are randomly scattered among radiant solutions. In such cases, we found that keeping the original purely geometric solution produced fits closer to the simulated trajectory.

3.4   Meteor shower and trajectory simulator

By developing a comprehensive meteor trajectory simulator we wish to generate synthetic measurements for specific video systems in realistic conditions. This involves generating model observations by stipulating real locations of meteor stations, instrument fields of view (FOV), cadence, sensitivity, and measurement uncertainties. In this work we require the simulator to produce simulated trajectories of shower meteors, but sporadic meteors can also be simulated given a sporadic source model. Meteor showers are simulated by specifying the radiant, radiant drift and radiant spread (assumed to be Gaussian), in addition to an activity profile.

The dynamics of the meteor's motion within the model are generated using the meteor ablation model of Campbell-Brown & Koschny (2004) for which the range of meteoroid masses, the mass index, the meteoroid bulk density distribution and the ablation coefficient are defined as inputs. The attraction of the meteoroid body to the Earth's center due to gravity is taken into account as well. Higher order gravitational coefficients are disregarded because their influence is not measurable using these methods. In what follows, we describe the details of the simulator and demonstrate that it produces meteor trajectories comparable to real observations. The
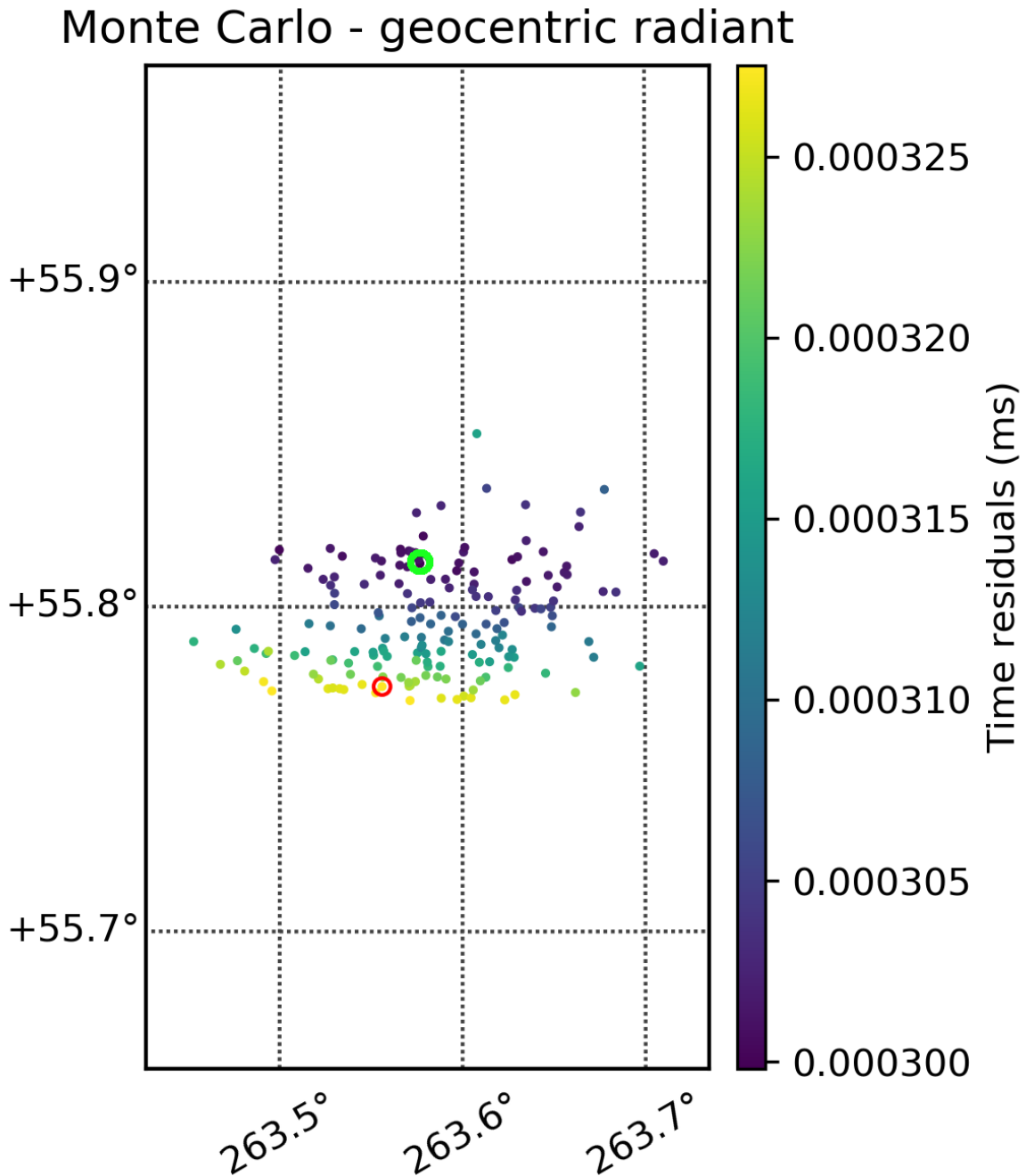
Figure 3.6: Spread in the geocentric radiant of the model Draconid. The square root of the timing residual $f_{\Delta t}$ is colour coded. The red circle marks the position of the initial solution $f_{\Delta t} = 0.000326$, and the green circle marks the position of the best solution $f_{\Delta t} = 0.000300$.
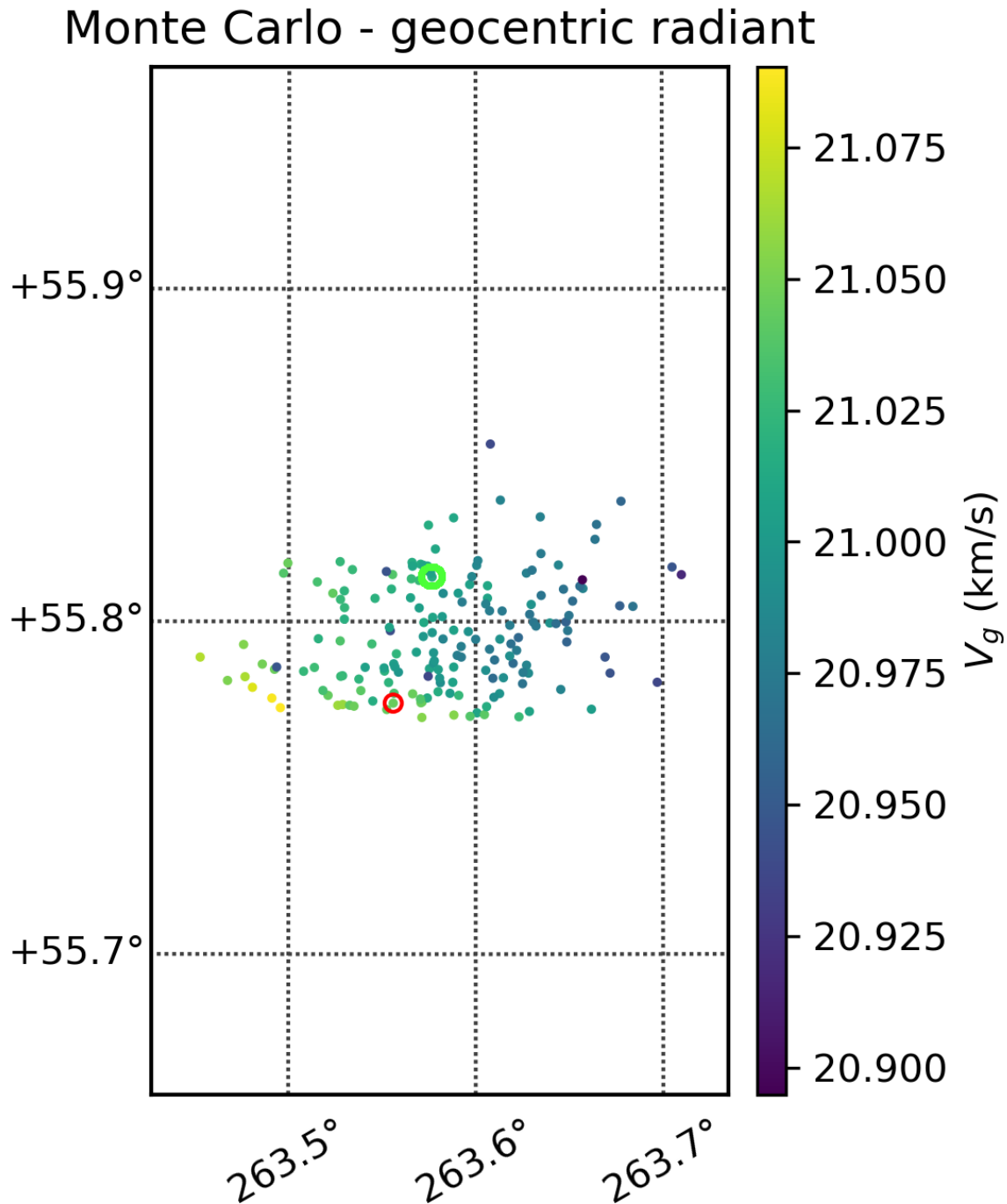
Figure 3.7: Spread in the geocentric radiant for the modelled Draconid; the geocentric velocity is colour coded. The red circle marks the position of the initial solution (V_g =21.05 km s^{-1}), and the green circle marks the position of the best solution (V_g =21.00 km s^{-1}).
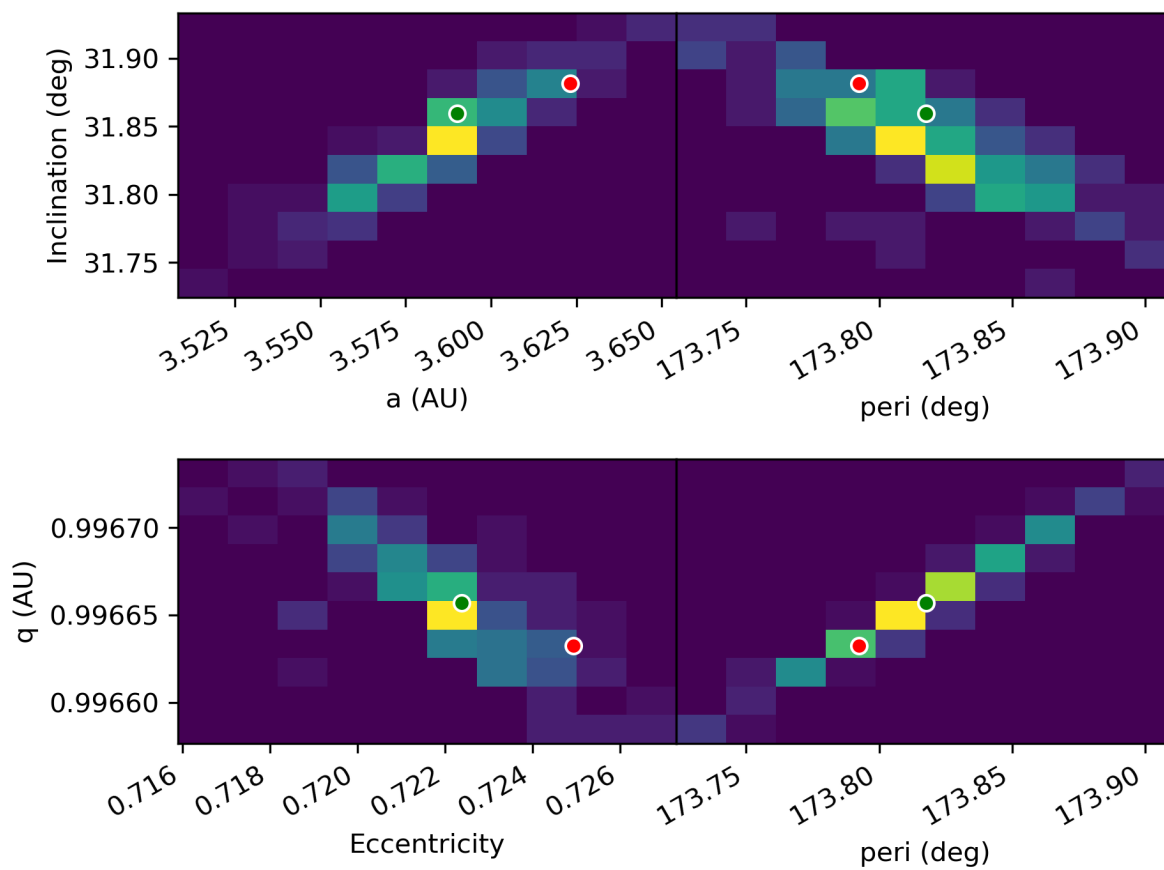
Figure 3.8: 2D histogram of the spread in orbital elements for the modelled Draconid. The red circle marks the position of the initial solution, and the green circle marks the position of the best solution. Brighter bins indicate more trials within the bin.
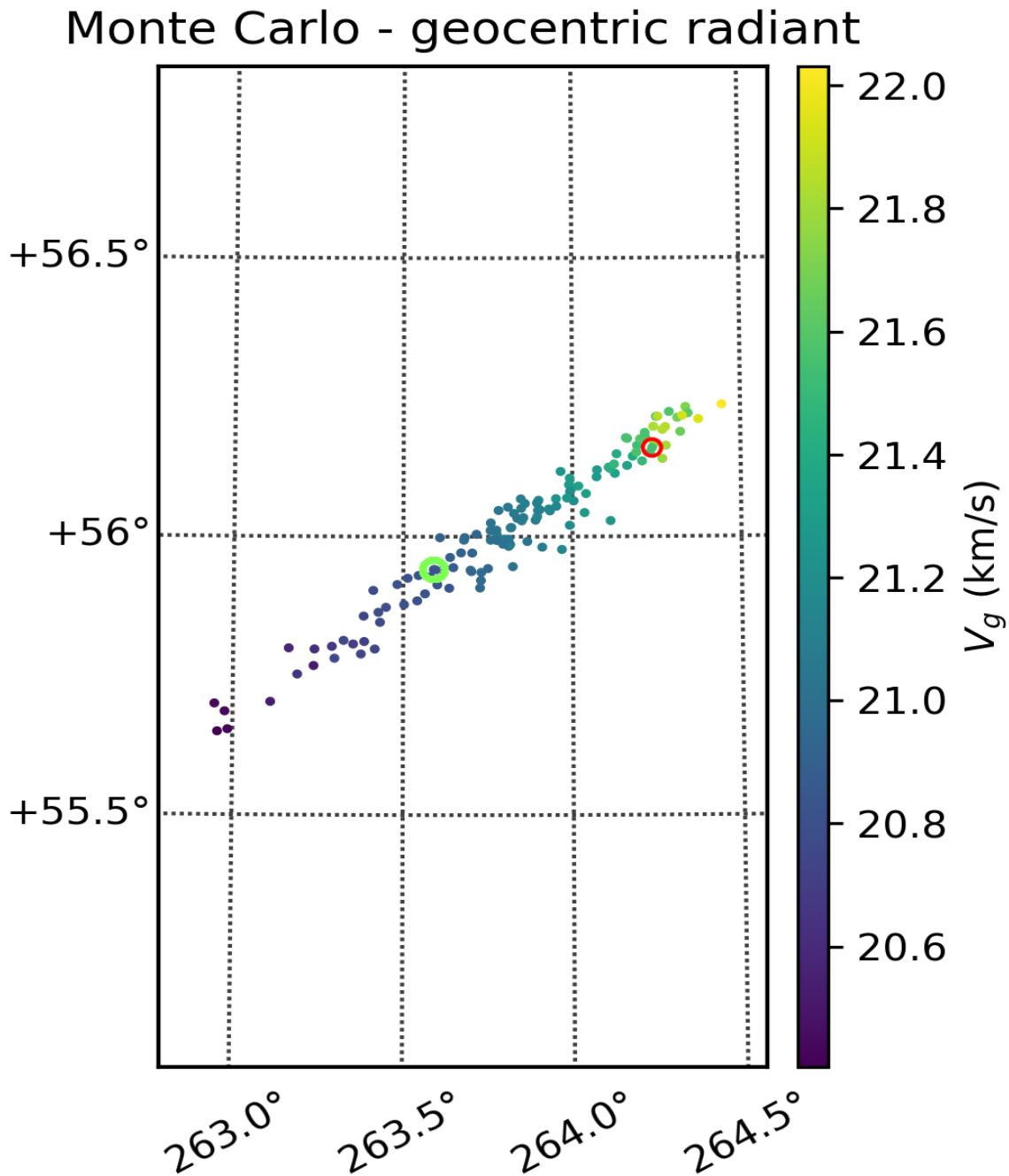
Figure 3.9: A separate simulation done to illustrate how elongated the radiant uncertainty can be. Here the geocentric velocity is colour coded. The red circle marks the position of the initial (geometrical) solution, and the green circle marks the position of the best (lowest lag cost function) solution. The original model input value of the geocentric velocity was $V_g = 20.893\,\mathrm{km\,s^{-1}}$. The initial lines of sight solution underestimated the velocity by $\Delta V_g = -0.661\,\mathrm{km\,s^{-1}}$, while the Monte Carlo method slightly overestimated by only $\Delta V_g = 0.017\,\mathrm{km\,s^{-1}}$.

trajectory simulator outputs sets of time, right ascension, declination, and apparent magnitude for every simulated meteor, emulating what would be seen by observers on the ground.

3.4.1 Simulating radiants and activity

For each model station, the following parameters are defined:

1. The geographical coordinates longitude λ, geodetic latitude φ and elevation above a WGS84 geoid of the Earth h

2. The sensor system parameters:

    (a) cadence (i.e. frames per second (FPS) of the video camera)

    (b) maximum possible deviation in time Δt_{max} from the absolute time

    (c) azimuth A and altitude a of the FOV center for each local site coordinates

    (d) width and height of the rectangular FOV

    (e) meteor limiting magnitude MLM

    (f) The radiant power of a zero-magnitude meteor P_{0m} (see Ayers, 1965)

For each station, the time offset from the absolute time and asynchronous timing shift between cameras is drawn from a uniform distribution $U(0, \Delta t_{max})$. The time offset and video frame rate are assumed constant over the duration of the meteor. The measurement precision of leading edge picks along the meteor track is simulated by adding Gaussian noise to each simulated measurement with a standard deviation equal to the scatter in residuals for real measurements.

To make the resulting trajectory solution averages per shower have realistic weighted geometries given the station locations, activity profiles for each shower are required. The activity profile of simulated meteor showers is defined by the solar longitude of the peak $\lambda_{\odot}^{max}$ and the slope of the activity profile B, where the activity is approximated as $ZHR = ZHR_{max} 10^{-B|\lambda_{\odot} - \lambda_{\odot}^{max}|}$

following Jenniskens (1994). The activity profile is assumed to be symmetric with respect to the peak. N samples are drawn from the activity profile using the inverse sampling transform method - every sample represents one simulated meteor. First, N samples are drawn from a uniform distribution $U(0, 1)$, producing a vector $(y_1, ..., y_N)$. Next, signs are drawn from a uniform distribution $U(-1, 1)$, producing a vector $(s_1, ..., s_N)$. The solar longitude of each sample is then computed as

$$\lambda_{\odot i} = \lambda_{\odot}^{max} + \text{sgn}(s_i) \frac{\log_{10} y_i}{B} \, , \tag{3.25}$$

and only those simulated shower meteors having solar longitudes which occurred between the local astronomical twilight and dawn of all observers are used.

Simulated meteor shower radiants are defined by their geocentric right ascension α_g and declination δ_g taken to be the mean radiant at the peak together with the standard deviation of the radiant dispersion σ_α, σ_δ. For times away from the peak, the radiant drift Δ_α and Δ_δ in degrees on the sky per degree of solar longitude is used. The shower geocentric velocity V_g, and speed dispersion σ_{V_g} plus drift Δ_{V_g} (if known) are also assigned.

N of individual meteor radiant realizations are drawn from a von Mises distribution (a close approximation to the circular normal distribution) using the centre of distribution at $\mu = 0$ and the dispersion parameter $\kappa = 1/\sigma^2$. α and δ are drawn independently. This procedure produces vectors $(\alpha'_1, ..., \alpha'_N)$ and $(\delta'_1, ..., \delta'_N)$. These vectors are offsets in right ascension and declination from the mean radiant position. To compute the proper distribution of radiants on the celestial sphere centered around (α_g, δ_g), the unit vector $\hat{R}_g = (1, 0, 0)$ is rotated by $-\delta'_i$ on the Y axis, and then by α'_i on the Z axis for every coordinate pair i. Next, the resulting vector is rotated by the negative declination of the mean radiant $-\delta_g$ on the Y axis, and then by α_g on the Z axis, and converted to right ascension and declination using

$$\alpha_{gi} = \text{atan2}\left(\hat{R}_{giy}, \hat{R}_{gix}\right) \, ,$$
$$\delta_{gi} = \arcsin \hat{R}_{giz} \, . \tag{3.26}$$

The radiant drift is applied as

$$
\alpha_{gi} = \alpha_{gi} + \Delta_\alpha (\lambda_{\odot i} - \lambda_\odot^{max}) ,
$$
$$
\delta_{gi} = \delta_{gi} + \Delta_\delta (\lambda_{\odot i} - \lambda_\odot^{max}) .
$$

(3.27)

Geocentric velocities V_{gi} are drawn from a Gaussian distribution $N(V_g, \sigma_{V_g})$, and a drift in V_g is applied as

$$
V_{gi} = V_{gi} + \Delta_{V_g} (\lambda_{\odot i} - \lambda_\odot^{max}) .
$$

(3.28)

3.4.2 Generating meteor state vectors and apparent radiants

The beginning of the luminous flight of the meteor is used as the point of reference (i.e. instantaneous measurement of the state vector). This point is randomly generated to be inside the fields of view of at least two stations in the simulation for a given start height. We use a start height of 120 km as a reference point between the trajectory and the ablation model. 120 km was chosen because almost no meteors end above this height, so the reference point on the trajectory is before or during the luminous phase.

The following paragraphs describe the procedure for generating initial meteor position vectors in 3D space.

Four rays representing the four corners of the FOV of one camera emanate from the coordinates of the station (equivalent to the center of the sensor focal plane). Earth-centered inertial (ECI) coordinates are used. A frustum (truncated pyramid) is obtained by taking 8 points in total, each laying on a FOV corner ray at heights -5 km and $+5$ km around the simulated beginning height for a particular meteor. A random point is generated inside the frustum of one station, and this random sampling is repeated until the point is inside a frustum of at least one another station. The overlap is checked using the quickhull algorithm (Barber et al., 1996). The resulting 3D position vector $\vec{S}$ is taken to be the beginning point of the simulated meteor in ECI coordinates. All initial positions are generated inside overlapping fields of view of at

least two cameras due to the computational simplicity of the approach.

From this initial point and the given geocentric radiant, the apparent radiant and the initial velocity is computed in the ECI frame. The initial velocity v_0 [m s^{-1}] is computed from the inverse of the geocentric velocity equation A.14 in Appendix A.3.2 as

$$v_0 = \sqrt{v_g^2 + \frac{2 * 6.67408 * 5.9722 * 10^{13}}{|\vec{S}|}}\,, \tag{3.29}$$

and the apparent values of the radiant (α_i, δ_i) are numerically inverted using forward mapping equations (see Appendix A.3.2). The apparent radiant unit vector $\hat{R}$ is computed by converting the spherical coordinates (α_i, δ_i) to their ECI components using equation 3.5. Note that the v_g is converted into the initial velocity by assuming that the stations are moving in the ECI coordinates, and thus the whole coordinate system rotates with the Earth, making a correction to the meteor velocity for Earth's rotation unnecessary; such a correction would be needed for an ECEF treatment. Radiants with zenith angles $z_c > 80°$ are skipped to avoid simulating meteors which do not propagate down in the atmosphere.

3.4.3   Simulating meteoroid dynamics

To simulate realistic meteor dynamics, the meteoroid ablation model of Campbell-Brown & Koschny (2004) is used. For each shower, a range of visible masses m_{min}, m_{max} and a mass index s based on literature values for a particular shower are defined. The masses are sampled using inverse transform sampling from the cumulative number as a function of mass distribution

$$f(m) = m^{1-s}\,. \tag{3.30}$$

Meteoroid densities are either sampled uniformly from a user defined range, or using density distributions given by Moorhead et al. (2017). The apparent ablation coefficient σ (usually given in [s^2 km^{-2}]) is applied in the ablation model through modification of the energy needed to ablate a unit mass L [J kg^{-1}], (make sure to convert σ to s^2 m^{-2}) which is computed as

$$L = \frac{\Lambda}{2\sigma\Gamma} , \qquad (3.31)$$

where $\Lambda = 0.5$ is the heat transfer coefficient, and $\Gamma = 1.0$ is the drag coefficient. Note that in the field of aerodynamics the notation C_d is used for the drag coefficient, where $\Gamma = 2C_d$. The ablation model provides vectors of height, length, and luminosity along the meteor path from the beginning point with a temporal resolution of 0.001 s. Note that σ is used throughout the text with different meanings. In equation 3.31 it is used for the ablation coefficient, while at all other places it is used for standard deviation.

3.4.4 Generating synthetic trajectory data

The duration t_{meteor} of a meteor is obtained from the ablation model. We assume the beginning time $t = 0$ corresponds to a given solar longitude for the corresponding reference Julian date JD_{ref}. A vector of times is obtained by sampling the range $(0, t_{meteor})$ with the step $1/FPS$.

The instantaneous model luminosity I at a given time is converted to a range-corrected apparent magnitude M_v and only those points above the meteor limiting magnitude of individual stations are taken

$$
\begin{aligned}
M_A &= -2.5 \log_{10} \frac{I}{P_{0m}} , \\
M_v &= M_A - 5 \log_{10} \frac{10^5}{r} ,
\end{aligned}
\qquad (3.32)
$$

where M_A is the absolute magnitude (magnitude at 100 km range) and r is the range in meters from the station to the meteor. P_{0m} is the power of a zero magnitude meteor for the appropriate bandpass taken from Weryk & Brown (2013). No correction for angular velocity or extinction loss is included.

The 3D meteor positions are projected to local spherical coordinates of stations to generate synthetic observations. We simulate the real movement of the stations due to Earth's rotation by computing ECI coordinates $\overrightarrow{ECI_j}$ of stations at every model point in time t_k. The position

of the meteor in ECI coordinates at time t_j is computed as

$$\vec{T_j} = \vec{S} - d(t_j)\hat{R},$$ (3.33)

where $\vec{S}$ is the initial position at $t = 0$, and $\hat{R}$ is the apparent radiant unit vector in ECI coordinates. The additional decrease in height due to Earth's gravity is applied using equation 3.21, where $\Delta h(t_j)$ is the decrease in height at every point in time due to gravity since the beginning (in meters). This procedure simulates the curvature of the trajectory due to gravity, assuming the pull is perpendicular to the WGS84 reference ellipsoid. $\Delta h(t_j)$ is computed as described in Appendix A.1. A unit vector pointing from the station to the position of the meteor on the trajectory is computed as

$$\hat{r} = \frac{\vec{T_j} - \overrightarrow{ECI_j}}{|\vec{T_j} - \overrightarrow{ECI_j}|}.$$ (3.34)

We simulate the observational precision of a system by adding Gaussian noise with a standard deviation σ, derived from real measurements of the actual systems, to the synthetic observations. We separate the vector $\hat{r}$ into orthogonal components $\hat{u}$ and $\hat{v}$

$$\begin{aligned}
\hat{z} &= [0, 0, 1], \\
\hat{u} &= \frac{\hat{r} \times \hat{z}}{|\hat{r} \times \hat{z}|}, \\
\hat{v} &= \frac{\hat{u} \times \hat{r}}{|\hat{u} \times \hat{r}|}.
\end{aligned}$$ (3.35)

The direction vector (all in ECI) with the added noise is then

$$\vec{r'} = \hat{r} + \mathcal{N}(0, \sigma)\,\hat{u} + \mathcal{N}(0, \sigma)\,\hat{v},$$ (3.36)

where $\mathcal{N}(0, \sigma)$ is a scalar drawn from a Gaussian distribution with a mean of 0 and a standard deviation of σ. The samples are drawn separately for each term. The direction vector is converted to equatorial coordinates in the epoch of date

$$\hat{r}' = \frac{\vec{r'}}{|\vec{r'}|},$$

$$\alpha_j = \text{atan2}\left(\hat{r}'_y, \hat{r}'_x\right),$$

$$\delta_j = \arcsin \hat{r}'_z. \tag{3.37}$$

Finally, the appropriate timing offset Δt for a given station (randomized on a per meteor basis) is added to time t_j, completing the set of synthetic measurements for each simulated meteor.

At the end of this procedure one obtains a set of N_{meas} synthetic measurements from every station for every generated meteor. Synthetic meteors are uniquely defined by the Julian date of their beginning JD_{ref}, set of relative times since the beginning $(t_0, ..., t_j)$, a set of right ascensions $(\alpha_0, ..., \alpha_j)$ and declinations $(\delta_0, ..., \delta_j)$ in the epoch of date. Note that the epoch here is not J2000; to avoid confusion we convert the model measurements to local azimuth $(A_0, ..., A_j)$ and altitude $(a_0, ..., a_j)$ in the epoch of date from a particular station using equations given in Appendix A.6.

Although the simulator reproduces many features of the observed data, a major difference with real meteors is that synthetic trajectories all start within the FOVs of at least 2 stations. It is not clear that this limitation is significant for the current work. While this might be alleviated by generating the state vectors slightly outside the FOV of one camera this would be at the expense of having to compute the propagation as well, which would significantly increase the computational load of finding a synthetic meteor that is actually visible from 2 or more stations.

3.5   Conclusion

In this work we developed a novel Monte Carlo meteor trajectory method which takes the dynamics of meteors into account without assuming any formulated meteor propagation model. This leverages the fact that modern meteor electro-optical systems have sufficient precision to routinely record deceleration, allowing an entirely independent check on the solution consistency between stations.

Next, we proposed improvements in weighting multi-station observations as well as a new method of initial velocity estimation. A limitation of the new Monte Carlo solver is that it does not work for meteors with no temporal overlap between stations. In those cases a dynamical model must be used to estimate timing differences and the velocity, but the radiant and its uncertainty can be estimated using purely geometrical methods, similar to earlier approaches (Weryk & Brown, 2012; Gural, 2012).

We develop a meteor trajectory simulator which uses a numerical meteor ablation model to simulate meteor dynamics. The simulator will be used in the second paper in this series to investigate radiant and velocity accuracy that can be achieved for various real-world optical systems and meteor showers.

Finally, we provide a detailed set of equations and explanations for estimating meteor trajectories and computing orbits starting just from a set of multi-station observations. We also have made the associated code-base openly available for all to use. Additional details are included in the accompanying appendices. An improved version of the MPF method incorporating the findings of this paper will be published in the future. We invite readers to continue to the second paper in this series for results.

3.5.1 Note on code availability

Implementation of the meteor simulator as well as implementation of all meteor solvers used in this work are published as open source on the following GitHub web page: `https://github.com/wmpg/WesternMeteorPyLib`. Readers are encouraged to contact the authors in the event they are not able to obtain the code on-line.

Bibliography

Ayers, W. G. 1965, NASA Technical Notes, TN D-2931

Barber, C. B., Dobkin, D. P., & Huhdanpaa, H. 1996, ACM Transactions on Mathematical
    Software (TOMS), 22, 469

Borovička, J. 1990, Bulletin of the Astronomical Institutes of Czechoslovakia, 41, 391

Borovička, J., Spurnỳ, P., & Koten, P. 2007, Astronomy & Astrophysics, 473, 661

Burke, J. G. 1986, Cosmic debris: Meteorites in history (Univ of California Press)

Campbell-Brown, M., & Koschny, D. 2004, Astronomy & Astrophysics, 418, 751

Ceplecha, Z. 1979, Bulletin of the Astronomical Institutes of Czechoslovakia, 30, 349

—. 1987, Bulletin of the Astronomical Institutes of Czechoslovakia, 38, 222

Ceplecha, Z., Borovička, J., Elford, W. G., et al. 1998, Space Science Reviews, 84, 327

Eberhart, R., & Kennedy, J. 1995, in Micro Machine and Human Science, 1995. MHS'95.,
    Proceedings of the Sixth International Symposium on, IEEE, 39–43

Egal, A., Gural, P., Vaubaillon, J., Colas, F., & Thuillot, W. 2017, Icarus

Gural, P. S. 2012, Meteoritics & Planetary Science, 47, 1405

Hawkes, R., & Jones, J. 1975, Monthly notices of the Royal Astronomical Society, 173, 339

Hughes, D. W. 1982, Vistas in astronomy, 26, 325

Jenniskens, P. 1994, Astronomy and Astrophysics, 287, 990

Jenniskens, P., Gural, P., Dynneson, L., et al. 2011, Icarus, 216, 40

Moorhead, A. V., Blaauw, R. C., Moser, D. E., et al. 2017, Monthly Notices of the Royal
    Astronomical Society, 472, 3833

Romig, M. F. 1966, Meteoritics & Planetary Science, 3, 11

Sansom, E. K., Rutten, M. G., & Bland, P. A. 2017, The Astronomical Journal, 153, 87

Schiaparelli, G. V., & von Boguslawski, G. 1871, Entwurf einer astronomischen Theorie der Sternschnuppen (Th. von der Nahmer)

Stokan, E., Campbell-Brown, M. D., Brown, P., et al. 2013, Monthly Notices of the Royal Astronomical Society, 433, 962. `http://mnras.oxfordjournals.org/cgi/doi/10.1093/mnras/stt779`

Subasinghe, D., Campbell-Brown, M., & Stokan, E. 2017, Planetary and Space Science, . `http://www.sciencedirect.com/science/article/pii/S0032063316303403`

Subasinghe, D., Campbell-Brown, M. D., & Stokan, E. 2016, Monthly Notices of the Royal Astronomical Society, 457, 1289

Vida, D., Brown, P., Campbell-Brown, M., & Huggins, S. 2018a, in International Meteor Conference, Petnica, Serbia, 21-24 September 2017, 18–24

Vida, D., Brown, P. G., & Campbell-Brown, M. 2018b, Monthly Notices of the Royal Astronomical Society, 479, 4307

Weryk, R., Campbell-Brown, M., Wiegert, P., et al. 2013, Icarus, 225, 614 . `http://www.sciencedirect.com/science/article/pii/S0019103513001905`

Weryk, R. J., & Brown, P. G. 2012, Planetary and Space Science, 62, 132 . `http://www.sciencedirect.com/science/article/pii/S0032063311003965`

—. 2013, Planetary and Space Science, 81, 32 . `http://www.sciencedirect.com/science/article/pii/S0032063313000718`

Whipple, F. L., & Jacchia, L. G. 1957, Smithsonian Contributions to Astrophysics, 1, 183

Chapter 4

Novel meteor trajectory simulator and solver - II. Results

A version of this chapter has been published as:

> Vida, D., Gural, P.S., Brown, P.G., Campbell-Brown, M., & Wiegert, P. (2020).
> *Estimating trajectories of meteors: an observational Monte Carlo approach – II.*
> *Results.* Monthly Notices of the Royal Astronomical Society, 491, 3996.

4.1   Introduction

This paper is a direct continuation of an earlier work (Vida et al., 2020, hereafter Paper 1), in which we developed both a new method for estimating meteor trajectories and a meteor trajectory simulator. Paper 1 also presented a summary of the theory behind earlier meteor trajectory determination algorithms. In this paper we attempt to answer the following question: For a given type of optical meteor observation system, what is the best trajectory solver to use, and what is the associated expected quantitative accuracy? We note that this is only the first step in the process of estimating a meteoroid's original heliocentric orbit. The necessary additional step is accounting for deceleration due to atmospheric drag prior to the earliest

measured luminous point of the meteor, a topic addressed in Vida et al. (2018).

In Paper 1 we analyzed the shortcomings of existing methods of meteor trajectory estimation, with particular focus on application to the high-precision data collected by the Canadian Automated Meteor Observatory's (CAMO) mirror tracking system (Weryk et al., 2013). In Paper 1 we examined the most commonly used meteor trajectory estimation methods in detail, including: the geometrical intersecting planes (Ceplecha, 1987) and lines of sight (Borovička, 1990) approaches, and the multi-parameter fit (MPF) method by Gural (2012). As pointed out by Egal et al. (2017), the true measurement accuracy of these methods for various meteor observation systems and showers is unknown, and the most advanced of them, the MPF method with the exponential deceleration velocity model, is numerically problematic to fit to observations.

In an attempt to improve on existing algorithms, we developed a novel meteor trajectory estimation method which uses both the geometry and the dynamics of a meteor to constrain a trajectory solution, but without an assumed underlying kinematic model. We also developed a meteor trajectory simulator which uses the meteor ablation model of Campbell-Brown & Koschny (2004) to simulate realistic dynamics and light curves of meteors given their physical properties as a means to compare and test meteor trajectory solvers.

In this work, we apply the simulator and explore the accuracy of each trajectory solver to three types of typical optical meteor observation systems: a low-resolution all-sky system, a moderate field of view system, and the high-precision CAMO mirror tracking system. For each system we used the simulator to investigate the ability of each solver to properly recover the geocentric radiant and velocity of three major showers spanning a wide range of meteor velocities and meteoroid types (Draconids, Geminids, Perseids). The parameters used for simulations and the comparison between simulations and real-world observations are given in section 4.2. We also perform dynamical modelling of the 2011 Draconid outburst, which was produced by recently ejected meteoroids (Vaubaillon et al., 2011) and thus should have a very tight radiant. We use this compact shower to estimate the radiant measurement accuracy needed to resolve

the true physical dispersion of a meteor shower.

In section 4.3 we present simulation results and compare the performance of various meteor trajectory estimation methods across all simulated meteor observation systems and our three chosen showers. In section 4.3.5 we examine solver performances as applied to a specific case study, namely the unique 2015 Taurid outburst. This outburst was arguably the first instance where we have both strong a priori knowledge of the expected orbits (particularly semi-major axis) and a large number of high - precision meteor trajectories (Spurnỳ et al., 2017). We also consider the special case of long duration fireballs where the influence of gravity is particularly important by simulating solver performance for an all-sky system as will be discussed in section 4.3.6. Finally, in section 4.3.7 we examine the accuracy of meteor trajectory error estimation by comparing estimated radiant errors to offsets from the simulated ground truth.

4.2 Simulation-based performance analysis of trajectory solvers

4.2.1 Hardware models

To compare the performance of various existing meteor trajectory solvers with the new Monte Carlo method, we appeal to simulations. The method of generating simulated meteor observations is described in detail in Paper 1 (Vida et al., 2020). We simulated three optical meteor observation systems to generate synthetic meteors to feed into each trajectory simulator. These three systems follow the optical model system choices previously discussed in Vida et al. (2018). The characteristics of these systems (which largely vary in terms of angular precision) include:

1. A low resolution all-sky CCD video fireball system based on the hardware of the Southern Ontario Meteor Network (SOMN) (Brown et al., 2010).

2. A moderate field of view CCD video system typical of CAMS (Jenniskens et al., 2011),

SonotaCo[1], the Croatian Meteor Network (Gural & Šegon, 2009), and the Global Meteor Network (Vida et al., 2019).

3. An image intensified mirror tracking system based on the Canadian Automated Meteor Observatory (CAMO) (Weryk et al., 2013).

These systems cover a wide range of observed meteoroid masses, fields of view, and astrometric precision. Details of each system are given in table 4.1.

Our simulated all-sky fireball network consisted of 3 stations in an equilateral triangle configuration with $100 \, \mathrm{km}$ long sides (stations A1, A2, A3 in the simulation). The cameras at each station are pointing straight up and have a field of view (FOV) of $120° \times 120°$. Larger FOVs were difficult to simulate as the volume of the sky that needed to be randomly sampled becomes very high, and most of it was outside the FOV of other cameras. The measurement uncertainly was assumed to be 2 arc minutes and the frames per second (FPS) of the cameras 30.

For the CAMS-like moderate FOV system, we also chose to use 3 stations in the equilateral triangle configuration (stations M1, M2, M3 in the simulation). These had FOVs of $64° \times 48°$, 30 FPS and a measurement uncertainly of 30 arc seconds. The elevation of the centres of the fields of view of all cameras was $65°$ and they where all pointed towards the centre of the triangle.

Finally, the simulated CAMO system mimics the real system which has 2 stations ("tavis" and "elgin" in the simulation) separated by $45 \, \mathrm{km}$, a FOV of $30° \times 30°$, cameras operated at 100 FPS, and a precision of 1 arc second. We note that the CAMO tracking is delayed by about $0.1 \, \mathrm{s}$ after the detection in the wide-field camera.

---

[1]SonotaCo: `http://sonotaco.jp/`

Table 4.1: Parameters of simulated optical meteor observation systems. Δt_{max} is the maximum time offset, FPS is the frames per second of the camera, σ_{obs} the measurement uncertainly in arc seconds, FOV width and height are the size of the field of view in degrees, MLM the meteor limiting magnitude, and P_{0m} is the power of a zero-magnitude meteor (power values taken from Weryk & Brown, 2013).

System	N stations	Δt_{max} (s)	FPS	σ_{obs} (arcsec)	FOV width (deg)	FOV height (deg)	MLM	P_{0m} (W)
CAMO	2	1	100	1	30	30	+5.5	840
Moderate	3	1	30	30	64	48	+5.0	1210
All-sky	3	1	30	120	120	120	-0.5	1210

4.2.2   Simulated meteor showers

To explore the performance of various meteor trajectory estimation methods when observing meteors of different velocities and physical properties we focused on generating synthetic meteors from three very different meteor showers. We simulated 100 meteors for every system for each of the following three meteor showers:

1. The 2011 Draconids, a low-velocity ($\sim$21 km s^{-1}) shower with fragile and fresh ($¡$100 years of age) cometary meteoroids (Borovička et al., 2007) that experienced an outburst in 2011 (Šegon et al., 2014; Ye et al., 2013).

2. The 2012 Geminids, a $\sim$34 km s^{-1} moderate speed shower of asteroidal origin containing meteoroids of ages from 1000 to 4000 years (Beech, 2002).

3. The 2012 Perseids, a $\sim$59 km s^{-1} fast shower of Halley-type comet origin whose meteoroids were ejected > 2000 years ago (Brown & Jones, 1998).

Realistic trajectories and dynamics were simulated using the Campbell-Brown & Koschny (2004) meteoroid ablation model procedure described in detail in Vida et al. (2018). Meteoroid fragmentation was not directly simulated, but applied though the ablation coefficient in our single-body simulations. Meteor shower parameters used in the simulations are given in table 4.2 - parameters of all showers except the Draconids were taken from observations published in the literature.

Note that the 2015 Taurid fireball outburst was also simulated, but only for the all-sky systems as discussed in section 4.3.5. The goal in applying our analysis to the unique 2015 Taurid outburst was to contrast the accuracy of various trajectory estimation methods when using low-precision (video) all-sky systems as compared to higher precision fireball systems.

4.2.3   Dynamical modelling of the 2011 Draconid outburst

The 2011 Draconids were the youngest of the simulated showers and should have the most compact radiant. The measured radiant spread should be dominated by measurement uncertainty when measured with less precise systems. To quantify the minimum accuracy required to observe the true physical radiant and velocity dispersion of the 2011 Draconids, we appeal to dynamical modelling of the shower, i.e. modelling the ejection of meteoroids from their parent comet and integrating their motion until they interest the Earth's orbit. Here we use the method of Wiegert et al. (2009) to obtain an estimate of both the true average location of the radiant and velocity of the outburst and its theoretical spread. We then use these as inputs to our simulation model to generate synthetic 2011 Draconids to virtually "observe" with each of our three optical systems and apply each meteor trajectory solver in turn.

To dynamically model the 2011 Draconid outburst, the orbital elements of the 1966 apparition of 21P/Giacobini-Zinner were integrated backwards 200 years with the RADAU (Everhart, 1985) integrator within a simulated Solar System containing the Sun and eight planets. The parent comet was then advanced forward in time while ejecting meteoroids with radii between $100\,\mu\text{m}$ and $10\,\text{cm}$ when within $3\,\text{AU}$ of the Sun. The ejection speed and direction follows the approach of the Brown & Jones (1998) model with an assumed comet radius of $1\,\text{km}$, albedo of 0.05 and bulk density of $300\,\text{kg}\,\text{m}^{-3}$.

Meteoroids arriving at Earth in 2011 were found to be produced by the 1838 and 1907 comet perihelion passages, with smaller contributions from 1920 and 1953. The simulated peak coincided with that reported by visual observers to the International Meteor Organization (IMO) Visual Meteor Database[2].

The radiants of the dynamically modelled stream that impacted the Earth are shown in figure 4.1. Note that these model radiants are without observational biases because they were directly computed from simulated meteoroids arriving at Earth. The position and the dispersion

---

[2]IMO VMDB 2011 Draconids: `https://www.imo.net/members/imo_live_shower?shower=DRA&year=2011`
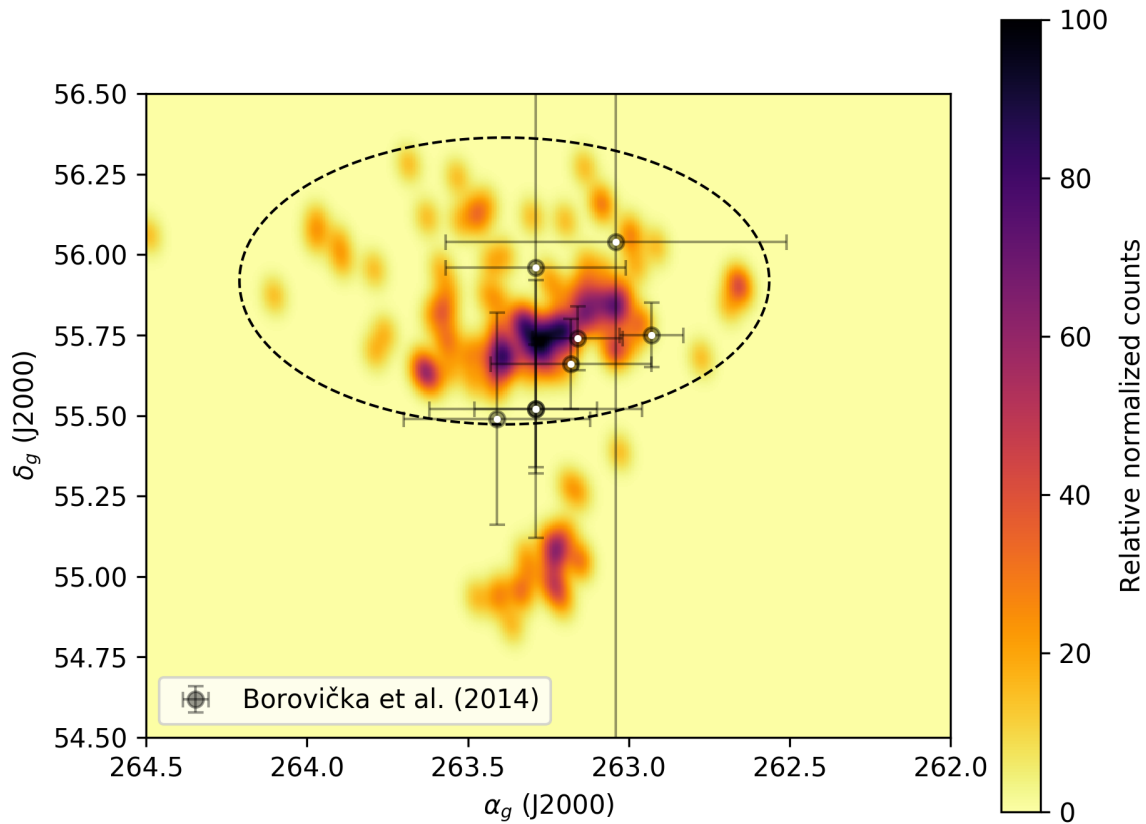
Figure 4.1: Density map of simulated geocentric equatorial (J2000.0) radiants of the 2011 Draconids at the time of peak activity. A bi-variate Gaussian was fit to the radiants (α_g = 263.387° ± 0.291°, δ_g = 55.9181° ± 0.158°). The corresponding 2σ level is shown as a black contour. Draconid radiants observed by Borovička et al. (2014) in 2011 are also shown.

of the modelled radiant at the time of peak activity was $\alpha_g = 263.387° \pm 0.291°$, $\delta_g = 55.9181° \pm 0.158°$. The values were derived by fitting a bi-variate Gaussian to the modelled radiants. Distinct radiant structure can also be seen - we estimate that an observational radiant precision of better than 3 to 6 arc minutes ($0.05°$ - $0.1°$) is needed for the true radiant structure to be unambiguously reconstructed from observations. We use these values as the absolute minimum radiant accuracy needed to resolve the true physical radiant spread for showers with the most compact radiants.

The video and high power large aperture (HPLA) radar observations of the Draconid outburst measured an almost order of magnitude larger dispersion than our model predicts, suggesting they did not record the intrinsic (physical) radiant spread of the shower (Šegon et al., 2014; Trigo-Rodríguez et al., 2013; Kero et al., 2012). We note that the video observations of the outburst incorporating high-quality manual reductions reported by Borovička et al. (2014) are an excellent match to our simulations in both radiant position, dispersion, and the simulated peak time, as shown in figure 4.1.

As both the Geminids and Perseids are older showers, we do not expect the physical radiant dispersion to be as compact as the Draconids, thus for simulation purposes we have used observed values for these quantities provided in Jenniskens et al. (2016) and Jenniskens (1994). We summarize the modeling parameters adopted of the simulated meteors showers in table 4.2 and the physical properties of shower meteoroids used in the ablation modeling in table 4.3.

Table 4.2: The model parameters adopted for simulated meteor showers. The parameters for the Draconids were computed from the simulation as discussed in the text. The parameters for the Geminids and Perseids were taken from Jenniskens et al. (2016) unless otherwise noted. Parameters for the 2015 Taurids were taken from Spurný et al. (2017). These were modified from the original so that they are centered around the peak solar longitude while the radiant spread was computed directly from data provided in Spurný et al. (2017). $\lambda_\odot^{max}$ is the solar longitude of the peak (degrees), B is the solar longitude slope of the rising portion of the activity profile following the procedure of Jenniskens (1994), α is the mean geocentric right ascension, $\Delta\alpha$ is the radiant drift (degree on the sky per degree of solar longitude), α_σ is the standard deviation in R.A., δ is the mean geocentric declination, $\Delta\delta$ is the declination radiant drift, δ_σ is the standard deviation of the declination, V_g is the mean geocentric velocity in km s^{-1}, ΔV_g is the change in geocentric velocity per degree of solar longitude, and $V_{g\sigma}$ is the standard deviation of the geocentric velocity.

Shower	Year	$\lambda_\odot^{max}$	B	α	$\Delta\alpha$	α_σ	δ	$\Delta\delta$	δ_σ	V_g	ΔV_g	$V_{g\sigma}$
Draconids	2011	198.07	17.5, 1*	263.39	0.0	0.29	55.92	0.0	0.16	20.93	0	0.04
Geminids	2012	262.0	~ 0.5, 2*	113.5	1.15	2.8	32.3	-0.16	1.5	33.8	0	2.0
Perseids	2012	140.0	0.4, 2*	48.2	1.4	2.8	58.1	0.26	1.7	59.1	0	2.4
Taurids - resonant branch	2015	221.0	0.15	53.06	0.554	0.33	14.66	0.06	0.27	29.69	-0.293	0.22

1* - (Koten et al., 2014), 2* - (Jenniskens, 1994)

Table 4.3: Physical properties of meteoroids adopted as input to the ablation model in simulating our four meteor showers. Here s is the mass index, ρ is the range of bulk densities of meteoroids, σ is the apparent ablation coefficient (Ceplecha & ReVelle, 2005), and L is the energy needed to ablate a unit of meteoroid mass.

Shower	s	ρ (kg m^{-3})	σ (s^2 km^{-2})	L (J kg^{-1})
Draconids	1.95, 1*	100 - 400, 2*	0.21, D-type, 3*	1.2×10^6
Geminids	1.7, 4*	1000 - 3000, 5*	0.042, A-type, 3*	6.0×10^6
Perseids	2.0, 7*	HTC distribution, 6*	0.1, C-type, 3*	2.5×10^6
Taurids	1.8, 8*	1200 - 1600, 9*	0.1, C-type, 3*	2.5×10^6

1* - (Koten et al., 2014), 2* - (Borovička et al., 2007), 3* - (Ceplecha et al., 1998), 4* - (Blaauw et al., 2011), 5* - (Borovička et al., 2009), 6* - (Moorhead et al., 2017), 7* - (Beech & Nikolova, 1999), 8* - (Moser et al., 2011), 9* - (Brown et al., 2013)

4.2.4 Simulation validation

To confirm the appropriateness of the simulations, we compare some metrics among our suite of simulated and observed meteors for the same optical system. Note that we did not attempt to reconstruct particular observed events though simulation; we only identified meteors of similar properties and quantitatively compared the trajectory fit residuals and deceleration. As an indicator of deceleration we computed the meteor's lag, i.e. how much the observed meteor falls behind a hypothetical meteoroid moving with a fixed speed equal to the initial velocity. We present several meteors from instrument data sets having comparable speed and duration to those we simulated. Table 4.4 compares the initial speed, mass and zenith angle of a selection of simulated and representative observed meteors. All observations were reduced using the Monte Carlo method.

As a first example, figures 4.2 and 4.3 show a sporadic meteor with a geocentric velocity $V_g = \sim 21\,\mathrm{km\,s^{-1}}$ observed with CAMO and comparable simulated CAMO Draconid. The "Jacchia fit" curve in lag plots is a fit of the exponential deceleration model of Whipple & Jacchia (1957) to the computed lag and is only used for visualization purposes. The amount of deceleration and the scatter in the spatial fit residuals (<1 m) are similar. The scatter in residuals shows that the dispersion due to random errors are comparable. CAMO measurements are slightly noisier compared to the model at the beginning because the tracking mirrors require
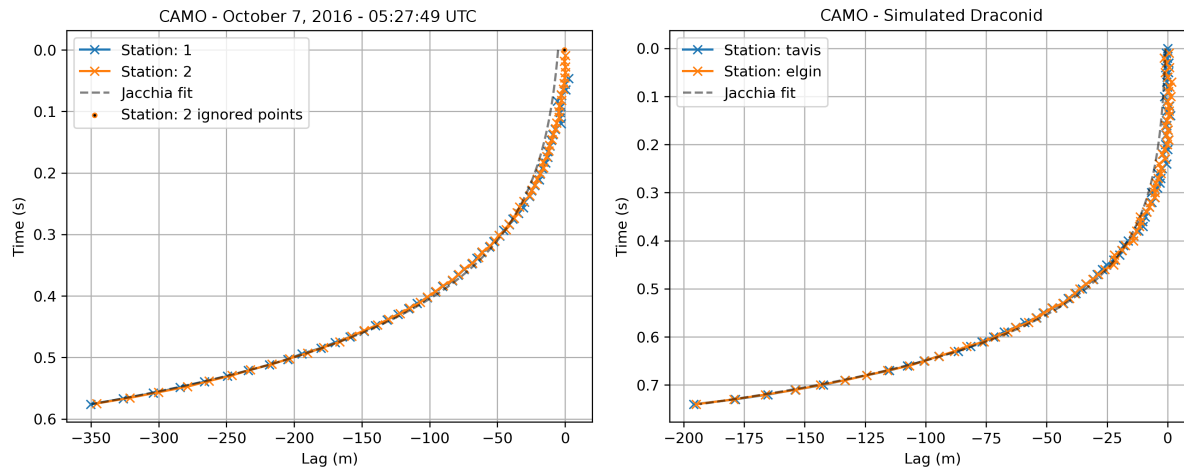
Figure 4.2: Left: Lag of a CAMO sporadic meteor observed on October 7, 2016 with $V_g =$ 21.4 km s^{-1}. As per the UWO station naming convention, the stations identifiers are numbers - 1 is Tavistock, 2 is Elginfield. Right: A simulated CAMO Draconid of similar mass and with $V_g = 20.9$ km s^{-1}.

several milliseconds to settle. The fit residuals were on the order of 1 arc second for both data sets. We note that the observed meteor showed significant visible fragmentation which was not included in the model; thus the magnitude of the observed lag is larger than in the simulation.

Figure 4.4 shows the lag for a Geminid observed by five CAMS stations in California compared to a simulated CAMS Geminid. The two meteors had similar velocities, masses, and entry angles. Both meteors show similar decelerations, and had spatial fit residuals of ~20 m.

Finally, figure 4.5 shows the comparison for a low-resolution, all-sky system, namely the Southern Ontario Meteor Network Brown et al. (2010) between an observed Southern Taurid ($V_g = 31.4$ km s^{-1}) and a simulated Geminid. Neither meteor shows visible deceleration due to the low precision of the measurements. However, deceleration may become visible and significant for much longer duration fireballs (see section 4.3.6).

4.3 Results

Following the theoretical development given in Paper 1, we numerically evaluated the performance of the following trajectory solvers (abbreviations used later in the text):
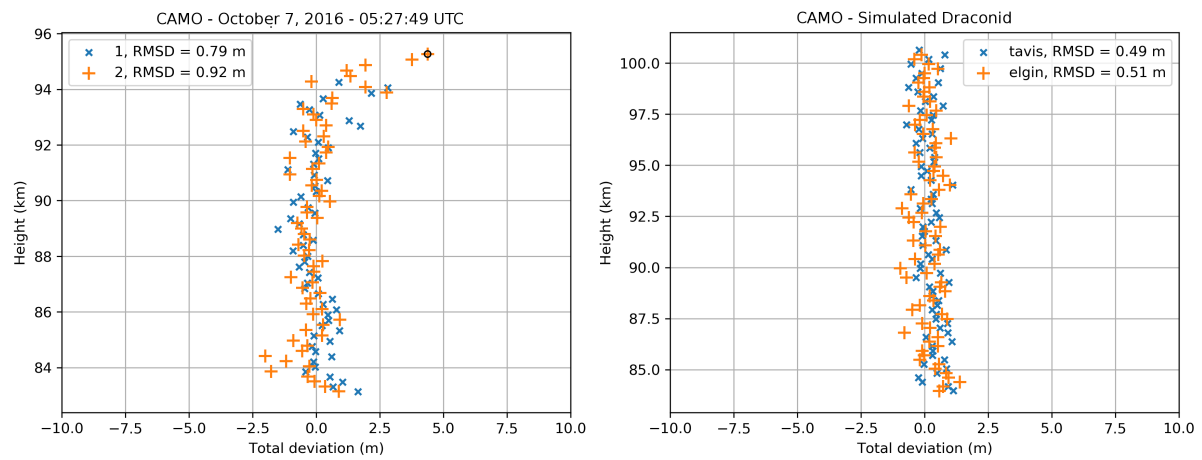
Figure 4.3: Left: Spatial residuals of a CAMO sporadic meteor observed on October 7, 2016 with $V_g = 21.4\,\mathrm{km\,s^{-1}}$. Station 1 is Tavistock, 2 is Elginfield. Right: A simulated CAMO Draconid of similar mass and with $V_g = 20.9\,\mathrm{km\,s^{-1}}$.
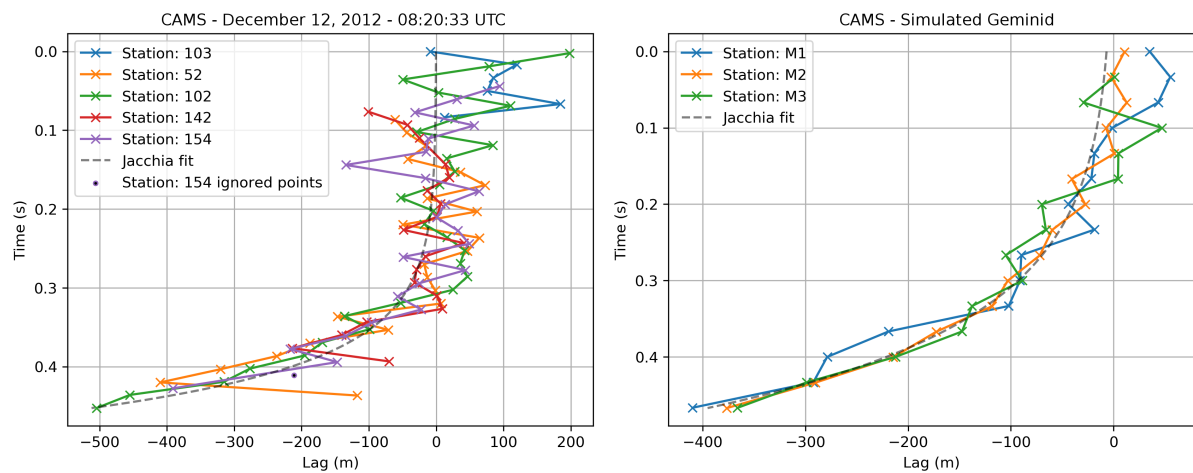
Figure 4.4: Left: Lag of a CAMS Geminid observed on December 12, 2012 with $V_g = 33.4\,\mathrm{km\,s^{-1}}$ by CAMS cameras in California. Right: A simulated CAMS Geminid of similar mass with $V_g = 34.6\,\mathrm{km\,s^{-1}}$.
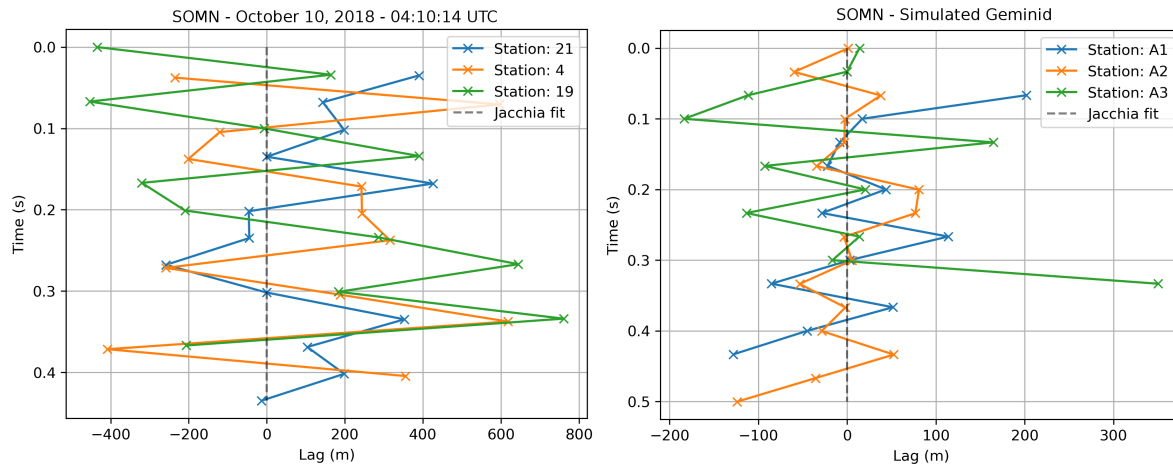
Figure 4.5: Left: Lag of a SOMN Southern Taurid meteor observed on October 10, 2018 with $V_g = 31.4\,\mathrm{km\,s^{-1}}$. Ignored points are those with angular error more than 3σ above the mean after the first trajectory estimation pass as described in Paper 1. Right: A simulated SOMN Geminid with $V_g = 34.0\,\mathrm{km\,s^{-1}}$.

Table 4.4: Comparison of several selected observed meteors and the close fits from among the simulated set of meteors. The photometric masses were computed using a dimensionless luminous efficiency of $\tau = 0.7\%$ (Vida et al., 2018) and a bandpass specific $P_{0m} = 1210\,\mathrm{W}$. The observed (calculated) masses are similar to simulated masses. Note that the range of simulated masses was taken from Vida et al. (2018) and is based on the masses calculated from observations by each type of system.

System	Initial speed (km/s)		Mass (g)		Zenith angle (deg)	
	Obs	Sim	Obs	Sim	Obs	Sim
CAMO	24.1	23.7	0.03	0.03	26	15
Moderate	35.2	36.4	0.02	0.01	22	21
All-sky	33.3	36.4	0.2	0.1	40	36

- IP - The intersecting planes method of Ceplecha (1987). The initial velocity is computed as the average velocity of the first half of the trajectory; better initial velocity accuracy might be achieved by using the method of Pecina & Ceplecha (1983, 1984).

- LoS - Our implementation of the Borovička (1990) method with our progressive initial velocity estimation method as described in Paper 1.

- LoS-FHAV - Our implementation of the Borovička (1990) method. The initial velocity is computed as the average velocity of the first half of the trajectory.

- MC - The Monte Carlo method presented in Paper 1.

- MPF const - The multi-parameter fit method of Gural (2012) using a constant velocity model.

- MPF const-FHAV - For this hybrid-solver, the radiant solution is taken from the MPF constant velocity model, but the lines of sight are re-projected on the trajectory and the initial velocity is estimated as the slope of the length vs. time along the track (effectively, the average velocity) of the first half of the trajectory.

- MPF linear - The Gural (2012) multi-parameter fit method with a linear deceleration velocity model.

- MPF exp - The Gural (2012) multi-parameter fit method with the exponential deceleration model of Whipple & Jacchia (1957)

Global results for all tested trajectory solvers for all-sky systems are given in table 4.5, for moderate FOV systems in table 4.6, and for CAMO in table 4.7 respectively. For every combination of observation system, meteor shower and trajectory solver we list:

1. The column labelled F in each table is the total number of failures for a given method out of 100 simulated runs. This is the number of trajectory solutions with radiant or

velocity difference between the true (simulated) and estimated values larger than the predetermined values given in the caption to each table.

2. The standard deviation between the estimated and true radiant angular separation (σ_R in tables).

3. The standard deviation between the estimated and true geocentric velocity (σ_V in tables).

The standard deviations are computed after iteratively rejecting solutions outside 3σ.

A trajectory solution was considered to be a failure if the radiant error (difference between estimated and true as initially input into the simulation) was more than Δ_{Rmax} degrees from the true radiant, or if the velocity error was more than Δ_{Vmax} from the model velocity. For the simulated all-sky system the values used were $\Delta_{Rmax} = 5°$, $\Delta_{Vmax} = 5\,\mathrm{km\,s^{-1}}$, while for the moderate FOV (CAMS-like) system we adopted $\Delta_{Rmax} = 1°$, $\Delta_{Vmax} = 1\,\mathrm{km\,s^{-1}}$. Finally, for the simulated CAMO–like system, we adopted $\Delta_{Rmax} = 0.5°$, $\Delta_{Vmax} = 0.5\,\mathrm{km\,s^{-1}}$.

Solutions were also removed from further consideration if any of the multi-station convergence angles were less than 15°, 10°, and 1° for the all-sky, CAMS, and CAMO simulations respectively. This procedure was adopted so that the general performance of different solvers can be compared, excluding excessive deviations due simply to low convergence angles. We explore in more depth the dependence of solution accuracy on the convergence angle in section 4.3.4.

In what follows, we show representative plots of the spread in the radiant and velocity accuracy for each trajectory solver for each optical system. In addition, we show a selection of individual results per shower and per solver in the form of 2D histograms (e.g. figure 4.7) which highlight the scatter of estimates among the 100 simulated meteors. On these plots, the angular distance between the real and the estimated geocentric radiant is shown on the X axis, the error in the geocentric velocity is shown on the Y axis, and the bin count is color coded (darker color means higher count).

Table 4.5: Comparison of solver accuracy for a simulated three station all-sky system. The trajectory was taken to be valid for simulation if the converge angle was larger than 15°. F is the number of failures (out of 100), i.e. the number of radiants that were outside the window bounded by $\Delta_{Rmax} = 5°$, $\Delta_{Vmax} = 5\,\text{km}\,\text{s}^{-1}$.

Solver	DRA			GEM			PER		
	F	σ_R	σ_V	F	σ_R	σ_V	F	σ_R	σ_V
IP	1	0.44°	0.38 km s⁻¹	1	0.21°	0.38 km s⁻¹	10	0.67°	0.99 km s⁻¹
LoS	1	0.56°	0.47 km s⁻¹	1	0.26°	0.42 km s⁻¹	3	0.66°	0.46 km s⁻¹
LoS-FHAV	1	0.51°	0.38 km s⁻¹	1	0.26°	0.38 km s⁻¹	7	0.66°	0.53 km s⁻¹
Monte Carlo	2	0.52°	0.36 km s⁻¹	1	0.24°	0.47 km s⁻¹	4	0.80°	0.38 km s⁻¹
MPF const	1	0.28°	0.46 km s⁻¹	0	0.24°	0.84 km s⁻¹	1	0.47°	0.37 km s⁻¹
MPF const-FHAV	1	0.27°	0.38 km s⁻¹	0	0.23°	0.41 km s⁻¹	4	0.35°	0.80 km s⁻¹
MPF linear	0	0.26°	0.54 km s⁻¹	4	0.23°	1.76 km s⁻¹	6	0.35°	0.60 km s⁻¹
MPF exp	0	0.41°	1.39 km s⁻¹	1	0.21°	1.65 km s⁻¹	12	0.32°	1.18 km s⁻¹

4.3.1 All-sky systems

Table 4.5 lists the accuracy of geocentric radiants computed for the simulated showers using different methods of meteor trajectory estimation for a three station all-sky system. Figure 4.6 is a visualization of the values in the table. The numbers above the vertical bars for each solver represent the failure rate (out of 100) for the Draconids, the Geminids and the Perseids (in that order). Figure 4.7 shows the distribution of radiant and velocity errors as 2D hexbin histograms for a selection of solvers applied to simulated Geminid data. The increasing bin count is color coded with increasingly darker colors. The gray boxes show the 3σ standard deviation.

From figure 4.6 it is apparent that the IP and LoS methods achieve decent radiant accuracy, but tend to have a larger number of failures for faster meteors (Perseids). Moreover, the estimated velocity accuracy decreases with meteor speed, a direct consequence of the smaller number of data points on which the velocity can be estimated for these methods. The Monte Carlo method does not provide any significant increase in accuracy as expected, as the limited precision does not produce useful lag measurements.

Figure 4.7 shows that the MPF exponential velocity model tends to overestimate velocities at infinity (a behaviour of the exponential deceleration function also noticed by Pecina & Ceplecha, 1983) and that it has a noticeably larger number of failures for faster meteoroids than

Figure 4.6: Comparison of geocentric radiant and velocity accuracy for a simulated three station all-sky system for three simulated showers and the various trajectory solvers. The numbers at the top of each vertical bar show the number of failures for a particular method (given in red text) for the Draconids, Geminids and Perseids simulated, respectively.
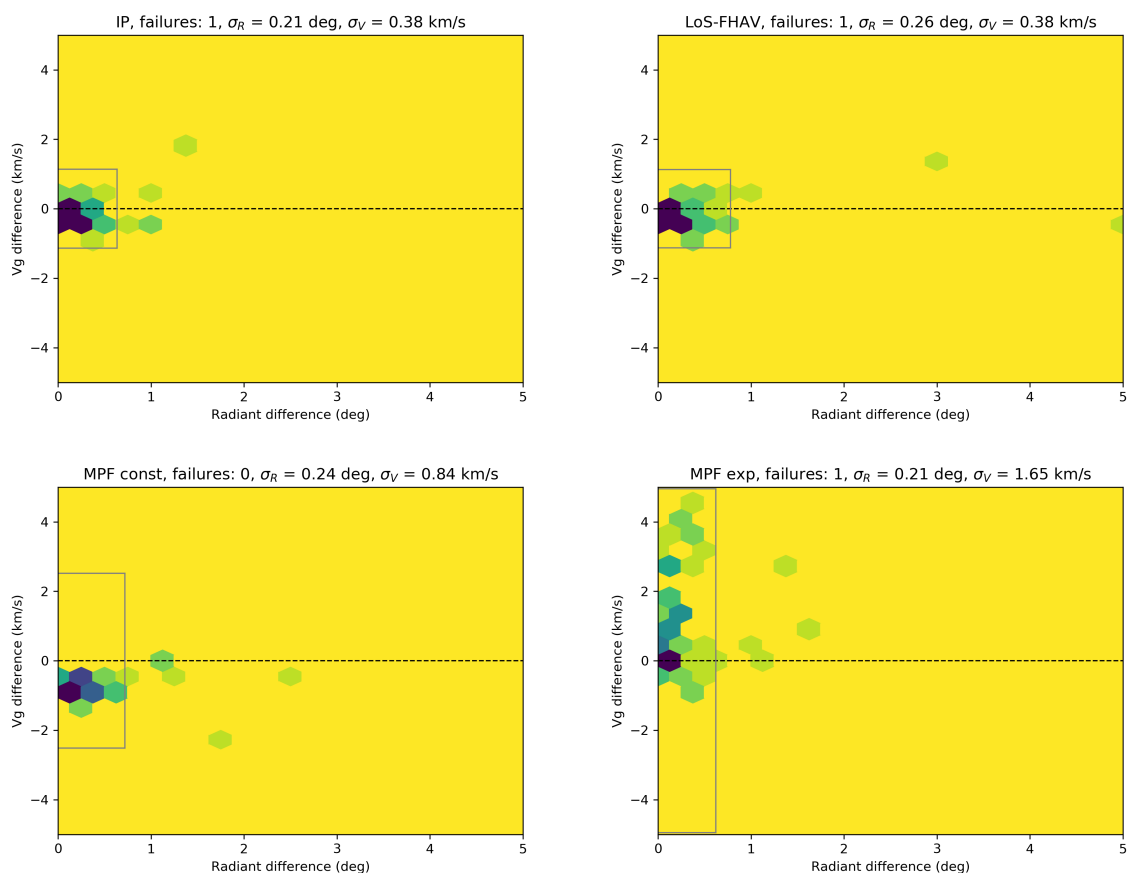
Figure 4.7: Accuracy of geocentric radiants for the Geminids simulated for all-sky systems shown as a density plot (darker is denser). Upper left: Intersecting planes. Upper right: Lines of sight, initial velocity estimated as the average velocity of the first half of the trajectory. Bottom left: Multi-parameter fit, constant velocity model. Bottom right: Multi-parameter fit, exponential velocity model.

other methods (except the IP). In contrast, the MPF constant velocity model is the most robust all-around solver for all-sky data, simultaneously achieving good radiant accuracy and a low number of failures, even for faster meteors. Note, however, that because the MPF constant velocity model only computes the average velocity, the velocity estimation is precise but not accurate; it is systematically underestimated. The use of the MPF const-FHAV was an attempt to improve on this deficiency by computing the initial velocity as equal to the average velocity of the first half of the trajectory. This works well for the Draconids and the Geminids, but produces a significantly higher error for the faster Perseids, where the reduction in number of measured points leads to a much larger error.

From our simulations, it appears that the optimal operational approach for low resolution (video) all-sky systems would be to adopt the MPF solver with the constant velocity model, plus a separate (empirical) deceleration correction. The expected geocentric radiant error with this solver is around $0.25°$ ($0.5°$ for the Perseids) and around $500 \, \mathrm{m \, s^{-1}}$ in velocity (or $250 \, \mathrm{m \, s^{-1}}$ if additional compensation for the early, pre-luminous deceleration is included).

4.3.2   Moderate FOV systems

Table 4.6 lists the accuracy of geocentric radiants computed for individual showers using different methods of meteor trajectory estimation for simulated meteors detected by a three station CAMS-type optical system. Figure 4.8 shows the visualization of the values in the table.

The situation is more complex than was the case for the all-sky system. For convergence angles $>10°$, the best results are produced by the classical intersecting planes and the lines of sight solvers, while the solvers which include kinematics perform either marginally worse in the case of the Monte Carlo solver, or significantly worse in the case of multi-parameter fit methods. For all solvers, events which led to a solution within our acceptance window correspond to expected radiant errors around $0.1°$. The velocity error is around $200 \, \mathrm{m \, s^{-1}}$ (around $100 \, \mathrm{m \, s^{-1}}$ after deceleration correction) for the better solvers. The exception are the Geminids which have a factor of 2 larger velocity uncertainties. They penetrate deeper into the

Table 4.6: Solver performance comparison for the simulated moderate FOV system. The trajectory was included in the statistics if the convergence angle was larger than 10°. F is the number of failures (out of 100), i.e. the number of radiants that were outside the $\Delta_{Rmax} = 1°$, $\Delta_{Vmax} = 1\,\mathrm{km\,s^{-1}}$ window.

Solver	DRA			GEM			PER		
	F	σ_R	σ_V	F	σ_R	σ_V	F	σ_R	σ_V
IP	1	0.07°	0.15 km s^{-1}	1	0.06°	0.31 km s^{-1}	5	0.07°	0.17 km s^{-1}
LoS	1	0.09°	0.17 km s^{-1}	1	0.06°	0.29 km s^{-1}	2	0.07°	0.16 km s^{-1}
LoS-FHAV	1	0.09°	0.13 km s^{-1}	1	0.06°	0.31 km s^{-1}	5	0.08°	0.17 km s^{-1}
Monte Carlo	2	0.08°	0.15 km s^{-1}	1	0.06°	0.28 km s^{-1}	2	0.09°	0.15 km s^{-1}
MPF const	1	0.08°	0.26 km s^{-1}	0	0.09°	0.67 km s^{-1}	0	0.06°	0.22 km s^{-1}
MPF const-FHAV	9	0.08°	0.35 km s^{-1}	6	0.08°	0.37 km s^{-1}	8	0.06°	0.32 km s^{-1}
MPF linear	19	0.07°	0.39 km s^{-1}	34	0.07°	0.45 km s^{-1}	6	0.05°	0.19 km s^{-1}
MPF exp	34	0.07°	0.50 km s^{-1}	38	0.07°	0.34 km s^{-1}	9	0.06°	0.37 km s^{-1}
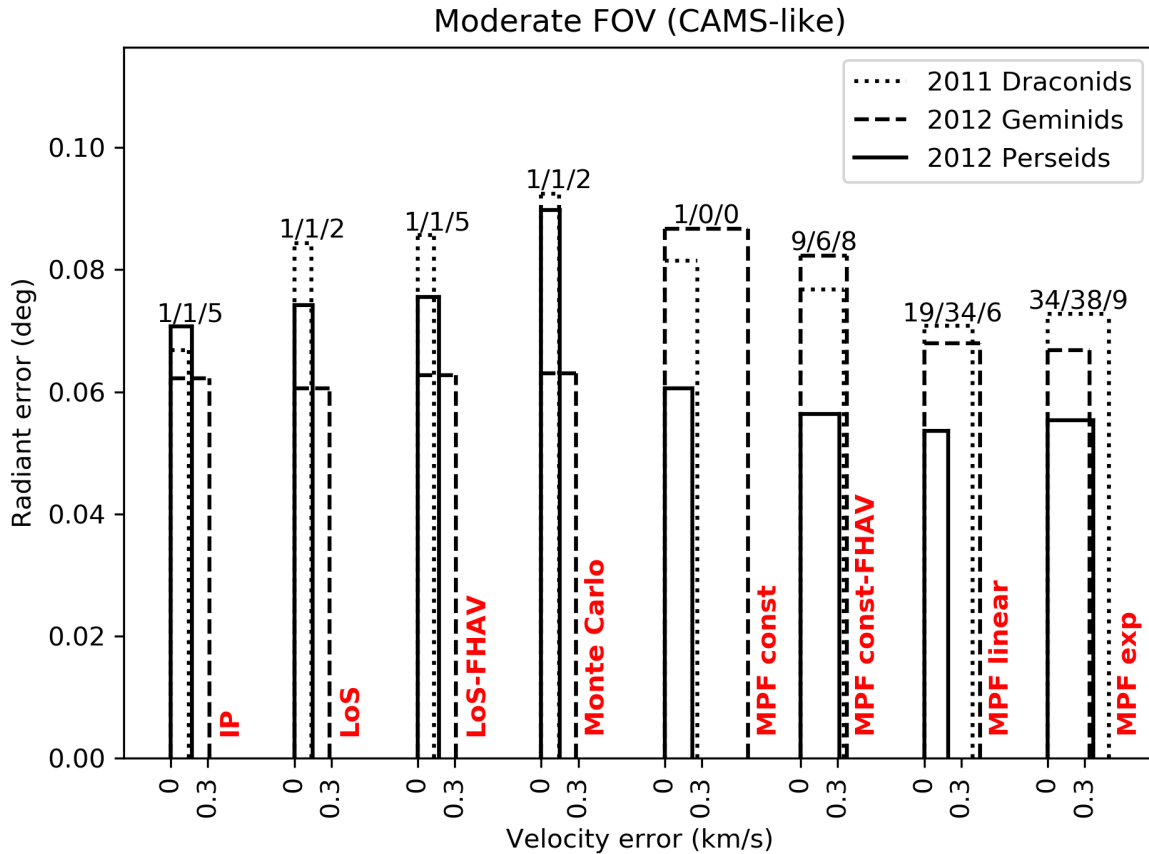
Figure 4.8: Comparison of the geocentric radiant and velocity accuracy for a simulated CAMS-type system for three showers and various trajectory solvers.

atmosphere due to their asteroidal composition, and decelerate more, which leads to a larger underestimation of the initial velocity.

We emphasize that the MPF methods sometimes do produce better estimates of the radiant, which is consistent with Gural (2012) who only investigated the precision of the radiant position for various solvers. On the other hand, MPF-based velocity estimates are consistently worse by a factor of 2 or more when compared to other methods, as shown in figure 4.9. The MPF method with the constant velocity model does produce robust (precise) solutions, but still requires either correcting for the deceleration or an alternate way of computing the initial velocity (and improving accuracy).

Computing the initial velocity as the average of the first half (MPF const-FHAV) does not result in an improvement but causes an even larger spread in the estimated velocities. Furthermore, the MPF method with the exponential deceleration model produces a high failure rate for this type of data as well, predominantly due to the overestimation of the initial velocity. On the other hand, the radiant estimation was as robust as the other solvers, for events which met our acceptance criteria. This finding is worrisome as this velocity model was used by the CAMS network (Jenniskens et al., 2016). Our simulations suggest that initial velocities obtained with MPF-exp for moderate field of view systems should ideally be compared to other solvers before acceptance.

4.3.3   CAMO system

Table 4.7 lists the accuracy of geocentric radiants for our three modelled showers using different methods of meteor trajectory estimation applied to simulated CAMO data. Figure 4.10 shows a visualization of the values in the table. Note that the Geminids are missing from the graph for the MPF const method, as most Geminid velocities estimated with that method were outside the $0.5 \, \text{km} \, \text{s}^{-1}$ threshold due to the larger deceleration of these asteroidal meteoroids. Thus, in this section we use the Draconids for the comparison between solvers.

The upper left inset of figure 4.11 shows the results obtained using the LoS-FHAV method
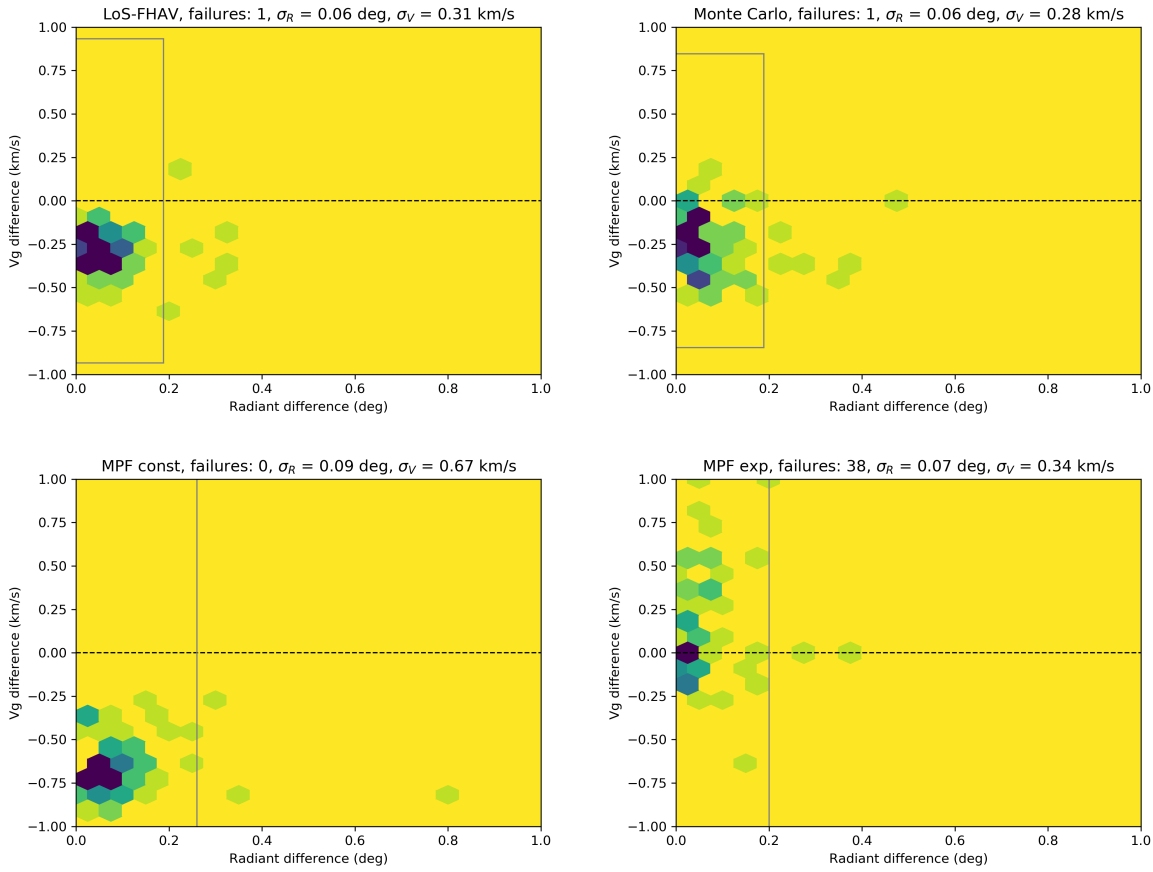
Figure 4.9: Accuracy of geocentric radiants for the Geminids simulated for CAMS-like systems. Upper left: Lines of sight, initial velocity estimated as the average velocity of the first half of the trajectory. Upper right: Monte Carlo. Bottom left: Multi-parameter fit, constant velocity model. Bottom right: Multi-parameter fit, exponential velocity model.

Table 4.7: Solver performance comparison for the simulated CAMO-like optical system. A simulated trajectory was included in the final statistics if the convergence angle was larger than $1°$. F is the number of failures (out of 100), i.e. the number of radiants that were outside the $\Delta_{Rmax} = 0.5°$, $\Delta_{Vmax} = 0.5\,\mathrm{km\,s^{-1}}$ window.

Solver	DRA			GEM			PER		
	F	σ_R	σ_V	F	σ_R	σ_V	F	σ_R	σ_V
IP	5	0.02°	0.18 km s⁻¹	24	0.01°	0.33 km s⁻¹	1	0.01°	0.14 km s⁻¹
LoS	8	0.02°	0.15 km s⁻¹	17	0.01°	0.27 km s⁻¹	1	0.01°	0.12 km s⁻¹
LoS-FHAV	5	0.02°	0.17 km s⁻¹	23	0.02°	0.33 km s⁻¹	1	0.01°	0.14 km s⁻¹
Monte Carlo	6	0.02°	0.15 km s⁻¹	18	0.01°	0.27 km s⁻¹	1	0.01°	0.11 km s⁻¹
MPF const	4	0.03°	0.29 km s⁻¹	99	0.31°	0.47 km s⁻¹	5	0.03°	0.23 km s⁻¹
MPF const-FHAV	12	0.03°	0.18 km s⁻¹	43	0.17°	0.35 km s⁻¹	28	0.03°	0.26 km s⁻¹
MPF linear	43	0.02°	0.22 km s⁻¹	62	0.03°	0.33 km s⁻¹	22	0.01°	0.19 km s⁻¹
MPF exp	52	0.02°	0.21 km s⁻¹	68	0.02°	0.27 km s⁻¹	56	0.01°	0.26 km s⁻¹

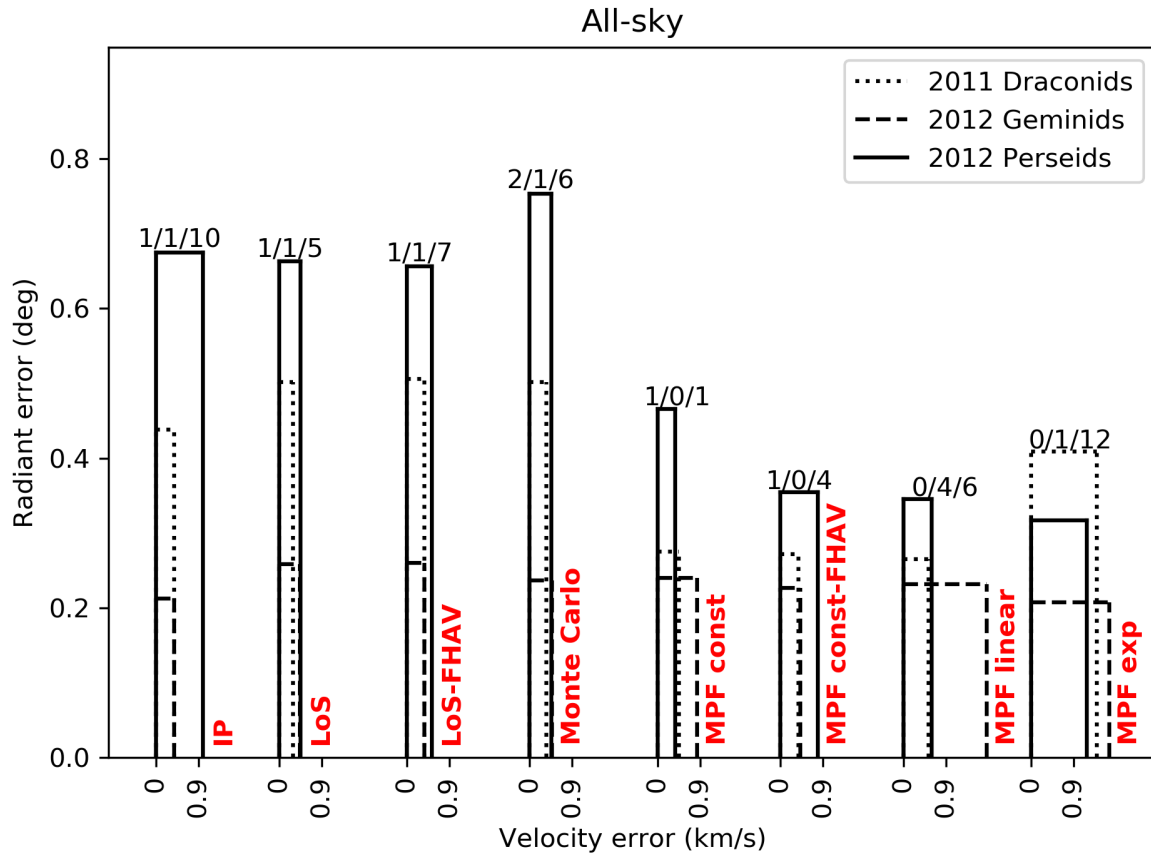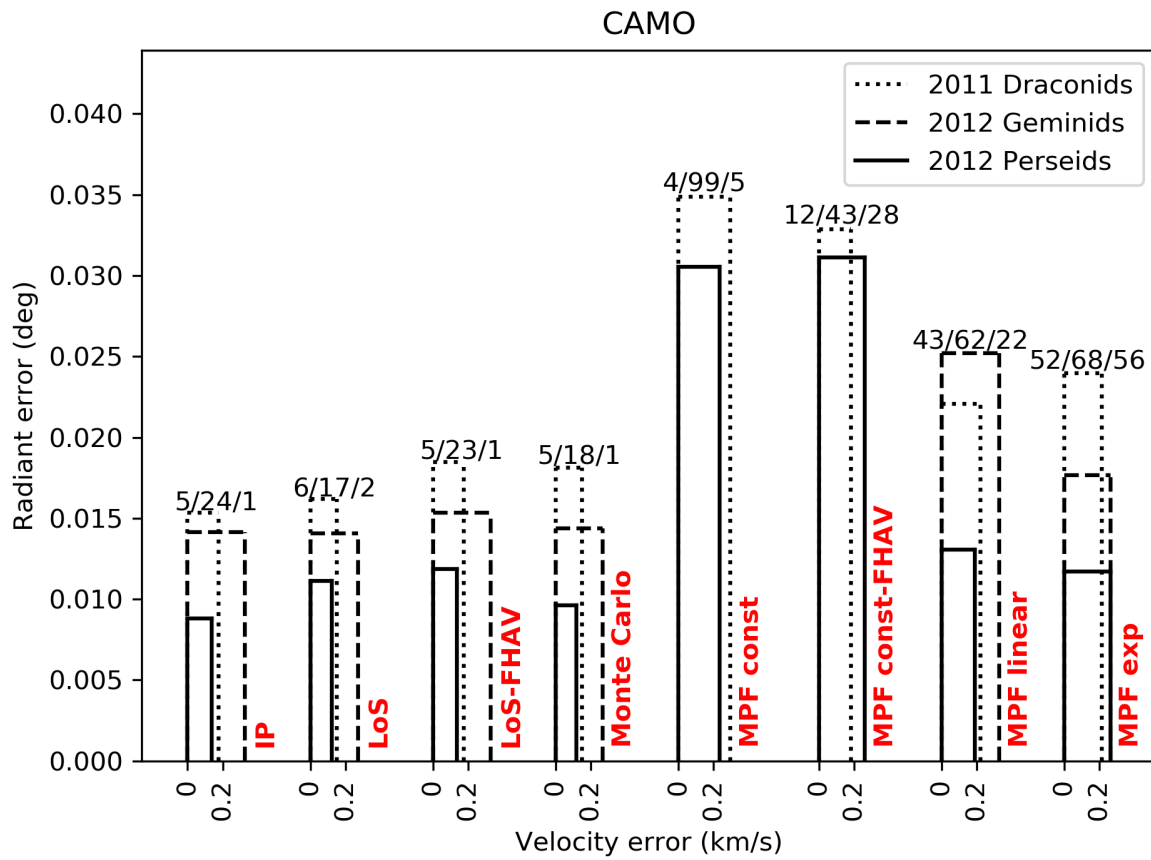Figure 4.10: Comparison of geocentric radiant and velocity accuracy for the simulated CAMO system for three simulated showers and various trajectory solvers.

for the Draconids. Only 5 out of 100 solutions failed. The geocentric velocities are systematically underestimated due to deceleration occurring prior to detection. For this system, the average underestimation is around $200\,\mathrm{m\,s^{-1}}$ for cometary, and $300\,\mathrm{m\,s^{-1}}$ for asteroidal meteoroids (see Vida et al., 2018, for a complete analysis). The measurement precision of the initial velocity is much better, around $50\,\mathrm{m\,s^{-1}}$. The accuracy of the radiant estimation is approximately $0.02°$.

The upper right inset of figure 4.11 shows the results obtained using the Monte Carlo solver. Overall this solver and the LoS solver provided the best precision for CAMO data. Both have very low failure rates; the radiant accuracy was around $0.01°$ and the geocentric velocity accuracy around $150\,\mathrm{m\,s^{-1}}$. The geocentric velocity was systematically underestimated due to deceleration prior to detection; the accuracy could be improved by applying the correction given in Vida et al. (2018).

The lower left inset of figure 4.11 shows simulation results using the MPF method with the constant velocity model for the Draconids. The geocentric velocity was underestimated more than with the LoS-FHAV method, as the initial velocity estimate is very heavily influenced by deceleration. The average difference between the initial velocity and true velocity for our 100 simulated Draconids was around $300\,\mathrm{m\,s^{-1}}$. This difference drives the error in the radiant, which had a standard deviation among our simulations of $0.04°$. For the Geminds, the velocity difference with this method was $>1\,\mathrm{km\,s^{-1}}$, which strongly indicates that using average meteor velocities is not suitable for computing orbits of asteroidal meteors.

Finally, the lower right inset of figure 4.11 shows results obtained using the MPF solver with the exponential deceleration model. This solver had a very large failure rate, above 50%. The failure was mostly driven by the overestimation of the initial velocity; in contrast the estimation of the radiant position remained fairly robust.
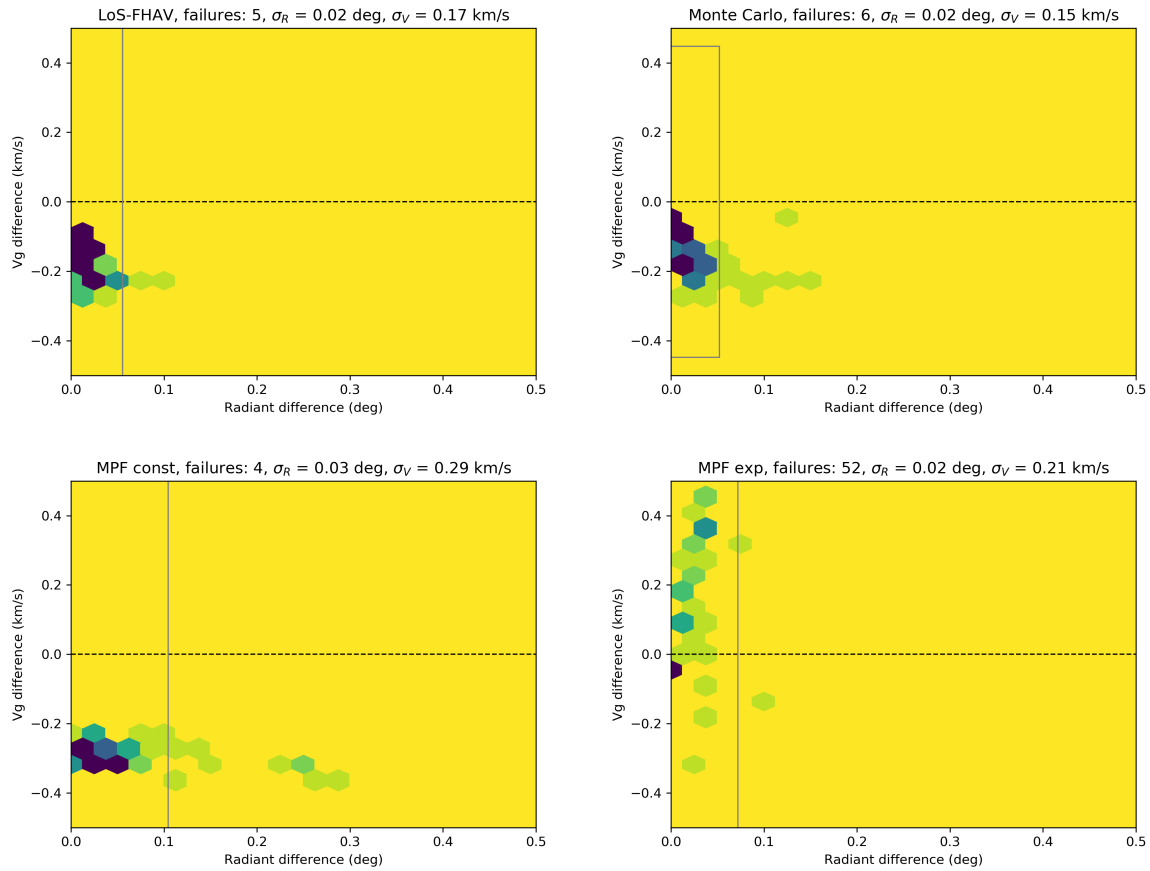
Figure 4.11: Accuracy of simulated CAMO geocentric radiants for the Draconids. Upper left: Lines of sight, initial velocity estimated as the average velocity of the first half of the trajectory. Upper right: Monte Carlo. Bottom left: Multi-parameter fit, constant velocity model. Bottom right: Multi-parameter fit, exponential velocity model.

4.3.4   Trajectory solution accuracy as a function of convergence angle

The maximum convergence angle between a meteor trajectory and stations is usually used as an indicator for the trajectory quality. Gural (2012) has shown that the radiant error is dependent on the convergence angle (among other factors). He found that the IP and LoS methods produced on average a factor of 10 increase in radiant error at low ($< 10°$) convergence angles. In that work, the constant velocity MPF method significantly improved the radiant accuracy, and the error for low convergence angles was only a factor of 2 higher as compared to larger angles. To test for convergence angle sensitivity amongst solvers, we generated 1000 synthetic Geminids with our ablation model for all three systems. We divided the range of convergence angles into 30 bins of equal numbers of data points; thus 1000 simulations were needed for better statistics.

Figure 4.12 shows radiant and velocity errors versus the convergence angle, Q_c, for a simulated all-sky (SOMN-like) system. Only two stations (A1 and A2) were used for the convergence angle analysis - when a third station is included, all maximum convergence angles are usually $> 30°$. The plotted data shows the median error value in every bin which contains ~ 33 meteors. The geometrical IP and LoS methods produce errors on the order of degrees for $Q_c < 15°$, while the Monte Carlo and MPF methods restrict the radiant error below $1°$ even for very low values of Q_c. Although the deceleration is not directly observable for such all-sky systems, the estimated speeds at different stations at low convergence angles do not match when geometrical methods are used. The Monte Carlo and MPF methods, in contrast, are designed to "find" the solution which satisfies both the spatial and dynamical constraints. As an example, figure 4.13 shows length vs. time of a low Q_c synthetic Geminid estimated by the LoS method (left inset) and the Monte Carlo method (right inset). Note that in all the convergence angle plots, the IP and LOS-FHAV use the same approach to compute speed and hence overlap exactly in the speed error (bottom) plots and are not separately observable in these figures.

Next, we investigated a moderate field of view (CAMS-like) system. As with the all-sky
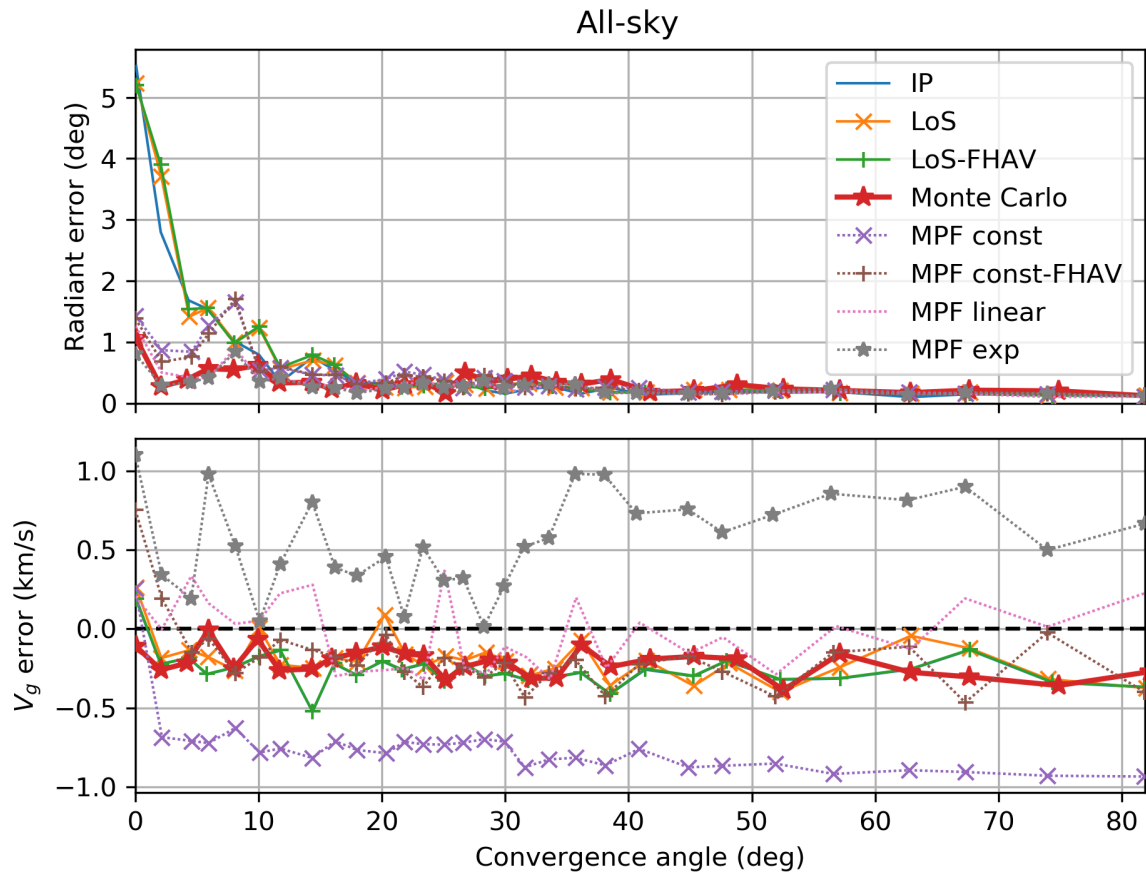
Figure 4.12: Radiant and velocity error as a function of convergence angle for 1000 Geminids simulated for an all-sky (SOMN-like) system.
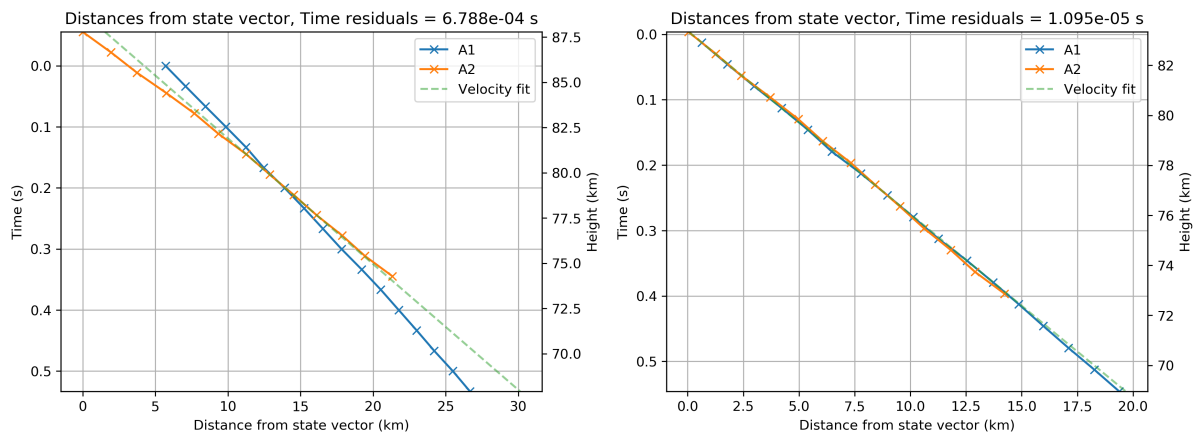
Figure 4.13: Length as a function of time of a low Q_c Geminid estimated with the LoS method (left) and the Monte Carlo method (right).
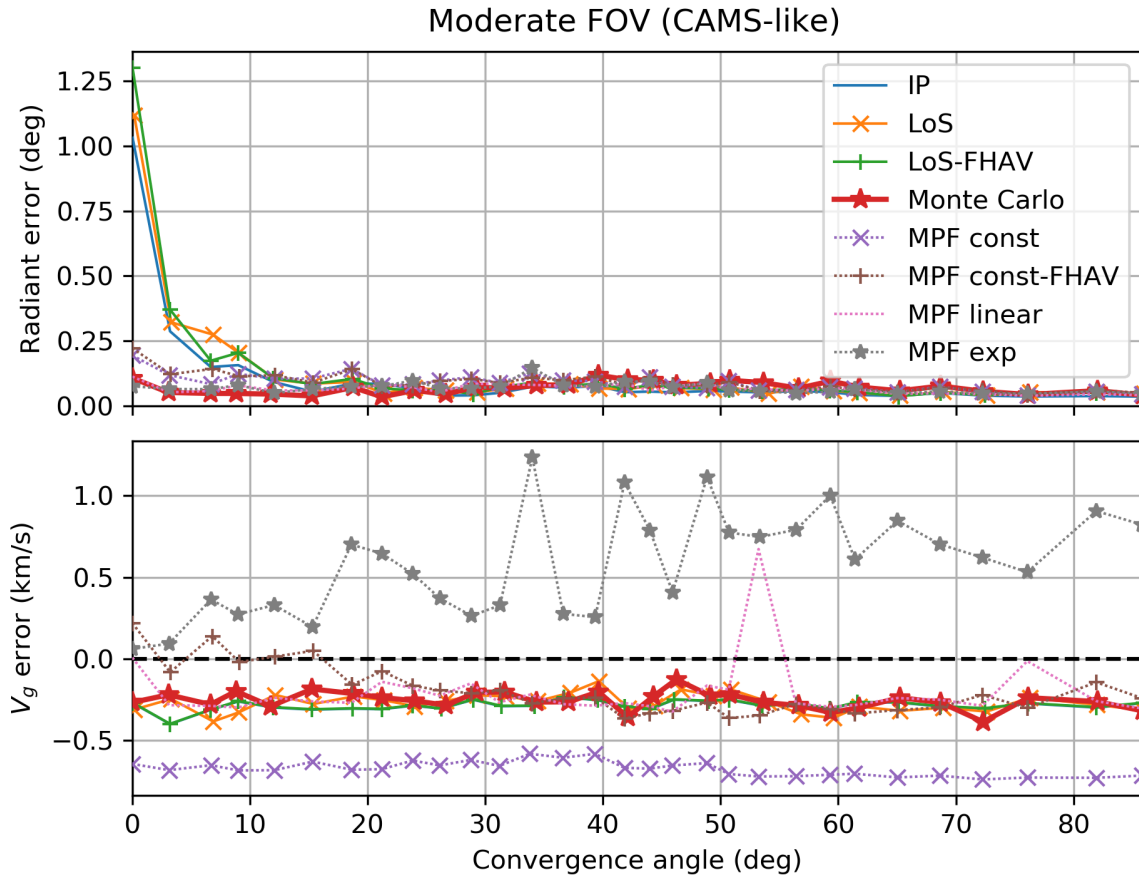
Figure 4.14: Radiant and velocity error vs convergence angle for 1000 Geminids simulated for a moderate field of view (CAMS-like) system.

system, only two stations were used in this analysis, as three-station solutions always have large convergence angles. As seen in figure 4.14, all trajectory solvers have a similar radiant error of ~0.1° for $Q_c > 10°$. For smaller convergence angles, the IP and LoS solvers produce errors on the order of 1°. On the other hand, the MPF and Monte Carlo solvers produce robust radiant solutions throughout. The velocity error is less strongly correlated with the convergence angle, but is completely dominated by solver-specific biases. In particular, the MPF-exp overestimates the initial velocity across all convergence angles, a product of the poorly conditioned convergence of this kinematic model. We are roughly able to reproduce the results of Jenniskens et al. (2011), where they found that geometrical methods work well for $Q_c > 25°$, and that MPF methods produce good radiant convergences even down to $Q_c \sim 2°$.
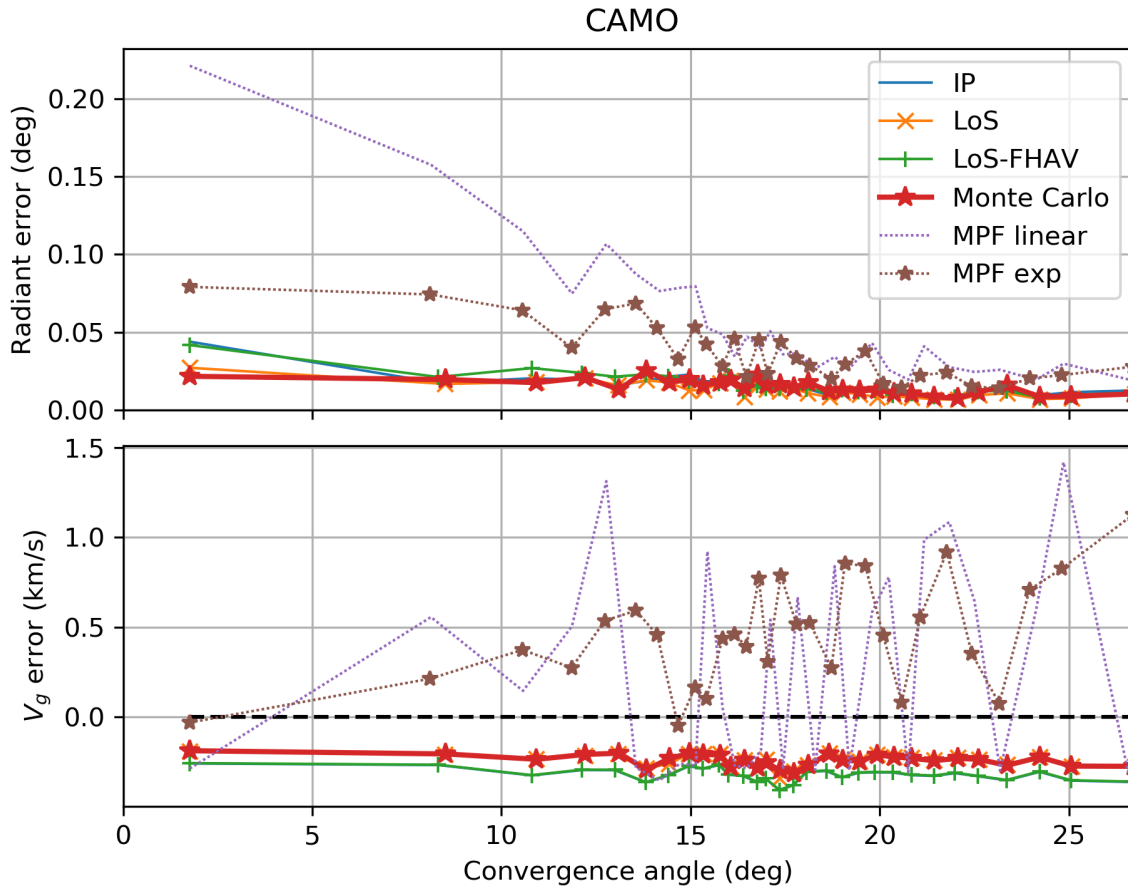
Figure 4.15: Radiant and velocity error as a function of convergence angle for 1000 Geminids simulated for the CAMO system.

Finally, figure 4.15 shows the dependence of radiant and velocity errors on the convergence angle for the CAMO system. The results of the MPF method with the constant velocity model are excluded because it produces very large errors since it fails to model the deceleration visible at the fine angular resolution of a CAMO-like system. Due to the limited geometry of the CAMO system, the maximum expected convergence angle is less than $30°$, but the solutions using the IP, LoS and Monte Carlo solvers are very stable even down to $Q_c \sim 1°$. The poorer performance of the MPF-methods for this system, particularly in reconstructing initial speed, likely reflect the high precision of CAMO which requires a more physical kinematic model than the empirical models used in the MPF approach.

4.3.5   The 2015 Taurid outburst - high-precision all-sky observations

In 2015 the Taurids displayed an activity outburst due to Earth encountering a resonant me-
teoroid swarm locked in a 7:2 resonance with Jupiter (Asher & Clube, 1993; Spurnỳ et al.,
2017). Securing accurate observations of fireballs for this resonant branch for the first time
is significant for planetary defence as the branch was also shown to contain asteroids on the
order of several 100s of meters in size. As the Earth encounters this swarm at regular intervals
it may be a major contributor to the overall impact hazard and supports some elements of the
proposed coherent catastrophism theory (Asher et al., 1994).

Spurnỳ et al. (2017) attribute the discovery of the Taurid branch, linked to the swarm return
in 2015, to the precision measurements made possible by their high-resolution all-sky digital
cameras and careful manual reduction of the data. Figure 14 in Spurnỳ et al. (2017) shows
that all meteoroids in the resonant swarm reside in a very narrow range of semi-major axes
(the extent of the 7:2 resonance given by Asher & Clube, 1993). This is arguably the strongest
evidence yet published for the real existence of the branch and swarm as the semi-major axis
is very sensitive to measurement errors in meteor velocity. Olech et al. (2017) also noticed a
possible connection to the 7:2 resonance, but their results were not as conclusive due to the
lower measurement accuracy.

Data for the outburst have only been published for fireball-sized meteoroids and we focus
on simulating these for comparison to measurements published in Spurnỳ et al. (2017). In this
section we investigate the precision needed to make a discovery of this nature and discuss the
limits of low-resolution all-sky systems.

We used the parameters of the Taurid meteoroid stream resonant branch as given in Spurnỳ
et al. (2017) and simulated 100 meteors from the branch as they would be detected by an
SOMN-like all-sky system. We only simulated meteors with the semi-major axis inside the
narrow region of the 7:2 resonance which spans 0.05 AU.

Figure 4.16 shows the comparison between the simulated semi-major axes and computed
values using various trajectory solvers for a three station SOMN-like system. As can be seen,
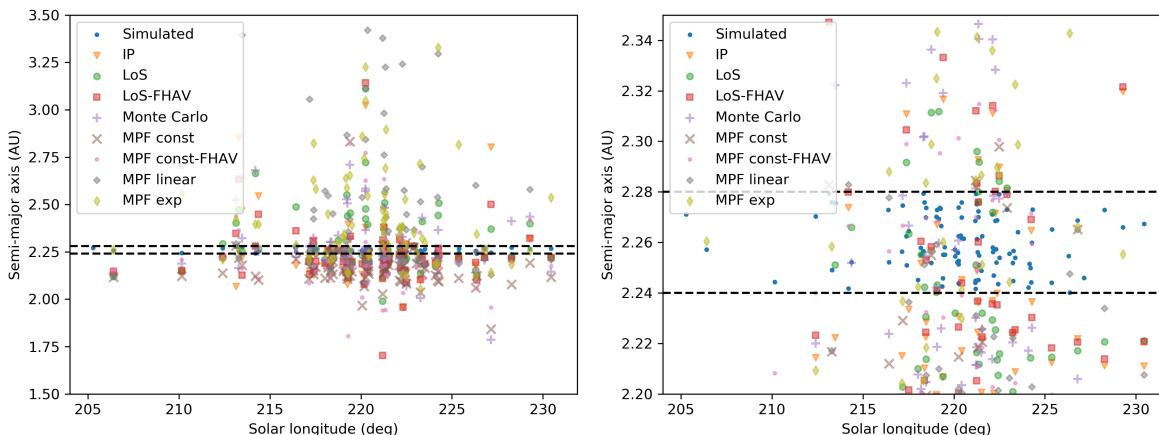
Figure 4.16: The semi-major axes of simulated 2015 Taurids from the resonant branch (blue dots bound within black dashed lines) and comparison with values estimated using different trajectory solvers. The right plot shows a narrower range of semi-major axes.

the observed scatter in a is too large to detect the branch with any solver using such low-quality data. This shows that existing low-resolution all-sky systems (circa 2019) have limited utility for any orbital determination (on a per camera basis) requiring high precision but are better suited to shower flux estimation or meteorite recovery. Deployment of higher resolution all-sky systems (Spurnỳ et al., 2006; Devillepoix et al., 2018) which can achieve a radiant precision on the order of 1 arc minute are clearly preferable for any orbit measurements requiring high accuracy.

4.3.6   Influence of gravity on trajectories of long-duration fireballs

The orbits of meteorite-dropping fireballs are of special interest as knowing their velocities allows a statistical estimate of the source region in the main asteroid belt and linkage to possible parent bodies (Granvik & Brown, 2018). Because these fireballs may remain luminous for long durations, often 5 or more seconds, their trajectories can be precisely estimated using data even from low-precision all-sky systems. This is due to the large number of observed points available in the data reduction. On the other hand, these events experience the largest gravitational bending of the trajectory, e.g. after 5 s the drop due to gravity is on the order

of 100 m. They violate the linear trajectory assumption implicit in many solvers. In extreme cases, Earth grazing fireballs may last for tens of seconds and their path (ignoring deceleration) is a hyperbola with respect to the Earth's surface, requiring a special approach to solve (e.g. Ceplecha, 1979; Sansom et al., 2019). Here we explore which trajectory solver is best for these long fireballs and investigate the influence of gravitational bending on the radiant precision.

As the parameter space of possible radiants and lengths of possible meteorite-dropping fireballs is beyond the scope of this paper, we use as a single case-study a specific fireball that was observed above Southwestern Ontario on September 23, 2017 by 3 stations of the SOMN. The fireball was first observed at 75 km and ended at 35 km, lasting 6.5 s. It entered the atmosphere at an angle of 30° from the ground and with an initial velocity of 14 km s^{-1}.

Simulations were performed using the estimated radiant and the velocity, but the initial positions of the fireball were randomly generated inside the fields of view of the simulated all-sky network to cover a wide range of geometries. The dynamics of the fireball were simulated by using the linear deceleration meteor propagation model. The deceleration prior to detection was not included in the simulation because these bright fireballs do not significantly decelerate prior to generating a visible trace in a video system (Vida et al., 2018). The duration of the fireball was set to 6.5 s, the time of the beginning of deceleration t_0 was randomly generated in the range [0.3, 0.6] of the total duration of the fireball, and the deceleration was randomly generated in the range [1500, 2750] m s^{-2}, which was comparable to the observed event, although the real deceleration was of course not constant.

Due to the large range of simulated starting points, not all of the 100 simulated fireballs were observed in full. Only those simulations in which all stations observed the fireball for at least 4 s where chosen, bringing the number down to 74 simulated meteors. Table 4.8 gives the comparison of the performance of various solvers applied to this simulated data. The estimated trajectories were quite precise because of the long duration, thus it was decided to constrain the failure window of interest to $\Delta_{Rmax} = 0.5°$, $\Delta_{Vmax} = 0.5$ km s^{-1}. We justify the reduction of these constraints compared to the SOMN constraints used above by the higher

Table 4.8: Trajectory solver performance for a simulated long-duration fireball observed by a three station all-sky system. The trajectory was incorporated in the simulation statistics if the convergence angle was larger than 5° - we use a lower threshold in this case due to the larger average duration of the event, which in turn means that there are more points for trajectory estimation. F is the percentage of failures (total of 74 meteors), i.e. the percentage of radiants that were outside the $\Delta_{Rmax} = 0.5°$, $\Delta_{Vmax} = 0.5\,\mathrm{km\,s^{-1}}$ window.

Solver	Fireball		
	F (%)	σ_R	σ_V
IP	22%	0.18°	$0.03\,\mathrm{km\,s^{-1}}$
LoS	8%	0.07°	$0.02\,\mathrm{km\,s^{-1}}$
LoS-FHAV	11%	0.13°	$0.02\,\mathrm{km\,s^{-1}}$
Monte Carlo	12%	0.09°	$0.03\,\mathrm{km\,s^{-1}}$
MPF const	92%	0.32°	$0.07\,\mathrm{km\,s^{-1}}$
MPF const-FHAV	89%	0.22°	$0.07\,\mathrm{km\,s^{-1}}$
MPF linear	50%	0.09°	$0.02\,\mathrm{km\,s^{-1}}$
MPF exp	88%	0.37°	$0.24\,\mathrm{km\,s^{-1}}$

number of observed points (thus better fits), and the fact that Granvik & Brown (2018) indicate that the precision of a fireball's initial velocity should be estimated to around $0.1\,\mathrm{km\,s^{-1}}$ for the statistical distribution of initial source regions to be stable.

The best performing solver was the Borovička (1990) LoS method with the initial velocity estimated using our newly proposed sliding fit and including compensation for gravity. The expected radiant precision is around 4 arc minutes, while the initial velocity can be estimated to within $20\,\mathrm{m\,s^{-1}}$. Figure 4.17 shows the 2D histogram of errors for all estimated trajectories. The Monte Carlo solver performs slightly worse, but we haven't manually chosen the solution based on the existence of directionality of the $f_{\Delta t}$ function, as proposed in Paper 1. On the other hand, MPF solvers have a high failure rate, even the MPF solver with the linear deceleration model which should have been able to exactly estimate the trajectory parameters.

Next, we investigated the radiant accuracy if the compensation for the curvature due to gravity was not taken into account, i.e. the term $\Delta h(t_{kj})$ was kept at 0 (see Paper 1 for details). Figure 4.18 shows an offset of about 0.15° from the true radiant, caused by the shift of the estimated radiant towards the local zenith. We point out that these results were obtained on simulated data which ignore any other forces acting on the meteoroid (which are expected to
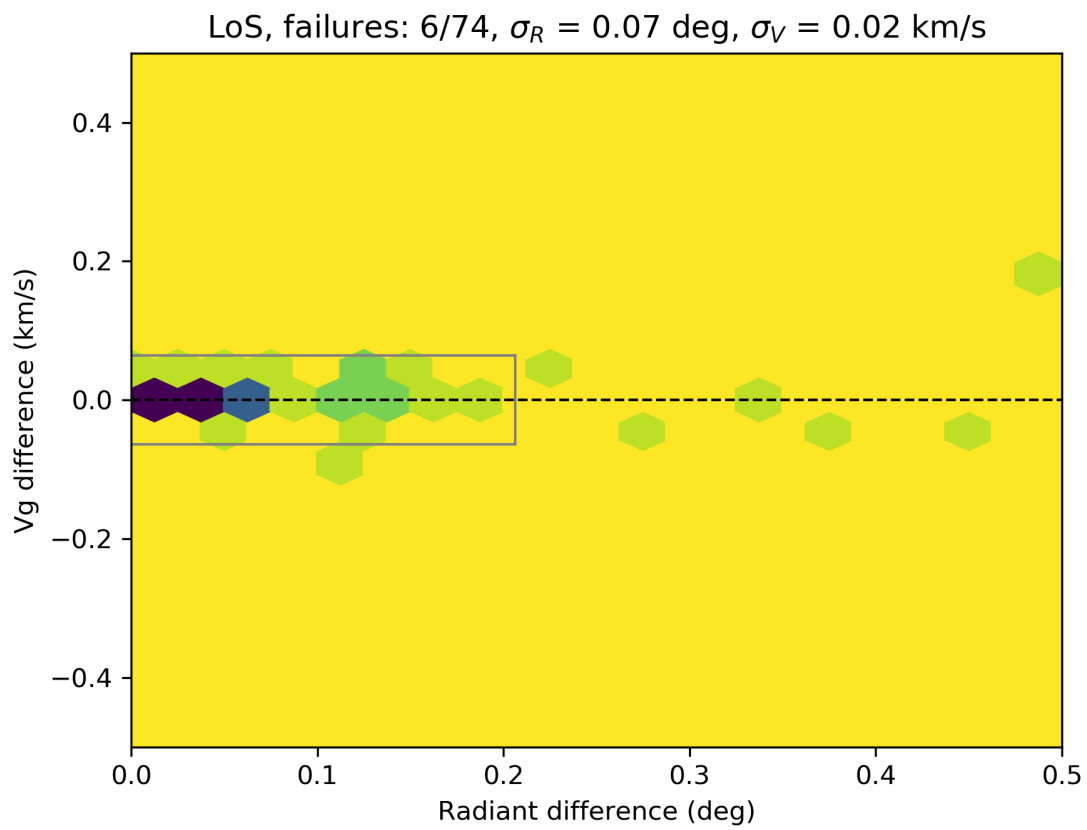
Figure 4.17: Accuracy of geocentric radiants for simulated fireballs. The solutions were done using the LoS method.
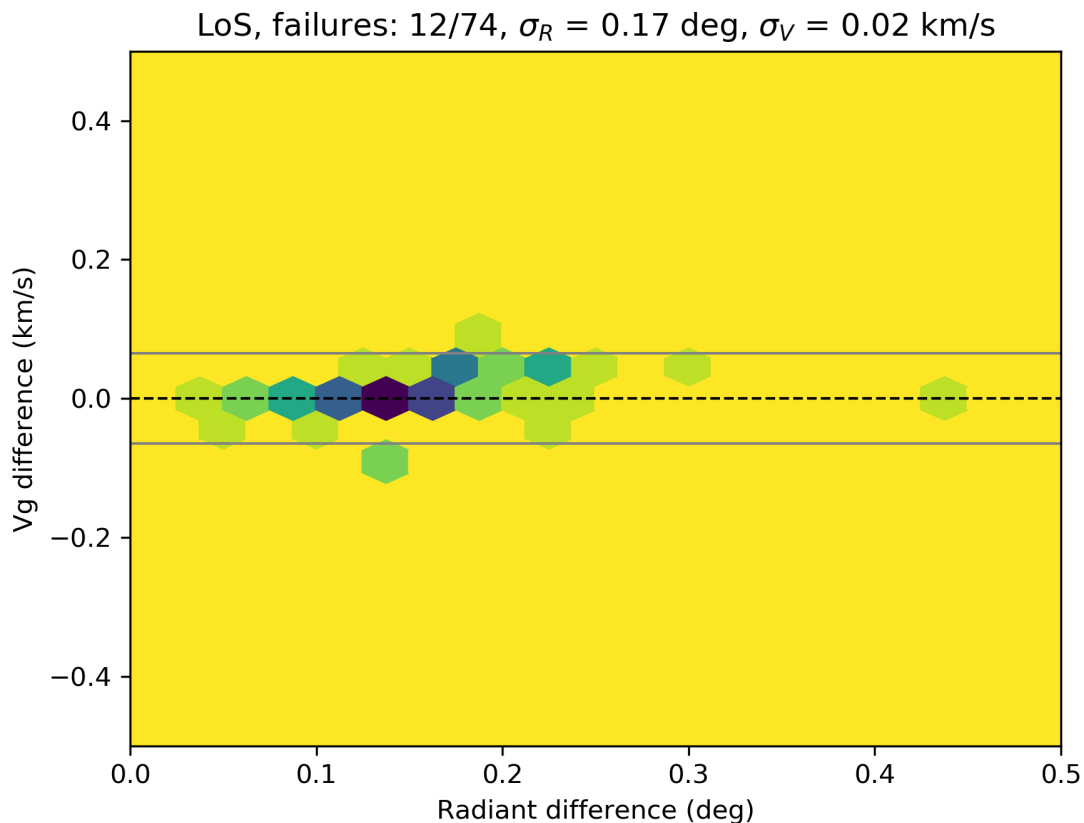
Figure 4.18: Accuracy of geocentric radiants for a simulated long-duration fireball. The solutions were done using the LoS method, with the option of compensating for the curvature due to gravity turned off.

be negligible in any case), which demonstrate that the curvature of the trajectory due to gravity should be compensated for directly during trajectory estimation, as it otherwise produces a significant bias in the direction of the radiant. This becomes more pronounced with the increasing duration of the fireball. Alternatively, an analytic zenith attraction correction could be developed (separate from the zenith attraction correction for computing geocentric radiants) which is dependent on the geometry and the duration of the fireball.

4.3.7 Estimated radiant error and true accuracy

In this final section we investigate if the radiant error estimated as the standard deviation from the mean accurately describes the true magnitude of the error. We do not investigate the ve-

locity error estimate, because the accuracy of pre-atmosphere velocity for smaller meteoroids is entirely driven by deceleration prior to detection (Vida et al., 2018), causing a systematic underestimate of top of atmosphere speeds.

Using the results of the Monte Carlo solver, we compute the angular separation θ between the estimated and the true geocentric radiant used as simulation input, and divide it by the hypotenuse of standard deviations in right ascension and declination:

$$\sigma_{err} = \frac{\theta}{\sqrt{(\sigma_\alpha \cos \delta)^2 + \sigma_\delta^2}}. \tag{4.1}$$

The value of σ_{err} indicates how many standard deviations from the mean the true radiant is. In an ideal case where the errors would be correctly estimated, the distribution of σ_{err} values for all trajectories would follow a truncated normal distribution with a standard deviation of one.

In practice, the errors seem to be on average underestimated by a factor two across all nine combinations of systems and showers. Figure 4.19 shows the cumulative histogram of σ_{err} values for 1000 simulated Geminids for a CAMS-like system. We fit a truncated normal distribution using the maximum-likelihood method to σ_{err} values and report standard deviations for all showers and systems in table 4.9. It appears that the truncated normal distribution is not representative of the underlying distribution of σ_{err} values, although its standard deviation is a rough proxy for the scale of the error underestimation. We also fit a χ^2 distribution which appears to be better suited (p-values are consistently high).

Regarding CAMO, the real radiant errors are 2 to 4 times larger than estimated, as seen in figure 4.20 which shows the error analysis for simulated Draconids. These results indicate that for a robust understanding of errors, a detailed analysis must be done for each system and shower using the shower simulator.
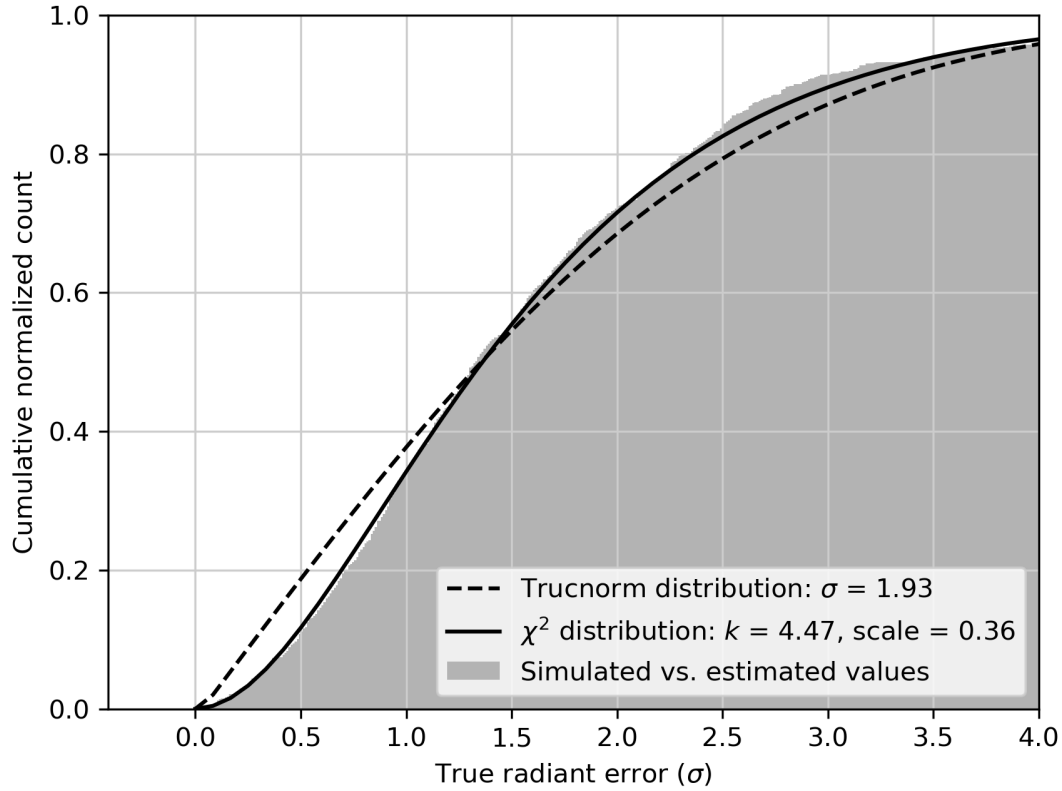
Figure 4.19: Quality of error estimation for a CAMS-like system and 1000 Geminids.

Table 4.9: Parameters of fitted truncated normal and χ^2 distributions to values of σ_{err} for different simulated showers and systems. σ is the standard deviation of fitted truncated normal distributions (it can be considered as a rough proxy for the magnitude of error underestimation), and "k" and "scale" are parameters of the χ^2 distribution.

Shower	DRA		GEM		PER	
	σ	k, scale	σ	k, scale	σ	k, scale
All-sky	2.37	3.23, 0.57	2.03	3.99, 0.42	2.43	4.70, 0.45
CAMS	2.02	4.61, 0.37	1.93	4.47, 0.36	2.02	6.37, 0.28
CAMO	3.57	12.00, 0.33	3.74	4.82, 0.67	2.35	2.84, 0.61
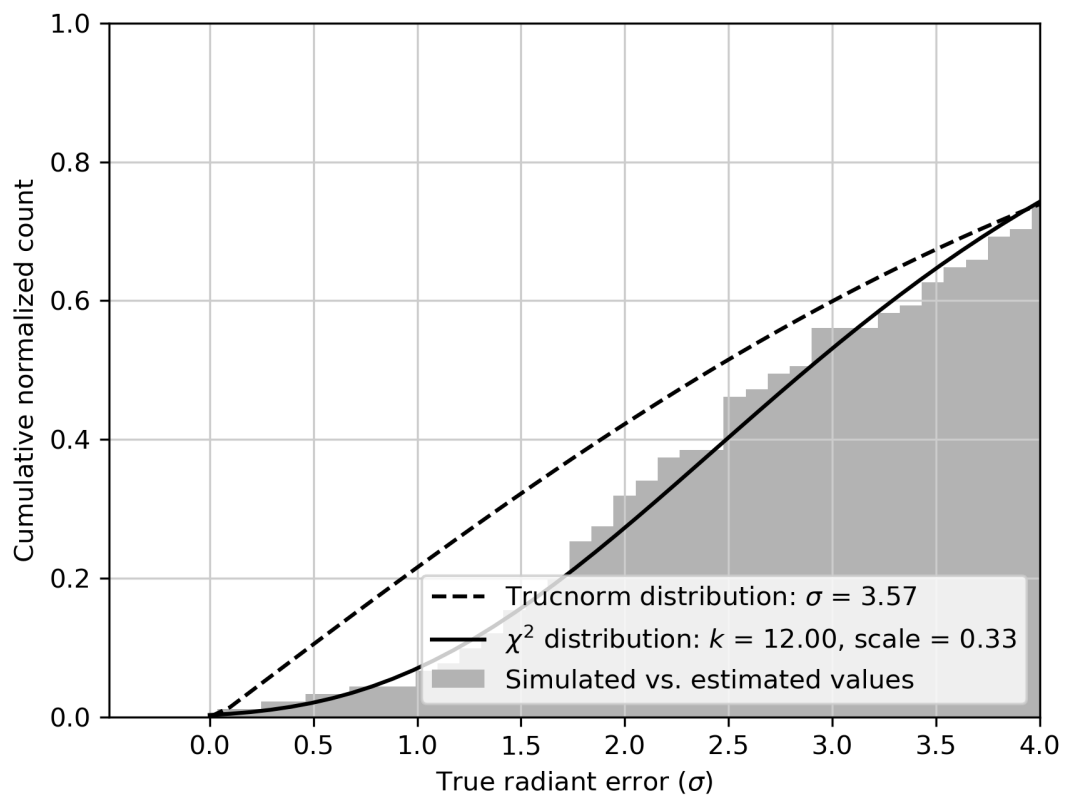
Figure 4.20: Quality of error estimation for CAMO and 100 Draconids.

4.4   Conclusion

In Paper 1 (Vida et al., 2020) we described and implemented in Python several trajectory solvers. In this paper we have applied each solver in turn to synthetic meteors with radiants, speeds, and physical properties appropriate to the Draconids, Geminids and the Perseids as they would be recorded by various simulated meteor observation systems. While we have generically investigated solver performance for common optical systems, the simulator allows for detailed simulation of individual real-world meteor observing systems and estimation of the measurement accuracy of meteor showers or individual events of interest. While we summarize some major trends of our simulation comparisons, it is important to emphasize that these results pertain only to the geometry and number of cameras assumed for each simulated system and shower. Ideally, for real observations, simulations would be repeated for specific geometries and camera systems on a per event basis.

With this caveat in mind, based on our simulations, the following is a summary of which trajectory solver performed best for our chosen showers for each meteor observation system:

- All-sky systems (SOMN-like) - As meteor deceleration is not usually seen by these systems, the MPF method with the constant velocity model produces the most robust fits and estimates radiants the most precisely, to within $0.25°$. The method significantly underestimates the initial velocity, but if a correct deceleration correction is applied an accuracy of $\sim 250\,\mathrm{m\,s^{-1}}$ could be achieved.

- Moderate field of view systems (CAMS-like) - The intersecting planes and the lines of sight methods produce good results overall when employed in conjunction with more advanced methods of initial velocity estimation, because meteor deceleration becomes visible at the resolutions of such systems. The Monte Carlo solver results are comparable to these solvers and does not provide further improvement of the solution except for meteors with low convergence angles. We recommend using this solver operationally for these systems. The MPF methods improve the radiant precision, but their estimates

of the initial velocity are a factor or 2 worse than with other methods. The expected average radiant and velocity accuracy is around $0.1°$ and $100\,\mathrm{m\,s^{-1}}$, provided the pre-detection deceleration correction from Vida et al. (2018) is used.

- The CAMO, high-precision system which observes meteor dynamics (deceleration) well - The Monte Carlo and LoS solvers perform the best. The expected average radiant accuracy is around $0.01°$ and $50\,\mathrm{m\,s^{-1}}$, provided the pre-detection deceleration correction from Vida et al. (2018) is used. The MPF approach enforces meteor propagation models which are mismatched to the actual deceleration behavior, resulting in fits with larger errors for these high angular and temporal resolution measurements.

- Meteoroid physical properties strongly influence the velocity accuracy. Meteoroids of asteroidal origin have a factor of 2 higher velocity uncertainties due to larger deceleration, a conclusion previously reported in Vida et al. (2018).

We show that a minimum radiant accuracy of order 3 to 6 arc minutes ($0.05°$ - $0.1°$) is needed to measure the true radiant dispersion of younger meteor showers. This value was derived by simulating the 2011 Draconids outburst, a year where the encounter with recently ejected meteoroids having a very low dispersion. With the use of an appropriate trajectory solver, this accuracy can be achieved using moderate FOV and CAMO resolution systems, i.e. systems with the angular resolution better than 3 arc-minutes per pixel (assuming a real precision of around 1 arc-minute is achievable through centroiding).

Simulation of the accuracy of low-precision all-sky systems with approximately 20 arc-minute per pixel angular resolution, shows that they are not precise enough to observe structures in meteor showers such as the Taurid resonant branch (Spurnỳ et al., 2017). For accurate orbital measurements we strongly suggest installation of more precise all-sky systems with angular resolutions approaching or exceeding one arc-minute per pixel so that the velocity accuracy of less than $0.1\,\mathrm{km\,s^{-1}}$ can be achieved, as recommended by Granvik & Brown (2018). We show that compensation for trajectory bending due to gravity should be taken into account

for longer fireballs (> 4 seconds) due to its significant influence on the radiant accuracy, as noted earlier by Ceplecha (1979) and Sansom et al. (2019).

Finally, we investigated the quality of our radiant error estimation approach by comparing estimated errors to known absolute error from the simulation input. We find that radiant errors are underestimated by a factor of 2 for all-sky and CAMS-like systems, and by a factor of 3 to 4 for CAMO.

Bibliography

Asher, D., & Clube, S. 1993, Quarterly Journal of the Royal Astronomical Society, 34, 481

Asher, D., Clube, S., Napier, W., & Steel, D. 1994, Vistas in Astronomy, 38, 1

Beech, M. 2002, Monthly Notices of the Royal Astronomical Society, 336, 559

Beech, M., & Nikolova, S. 1999, Meteoritics & Planetary Science, 34, 849

Blaauw, R., Campbell-Brown, M., & Weryk, R. 2011, Monthly Notices of the Royal Astro-
nomical Society, 414, 3322

Borovička, J. 1990, Bulletin of the Astronomical Institutes of Czechoslovakia, 41, 391

Borovička, J., Koten, P., Shrbenỳ, L., Štork, R., & Hornoch, K. 2014, Earth, Moon, and Planets,
113, 15

Borovička, J., Koten, P., Spurnỳ, P., et al. 2009, Proceedings of the International Astronomical
Union, 5, 218

Borovička, J., Spurnỳ, P., & Koten, P. 2007, Astronomy & Astrophysics, 473, 661

Brown, P., & Jones, J. 1998, Icarus, 133, 36

Brown, P., Marchenko, V., Moser, D. E., Weryk, R., & Cooke, W. 2013, Meteoritics & Plane-
tary Science, 48, 270

Brown, P., Weryk, R., Kohut, S., Edwards, W., & Krzeminski, Z. 2010, WGN, Journal of the
International Meteor Organization, 38, 25

Campbell-Brown, M., & Koschny, D. 2004, Astronomy & Astrophysics, 418, 751

Ceplecha, Z. 1979, Bulletin of the Astronomical Institutes of Czechoslovakia, 30, 349

—. 1987, Bulletin of the Astronomical Institutes of Czechoslovakia, 38, 222

Ceplecha, Z., Borovička, J., Elford, W. G., et al. 1998, Space Science Reviews, 84, 327

Ceplecha, Z., & ReVelle, D. 2005, Meteoritics And Planetary Science, 40, 35

Devillepoix, H. A., Bland, P. A., Sansom, E. K., et al. 2018, arXiv preprint arXiv:1808.09195

Egal, A., Gural, P., Vaubaillon, J., Colas, F., & Thuillot, W. 2017, Icarus

Everhart, E. 1985, in Dynamics of Comets: Their Origin and Evolution, ed. A. Carusi & G. B.
    Valsecchi (Dordrecht: Kluwer), 185–202

Granvik, M., & Brown, P. 2018, Icarus, 311, 271

Gural, P., & Šegon, D. 2009, WGN, Journal of the International Meteor Organization, 37, 28

Gural, P. S. 2012, Meteoritics & Planetary Science, 47, 1405

Jenniskens, P. 1994, Astronomy and Astrophysics, 287, 990

Jenniskens, P., Gural, P., Dynneson, L., et al. 2011, Icarus, 216, 40 . `http://www.`
    `sciencedirect.com/science/article/pii/S0019103511003290`

Jenniskens, P., Nénon, Q., Albers, J., et al. 2016, Icarus, 266, 331

Kero, J., Fujiwara, Y., Abo, M., Szasz, C., & Nakamura, T. 2012, Monthly Notices of the Royal
    Astronomical Society, 424, 1799

Koten, P., Vaubaillon, J., Tóth, J., Margonis, A., & Ďuriš, F. 2014, Earth, Moon, and Planets,
    112, 15

Moorhead, A. V., Blaauw, R. C., Moser, D. E., et al. 2017, Monthly Notices of the Royal
    Astronomical Society, 472, 3833

Moser, D., Suggs, R., Swift, W., et al. 2011, in Meteoroids: The Smallest Solar System Bodies,
    142

Olech, A., Żołądek, P., Wiśniewski, M., et al. 2017, Monthly Notices of the Royal Astronomi-
    cal Society, 469, 2077

Pecina, P., & Ceplecha, Z. 1983, Bulletin of the Astronomical Institutes of Czechoslovakia, 34,
    102

—. 1984, Bulletin of the Astronomical Institutes of Czechoslovakia, 35, 120

Sansom, E. K., Jansen-Sturgeon, T., Rutten, M. G., et al. 2019, Icarus, 321, 388

Šegon, D., Andreić, Ž., Gural, P. S., et al. 2014, Earth, Moon, and Planets, 112, 33

Spurnỳ, P., Borovička, J., Mucke, H., & Svoreň, J. 2017, Astronomy & Astrophysics, 605, A68

Spurnỳ, P., Borovička, J., & Shrbenỳ, L. 2006, Proceedings of the International Astronomical
    Union, 2, 121

Trigo-Rodríguez, J. M., Madiedo, J. M., Williams, I. P., et al. 2013, Monthly Notices of the
    Royal Astronomical Society, 433, 560

Vaubaillon, J., Watanabe, J., Sato, M., Horii, S., & Koten, P. 2011, WGN, Journal of the IMO,
    39, 3

Vida, D., Brown, P. G., & Campbell-Brown, M. 2018, Monthly Notices of the Royal Astro-
    nomical Society, 479, 4307

Vida, D., Gural, P. S., Brown, P. G., Campbell-Brown, M., & Wiegert, P. 2020, Monthly No-
    tices of the Royal Astronomical Society, 491, 2688

Vida, D., Šegon, D., & Merlak, A. 2019, e-Zine for meteor observers meteornews. net, 22

Weryk, R., Campbell-Brown, M., Wiegert, P., et al. 2013, Icarus, 225, 614 . http://www.
    sciencedirect.com/science/article/pii/S0019103513001905

Weryk, R. J., & Brown, P. G. 2013, Planetary and Space Science, 81, 32 . `http://www.sciencedirect.com/science/article/pii/S0032063313000718`

Whipple, F. L., & Jacchia, L. G. 1957, Smithsonian Contributions to Astrophysics, 1, 183

Wiegert, P., Vaubaillon, J., & Campbell-Brown, M. 2009, Icarus, 201, 295

Ye, Q., Brown, P. G., Campbell-Brown, M. D., & Weryk, R. J. 2013, Monthly Notices of the Royal Astronomical Society, 436, 675

Chapter 5

A new method for measuring the meteor mass index: application to the 2018 Draconid meteor shower outburst

A version of this chapter has been published as:

5.1   Introduction

The Draconids are an annual meteor shower whose parent body is the Jupiter-family comet 21P/Giacobini-Zinner. The shower usually has very low activity with a Zenithal hourly rate (ZHR) of ~ 1 (Jenniskens, 2006). It produced large meteor storms in 1933 and 1946 and strong outbursts in a number of other years (Egal et al., 2019). Many of these outbursts were not predicted beforehand. The occasionally high intensity and unpredictability of the shower have

made it a focus of research, particularly as it can pose a significant impact risk to spacecraft in the near-Earth environment (Beech et al., 1995; Cooke & Moser, 2010; Egal et al., 2018).

In recent years, the shower has produced several notable outbursts. In 2011 an outburst was predicted in advance (Watanabe & Sato, 2008; Maslov, 2011; Vaubaillon et al., 2011) and was well observed using both radar (Kero et al., 2012; Ye et al., 2013a) and optical methods (Trigo-Rodríguez et al., 2013; Borovička et al., 2014; Koten et al., 2014; Šegon et al., 2014; Vaubaillon et al., 2015). That year the outburst reached a ZHR of 350, and had an average mass index of 2.0 ± 0.1, but this latter varied between 1.84 and 2.30 over 1hr during the peak (Koten et al., 2014).

In contrast, the 2012 outburst was not predicted and was only well observed by the Canadian Meteor Orbit Radar (CMOR) (Brown & Ye, 2012). The shower produced a meteor storm at radar sizes (ZHR $\approx$ 9000 ± 1000), but visual observers reported a ZHR almost two orders of magnitude lower, ZHR $\sim$ 200, suggesting a high mass-distribution index, that is, the stream was rich in small meteoroids. Unfortunately, due to the timing of the peak (maximum over central Asia) and unfavorable weather conditions elsewhere, no optical orbits associated with the outburst were secured. The 2012 outburst was also peculiar in that modeling suggested a very high (> 100 m/s) meteoroid ejection velocity from the parent comet was needed (Ye et al., 2013b).

The 2018 outburst was predicted by various authors (Kresák, 1993; Maslov, 2011; Ye et al., 2013b; Kastinen & Kero, 2017; Egal et al., 2018), but the predicted activity varied from weak (ZHR 10 - 20; Maslov, 2011) to possible meteor storm levels (Kastinen & Kero, 2017). The most recent work by Egal et al. (2018), which accurately reproduced most historic Draconid activity, predicted a peak ZHR of $\sim$ 80 at 00:00 UTC on October 9, 2018.

In this work we analyze 1.5 hours of optical observations from Southwestern Ontario just after the peak[1] of the 2018 outburst, from 00:00 UTC to 01:30 UTC. We also develop a novel method of population and mass index estimation, and compute these indices using our obser-

---

[1]According to visual observations in the IMO database: `https://www.imo.net/members/imo_live_shower?shower=DRA&year=2018`

vations. Finally, we compare model-predicted radiants with our multi-station observations and compute the shower flux.

5.2 Instruments and observations

Optical observations were conducted using low-light-level video systems in Southwestern Ontario, Canada, operated by the University of Western Ontario Meteor Physics Group. The observations started shortly after local sunset between October 8 and 9 at around 00:00 UTC and ended at 01:30 UTC due to cloudy weather – thus only a short period after the peak was observed.

The double station observations were made using four Electron Multiplying Charge Coupled Device (EMCCD) Nüvü HNü 1024 cameras[2] with Nikkor 50 mm f/1.2 lenses. The systems were operated at 32 frames per second, had a limiting stellar magnitude of $+10.0^M$, and a field of view of 15×15 degrees.

Despite clear skies in the region, none of the dozen Southern Ontario Meteor Network (SOMN) all-sky cameras (Brown et al., 2010) observed a single Draconid during all of October 8-9. These all-sky cameras have an effective limiting meteor magnitude of -2^M, qualitatively suggestive of an absence of larger meteoroids in the falling branch of the outburst. The EMCCD cameras did observe many Draconid meteors, which we use in the following analysis. In this section we describe the EMCCD hardware and give details of the data-reduction procedure.

5.2.1 Electron Multiplying Charge Coupled Device systems

The Nüvü HNü 1024 EMCCD cameras are the most recent addition to the Canadian Automated Meteor Observatory (CAMO) systems (Weryk et al., 2013). These 16-bit cameras use electron multiplying technology to increase the number of electrons accumulated in the registers before

---

[2]`http://www.nuvucameras.com/fr/files/2019/05/NUVUCAMERAS_HNu1024.pdf`

they are amplified, digitized, and read out, which greatly increases the signal-to-noise ratio. In combination with a fast 50 mm f/1.2 lens, the single-frame limiting magnitude at 32 frames per second for stars is around $+10.0^M$, and $+7.5^M$ for meteors. The native resolution of the camera is 1024×1024 pixels, but the frames are binned to 512×512 to make the higher frame rate possible, which allows better trajectory precision. The data was saved to disk in the raw format, without any lossy compression. The field of view is $14.75° \times 14.75°$, and the pixel scale is 1.7 arcmin/pixel. All cameras were run at a gain setting of 200. These systems are more sensitive and have less noise than the previous generation of systems which relied on Gen III image intensifiers (Campbell-Brown, 2015). The cameras each have external Global Positioning System (GPS) timing directly encoded at the frame acquisition stage. Figure 5.1 shows a sample meteor captured with the EMCCD camera and Figure 5.2 shows the light curve of the same meteor. We highlight the agreement between the sites in range-corrected magnitudes (normalized to 100 km).

Two cameras are deployed at the each of the two CAMO sites in Southwestern Ontario. Cameras 01F and 01G are located at Tavistock (43.264 20° N, 80.772 09° W, 329 m), and 02F and 02G at Elginfield (43.192 79° N, 81.315 65° W, 324 m). The distance between the stations is about 45 km. Both pairs are pointed roughly north, one pair (the G cameras) at the elevation of 45 degrees, the other (F cameras) at 65 degrees. There was no volume overlap between the F and G cameras. One camera from each site had the Draconid radiant inside the field of view. We are aware that this geometry is not favorable, but the systems were a part of another long-term study and the pointing was thus not modified to preserve continuity. The EMCCDs captured a total of 92 double station Draconids ranging in peak magnitudes from $+1^M$ to $+6.5^M$, of which only 68 had complete light curves from at least one camera.
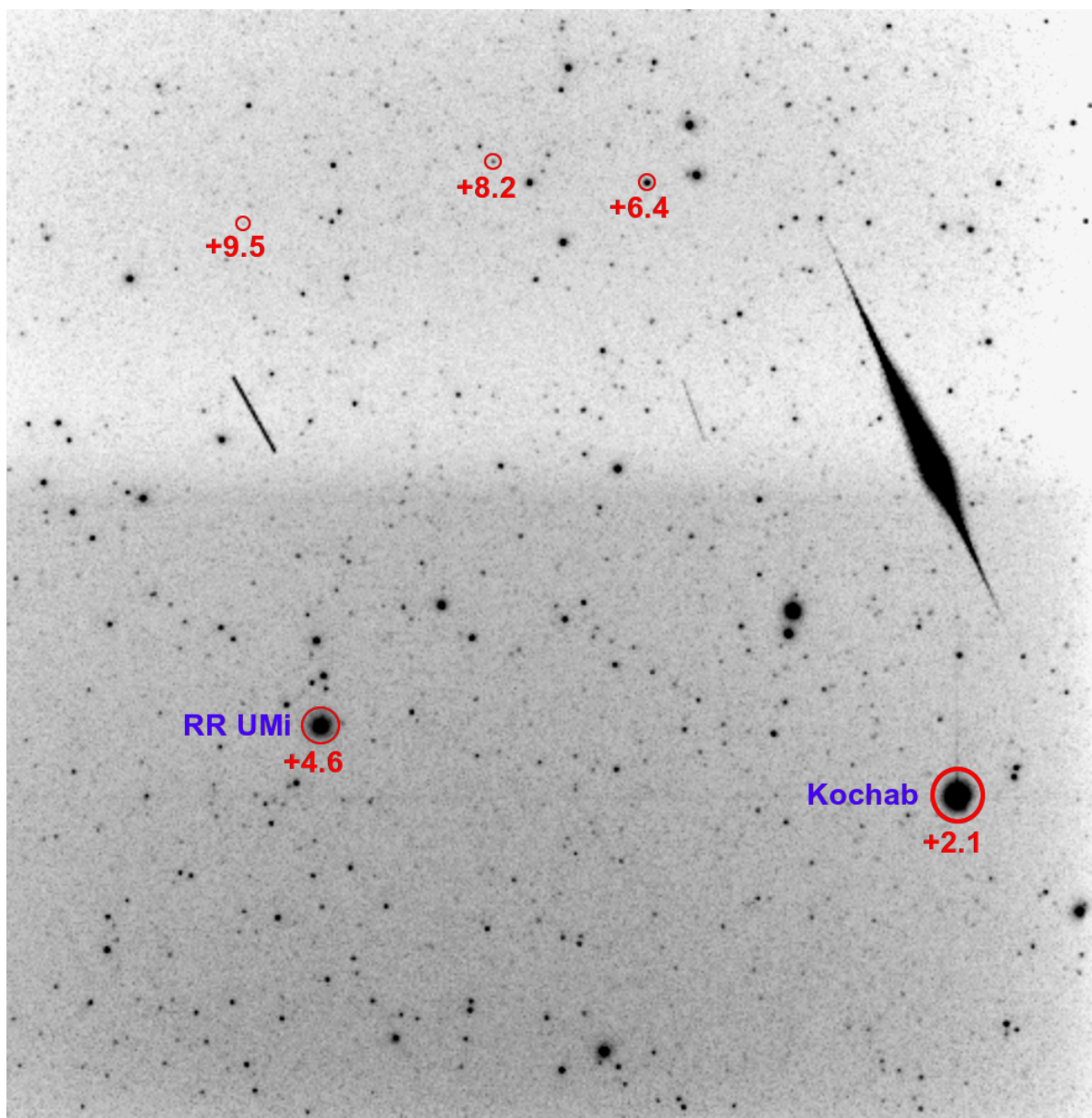
Figure 5.1: Stack of raw frames showing a $+1^M$ Draconid recorded with camera 01G on October 9, 2018 at 00:01:48 UTC. The meteor was first detected at an apparent magnitude of $+7.0^M$. V-band magnitudes of a selection of stars are shown as well. The vertical gradient of the image background is intrinsic to this specific camera and is compensated for by flat field correction during data reduction. The two thinner and fainter lines left of the meteor are satellites.
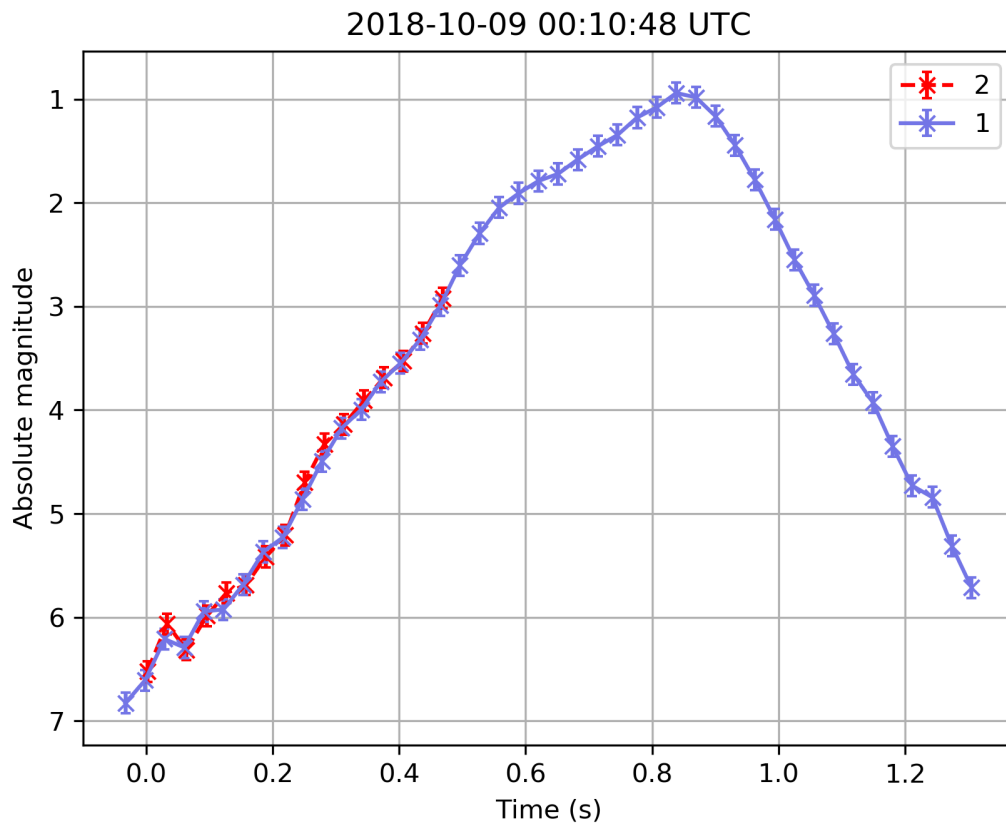
Figure 5.2: Absolute GAIA G-band magnitude light curve of the meteor in Figure 5.1. The error bars are ~ 0.1 magnitude. Observations from camera 01G (Tavistock) are shown in blue, and observations from camera 02G (Elginfield) are shown in red.

5.2.2 Data reduction and calibration

Using the tools available in the open-source RMS (Raspberry pi Meteor Station) library[3], automated meteor detection (described in detail in Vida et al., 2016) was run on all collected data and both the astrometric and photometric calibrations were performed manually. The automated detections were manually classified and only Draconids were extracted for further analysis.

The astrometric and photometric calibrations were done using the Gaia DR2 star catalog (Gaia Collaboration et al., 2018) as the GAIA G spectral band matches the spectral response of the EMCCDs well. We applied flat fields and bias frames to the video data using the method described in Berry & Burnell (2000). The average residuals of the astrometric calibration were $\sim 1/10$ pixels or ~ 10 arcseconds, and the accuracy of the photometric calibration was ± 0.1 mag. Figure 5.3 shows the photometric calibration, and Table 5.1 details the astrometric calibration for the 01F EMCCD camera.

---

[3]RMS GitHub web page: `https://github.com/CroatianMeteorNetwork/RMS`
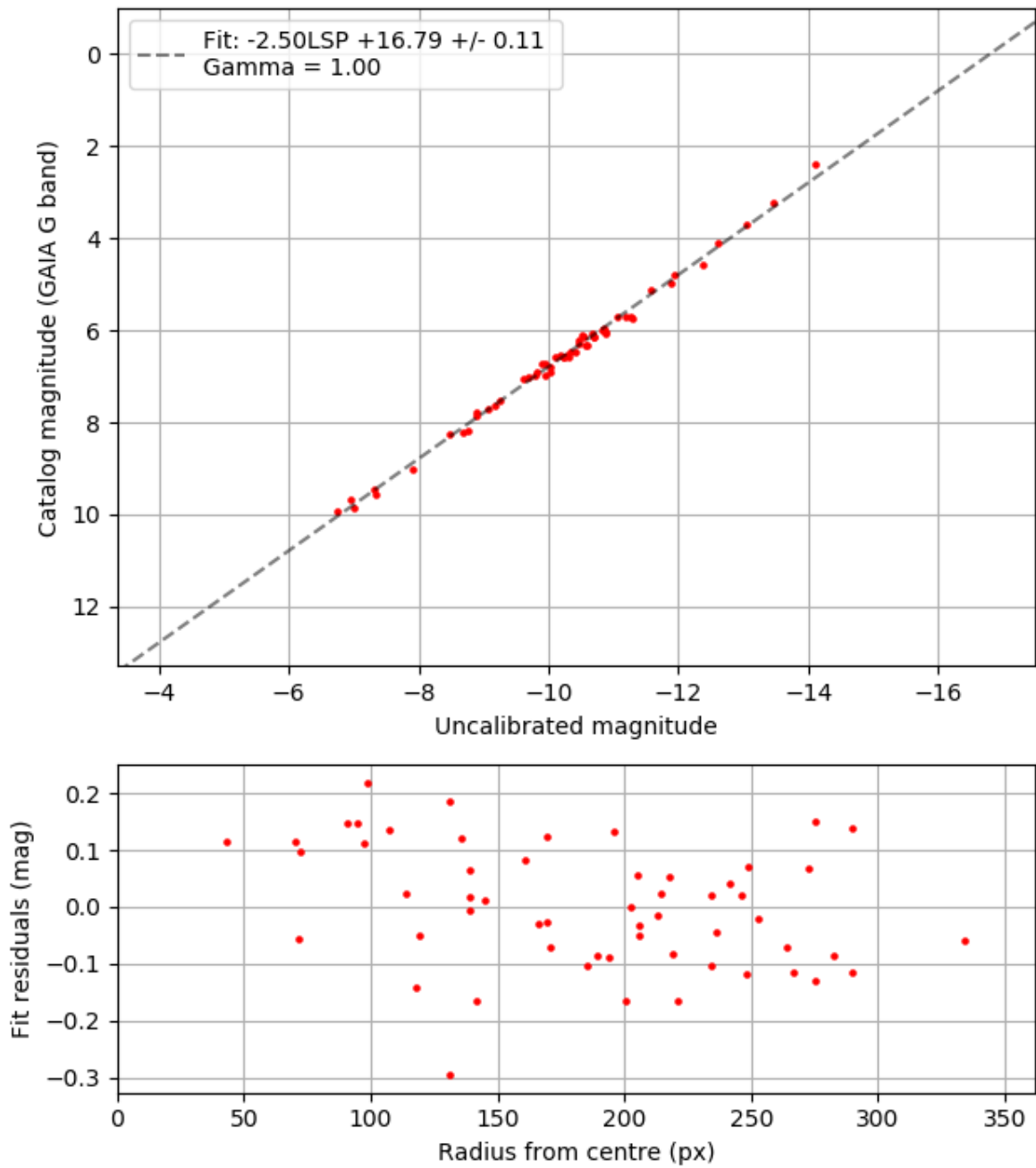
Figure 5.3: Photometric calibration of the 01F camera. The uncalibrated magnitude is simply $-2.5 \log_{10} I_s$, where I_s is the background-subtracted sum of pixel intensities of all star pixels (LSP in the figure). The sensor response was linear (Gamma = 1.0). The magnitudes of stars used for calibration ranged from $+2.3^M$ to 9.9^M.

Table 5.1: Example astrometric calibration for the 01F EMCCD camera. The estimated field of view was 14.75° × 14.75°. The average error was 0.08 px and 0.15 arc minutes. Img X and Y are star image coordinates on the chip, RA and Dec are equatorial coordinates in J2000, Mag is the GAIA G band magnitude, -2.5*LSP is the uncalibrated magnitude (LSP is the logarithm of the sum of pixel intensities), Cat X and Y are predicted catalog star positions in image coordinates, error columns are fit residuals in arc minutes and pixel, and θ is the angle of a vector pointing from the predicted to the measured star position. The photometric offset was +16.80 ± 0.11, but some stars used for photometry were not used for astrometry due to their smaller signal to noise ratio.

No	Img X (px)	Img Y (px)	RA (deg)	Dec (deg)	Mag	-2.5*LSP	Cat X (px)	Cat Y (px)	Error (arcmin)	Error (px)	Error θ (deg)
1	234.34	163.91	267.193	+48.836	+6.91	-10.02	234.50	163.97	0.29	0.17	+21.8
2	370.26	15.08	272.091	+44.113	+6.72	-9.95	370.31	15.06	0.10	0.06	-21.2
3	417.60	200.09	275.386	+49.122	+4.10	-12.62	417.56	200.10	0.16	0.04	+158.7
4	414.03	481.25	278.144	+57.046	+4.56	-12.37	414.02	481.28	0.02	0.03	+101.4
5	187.10	62.08	264.866	+46.006	+3.70	-13.03	187.16	61.96	0.22	0.13	-64.1
6	407.94	59.93	273.885	+45.209	+6.13	-10.53	407.93	59.93	0.11	0.02	+178.2
7	123.98	472.02	262.682	+57.877	+5.72	-11.05	124.05	472.06	0.12	0.08	+31.2
8	100.16	294.76	261.350	+52.790	+6.30	-10.57	100.17	294.77	0.02	0.01	+26.3
9	326.99	244.11	271.723	+50.823	+6.02	-10.87	326.98	244.12	0.10	0.02	+123.6
10	393.84	274.09	274.983	+51.348	+5.99	-10.82	393.82	274.09	0.12	0.02	+166.3
11	130.40	107.98	262.570	+47.403	+7.01	-9.69	130.46	108.11	0.28	0.15	+64.0
12	262.78	327.09	269.245	+53.444	+8.25	-8.48	262.84	327.19	0.34	0.11	+56.8

Table 5.1: continued.

No	Img X (px)	Img Y (px)	RA (deg)	Dec (deg)	Mag	-2.5*LSP	Cat X (px)	Cat Y (px)	Error (arcmin)	Error (px)	Error θ (deg)
13	185.98	263.89	265.341	+51.818	+5.70	-11.20	185.95	263.97	0.09	0.08	+113.6
14	344.09	278.87	272.756	+51.740	+6.99	-9.94	344.17	278.95	0.31	0.11	+45.8
15	260.64	89.92	268.004	+46.643	+6.08	-10.68	260.43	89.93	0.35	0.21	+176.2
16	372.69	231.22	273.677	+50.244	+7.85	-8.89	372.67	231.23	0.12	0.03	+157.8
17	92.56	381.21	260.991	+55.279	+7.69	-9.06	92.56	381.26	0.05	0.05	+80.9
18	181.62	192.91	264.950	+49.780	+6.58	-10.32	181.58	192.95	0.11	0.07	+136.5
19	289.11	467.85	271.500	+57.360	+6.58	-10.23	289.12	467.85	0.14	0.00	+44.8
20	89.87	441.60	260.844	+57.012	+6.46	-10.40	89.85	441.63	0.02	0.04	+118.2
21	452.50	314.07	278.047	+52.116	+6.55	-10.29	452.48	314.18	0.23	0.11	+105.6
22	485.15	102.90	277.345	+45.982	+7.04	-9.62	485.25	102.86	0.19	0.10	-21.0
23	491.59	327.00	279.970	+52.196	+5.97	-10.84	491.55	327.01	0.09	0.04	+167.3
24	21.27	282.99	257.628	+52.409	+6.27	-10.47	21.23	282.97	0.11	0.05	-153.8
25	23.80	190.04	257.918	+49.746	+6.14	-10.69	23.79	190.07	0.21	0.03	+105.6
26	73.40	134.86	260.142	+48.189	+6.23	-10.48	73.47	134.81	0.12	0.09	-36.6
27	68.41	34.63	259.962	+45.309	+6.57	-10.10	68.39	34.51	0.29	0.13	-96.3

Table 5.1: continued.

No	Img X (px)	Img Y (px)	RA (deg)	Dec (deg)	Mag	-2.5*LSP	Cat X (px)	Cat Y (px)	Error (arcmin)	Error (px)	Error θ (deg)
28	195.19	333.37	265.997	+53.802	+5.72	-11.28	195.18	333.44	0.18	0.07	+94.7
29	232.94	443.85	268.383	+56.873	+3.23	-13.47	232.89	443.75	0.29	0.11	-115.5
30	165.82	150.51	264.157	+48.586	+4.97	-11.89	165.81	150.62	0.11	0.11	+100.3
31	244.07	55.53	267.197	+45.700	+6.11	-10.51	244.16	55.46	0.20	0.12	-39.3
32	327.33	365.79	272.633	+54.288	+5.71	-11.26	327.35	365.72	0.06	0.08	-74.2
33	491.40	424.76	281.231	+54.897	+6.05	-10.87	491.48	424.57	0.30	0.21	-67.5
34	380.38	194.53	273.734	+49.159	+6.45	-10.33	380.49	194.43	0.22	0.15	-42.7
35	71.79	66.96	260.088	+46.241	+4.78	-11.94	71.72	66.98	0.14	0.07	+161.1
36	126.96	278.26	262.608	+52.301	+2.38	-14.11	127.01	278.21	0.15	0.08	-41.6
37	163.55	309.90	264.399	+53.172	+9.01	-7.92	163.53	309.75	0.27	0.15	-96.3
38	280.97	220.65	269.504	+50.324	+8.21	-8.69	280.87	220.56	0.29	0.14	-140.6
39	449.31	388.20	278.748	+54.209	+7.64	-9.17	449.28	388.35	0.23	0.15	+103.5
40	164.16	82.80	263.945	+46.642	+8.17	-8.75	163.97	82.90	0.37	0.21	+151.7
41	323.33	411.60	272.809	+55.611	+9.45	-7.31	323.34	411.65	0.05	0.05	+74.8
42	35.30	30.66	258.624	+45.187	+6.30	-10.01	35.35	30.71	0.12	0.08	+49.1

Table 5.1: continued.

No	Img X (px)	Img Y (px)	RA (deg)	Dec (deg)	Mag	-2.5*LSP	Cat X (px)	Cat Y (px)	Error (arcmin)	Error (px)	Error θ (deg)
43	15.62	488.13	256.793	+58.269	+6.90	-9.83	15.60	488.13	0.26	0.03	+177.5
44	13.33	400.72	256.952	+55.768	+6.53	-10.17	13.33	400.68	0.01	0.04	-85.5
45	416.91	103.96	274.575	+46.407	+6.74	-9.89	416.92	103.94	0.10	0.02	-70.7
46	351.89	364.77	273.815	+54.140	+6.56	-10.24	351.84	364.75	0.09	0.05	-158.5
47	494.27	388.18	280.871	+53.872	+6.15	-10.70	494.26	388.23	0.13	0.06	+104.8
48	468.06	25.16	276.000	+43.908	+5.72	-10.77	467.98	25.20	0.13	0.08	+155.9
49	491.94	42.70	277.079	+44.257	+7.12	-9.36	491.91	42.71	0.05	0.03	+162.6
50	400.40	344.59	275.950	+53.301	+6.33	-10.58	400.40	344.59	0.05	0.01	+45.8
51	81.12	316.66	260.439	+53.420	+5.11	-11.57	81.16	316.66	0.08	0.04	-3.3
52	312.67	28.33	269.867	+44.718	+7.79	-8.89	312.73	28.39	0.16	0.08	+50.5
53	168.60	438.58	264.986	+56.870	+6.99	-9.79	168.59	438.61	0.05	0.04	+101.5
54	468.69	238.67	277.966	+49.891	+7.51	-9.26	468.69	238.60	0.01	0.06	-94.0
55	260.70	369.63	269.380	+54.665	+6.80	-10.01	260.67	369.60	0.07	0.04	-135.3

5.3   Maximum likelihood estimation method of computing population and mass indices

Population and mass indices are essential for computing meteor shower fluxes and investigating their evolutionary history. It is usually assumed that the cumulative number of meteor peak magnitudes and the cumulative logarithm of the number of meteoroids above a certain mass threshold follow single power-law distributions.

Brown & Rendtel (1996) define the population index r as

$$r = \frac{N(M_v + 1)}{N(M_v)},$$

(5.1)

where $N(M_v)$ is the number of meteors with peak magnitude $M \leq M_v$.

Assuming that dN is the number of meteoroids with a range of masses between m and $m + dm$, McKinley (1961) defines the mass index s as

$$dN \propto m^{-s} dm.$$

(5.2)

The population and the mass index are the slopes of the best fit lines on a log-log (magnitude or logarithm of mass vs. logarithm of the number of meteors) cumulative distribution of magnitudes or masses. These lines can be simply parameterized as

$$f(x) = 10^{ax+b},$$

(5.3)

where x is either the magnitude (in case of the population index) or the logarithm of the mass (mass index). We note that we assume that the cumulative distribution is normalized to the $[0, 1]$ range.

Because all observation systems have some limiting sensitivity, the number of observed meteors is finite and detection efficiency drops off rapidly at magnitudes close to the limiting sensitivity. Thus there is only one part of the parameter space in which the power-law assump-

tion is valid. As a result, operationally a power law is only fit up to some limiting sensitivity x_{min}. A similar approach is used in other fields as well, although ways of estimating the value of x_{min} differ (Corral & González, 2019). Pokornỳ & Brown (2016) suggested fitting two parameters x_{min}, x_{max} which describe the range of magnitudes or radar echo amplitudes for which the linear approximation is valid. Pokornỳ & Brown (2016) argue that the addition of the upper boundary x_{max} is necessary as small-number statistics may skew the power law at larger amplitudes or masses. They used MultiNest (Feroz et al., 2009) to fit their model, an advanced Bayesian regression method which can also perform robust error estimation.

Note that it has historically been assumed that meteor peak magnitudes follow a power-law distribution, and that most of the terminology and data reduction procedures have been developed with this in mind. With the advent of low-light meteor cameras for which good photometric calibration can be obtained, we appeal to using photometric meteoroid masses instead, which should follow a power-law distribution.

In many studies (e.g., Brown et al., 2002), the meteoroid mass or population index is found by constructing a cumulative histogram and performing linear regression on binned data. This approach has many serious problems, as detailed in Clauset et al. (2009), the most important of which is that the result may change with histogram binning, especially when data sets with a small number of meteors are used. Molau et al. (2014) proposed a more advanced method capable of estimating the population index and the meteor flux at the same time. The drawback of this latter method is that it requires a running estimation of the meteor limiting magnitude from observations. Furthermore, it is constructed such that estimating the exact value of the population index is rather subjective, and no details of the error analysis are provided.

5.3.1   Description of the new method

To estimate the population and the mass index robustly, in a statistical manner, and with a reliable error estimate, we use the maximum likelihood estimation (MLE) method to fit a gamma distribution to the observed distribution of magnitudes and/or masses. This approach was in-

spired by the work of Clauset et al. (2009) where they question the validity of the power-law assumption in many real-world applications.

First, we tried to fit a Gumbel distribution to the mass distribution following Blaauw et al. (2016), but we found that it always produced fits with smaller p-values than the gamma distribution; under the null hypothesis the data and model distributions are identical.

Our choice of the gamma distribution for our probability distribution has a theoretical basis. If we assume that meteors appear at a rate λ per unit time, then the time between meteors follows an exponential distribution with rate λ while the total number of meteors in a given time span t follows a Poisson distribution $P(\lambda t)$. A gamma distribution $Gamma(n, \lambda)$ is the sum of independent exponentially distributed random variables, and describes the length of time needed to observe a number of meteors n (Akkouchi, 2008; Leemis & McQueston, 2008).

By replacing the time in this analogy with magnitude or mass, the theory still applies. Given a meteor rate per unit magnitude or mass (i.e., a population or mass index), a gamma distribution describes the distribution of magnitudes or masses one expects given a certain total number of meteors. In the special case where the rate is a constant in our chosen time interval, the sum can be simplified to an Erlang distribution. Because historical observations show that the mass index is not constant even on short timescales for certain showers (Koten et al., 2014), we use the more general gamma distribution.

We can show the above argument is correct quantitatively. We note that in the paragraph above we implicitly assume an exponential distribution, not a power law. The power law assumption for the distribution of meteoroid masses used in meteor astronomy comes from the foundational theoretical paper by Dohnanyi (1969) who assumed that when asteroids and/or meteoroids collide, the resulting fragment mass distribution follows a power law (Clauset et al., 2009)

$$p(x) = \frac{s-1}{x_{min}} \left(\frac{x}{x_{min}} \right)^{-s} , \tag{5.4}$$

where s is the scaling parameter (differential mass index in our example) and x_{min} is the lower

bound of the power-law behavior. The power-law assumption continues to propagate through the analytical derivation of Dohnanyi (1969), resulting in a population-wide differential mass distribution index of $s = 1.834$, assuming collisional steady-state conditions. Dohnanyi (1969) justified the use of the power law by appealing to the experimental work of Gault et al. (1963), who showed that the cumulative mass–size distribution of fragmented rock from craters formed by hyper-velocity impacts in the lab follows a power-law, a result confirmed in more recent experiments and simulations (e.g., Kun & Herrmann, 1996).

In reality, the number of meteors naturally tapers off as the limiting system magnitude is approached. This can be modeled as a power-law distribution with an exponential cutoff. Its probability density function $p(x)$ is given by Clauset et al. (2009):

$$p(x) = Cf(x),\tag{5.5}$$

$$f(x) = x^{-s}e^{-\lambda x},\tag{5.6}$$

$$C = \frac{\lambda^{1-s}}{\Gamma(1-s)},\tag{5.7}$$

where λ is the decay rate, $f(x)$ the basic functional form, C the normalization constant such that $\int_0^\infty Cf(x)dx = 1$, and Γ is the gamma function. If we define a shape parameter as $k = 1-s$, it can easily be shown that the resulting probability distribution is the gamma distribution

$$p(x) = \frac{\lambda^k x^{k-1} e^{-\lambda x}}{\Gamma(k)}.\tag{5.8}$$

Figure 5.4 shows a comparison of the cumulative density functions (CDFs) of a power law and those of a gamma distribution. Both distributions follow the same trend at smaller values, but the exponential tapering overwhelms the power-law component in the gamma distribution at around $x \sim 10^{-1}$ in this example. To estimate the power-law scaling parameter from the gamma distribution, one can compute the slope of the gamma CDF before the tapering becomes significant. In theory, one may derive the slope directly as $s = 1 - k$, but in practice

(especially when one works on a small data set) we find that this does not give robust estimates of population and mass indices. It appears that the fit sometimes prefers larger values of s which it compensates for by using larger values of λ. For that reason, we develop a more robust method described below.

We use the gamma distribution MLE fit from the functions in the Python `scipy` library[4]. We refer readers to the documentation of the `scipy` library for details. The Python source code of our new method can be found in the Western Meteor Python Library[5] under `wmpl/Analysis/FitPopulationAndMassIndex.py`.

Figure 5.5 shows an example of the gamma distribution fit to meteor magnitude data. After the fit is performed, the inflection point in the probability density function (PDF) is found (the minimum of the first derivative of the PDF). This inflection point is taken as the limiting sensitivity at which data are complete; this means that the number of meteors has started decreasing at this point purely due to sensitivity losses. In our approach, the inflection point is used as an anchor; it indicates that the optimal position where the slope of the population or mass index should be estimated is at brighter magnitudes or larger masses from that point.

We operationally define the optimal reference point x_{ref} for: the population index, as one magnitude brighter than the inflection point; and for the mass index, as 0.4 dex larger in mass than the inflection point – a 0.4 dex in mass roughly corresponds to the difference of one meteor magnitude (Vida et al., 2018).

Assuming an 8-bit camera is used to capture meteor data, it gives $\log_{2.512} 256 \approx 6$ magnitudes of dynamic range. As shown by the examples below, the data are often not complete for the faintest three magnitudes, leaving only three magnitudes before reaching the point of saturation. One magnitude brighter than the completeness magnitude is a rough midpoint between the point of completeness and sensor saturation, allowing for some leeway in case the saturation point is shifted because of different meteor angular speeds.

---

[4]Gamma function, `scipy` library: `https://docs.scipy.org/doc/scipy/reference/generated/scipy.stats.gamma.html`

[5]WMPL source code: `https://github.com/wmpg/WesternMeteorPyLib`
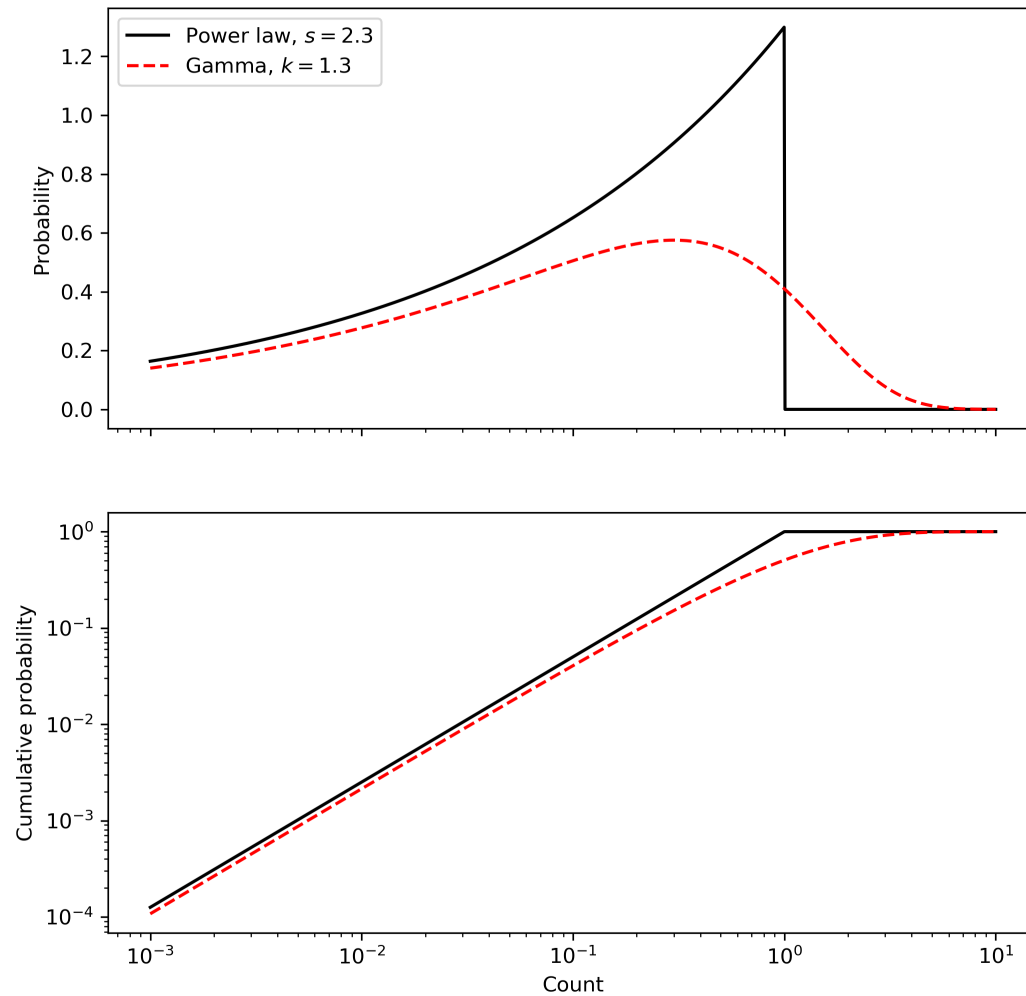
Figure 5.4: Comparison of the probability and cumulative density function for a power law and a gamma function. An exponent of $s = 2.3$ is used. Note that the greatest difference between the two distributions is in their tails.

The mass index s or the population index r can then be computed from the slope a of the log survival function S (i.e., complementary cumulative distribution function) of the gamma distribution at the reference point x_{ref} as

$$a_s = 10^{-\frac{d}{dx} \log S_s(x_{s,ref})},$$ (5.9)

$$s = 1 + a_s,$$ (5.10)

$$a_r = 10^{-\frac{d}{dx} \log S_r(x_{r,ref})},$$ (5.11)

$$r = 10^{a_r},$$ (5.12)

where S_s and $x_{s,ref}$ are fit to logarithms of mass, and S_r and $x_{r,ref}$ are fit to magnitudes. Given a generic cumulative density function $F(x)$, the survival function $S(x)$ is simply

$$S(x) = 1 - F(x),$$ (5.13)

and we compute the derivative in a numerically. The intercept b in equation 5.3 can be computed as

$$b = \log S(x_{ref}) + a x_{ref}.$$ (5.14)

The two-sample Kolmogorov-Smirnov test is used to compute the p-value which we use as a measure of goodness of fit.

Next, we compute the effective meteor limiting magnitude or mass l_m used in flux estimation as a point where the line $f(x) = 10^{ax+b}$ is equal to the normalized cumulative value of 1, i.e., $F(x) = 1$

$$l_m = -b/a.$$ (5.15)

We find that this approach is equivalent to the method of Blaauw et al. (2016) who take the

mode of the fitted Gumbel distribution as the effective limiting magnitude. We suggest that estimating the limiting meteor magnitude directly from meteor data is preferable to estimating it using the stellar limiting magnitude and then applying angular velocity corrections, as our approach naturally includes all observational and instrumental biases.

The uncertainty of measured slopes is estimated using the bootstrap method (Ivezić et al., 2014, page 140). The input data set is resampled with replacement, with the sample size being equal to the size of the input data set, and the fit is repeated on the sample. The procedure is repeated 1000 times and population or mass indices are computed for each run. Slopes that are outside 3 sigma of the mean are rejected, and the resulting standard deviation is reported as the uncertainty.

We note that in this work we assumed that the distribution of peak magnitudes is continuous, and not binned. This is valid for masses because they are computed from integrated meteor light curves with tens of points, and thus any magnitude binning due to measurement uncertainty is mitigated. Furthermore, we also assume that the magnitudes are not binned because hundreds of pixel values are added together to compute the meteor intensity on every video frame, thus all intensity quantization is smoothed out. Finally, our implementation of the method automatically shifts the data to x_{min} (the smallest number in the data set), as equation 5.8 is only defined for $x > 0$.

5.3.2 Testing the method

Figure 5.5 shows the distribution of peak magnitudes of 2604 manually reduced double station sporadic meteors captured by the Canadian Automated Meteor Observatory's (CAMO) influx camera (Weryk et al., 2013). The data set covers a period between June 2009 and August 2014, and only those meteors which had complete light curves (i.e., both the beginning and the end was visible inside the field of view of at least one camera) were used in the analysis. We note that imposing the visibility criterion was essential, as including meteors with partially observed tracks produced a bimodal magnitude distribution which greatly skewed the results. Although

the CAMO influx camera is not used for the analysis of the Draconids, we use this high-quality data set used in previous work (e.g., Campbell-Brown, 2015) to demonstrate the robustness of the method. The system has a meteor limiting magnitude of $+5.5^M$, but using our approach we find that the data set is complete only up to magnitude $+3.2^M$, indicated by the inflection point, while the population index is estimated at magnitude $+2.2^M$.

Figure 5.6 shows the cumulative distribution of peak magnitudes and the line representing the tangent to the log cumulative distribution function of the fitted gamma function. The estimated slope of the line, that is, the population index, is $r = 2.55 \pm 0.06$, which is consistent with other studies which have measured the expected yearly average sporadic population index from video data (e.g. Molau, 2015). We note that the estimated slope follows the data histogram well. If the slope was to be estimated at the inflection point, the population index would be $r = 2.20$ and the slope would significantly deviate from the data histogram.

Figures 5.7 and 5.8 show the distribution of masses and the cumulative histogram of masses for the same CAMO data set. The computed mass index of $s = 2.18 \pm 0.05$ is very consistent with expected values from other authors (e.g., Blaauw et al., 2011a). We note that Pokorný & Brown (2016) used the same data set, but their algorithm fitted a line to the histogram on the part after the inflection point, slightly reducing the value of the mass index to $s = 2.09$.

Due to the large number of data points, the estimate of the mass index of sporadic meteors can be accurately estimated, but often in practice, only tens of shower meteors are available. To demonstrate the robustness of the method, we estimate the mass index from 38 Geminids (all observed in 2012 within $0.5°$ of solar longitude around the peak) from the CAMO influx data set (Figures 5.9 and 5.10). The fit is much more uncertain, but the estimated value of the mass index for the Geminids is $s = 1.70 \pm 0.14$, which is consistent with previous work (Jones & Morton, 1982; Arlt & Rendtel, 2006; Blaauw et al., 2011b).

In the examples above, the p-values derived using the Kolmogorov-Smirnov test are larger than 0.05, which means that the null hypothesis that the model fits well to the data cannot be rejected with a 95% confidence level in any of the cases, even for the Geminids with a small
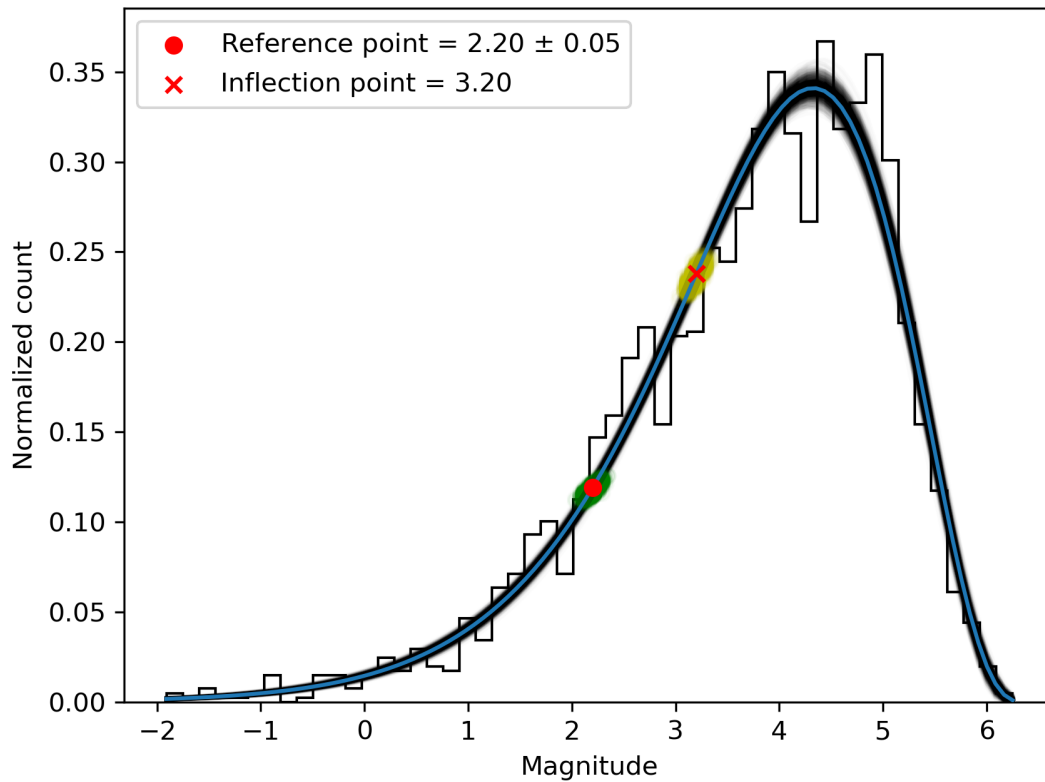
Figure 5.5: Distribution of peak R-magnitudes of sporadic meteors from the CAMO influx camera (histogram) and the gamma distribution fit (blue line is the main fit, black lines are all Monte Carlo runs). Equation 5.8 was used for the fit, and x in the equation is the meteor peak magnitude.

The jaggedness of the histogram is due to the limited precision of the magnitudes in the data file. The yellow shaded area around the inflection point represents the uncertainty in the inflection point location, and the green shaded area the uncertainty around the reference point.
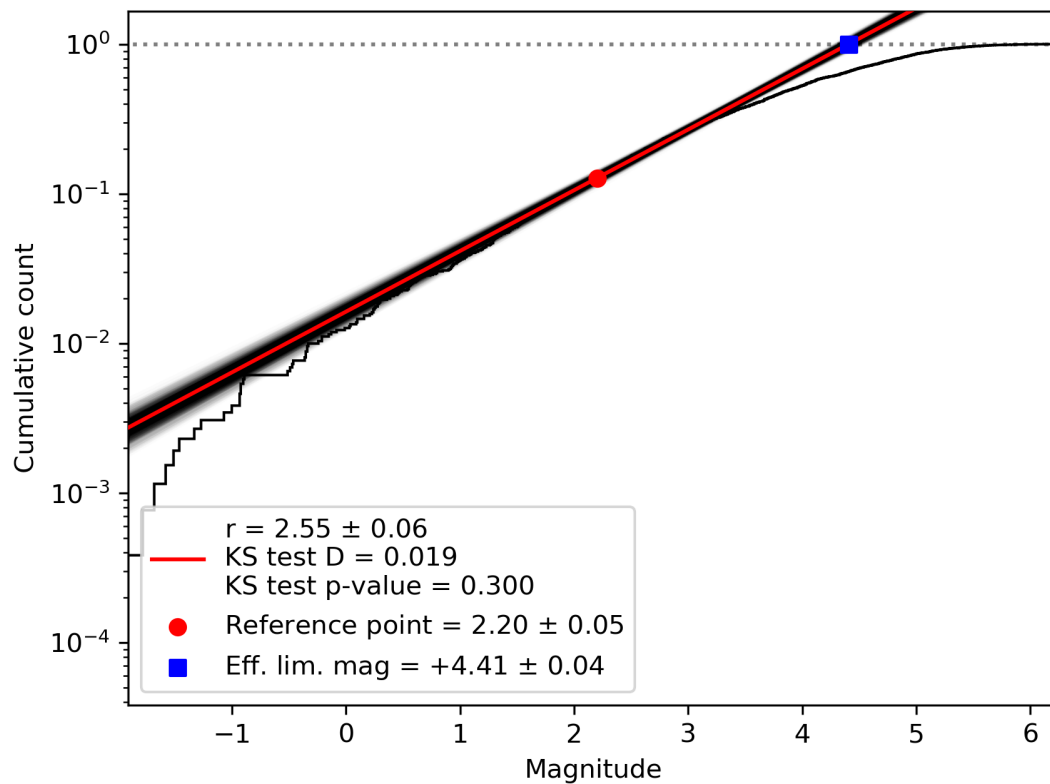
Figure 5.6: Cumulative distribution of peak magnitudes of sporadic meteors captured by the CAMO influx camera. The population index r was computed from the fitted gamma distribution using equation 5.9. The red line indicates the slope of the fitted population index, the jagged line is the histogram of the data, and black lines are all slopes estimated during the bootstraping uncertainty estimation procedure.
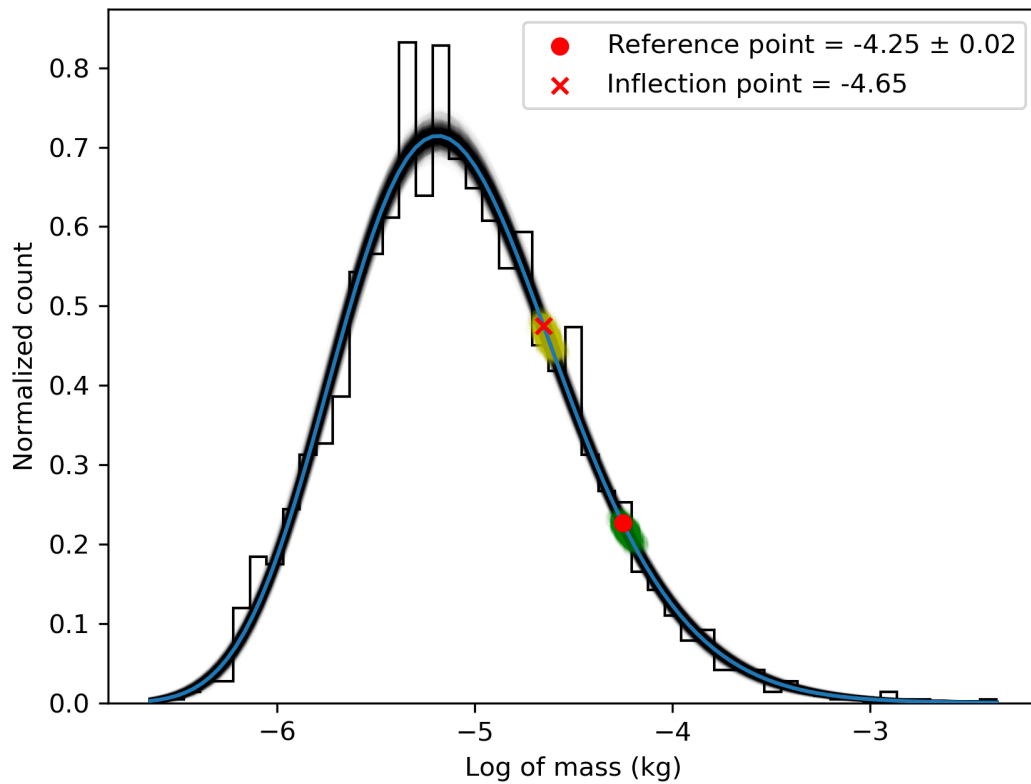
Figure 5.7: Distribution of masses of sporadic meteors from the CAMO influx camera (histogram) and the gamma distribution fit (blue line). The mass index s was computed from the fitted gamma distribution using equation 5.9. Black lines are all slopes estimated during the bootstraping uncertainty estimation procedure. Masses were computed using a fixed dimensionless luminous efficiency $\tau = 0.7\%$.
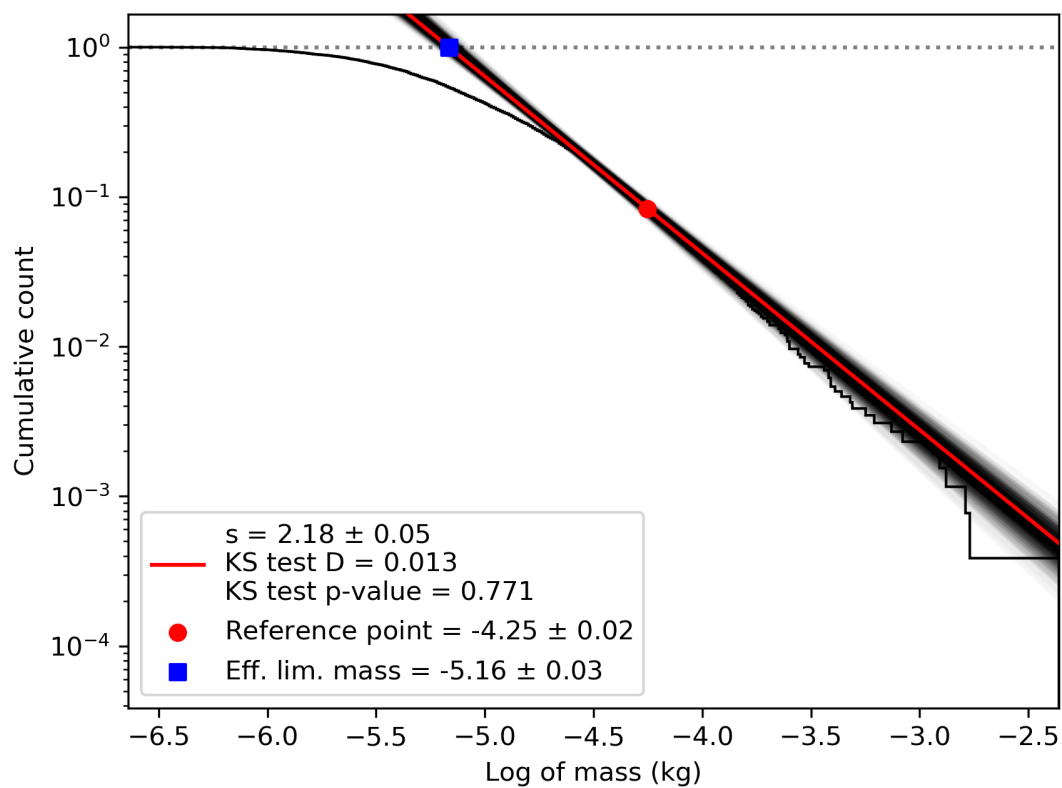
Figure 5.8: Cumulative distribution of masses of sporadic meteors from the CAMO influx camera. The red line indicates the slope of the fitted mass index, while the shaded black lines represent the Monte Carlo fits of the resampled set as described in the text.
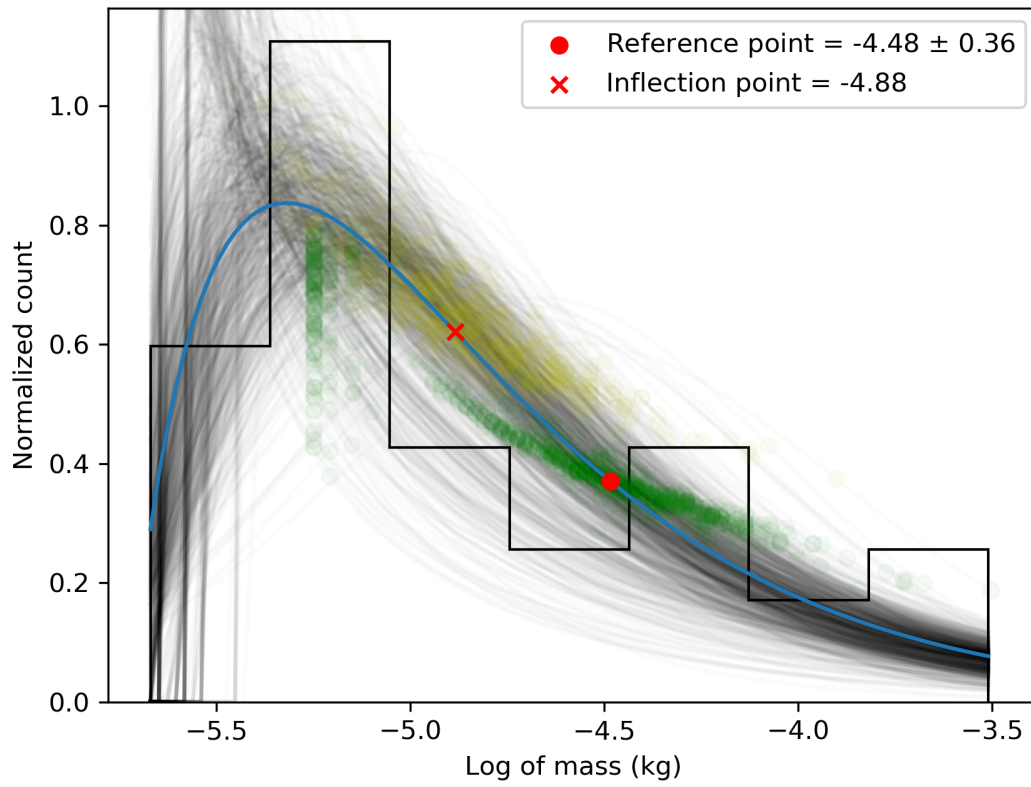
Figure 5.9: Distribution of masses of 38 Geminid meteors from the CAMO influx camera and the gamma distribution fit. See Fig 5.5 caption for the explanation of plot details.
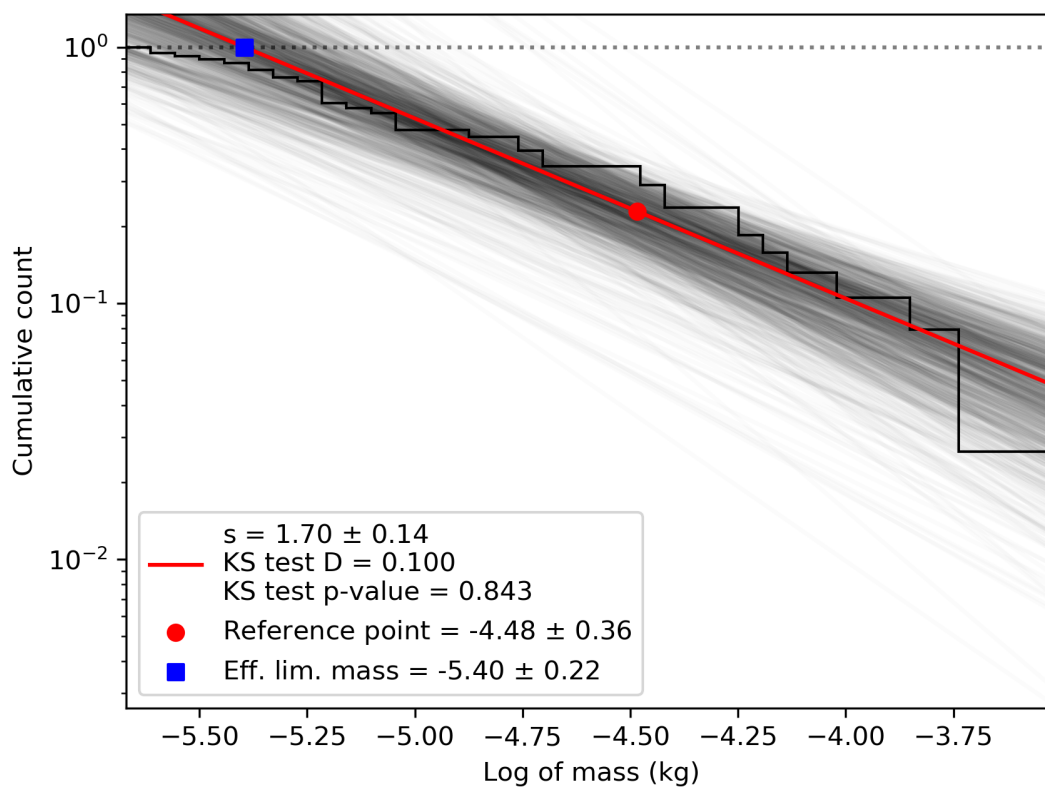
Figure 5.10: Cumulative distribution of masses of 38 Geminid meteors from the CAMO influx camera. The line indicates the slope of the fitted mass index. See Fig. 5.5 caption for the explanation of plot details.

number of meteors. This suggests that our theoretical assumptions are valid.

We investigated how the population and the mass index of sporadic meteors change throughout the year using the new method. The results are shown in Figures 5.11 and 5.12. The data were divided into ten bins of equal number of meteors (around 260 in each bin) but of variable ranges of solar longitudes. Large variations in both population and mass index can be seen at these optical meteoroid sizes, variations that are larger than the fairly stable values in radar sizes (Blaauw et al., 2011a; Pokornỳ & Brown, 2016) but following the same trend. The variations and features in the population index are comparable to those derived from visual data by Rendtel (2004), except after $\lambda_\odot > 250°$ where the number of CAMO observations is very low due to bad weather conditions in winter and large bins of solar longitude had to be used. In Figure 5.12, the mass index estimated using our novel method is plotted as a solid line, and the mass index computed from the population index using the classical relation $s = 1 + 2.3 \log r$ (McKinley, 1961) is shown as a dashed line. Comparing the two, it can be seen that the peak magnitude alone is not a good proxy of the total meteoroid mass or the mass distribution for sporadics.

Finally, we apply the method to EMCCD data collected on the night of August 13, 2018 ($\lambda_\odot = 140°$). The meteors were detected using a hybrid cluster–template-matching matched filter algorithm (Gural, 2007, 2016), which detects even very faint meteors close to the noise floor. The method will be described in a future paper. In total, 134 double-station Perseids were observed with the two pairs of cameras during 6.5 hours of observation. The meteor limiting magnitude was +5.0 for these fast Perseid meteors, and only those meteors which had complete light curves obtained by at least one camera were used in the analysis. We measured the population index for the Perseids to be $r = 2.43 \pm 0.29$, and the mass index to be $s = 1.90 \pm 0.12$, comparable to long-term visual measurements at the same solar longitude (Rendtel, 2014). In the same night, there were 283 sporadics whose population index was $r = 3.56 \pm 0.50$ and mass index $s = 2.30 \pm 0.14$, significantly higher than that of the Perseids, as expected.
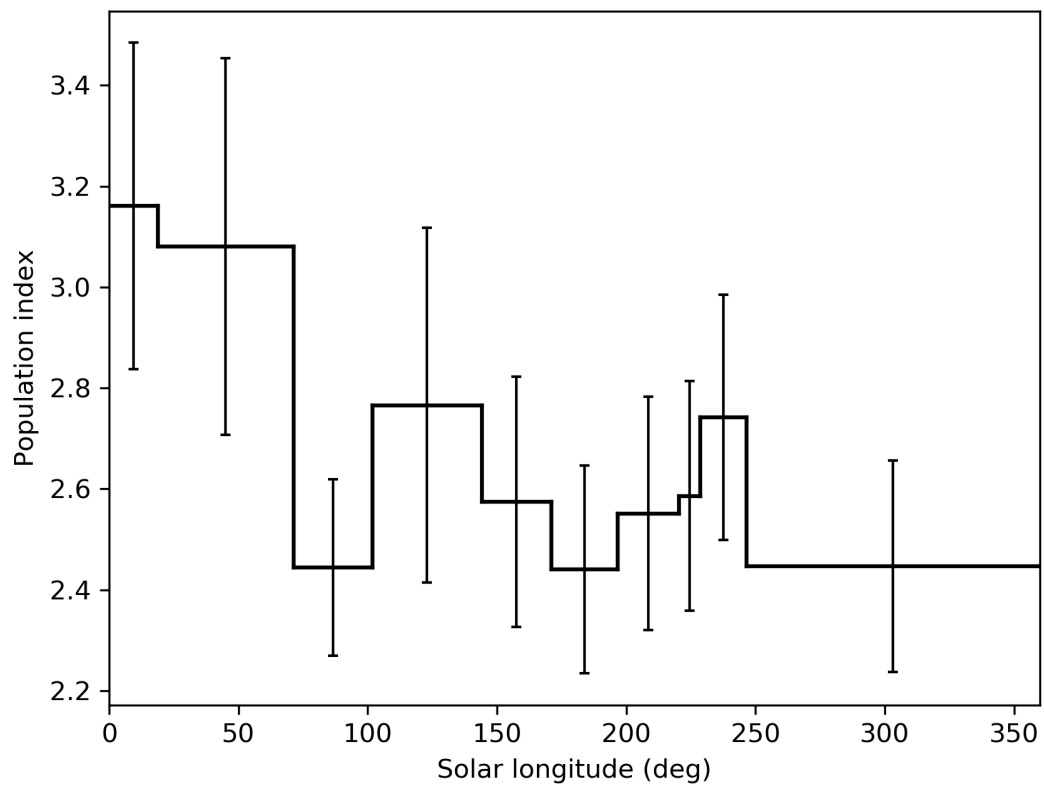
Figure 5.11: Annual variation in the population index for sporadic meteors using data from the CAMO influx camera.
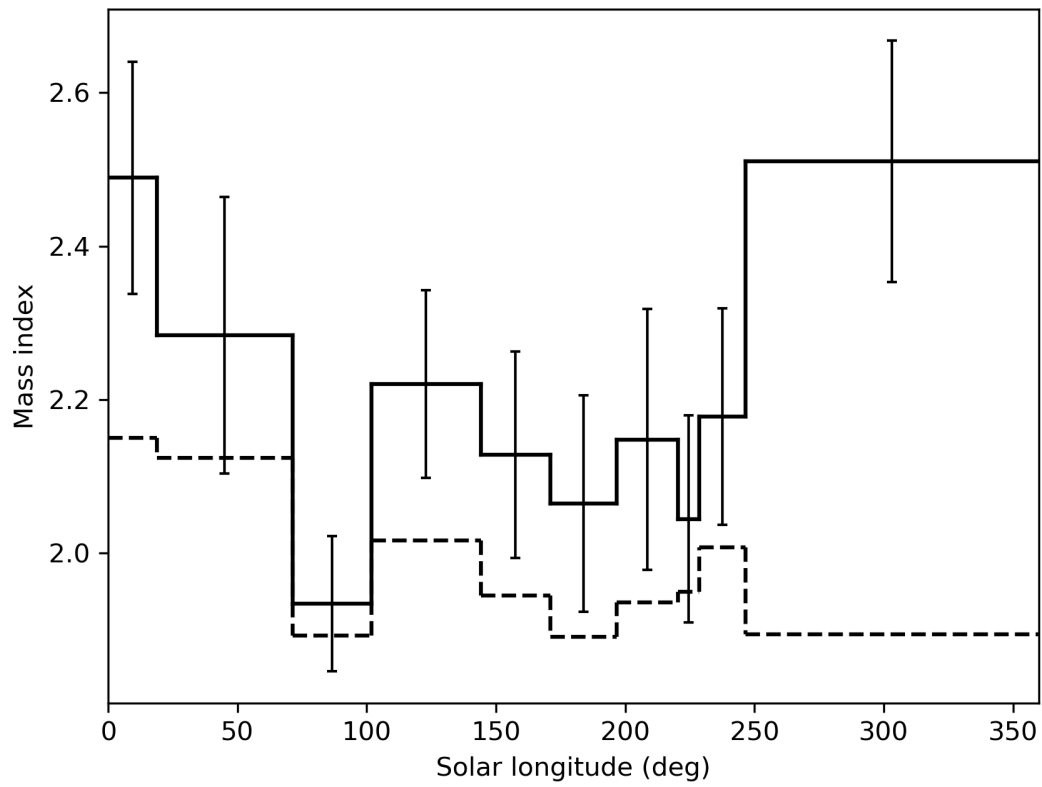
Figure 5.12: Annual variation in the sporadic mass index (solid line) as derived using the CAMO influx camera. The dashed line is the mass index derived from the population index using the classical relation $s = 1 + 2.3 \log r$.

5.4 Mass and population index of the 2018 Draconids

We apply the new population and mass index estimation method to the Draconids observed on the night between October 8 and 9, 2018, using the EMCCD cameras. Meteor detection and calibration was done using RMS software (Vida et al., 2016). Instead of computing photometric masses, we computed the integrated luminous intensity and used it as a proxy for mass.

Following Vida et al. (2018), the meteoroid mass m can be computed as

$$I(t) = P_{0m} 10^{-0.4 M_A(t)}, \tag{5.16}$$

$$m = \frac{2}{v^2 \tau} \int_0^t I(t), \tag{5.17}$$

where I is the luminous intensity, P_{0M} is the power of a zero-magnitude meteor, M_A the range-corrected GAIA G-magnitude (normalized to $100\,\mathrm{km}$), τ the luminous efficiency, and v the velocity of the meteor. P_{0M} and the term before the integral simply scale the mass, and as we are only interested in the slope of cumulative logarithms of mass, the scaling has no influence on the slope if we assume that all meteors have similar velocities. This is exactly the case, as all meteors are members of the same shower. Thus, we drop these terms and compute the dimensionless integrated luminous intensity I^* as a proxy for mass

$$I^* = \int_0^t 10^{-0.4 M_A(t)}. \tag{5.18}$$

The two pairs of EMCCDs recorded a total of 68 double-station Draconids with complete light curves, ranging in peak magnitudes from $+1^M$ to $+6.6^M$. We divided the data into two time bins: Bin (1) is a $\sim$ 30 minute bin from 00:03:33 UTC (beginning of observation) to 00:32:01 UTC that had a total of 30 Draconids and captures a part of the predicted peak; and Bin (2) is a $\sim$ 60 minute bin from 00:32:01 UTC to 01:28:58 UTC (end of observation) that had a total of 38 Draconids and captures the post-peak declining activity.

5.4.1   Bin 1

The first bin close to the peak, Bin 1, produced a population index of 1.98 ± 0.50 with an estimated completeness magnitude of $+4.30^M \pm 0.97$. Figure 5.13 shows that the observations roughly follow a power-law until the reference point at $+3.30^M \pm 0.97$, after which there is a rapid drop-off in the number of observed meteors. The model fit in this case does not seem to be robust, as indicated by the uncertainty, despite the large p-value of 0.843. The population index might have been underestimated due to the overabundance of meteors with peak magnitudes of around 4^M, possibly because of small-number statistics. Alternatively, the population index might have been increasing rapidly, as evidenced by the measured value in the second bin; thus the measured value is only the average of the population index function. Because this would break the underlying assumption of a fixed power-law, this population index, the associated effective meteor limiting magnitude of $+5.42^M \pm 0.64$, and the flux derived from it are to be taken with caution.

Figure 5.14 shows the cumulative histogram of dimensionless integrated luminous intensities and the mass index estimate of 1.74 ± 0.18 with the value of integrated intensity completeness being -2.40 ± 0.39. The fit appears to be robust, and we note that the mass index estimate has a much lower uncertainty than the population index estimate. This value of the mass compares well with the value for the 2011 outburst at the peak (Koten et al., 2014).

5.4.2   Bin 2

For the data in the second bin, Bin 2, we measure a much larger and more uncertain population index of 3.36 ± 1.31 (Figure 5.15), and a mass index of 2.32 ± 0.26 (Figure 5.16). The large difference from the values estimated for Bin 1 indicates a fast change in the particle size distribution as the Earth moves through the stream. This rapid change is the probable cause of the increased uncertainty, and this 60-minute bin likely encompasses a range of meteoroid size distributions. We note that the speed of the mass index increase is similar to what was observed for the 2011 Draconids, when the mass index changed from 1.84 to 2.30 in one hour (Koten
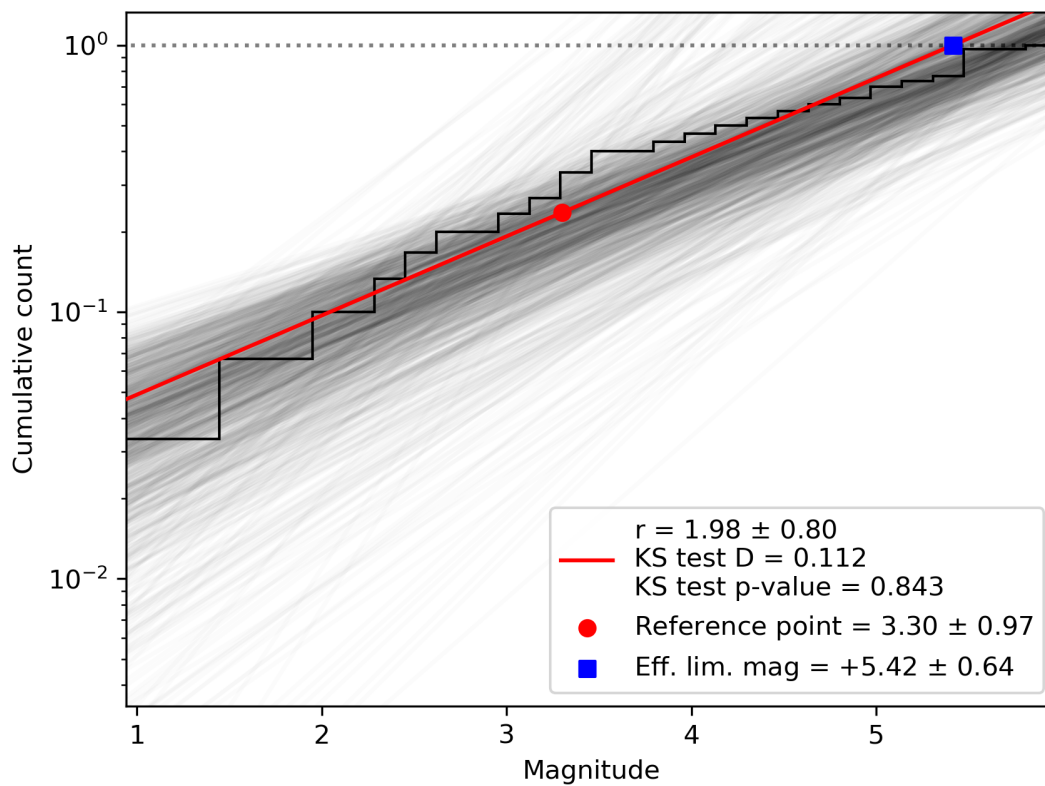
Figure 5.13: Cumulative histogram of magnitudes using the Draconid data in Bin 1. Note that the population index in some runs was significantly different than the one from the nominal solution - this was due to resampling such a small sample of data.
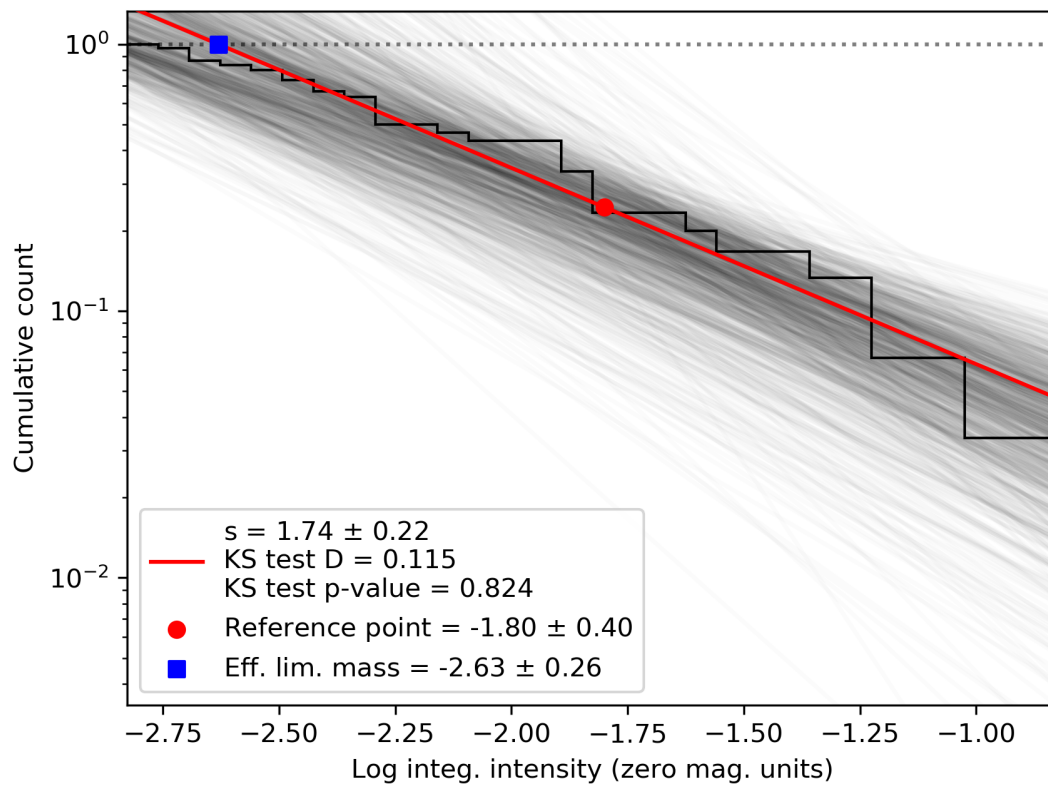
Figure 5.14: Cumulative histogram of integrated luminous intensities using the Draconid data in Bin 1.
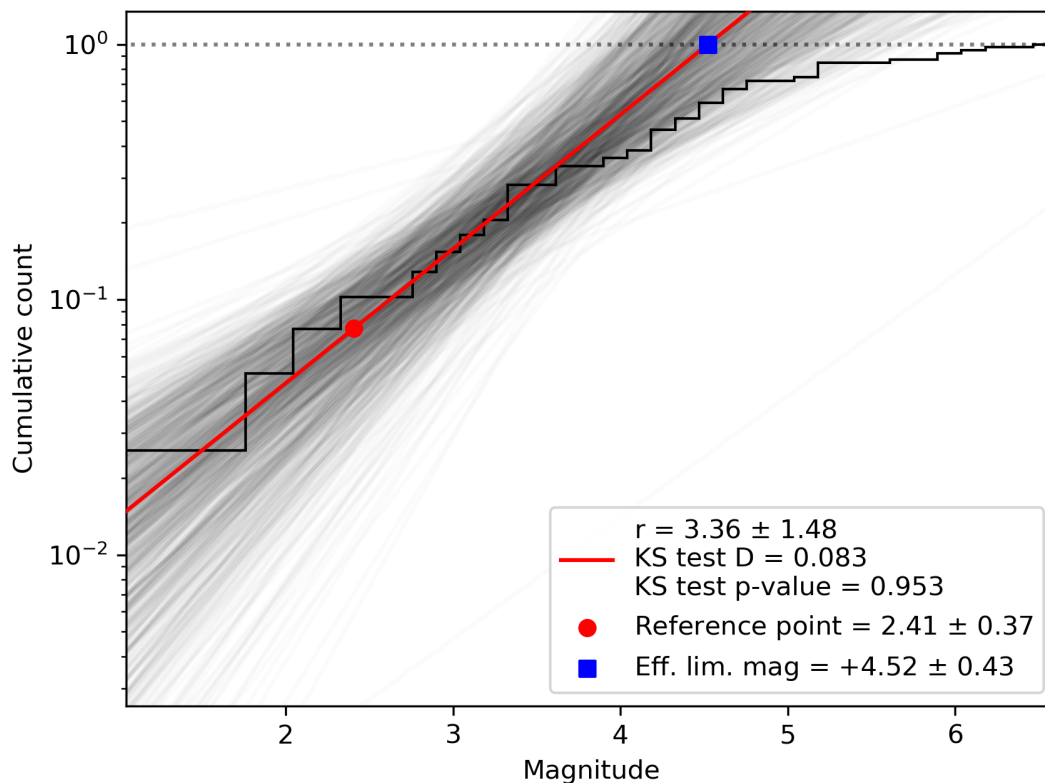
Figure 5.15: Cumulative histogram of magnitudes using the Draconid data in Bin 2.

et al., 2014).

5.5 Flux

Collecting areas for the two pairs of EMCCD cameras were calculated using the method of
Campbell-Brown et al. (2016). A grid of points spaced by 4 km was placed at heights of be-
tween 92 and 98 km to capture the typical heights of Draconid meteors. At each height, the bias
for each point in the grid was calculated, taking into account the radial speed of Draconids at
the time of the observation, the sensitivities of the two cameras, and the range to each camera.
The area of the 4×4 km region was scaled to account for meteors not seen due to lower sensi-
tivity using the measured mass index of the stream. An average of the areas at the heights of
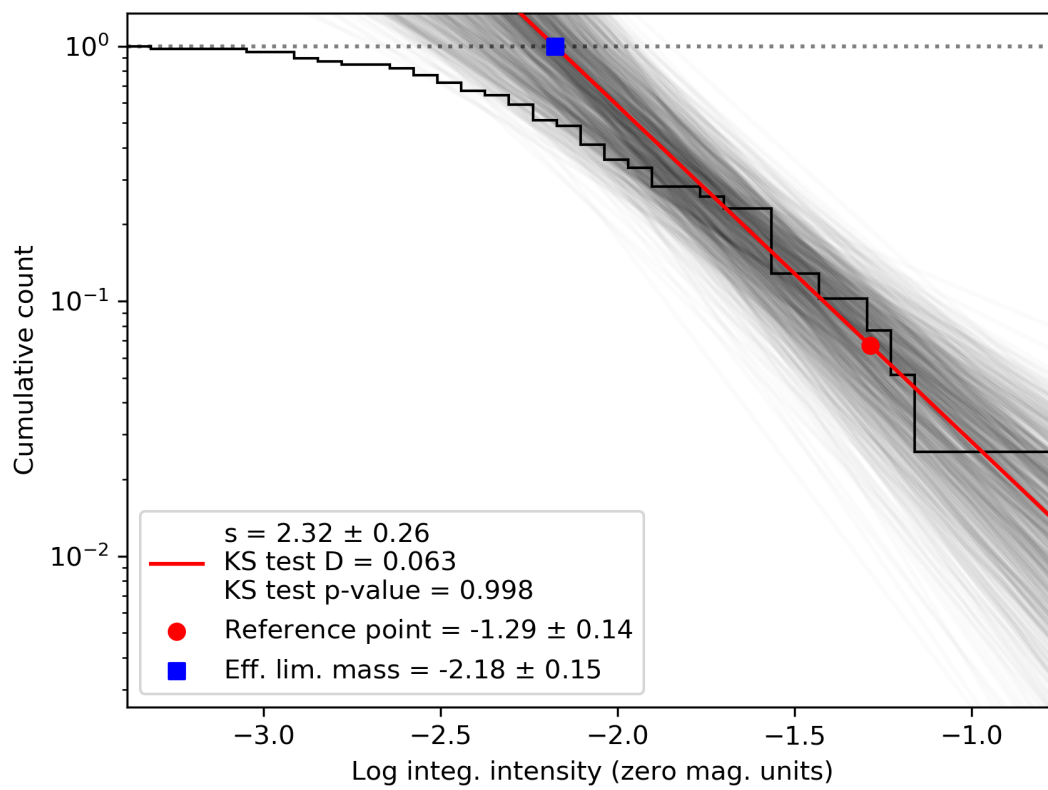
Figure 5.16: Cumulative histogram of integrated luminous intensities using the data in Bin 2.

interest was taken, though the collecting area of both systems was relatively constant at those heights.

The flux was calculated by dividing the number of single-station Draconids by the collecting area of each camera. The collecting area used here is the effective collecting area, which accounts for the changing sensitivity due to the range to each camera, the sensitivity of the cameras, and the angular speed in each part of the field of view. The sensitivity correction is a strong function of mass index. Furthermore, there are two effects from the zenith distance θ: the first is the usual $\cos \theta$ factor which takes into account how much fainter meteors are when they come in at a grazing angle than if they come straight down. The second is the change in angular speed in the cameras with the changing radiant position. The same two time intervals used in the mass index calculation were used for this calculation, and the flux of the first (half-hour) bin multiplied by two to get the number of meteoroids per hour. This calculation was performed for each pair of cameras separately, and then the numbers and collecting areas were added and the flux from both sets of cameras was calculated. The flux was then corrected using the s value from the system limiting magnitudes of +5.4 and +4.5 to a limiting magnitude of +6.5, which is standard when, for example, calculating ZHRs. All of these numbers, including the ZHR, are given in Table 5.2. The ZHR was computed using the expression given in Brown & Rendtel (1996).

Table 5.2: Fluxes of Draconids, in meteoroids per square km, per hour per EMCCD camera pair (F and G). The first two rows show the measured mass index per time bin; the last two rows show the upper and lower bounds to within 1σ of the mass index for bin 1, demonstrating the large sensitivity in flux and ZHR depending on the adopted mass index. The number of Draconids per camera pair are shown together with collecting areas per camera pair and flux.

Bin	s	Number F	Number G	Collecting Area F (km^2)	Collecting Area G (km^2)	Flux F	Flux G	Flux to LM	Flux +6.5^M	ZHR
Bin 1	1.74	14	13	328	687	0.085	0.038	0.053	0.11	586
Bin 2	2.32	22	29	214	420	0.10	0.071	0.082	0.99	681
Bin 1	1.56	14	13	373	784	0.075	0.033	0.047	0.081	1150
Bin 1	1.92	14	13	288	603	0.097	0.043	0.061	0.15	389

It is obvious that the collecting area of these systems is a strong function of the mass index: if the population index is higher (more faint meteors) the effective collecting area is smaller because many more meteors are expected to be missed in the less sensitive parts of the collecting area. We expect the flux in the second time bin to be lower than in the first because the peak occurred a short time before observations began, but the flux is nearly an order of magnitude larger, and the ZHR slightly higher. We note that both camera pairs were pointed close to the apparent radiant, which may skew flux calculations. Furthermore, the geometric overlap for the G cameras is nearly twice that of the F cameras. The range is larger, so they don't see as faint meteors as the F cameras, but the effects do not cancel out. The numbers could be an effect of small number statistics.

To get a sense of the uncertainty in the flux, which comes from the uncertainty in the mass index, for the first time bin we recomputed the collecting area with the mass index varying the uncertainty limits from 1.56 to 1.92. At the limiting magnitude of the system, this changed the flux from 0.047 meteoroids km^{-2} hr^{-1} (at the lowest mass index) to 0.061 (at the highest); extrapolating to a limiting magnitude of +6.5 produced values from 0.081 to 0.15 meteoroids km^{-2} hr^{-1}. The uncertainty in the ZHR is significantly higher, varying from 389 to 1150 for the two different mass indices. There is some uncertainty in the limiting magnitude as well, which will contribute further uncertainty to these values. All of the ZHR values are higher than those observed visually by the IMO[6], which were of order 100. Because of the rapidly changing mass index, the flux values here should be treated with caution.

5.6   Radiant distribution

Trajectories and orbits were computed with the Monte Carlo method of Vida et al. (2020b), and the initial velocities were estimated using the sliding fit proposed in this latter paper using 40% or more points from the beginning of the meteor. We did not apply the deceleration correction

---

[6]IMO web site: `www.imo.net/draconids-outburst-on-oct-8-9/`

proposed by Vida et al. (2018) as accurate velocities were not the focus of this work, and this should not influence the radiant dispersion.

Figure 5.17 shows a probabilistic radiant map in Sun-centered geocentric ecliptic coordinates generated by combining trajectory solutions of all Monte Carlo runs (200 per meteor) using kernel density estimation and a Gaussian kernel. Figure 5.18 shows the nominal radiants with error bars in equatorial coordinates with color-coded solar longitude. Both plots include a comparison between the observed and simulated radiants as produced by Egal et al. (2018). In the simulation, the meteors were produced by meteoroids ejected in 1953, and we only selected simulations which hit the Earth in the range of solar longitude between 195° and 196°.

The observed radiant is quite compact and the bulk of the shower falls within a circle of 0.6° in diameter (dashed circle in the plot), centered around a median shower radiant $\alpha_g = 261.997°$ and $\delta_g = 56.007°$, or $\lambda_g - \lambda_\odot = 50.985°$ and $\beta_g = 78.786°$. The bulk of radiants with small measurement uncertainties are within this circle, while most with large uncertainties are outside it. We note that were are also several radiants with low uncertainties that are outside it, which we believe to be sporadic meteor that were classified as Draconids by our automated meteor shower classification algorithm. The probabilistic radiant map shows an area of higher density at $\alpha_g = 262.140°$ and $\delta_g = 56.095°$, or $\lambda_g - \lambda_\odot = 51.2°$ and $\beta_g = 78.9°$, which is marked with a smaller circle in Figure 5.17, but we cannot exclude this being an artifact due to small-number statistics (only five concentrated radiants with small uncertainty). The observed radiants match the width of simulated radiants well, but there is an offset in solar longitude.

Following Kresák & Porubčan (1970), we compute the dispersion as the median angular offset from the mean radiant. Because the observation period was short, we did not perform the radiant drift correction. Figure 5.19 shows a histogram of angular offsets from the mean radiant. The median angular offset was 0.25°.

In Figure 5.18, the Egal et al. (2018) simulations show an obvious correlation of the radiant position with the solar longitude. Our observing period spanned the solar longitudes from 195.400 696° to 195.456 238°, but the simulated radiant positions matched the observations

best for $\lambda_\odot \sim 195.8°$, indicating that the position of simulated particles is shifted along the orbit when compared to observations. Due to the high precision of these observations, it may possible to optimize the meteoroid ejection and integration parameters until a good match in both the position and time is achieved, improving future predictions.

Figure 5.20 shows histograms of simulated and measured geocentric velocities for the 2018 Draconids. The histograms were normalized so that their area is equal to 1. The mean and standard deviation were $20.05 \pm 0.93 \,\mathrm{km\,s^{-1}}$ and $20.94 \pm 0.08 \,\mathrm{km\,s^{-1}}$ for observed and simulated data, respectively. The observed geocentric velocities have a larger scatter than the simulations due to the limited velocity measurement precision. Furthermore, there is a systematic $\sim 0.9 \,\mathrm{km\,s^{-1}}$ underestimation of the geocentric velocity, a combined effect of meteor deceleration prior to detection (Vida et al., 2018) and using the average velocity of the first 40% (or more) of the meteor as the initial velocity. In Table B.1 we give a list of all meteors and their geocentric radiants, orbits, magnitudes, and mass proxies. We note that due to the underestimation of the geocentric velocity from lack of deceleration correction, the semi-major axes listed in the table are also underestimated.

5.7   Conclusions

We analyzed 90 minutes of optical meteor data of the 2018 Draconid meteor shower outburst. The observations started shortly after the predicted peak at 00:00 UTC on October 9, 2018. We performed multi-station observations with the SOMN all-sky network and four sensitive EMCCD cameras. The all-sky system did not record any bright Draconid meteors, but 68 multi-station Draconids with complete light curves were recorded with the EMCCD systems. The astrometric and photometric calibration of the EMCCD systems has been discussed in detail, and we show that the EMCCD systems have a limiting stellar magnitude of $+10.0^M$ and an astrometric precision of 10 arc seconds.

We developed a novel method of population and mass index computation which is based
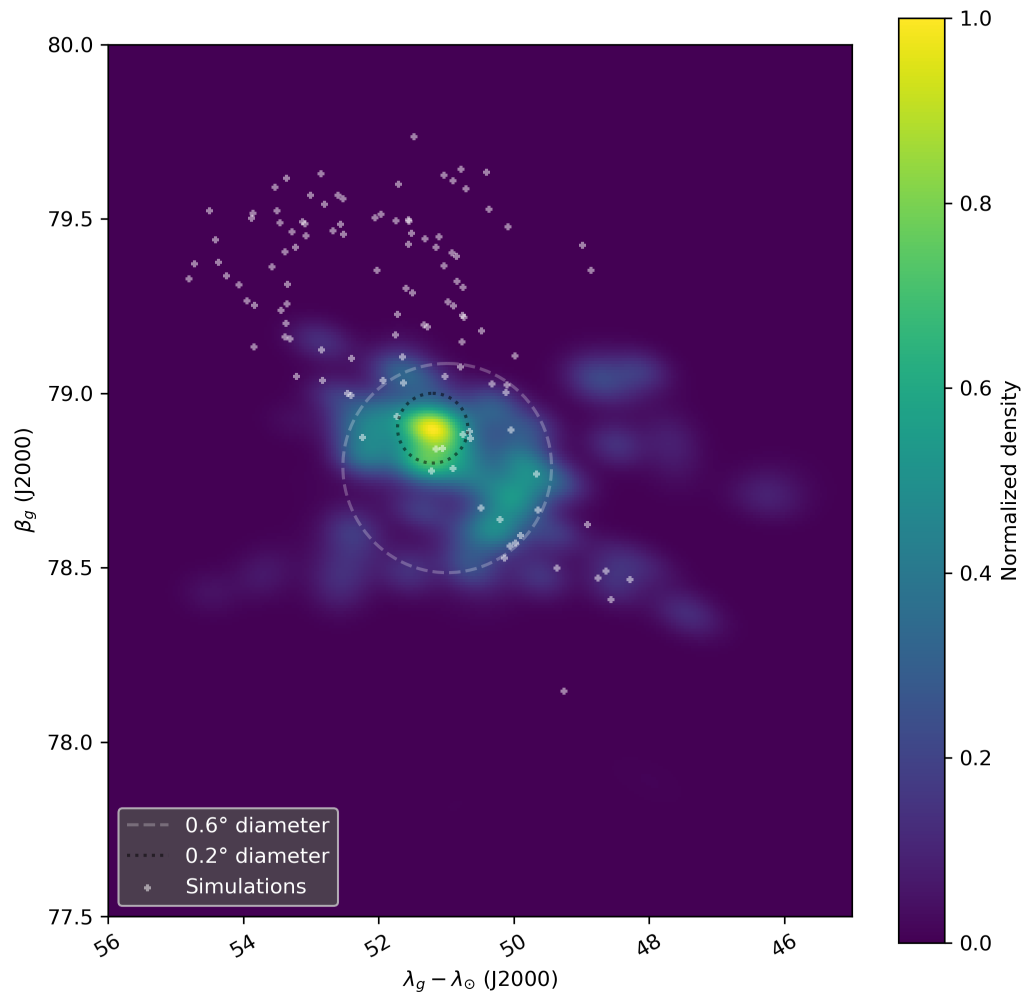
Figure 5.17: Sun-centered geocentric ecliptic radiant distribution of the 2018 Draconids observed with the EMCCD systems. The normalized density is color coded.
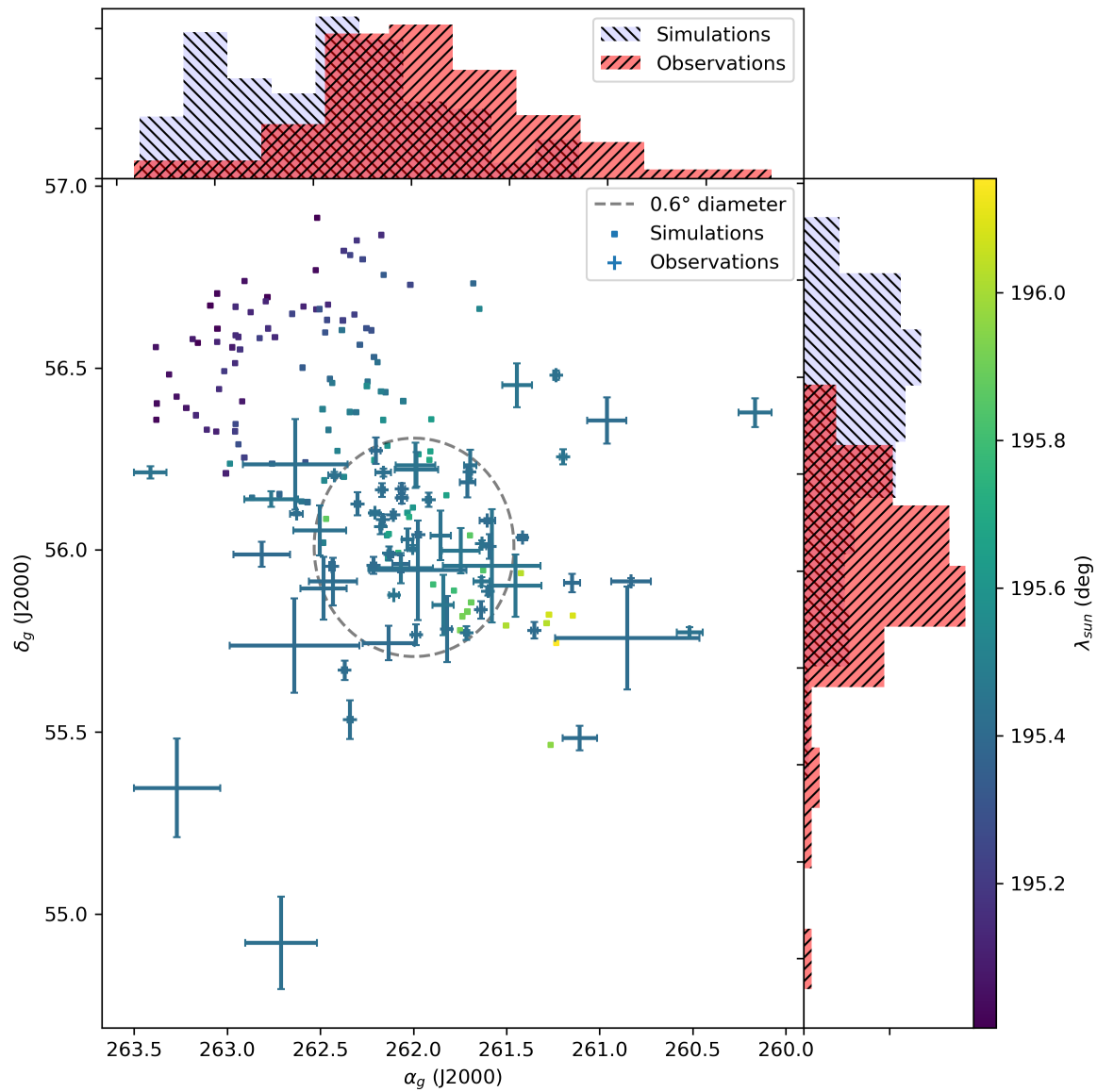
Figure 5.18: Geocentric radiant distribution of the 2018 Draconids observed with the EMCCD systems. The solar longitude is color coded, and the error bars show the one standard deviation uncertainty. The squares show the simulated radiants by (Egal et al., 2018).
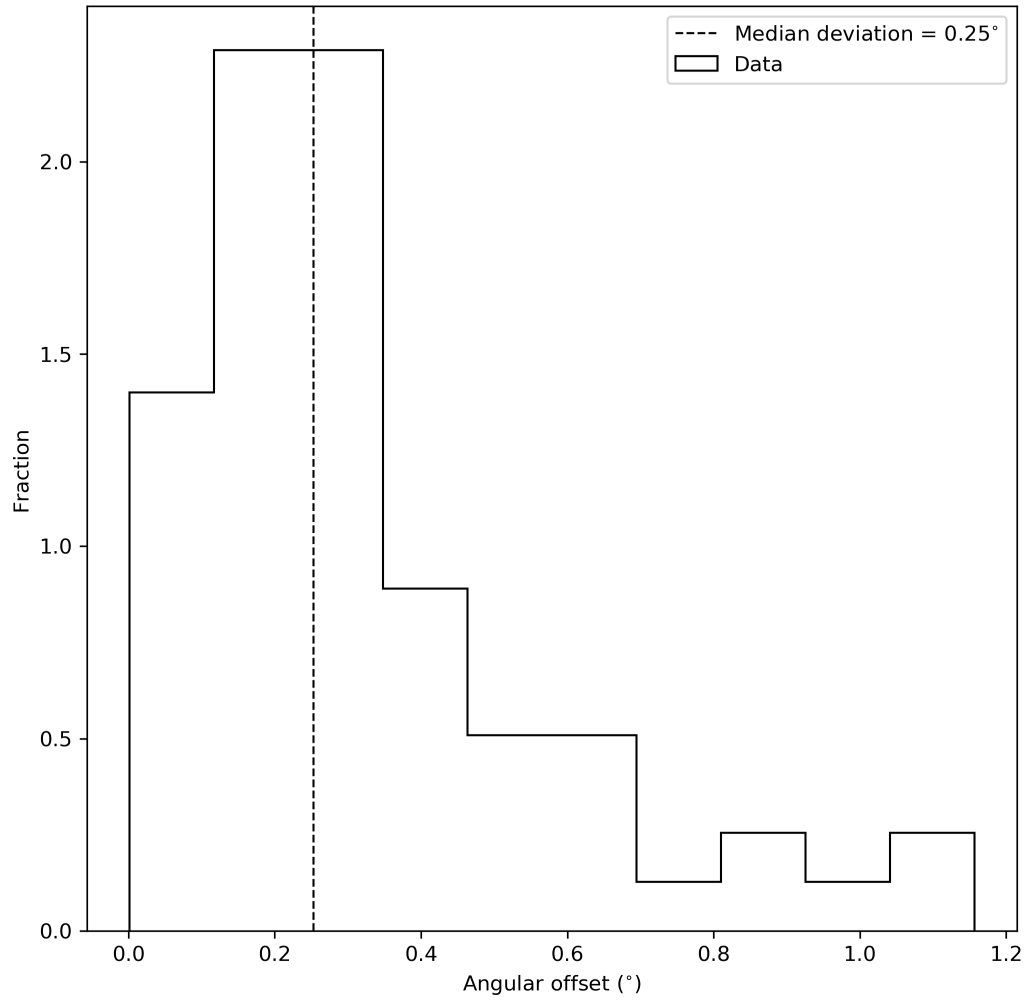
Figure 5.19: Distribution of angular offsets from the mean radiant of the 2018 Draconids. The vertical line marks the median angular offset of 0.25°.
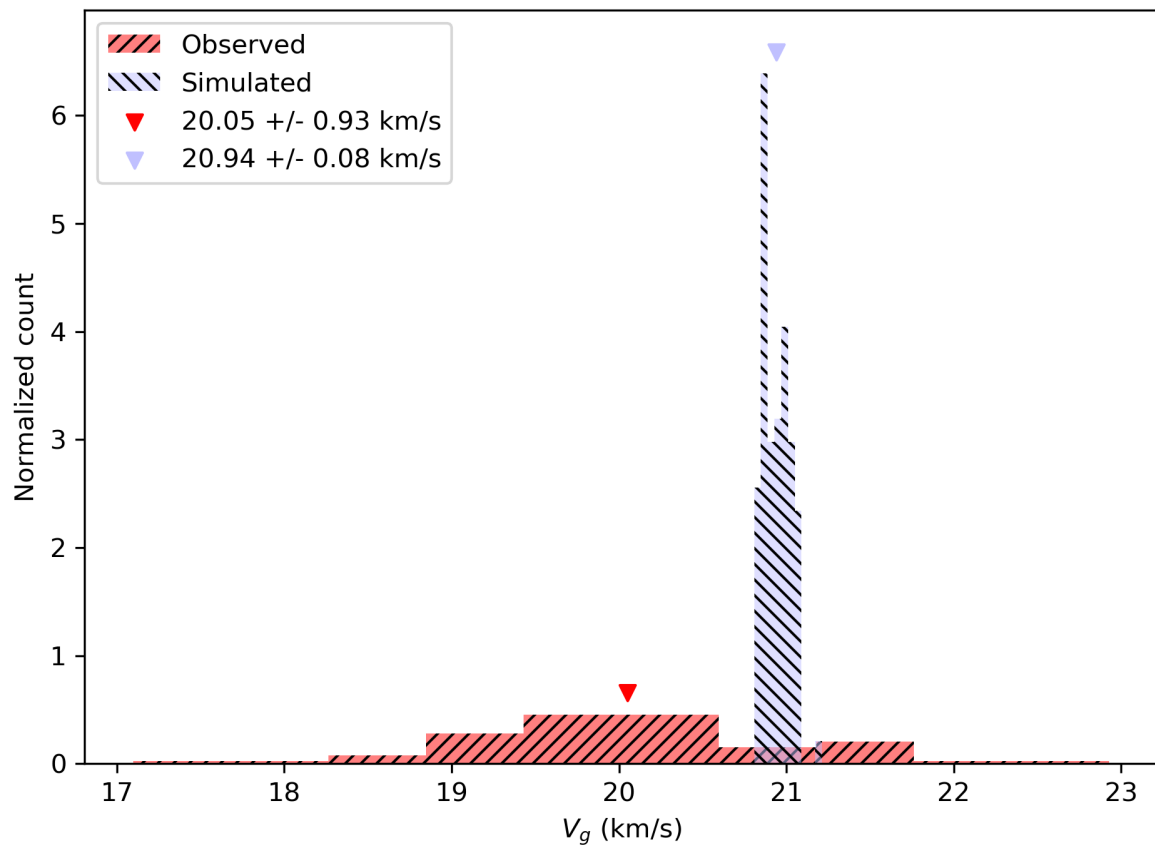
Figure 5.20: Comparison of simulated (blue) and observed (red) geocentric velocities.

on maximum likelihood estimation. The method fits a gamma function to the distribution of magnitudes or logarithms of mass to estimate the slope of the cumulative distribution (i.e., population or mass index) before the sensitivity effects become important. We validated this approach on past data obtained with the CAMO influx system. The method also enables robust error estimation.

We divided EMCCD data of the 2018 Draconid outburst into two time bins of approximately equal number of meteors: the first bin spanned the time from 00:00 UTC to 00:30 UTC, and the second bin spanned from 00:30 UTC to 01:30 UTC, on October 9, 2018. The mass index was 1.74 ± 0.18 in the first bin and 2.32 ± 0.27 in the second bin, an increase of similar magnitude and rate of change to the 2011 Draconids (Koten et al., 2014).

Because of the rapid rate of change of the mass index of the shower and small-number statistics, the values derived for the mass index and flux are very uncertain, particularly for the first time bin. The fluxes in the two bins were 0.11 and 0.99 meteoroids $\text{km}^{-2}\,\text{hr}^{-1}$, respectively, corrected to a limiting meteor magnitude of +6.5. From visual observations, we expect the flux was actually falling from the first to the second time interval; the reversed trend in this data is most likely due to the assumption of a single power law in each time bin, which does not adequately describe the data. For this reason, we do not attempt to describe the flux profile of the shower.

The measured shower radiant diameter was ~0.6° which matches simulations by Egal et al. (2018) well, but there is an offset in solar longitude of 0.4°. The measured radiant dispersion is a good match to the 2011 outburst, both the high-precision radiant measurements by Borovička et al. (2014), and the meteoroid ejection simulations by Vida et al. (2020a).

5.7.1   Complete input data and trajectory solutions for EMCCD meteors

We provide the input data and detailed trajectory solutions for the Draconids observed with the EMCCD systems, in electronic form at the CDS via anonymous ftp to `cdsarc.u-strasbg.fr` (`130.79.128.5`) or via `http://cdsweb.u-strasbg.fr/cgi-bin/qcat?J/A+A/`.

Bibliography

Akkouchi, M. 2008, J. Chungcheong Math. Soc, 21, 501

Arlt, R., & Rendtel, J. 2006, Monthly Notices of the Royal Astronomical Society, 367, 1721

Beech, M., Brown, P., & Jones, J. 1995, Quarterly Journal of the Royal Astronomical Society, 36, 127

Berry, R., & Burnell, J. 2000, Astronomical Image Processing (Willmann-Bell)

Blaauw, R., Campbell-Brown, M., & Weryk, R. 2011a, Monthly Notices of the Royal Astronomical Society, 412, 2033

—. 2011b, Monthly Notices of the Royal Astronomical Society, 414, 3322

Blaauw, R. C., Campbell-Brown, M., & Kingery, A. 2016, Monthly Notices of the Royal Astronomical Society, 463, 441. `https://doi.org/10.1093/mnras/stw1979`

Borovička, J., Koten, P., Shrbený, L., Štork, R., & Hornoch, K. 2014, Earth, Moon, and Planets, 113, 15

Brown, P., & Rendtel, J. 1996, Icarus, 124, 414

Brown, P., Weryk, R., Kohut, S., Edwards, W., & Krzeminski, Z. 2010, WGN, Journal of the International Meteor Organization, 38, 25

Brown, P., & Ye, Q. 2012, Central Bureau Electronic Telegrams, 3249, 1

Brown, P. G., Campbell-Brown, M. D., Hawkes, R., Theijsmeijer, C., & Jones, J. 2002, Planetary and Space Science, 50, 45. `http://linkinghub.elsevier.com/retrieve/pii/S003206330100112X`

Campbell-Brown, M. 2015, Planetary and Space Science, 118, 8

Campbell-Brown, M. D., Blaauw, R., & Kingery, A. 2016, Icarus, 277, 141

Clauset, A., Shalizi, C. R., & Newman, M. E. 2009, SIAM review, 51, 661

Cooke, W. J., & Moser, D. E. 2010, Meteoroids 2010: An International Conference on the Minor Bodies in the Solar System; 24-28 May 2010; Breckenridge, CO; United States

Corral, Á., & González, Á. 2019, Earth and Space Science, 6, 673

Dohnanyi, J. 1969, Journal of Geophysical Research, 74, 2531

Egal, A., Wiegert, P., Brown, P. G., et al. 2019, Icarus, 330, 123. `https://doi.org/10.1016/j.icarus.2019.04.021https://linkinghub.elsevier.com/retrieve/pii/S0019103518308017`

—. 2018, The Astrophysical Journal Letters, 866, L8

Feroz, F., Hobson, M., & Bridges, M. 2009, Monthly Notices of the Royal Astronomical Society, 398, 1601

Gaia Collaboration, Brown, A. G. A., Vallenari, A., et al. 2018, A&A, 616, A1. `https://doi.org/10.1051/0004-6361/201833051`

Gault, D. E., Shoemaker, E. M., & Moore, H. J. 1963, Spray ejected from the lunar surface by meteoroid impact, Vol. TN-D-1767 (NASA)

Gural, P. 2016, in International Meteor Conference Egmond, the Netherlands, 2-5 June 2016, 96–104

Gural, P. S. 2007, in Advances in Meteoroid and Meteor Science (Springer), 269–275

Ivezić, Ž., Connolly, A. J., VanderPlas, J. T., & Gray, A. 2014, Statistics, Data Mining, and Machine Learning in Astronomy: A Practical Python Guide for the Analysis of Survey Data (Princeton University Press)

Jenniskens, P. 2006, Meteor showers and their parent comets (Cambridge University Press)

Jones, J., & Morton, J. 1982, Monthly Notices of the Royal Astronomical Society, 200, 281

Kastinen, D., & Kero, J. 2017, Planetary and Space Science, 143, 53

Kero, J., Fujiwara, Y., Abo, M., Szasz, C., & Nakamura, T. 2012, Monthly Notices of the Royal Astronomical Society, 424, 1799

Koten, P., Vaubaillon, J., Tóth, J., Margonis, A., & Ďuriš, F. 2014, Earth, Moon, and Planets, 112, 15

Kresák, L. 1993, in Meteoroids and their parent bodies, Proceedings of the International Astronomical Symposium held at Smolenice, Slovakia, July 6-12, 1992, Bratislava, edited by J. Stohl and I.P. Williams (Astronomical Institute, Slovak Academy of Sciences), 147

Kresák, L., & Porubčan, V. 1970, Bulletin of the Astronomical Institutes of Czechoslovakia, 21, 153

Kun, F., & Herrmann, H. J. 1996, Computer Methods in Applied Mechanics and Engineering, 138, 3. https://www.sciencedirect.com/science/article/pii/S0045782596010122

Leemis, L. M., & McQueston, J. T. 2008, The American Statistician, 62, 45. https://doi.org/10.1198/000313008X270448

Maslov, M. 2011, WGN, Journal of the IMO, 39, 3

McKinley, D. W. R. 1961, Meteor science and engineering. (New York, McGraw-Hill)

Molau, S. 2015, in International Meteor Conference Mistelbach, Austria, 11–15

Molau, S., Barentsen, G., & Crivello, S. 2014, in Proceedings of the International Meteor Conference, Giron, France, 18-21 September 2014, 74–80

Pokornỳ, P., & Brown, P. G. 2016, Astronomy & Astrophysics, 592, A150

Rendtel, J. 2004, in Proceedings of the International Meteor Conference, 22nd IMC, Boll-
    mannsruh, Germany, 2003, 114–122

Rendtel, J. 2014, Meteor Shower Workbook 2014 (International Meteor Organization), 88

Šegon, D., Andreić, Ž., Gural, P. S., et al. 2014, Earth, Moon, and Planets, 112, 33

Trigo-Rodríguez, J. M., Madiedo, J. M., Williams, I. P., et al. 2013, Monthly Notices of the
    Royal Astronomical Society, 433, 560

Vaubaillon, J., Watanabe, J., Sato, M., Horii, S., & Koten, P. 2011, WGN, Journal of the IMO,
    39, 3

Vaubaillon, J., Koten, P., Margonis, A., et al. 2015, Earth, Moon, and Planets, 114, 137

Vida, D., Brown, P. G., & Campbell-Brown, M. 2018, Monthly Notices of the Royal Astro-
    nomical Society, 479, 4307

Vida, D., Brown, P. G., Campbell-Brown, M., Wiegert, P., & Gural, P. S. 2020a, Monthly
    Notices of the Royal Astronomical Society, 491, 3996

Vida, D., Gural, P. S., Brown, P. G., Campbell-Brown, M., & Wiegert, P. 2020b, Monthly
    Notices of the Royal Astronomical Society, 491, 2688

Vida, D., Zubović, D., Šegon, D., Gural, P., & Cupec, R. 2016, in Proceedings of the Interna-
    tional Meteor Conference (IMC2016), Egmond, The Netherlands, 2–5

Watanabe, J.-I., & Sato, M. 2008, in Advances in Meteoroid and Meteor Science (Springer),
    111–116

Weryk, R., Campbell-Brown, M., Wiegert, P., et al. 2013, Icarus, 225, 614

Ye, Q., Brown, P. G., Campbell-Brown, M. D., & Weryk, R. J. 2013a, Monthly Notices of the
    Royal Astronomical Society, 436, 675

Ye, Q., Wiegert, P. A., Brown, P. G., Campbell-Brown, M. D., & Weryk, R. J. 2013b, Monthly
    Notices of the Royal Astronomical Society, 437, 3812

Chapter 6

High precision meteor observations with the Canadian Automated Meteor Observatory: Data reduction pipeline and application to meteoroid mechanical strength measurements

A version of this chapter has been submitted for publication as:

Vida, D., Brown, P.G., Campbell-Brown, M., Weryk, R.J., Stober, G., and McCormack, J.P. (2020). *High precision meteor observations with the Canadian Automated Meteor Observatory: Data reduction pipeline and application to meteoroid mechanical strength measurements*. Icarus, submitted

6.1 Introduction

Most currently operational optical meteor observation systems consist of a fixed low-light camera operating at typical video frame rates of 25 to 30 frames per second. Such systems vary from all-sky to moderate fields of view, with plate scales at best 1 arcmin/pixel (e.g. Tóth et al., 2015; Jenniskens et al., 2011). Since the appearance of low-light CCD sensors in the early 1990's, video meteor cameras have proved to be an invaluable source of data used for meteoroid orbital studies, models of meteoroid fragmentation and physical structure, as well as recovery of meteorites produced by meteorite-dropping fireballs (Koten et al., 2019).

Dynamical and photometric data from such cameras have allowed the densities of meteoroids, a critical parameter used in spacecraft risk models (Kikwaya et al., 2011; McNamara et al., 2005), to be systematically estimated. However, such fixed optical systems are not able to observe individual meteor fragments as they move relative to the fixed sensor during frame integration, and the pixel scale on the order of 10s of meters per pixel at 100 km does not allow the meteor morphology to be fully resolved (Stokan et al., 2013). This obscures the true amount and nature of fragmentation and deceleration, which are essential for constraining the physical properties of meteoroids through ablation modelling (Vojáček et al., 2019) and are the limiting factor in improving accuracy of meteoroid orbits (Vida et al., 2018b). Finally, moderate field of view optical systems, in ideal conditions, can achieve meteor trajectory radiant accuracy of 0.1°, which is near the limit of resolving the true radiant dispersion of the tightest (youngest) meteor showers (Vida et al., 2019a).

The Canadian Automated Meteor Observatory's (CAMO) mirror tracking system is an optical system consisting of a wide-field camera (34° × 34°) which runs a real time meteor detection algorithm. Upon detection, it cues a pair of mirrors to track the meteor and redirect its light through an 80 mm telescope with a very narrow field of view (1.5° × 1.5°) equipped with a 3rd generation image-intensifier lens coupled to a high frame rate machine vision CCD camera, giving a plate scale of 6 arcsec/px (Weryk et al., 2013). A block diagram of the tracking system is shown in Figure 6.1 and more details about the hardware are given in Section 6.2.1. The data
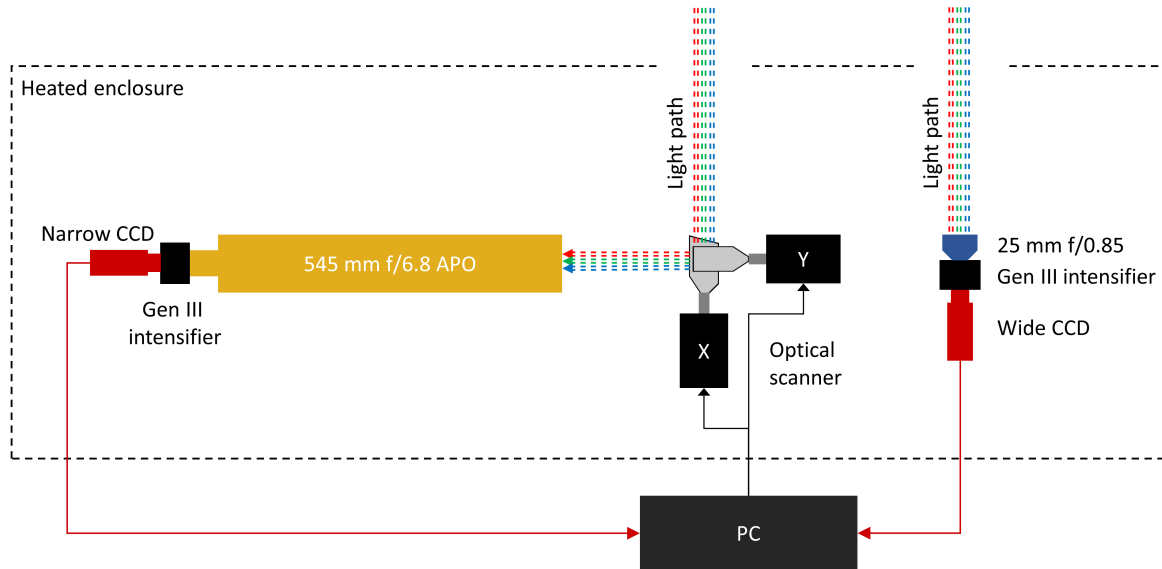
Figure 6.1: Block diagram of the CAMO mirror tracking system.

collected with CAMO provide a direct way of studying the details of fragmentation for mm-sized meteoroids and offer the prospect of order of magnitude more precise meteoroid orbits as compared to classical fixed-camera systems (Vida et al., 2019a). Observing meteor morphology and distinguishing the wake reveals the underlying physics of ablation and fragmentation, and allows direct measurements of individual fragments: their dynamics, differential deceleration, mass, mass distribution, and strengths. Figure 6.2 shows an example composite image of two meteors observed with the CAMO narrow field of view camera.

6.1.1   Previous research done using CAMO data

The CAMO mirror tracking system has been operational since 2009. An early study by Subasinghe et al. (2016) showed that 90% of the mm-sized meteors observed by CAMO display observable fragmentation while Campbell-Brown (2017) recognized that light curves of meteors with short or invisible wakes (resembling single-body meteors) cannot be explained without including continuous fragmentation in the ablation model. In an effort to explain meteors with double-peaked light curves, Subasinghe & Campbell-Brown (2019) found that even allowing for large compositional differences within meteoroids to produce multiple peaks, fragmenta-
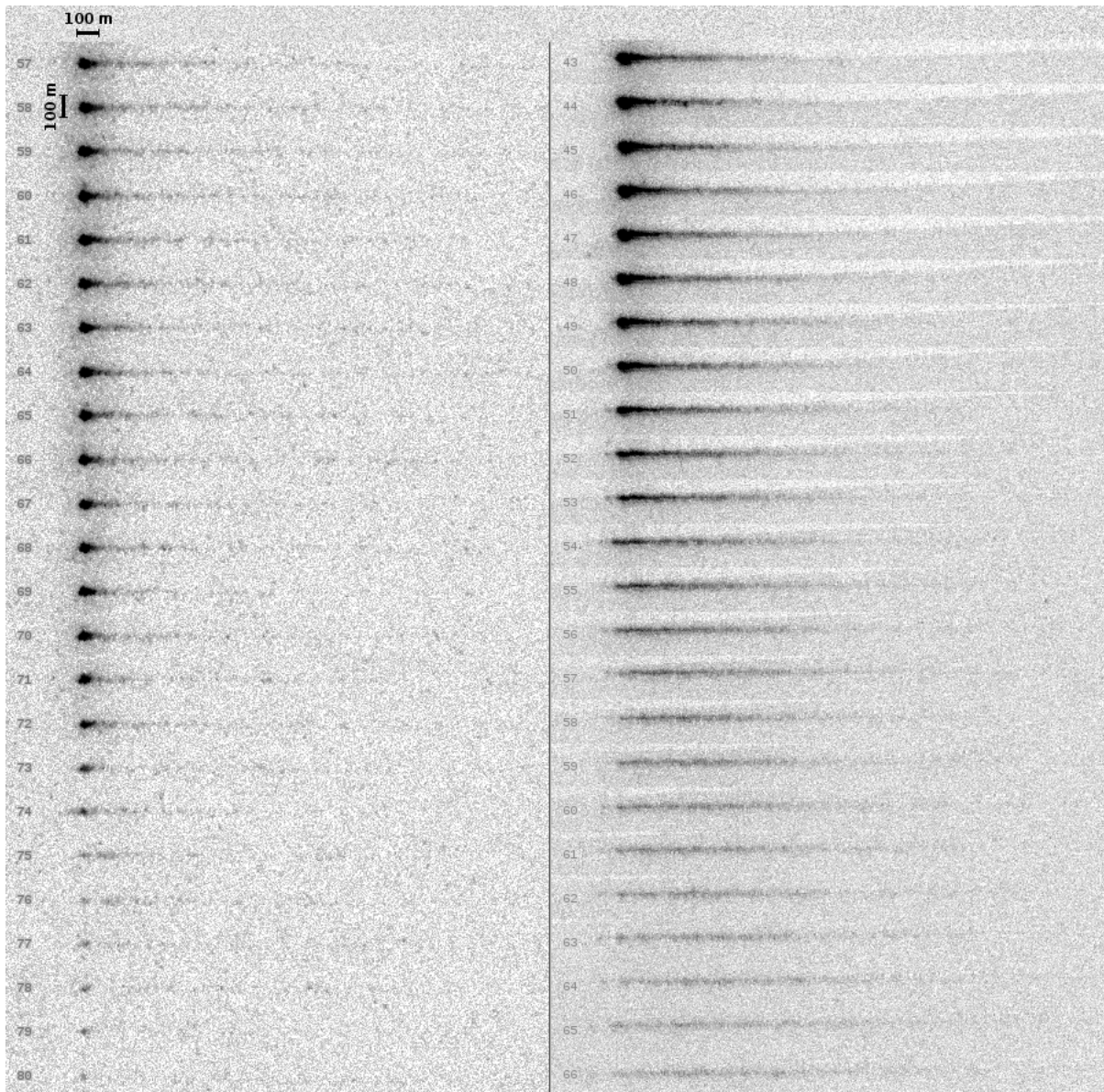
Figure 6.2: Composite grey-inverted image of two meteors recorded using the narrow-field camera. Both meteors are rotated and their leading edges aligned so the evolving meteor morphology is highlighted in this vertical stack, with time increasing from top to bottom and frame number given to the left. Left: An α Capricornid recorded on August 4, 2019 at 06:02:42 UTC. Right: An α Capricornid recorded on July 27, 2019 at 04:21:22 UTC. Note that even though they are of the same origin, the meteor on the left erodes away leaving a single distinct fragment with no wake, while the one on the right completely disintegrates into a long cylinder of dust.

tion still had to be included to explain the observed span of ablation heights. These conclusions from direct observations are in accordance with classical works (e.g. Verniani, 1969), and strongly support the notion that meteors cannot be modelled as single bodies and that fragmentation is an essential process of the meteor phenomenon.

Stokan et al. (2013) directly measured optical trail widths of meteors using CAMO, a parameter vital for computing meteoroid masses from radar observations. Stokan & Campbell-Brown (2014) were the first to recognize a class of fragmenting mm-sized meteors producing large lateral fragment separations. The transverse speeds of fragments produced by these faint meteors approached $100\,\mathrm{m\,s^{-1}}$, constraining the range of meteoroid strengths by assuming rotational- or charge-based fragmentation. Subasinghe et al. (2016) classified meteors by their fragmentation morphology and found that the frequency and type of fragmentation does not correlate with orbital classes, i.e. meteoroids on asteroidal-type orbits fragment in the same way and as often as those on cometary-type orbits. Subasinghe & Campbell-Brown (2019) found that meteors with double-peaked light curves on asteroidal-type orbits usually have a very sharp second lightcurve peak, indicating that the meteoroid either disrupted or suddenly released many small grains; in contrast, meteoroids on cometary-like orbits had smooth two-peaked light curves.

Using the fact that the CAMO mirror tracking system is able to gather data allowing for precise measurement of meteoroid deceleration, Subasinghe et al. (2017) and Subasinghe & Campbell-Brown (2018) derived luminous efficiencies of meteors by comparing the dynamic and photometric masses. Their results were broadly consistent with both theory and previous measurements, but measurement errors were still too high to accurately identify the best-matching theoretical model of luminous efficiency. In contrast to the luminous efficiencies estimated for fireballs (Ceplecha & Revelle, 2005), Subasinghe & Campbell-Brown (2018) found a negative linear correlation of luminous efficiency with initial meteoroid mass, a trend also recently reported by Čapek et al. (2019) who computed luminous efficiencies for iron meteoroids by comparing observed and simulated meteor re-radiation energies.

As meteor wakes are easily visible with CAMO, they provide an additional constraint on meteoroid ablation and fragmentation models beyond observed light curves and deceleration. Campbell-Brown et al. (2013) compared fits of the thermal disruption model of Campbell-Brown & Koschny (2004) and the thermal erosion model of Borovička et al. (2007) for several CAMO meteors. In most cases, they were able to match the observed light curve and deceleration, but not the wake. Campbell-Brown (2017) was able to fit all three features of one meteor with a short and faint wake using a modified ablation model, where short bursts of fragments were continuously released, a fragmentation model similar to the Borovička et al. (2007) erosion model.

This emphasizes the complexity of fragmentation for mm-sized meteoroids as well as the different modes of such fragmentation. In some instances, for example, discrete fragments are visible in CAMO imagery and the fragment release heights are measurable. For such cases, it may be possible to extend CAMO observations to infer the compressive strengths of small meteoroids, an otherwise difficult to measure parameter.

6.1.2 Introduction to meteoroid strength measurements

Measuring mechanical strengths of meteoroids provides insights into the corresponding surface strengths of their parent bodies. Biele et al. (2009) thoroughly reviewed past meteoroid strength studies for the purpose of designing the landing gear and landing procedure for Rosetta's ill-fated Philae comet lander. As comets consist of the most pristine material leftover from the formation of the Solar System (Blum et al., 2017), understanding mechanical properties of their constituent particles informs models of dust aggregate growth in protoplanetary disks (Güttler et al., 2009). Finally, understanding the comet mechanical surface strength is essential for models of comet activity and dust mass distribution (Gundlach et al., 2018).

Global-scale strengths of comets can be investigated though some types of comet and asteroid break-ups, such as rotational (e.g. Lisse et al., 1999; Davidsson, 2001; Sánchez & Scheeres, 2014), or tidally-driven (Asphaug & Benz, 1996). At millimeter to meter scales, strengths can

be derived either theoretically (e.g. Güttler et al., 2009) or from direct measurements. The measurements done in-situ are rather limited in number due to the complexity of the task.

Hornung et al. (2016) analyzed the dust from comet 67P /Churyumov-Gerasimenko at sizes between $10\,\mu$m and $300\,\mu$m, collected by the COSIMA instrument onboard the Rosetta spacecraft. They found that particles smaller than $100\,\mu$m remained largely undamaged when they collided with the instrument collection plate at velocities of several meters per second, but that particles larger than $100\,\mu$m (i.e. optical meteor sizes) mostly fragmented upon collision into smaller grains of several tens of microns in size. They estimate that the mechanical strength of larger particles is of the order of several kilopascals (± factor of 2), a result supported by subsequent experimental work of Gundlach et al. (2018).

Microscopic imaging of dust particles collected by COSIMA (Hornung et al., 2016) shows that the dust has an agglomerate structure, with the constituent particles on the order of a few tens of microns. Their critical observation with implications for meteoroids is, quoting from Hornung et al. (2016): "... these sub-units, which we denoted as 'elements' for not-fragmented dust particles are essentially within the same size range as the individual 'fragments' dispersed by the impact-fragmented dust particles. This observation seems to show that the fragments are not formed by the impact, but pre-existing in the parent dust agglomerate, and simply broken apart during the impact." In section 6.6.2 we discuss a meteor observed by CAMO which supports this statement. We also note that the sizes of elemental grains observed by Hornung et al. (2016) match the grain size distribution derived from meteor flares (Simonenko, 1968) and meteoroid erosion models (Borovička et al., 2007; Vojáček et al., 2019).

Due to the unsuccessful landing of the Philae lander, during which it bounced off the surface of 67P/Churyumov-Gerasimenko several times, Biele et al. (2015) were able to estimate that the compressive strength of softer surface regions was on the order of $1\,$kPa on 10cm-to-meter scales, the maximum being between $2-3\,$kPa. The lander finally landed on a hard surface with a compressive strength of $>2\,$MPa.

For the purpose of understanding the physics of planetesimal formation in protoplanetary

disks, many authors have performed experiments in which they investigate growth of dust agglomerates from micron-sized dust through sticking (Blum et al., 2000; Blum & Wurm, 2000; Krause & Blum, 2004). The growth to mm-sized fractal dust aggregates is supported by the theoretical relative collision velocities found in protoplanetary disks, but as the particles grow in size so do the velocities, which should in theory lead to fragmentation of these larger particles (Blum & Wurm, 2008). To overcome the mm-size fragmentation boundary, lower collision velocities are needed to facilitate further sticking. It is believed that gas compression may play a role at those sizes (Kataoka et al., 2013; Birnstiel et al., 2016). To determine how low the velocities must be, Weidling et al. (2012) performed a microgravity experiment where they investigated the sticking of mm-sized SiO_2 dust aggregate analogs at velocities as low as $1 \, \mathrm{mm \, s^{-1}}$. They reproduced the sticking behaviour and shown that the contact strength of dust aggregates in their experiments is at least $640 \, \mathrm{Pa}$.

6.1.3 Strength measurements from meteoroid fragmentation in the atmosphere

Mechanical strengths can also be derived from fragmentation of meteoroids in the atmosphere. If the height of fragmentation is known, one can assume that the dynamic ram pressure exerted on the meteoroid at the moment of fragmentation is a proxy for the compressive strength. Note that other authors may call this the "tensile" strength (Baldwin & Sheaffer, 1971; Trigo-Rodríguez & Llorca, 2006) due to the assumption of e.g. differential thermal heating causing internal thermal stress, or bending due to a non-spherical shape. Because we do not use a thermal model, nor attempt to measure the meteoroid shape, we assume that the fragmentation happens due to mechanical failure caused the by pressure difference between the front and the back of the meteoroid, thus we use the term "compressive" strength (Kataoka, 2017). Nevertheless, we note that thermal stress due to differential thermal heating may play a role for >1 mm sized meteoroids (it is negligible at smaller sizes; Verniani, 1969). Past models of thermal stresses within meteoroids during entry often assume cm-sized meteoroids to be

non-porous (basalt-like) stony particles. These are expected to show large internal temperature gradients (Elford, 1999; Bariselli et al., 2020) which should in theory catastrophically fragment before ablation begins (Jones & Kaiser, 1966). However, high resolution CAMO observations reported by Subasinghe et al. (2016) show that gross fragmentation only occurs in 5% of the cases, and most happen after the onset of ablation. It is unclear whether thermal fragmentation remains a plausible process for highly porous dust aggregates; the recent work by Markkanen & Agarwal (2019) shows that 0.5 mm porous aggregates are able to withstand internal temperature gradients of more than 150 K. This mechanism should be investigated in more detail. Here we assume dynamic pressure is the dominant process of gross fragmentation.

Using a model of atmosphere mass density, the dynamic pressure can be simply computed using the following expression:

$$P_{dyn} = \Gamma v^2 \rho(h),   \tag{6.1}$$

where Γ is the drag coefficient (usually assumed to be unity in free molecular flow, appropriate to most events observed by CAMO), v is the meteoroid speed at the moment of fragmentation, and $\rho(h)$ is the atmosphere mass density at the height of fragmentation h.

It has long been understood that if smaller meteoroids do fragment when they enter the atmosphere, this fragmentation occurs at the dynamic pressure of around $1 - 2$ kPa (Verniani, 1969). Past in-atmosphere meteoroid strength studies either used a rule of thumb or an ablation model to estimate when this fragmentation may occur; Blum et al. (2014) gives an overview of past work. Trigo-Rodríguez & Llorca (2006) measured strengths in the range from 400 Pa for the Draconids to 340 kPa for the Taurids, assuming that meteoroids disrupted at the point of maximum brightness. On the other hand, Borovička et al. (2007) fit observed meteor light curves and decelerations to a meteoroid ablation model and concluded that except for bright fireballs, fragmentation does not coincide with the point of maximum brightness. They estimated that the compressive strengths of more compact parts of Draconid meteoroids are in the range of $5 - 20$ kPa. They also note that meteoroid erosion (continuous fragmentation into con-

stituent grains) can start earlier and may not be due to mechanical forces, and that only fireball flares are caused by disruption (catastrophic fragmentation) which could reveal the compressive strength. Regardless of the possible mechanisms of disruption/fragmentation, precise determination of the fragmentation time can set concrete upper limits to mechanical bulk strengths of meteoroids.

6.1.4   Motivation and overview

This paper was preceded by two theoretical papers which investigated the limits of meteor trajectory accuracy achievable with CAMO. When computing meteoroid orbits, understanding the accuracy of two separate components is essential: the meteoroid pre-atmosphere velocity and the radiant. In Vida et al. (2018b) an ablation model was used to simulate meteoroids of different physical properties as they would be observed by various optical observations systems, including CAMO. In particular, they investigated whether measuring the meteor velocity at the beginning of the luminous trajectory produced accurate pre-atmosphere velocity measurements. They found that meteoroids producing optical meteors can significantly decelerate before their ablation becomes visible, up to $750\,\mathrm{m\,s^{-1}}$, which is an order of magnitude more than the velocity measurement precision of the CAMO system. Vida et al. (2018b) have also shown that this deceleration is highly influenced by meteoroid density and other physical properties, implying that ablation models must be used to fit the observed meteor to invert for the true pre-atmosphere velocity; thus the ultimate limitation on velocity accuracy is the efficacy of the adopted ablation model.

Vida et al. (2019b) and Vida et al. (2019a) investigated the radiant accuracy that can be achieved by CAMO and found that it is an order of magnitude more accurate (~0.01°) than what is needed to measure the model-estimated true physical radiant dispersion of the most compact meteor showers, specifically the Draconids. They also found that existing methods of meteor trajectory estimation were not suitable for the high-precision CAMO data, so an improved method was developed which simultaneously uses both the geometrical and dynamical

information to constrain meteor trajectory solutions, but without forcing a kinematic model.

In this work, we first describe recent upgrades to the CAMO hardware, software, and data reduction procedure in detail. In section 6.5 we present the first results of high-precision meteor reductions on CAMO data and discuss the implications of the observed meteor morphology on trajectory accuracy. Next, in section 6.6, we estimate compressive strengths of select meteors by taking the dynamic pressure at the moment of observable gross fragmentation as a proxy of strength. The measurements were only done for meteoroids where the exact moment of fragmentation was directly visible in the CAMO recordings. In section 6.6.1 we perform a brief sensitivity analysis of computing dynamic pressures in practice, with a special focus on the uncertainty of the atmosphere density. Next, in section 6.6.2 we describe an event observed with the CAMO tracking system on July 21, 2017 which shows the exact moment of gross fragmentation that prompted us to develop a method of direct compressive strength measurement (Vida et al., 2018a). Finally, in section 6.6.3 we present compressive strength results for a small number of events by applying our approach to several meteors showing gross fragmentaion.

6.2   CAMO mirror tracking system specifications

The first version of the CAMO system started regular operations in 2009 and was described by Weryk et al. (2013). CAMO is comprised of two identical systems in Southwestern Ontario, Canada, separated by ~45 km. The first is located near Tavistock and is co-located with the Canadian Meteor Orbit Radar (CMOR) (43.264 20° N, 80.772 09° W, 329 m), while the other is at the Elginfield Observatory (43.192 79° N, 81.315 65° W, 324 m). Both systems are pointed roughly northward at an elevation of 45° to avoid sunlight, moonlight, and the galactic plane. Their common volume overlap is optimized for heights between 70 km and 120 km. This configuration limits the maximum convergence angle between stations to ~27°, but this has no detrimental effect on meteor trajectory accuracy due to the fine astrometric scale of the data

when an appropriate trajectory solver is used (Vida et al., 2019a).

6.2.1   System hardware

In mid-2017, the system hardware was upgraded to extend CAMO's operational lifespan. Both the wide and the narrow-field cameras, which are lens coupled to Generation 3 image intensifiers, were replaced with 14-bit Prosilica GX1050 digital progressive scan CCD cameras which use a Gigabit Ethernet interface, and have an image resolution of 1024×1024 pixels. The video is cropped to 900×900 pixels, as the edges of the field of view are not covered by the intensifier. The wide-field camera is operated at 80 frames per second, and the narrow-field camera at 100. The intensifiers were upgraded to new 18 mm diameter ITT FS9910 series Generation 3 image intensifiers with 64 line pairs per millimeter resolution, providing a close to 1:1 match to the camera resolution. The intensifier on the wide-field camera is operated continuously during observations, but the narrow-field intensifier is gated and only turns on if a meteor is being tracked. This saves up to 99% of intensifier time, significantly prolonging its lifetime.

The lens setup remained the same as before, with a 25 mm f/0.85 lens on the wide-field, giving a field of view of $34° \times 34°$. The narrow-field optics are also unchanged and consist of an 80 mm aperture APO telescope with a 545 mm focal length. As the telescope is looking at mirrors with an effective radius of 50 mm, the narrow-field setup's focal ratio is reduced to f/11, giving it a field of view of $1.5° \times 1.5°$ and a plate scale of 6 arcsec per pixel.

Assuming that ideal centroiding can improve position measurements by a factor of three, this system is at the limit of the average atmospheric seeing in Southwestern Ontario, thus no further improvement in resolution can be achieved under these conditions. The two mirrors on orthogonal axes are attached to a Cambridge Technology 6900 optical scanner, a galvanometer-based system with a maximum slew rate of 2000 deg/s and a field of regard of $39°\times38°$. Figure 6.3 shows the comparison of the fields of view of all optical subsystems. The mirrors on the optical scanner are precisely positioned by changing the voltage of each axis between -10 V and 10 V using a 16-bit digital-to-analog converter, giving an angular step-size resolution of

~ 2.2 arcsec/ADU, equivalent to 1/3 of a pixel in the narrow-field camera.

The clock on the computers that operate each camera is GPS conditioned using the network time protocol (NTP), but the video frames are timestamped on the camera to avoid timing errors due to Ethernet network latency. We found that the camera's internal clock drifts over time relative to the NTP computer clock, so we apply a frame time correction by occasionally checking the temporal drift and fitting a linear model through the time differences during night-time observations. Total time drifts remain sub-frame between time calibrations, which occur every two hours during operations.

The optical system is contained within a weather-resistant enclosure inside a roll-off roof shed which only opens during optimal weather conditions (Weryk et al., 2013). The system layout is shown in Figure 6.4.

6.2.2   Detection software and tracking

The meteor detection algorithm used by CAMO has been described in detail in Weryk et al. (2013). In this paper we only give a short summary, but thoroughly describe the calibration methods which were not discussed in detail in Weryk et al. (2013).

As image-intensified video is dominated by high frequency shot noise, we use a normalised first-order low-pass finite impulse response filter in our detection algorithm (Weryk & Brown, 2012). This approach eliminates bright and short bursts of noise, while being sensitive to any medium frequency events (such as meteors) which appear above the static background. The shot noise does not typically have enough trigger pixels to form a detection. The algorithm runs in real time on the wide-field video feed and once it detects a meteor in 8 frames, it fits a constant angular speed model based on these detections. The mirrors then slew to and track according to the model-predicted motion, having their positions updated 2000 times a second. Due to the mirror inertia and high speed of position updates, their motion becomes fluid, allowing the imaging to match the reference frame of each tracked meteor. A record of mirror position at every update is kept, making high-precision astrometry using narrow-
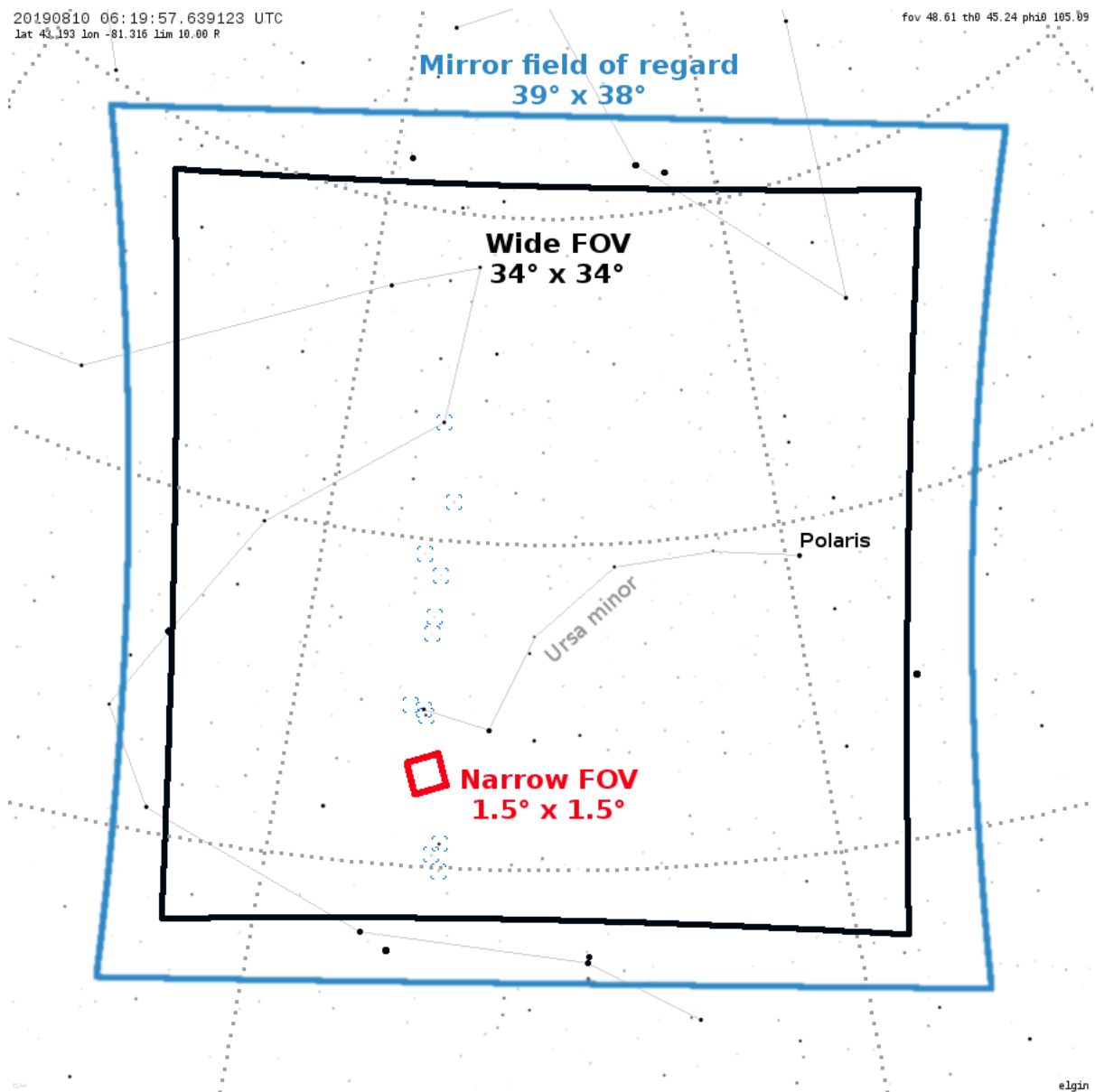
Figure 6.3: Fields of view of all CAMO optical subsystems at the Elginfield site. The narrow field of view can move to any location inside the mirror field of regard.
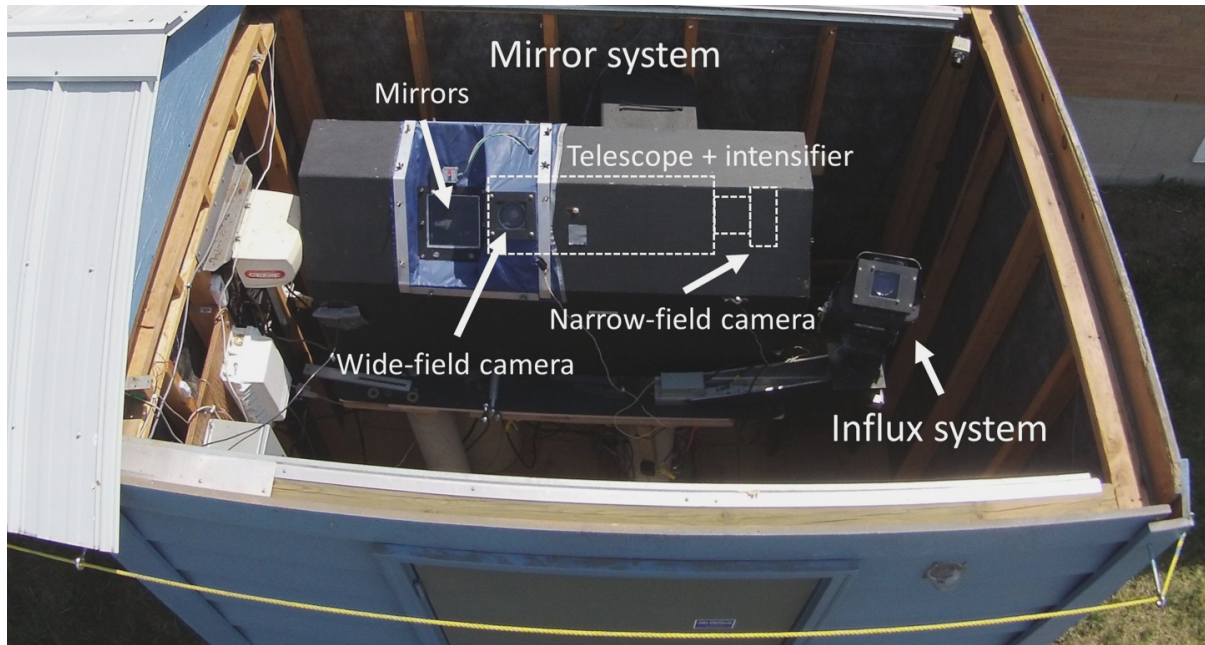
Figure 6.4: Layout of CAMO systems. The enclosure of the mirror tracking system with BK7 glass windows of individual cameras is shown. The position of the telescope (inside the block enclosure) is outlined and superimposed on the image. The CAMO influx camera (Musci et al., 2012) is at the lower right, but is not used in this work.

field data possible. Note that there are no encoders which read the actual position, thus the "commanded to" and the actual position may differ. We find that this simple tracking algorithm is able to keep meteors within the narrow field of view camera in most cases over their full visible trajectory. Finally, note that because of the tracking delay of 8 frames (0.1 s at 80 FPS), the high-precision position measurements are also delayed, which may cause initial velocities of meteors to be underestimated.

6.3   Calibration

6.3.1   Operational plates for tracking

To steer the mirrors when a meteor is being tracked, wide-field camera imagery coordinates (w_x, w_y) are converted into analog-digital units (h_x, h_y) of the 16-bit voltage controller which positions the mirrors. As the telescope optical axis is fixed with respect to the mirror, it also

points at h_x, h_y - this always corresponds to the centre of the narrow-field camera image axis. This mapping is achieved using a `guide` plate, an affine transform mapping between w_x, w_y and h_x, h_y. Thus when a good `guide` plate is used, tracked meteors should be in the centre of the field of view of the narrow-field camera. `guide` plates are created by pairing stars in the wide-field camera imagery with the same stars centred in the narrow-field camera, and fitting an affine `AFF` type plate (see C.2 for details). As the narrow-field camera has a very small field of view, it would be difficult to do this pairing manually, so a mosaic of narrow-field images taken across the whole mirror field of regard is constructed to produce a first fit when the optical system components are installed or have been moved.

The fitting procedure requires the paired stars to be centered in the narrow field of view images to produce a quality fit. When the mosaic is created, the stars can be anywhere inside the narrow field of view. To "virtually" center them, a `scale` plate is used which maps offsets from the narrow-field image centre $(\Delta n_x, \Delta n_y)$ to offsets in mirror units $(\Delta h_x, \Delta h_y)$. Thus the `scale` plate is used to compute h_x, h_y coordinates of paired narrow-field stars, and a `guide` plate can be fit.

A `scale` plate is made by locking and centering the mirrors onto a bright star, then moving the mirrors by small steps in a specific pattern to obtain pairs of $\Delta n_x, \Delta n_y$ and $\Delta h_x, \Delta h_y$. An affine type (AFF) plate is fit on those data pairs. Figure 6.5 shows the movement pattern which produces a set of points in the `scale` plate parameter space which form a hexagon. The data points are distributed in such a way as to equalize the distance between the edges of the parameter space and the points themselves, optimally populating the parameter space.

In general the `scale` plate does not change over long periods as it reflects the stability of the fixed effective focal length of the narrow field optics. The `guide` plate is also relatively invariant as long as the wide field and narrow field systems remain fixed relative to one another; this typically does not require updating more than a few times per year.
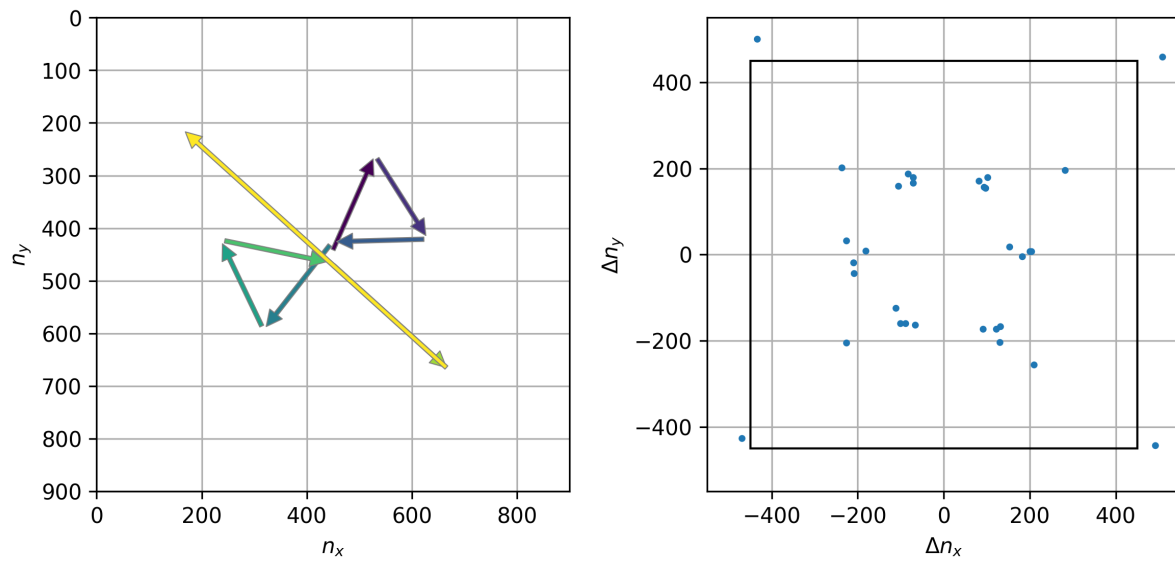
Figure 6.5: Left: One of four patterns used for moving a star within the narrow-field system which produces a hexagonal pattern in the `scale` plate phase space. The pattern starts after the star has been centered. The first movement is represented with the darkest arrow. Right: Points organized in a hexagon in the `scale` plate phase space produced by all four patterns of movement. The black rectangle outlines the range of possible input values of the scale plate, which is ± half the image size in each dimension. The points outside the rectangle are used to improve the fit at the edges of the phase space and were obtained by moving a star past the centre of the image. One such movement is represented by the lightest long diagonal arrow in the left inset, which produced a point around $\Delta n_x = 450$, $\Delta n_y = -450$ in this example.

6.3.2 Astrometry calibration plates

Table 6.1 summarizes all calibration plates used by CAMO. To compute meteor trajectories after data collection, image and mirror coordinates have to be converted into celestial coordinates. The astrometric calibration of the wide-field camera is done by manually pairing image stars with catalog stars and fitting an astrometric `AST` type plate (see appendix C.1 for details). Star positions and magnitudes are taken from the SKY2000 catalog (Weryk et al., 2013). This procedure produces a `calib` plate which maps wide-field image coordinates w_x, w_y into local horizontal celestial coordinates: the zenith angle θ, the azimuth φ measured North of East. The `calib` plate may change slightly under different thermal conditions as the wide field camera mounting moves, but this is usually a small change night-to night (of order a few hundredths of a degree).

The `exact` plate maps mirror coordinates h_x, h_y into θ, φ and is used for computing high-precision astrometry using narrow-field video data. The `exact` plate is created in several steps. First, a list of stars in the wide field of view sorted by their brightness is produced using the star catalog and the `calib` plate. Next, the mirrors are pointed to the 80 brightest stars using the `guide` plate. Off-center stars are moved to the center of the narrow field of view using the `scale` plate. This procedure is done every two hours during system operations to ensure the quality of the astrometry. Finally, the collected pairs of mirror coordinates h_x, h_x and star coordinates θ, φ are used to fit an `exact` AST type plate. The `exact` plate avoids using the `calib` plate which is limited by the spatial resolution of the wide-field camera. The `exact` plate is the most time-varying, as very slight changes in the mirror directions produced by thermal effects may cause drift in the encoder positions relative to the sky. The `exact` plate has to be computed and updated nightly, sometimes even multiple times per night to maintain the full narrow field positional accuracy.

Table 6.1: Meaning of the various plates used for CAMO calibration. w_x, w_y are pixel coordinates of the wide-field camera, n_x, n_y are pixel coordinates of the narrow-field camera, and h_x, h_y are mirror encoder coordinates. θ, φ are local coordinates, namely the zenith angle and the azimuth (+N of due E), as described in Appendix C.1.

Plate	Input	Output	Type	Description
calib	w_x, w_y	θ, φ	AST	Wide-field astrometric calibration.
guide	w_x, w_y	h_x, h_y	AFF	Pointing mirrors to the given wide-filed pixel.
scale	$\Delta n_x, \Delta n_y$	$\Delta h_x, \Delta h_y$	AFF	Narrow-field offsets from image centre to offsets in mirror encoder coordinates.
exact	h_x, h_y	θ, φ	AST	Mirror astrometric calibration.

6.4   Data reduction

6.4.1   CAMO tracking system weblog

After a full night of automated meteor detection is complete, event data (cutouts of wide- and narrow-field videos) are sent to a central server where meteoroid orbits are computed based on the operational astrometric plates. Every morning, a weblog page is generated with images and preliminary orbits of events based on wide-field imagery automatically detected the previous night. CAMO successfully detects and tracks about a dozen meteors to a limiting stellar magnitude of +5 at two stations on an average clear night with nominal meteor activity. Videos of tracked events can be inspected which helps to identify events suited for further in-depth study (through manual data reduction). Figure 6.6 shows a screenshot of the weblog page showing three Perseid meteors from August 13, 2019.

6.4.2   Manual reduction of wide-field data

The reduction of data from the wide FOV camera is described in detail in Weryk et al. (2013). Briefly, the ASGARD automated meteor detection software (Weryk et al., 2007), stores raw video frames of meteor detections. Flat fields are created by median co-adding a large number of video frames from throughout the night, which eliminates star trails. calib astrometric plates are manually fit on the video data from both the Elginfield and Tavistock sites to ensure

Figure 6.6: Screenshot of the CAMO weblog page showing three Perseids. Co-added video frames from all sites and both wide and narrow field of view cameras are shown.

good quality of the astrometry and photometry.

Meteor position picks are done by manually defining the centroiding region position and radius (the semi-automated algorithm computes intensity-weighted centre of mass) and the photometry is done by masking which pixels belong to the meteor on each video frame. The astrometric picks are run through the meteor trajectory estimation code based on Borovička (1990) which uses a lines of sight method, and a heliocentric meteoroid orbit is computed. This initial solution is only used to decide whether the meteor warrants additional manual reduction.

6.4.3   Manual reduction of narrow-field data

Narrow-field data is manually reduced using the `mirfit` software (previously used in Subasinghe et al., 2017). With this software, the raw video frames and astrometric plates (`exact` and `scale`) which were created closest to the time of each event are loaded. The quality of the astrometric solution is confirmed by reverse mapping star catalog positions onto each video frame, and checking that they match the true positions of stars. Figure 6.7 shows the `mirfit` graphical user interface and an example with two stars in the narrow field of view.

Making meteor position picks on every frame is often difficult and subjective due to the complex morphology and fragmentation that may be present. In many cases, the precision of the meteor trajectory is limited by the morphology, regardless of the resolving power and precision of the CAMO tracking system. For example, Figure 6.8 shows a meteor that disintegrated into a long cylinder of luminous dust, making any consistent and precise astrometric picks after fragmentation impossible. However, we found that the best approach is to centroid on the most consistent leading fragment or feature that exists throughout the event as long as possible. This maximizes the number of picks, and better ensures a common feature is tracked from both sites. Sometimes the picks must be set manually to a pixel at the leading edge of the trail during fragmentation, as individual features cannot always be resolved.

Computing celestial coordinates of observed meteors using narrow-field data is done in
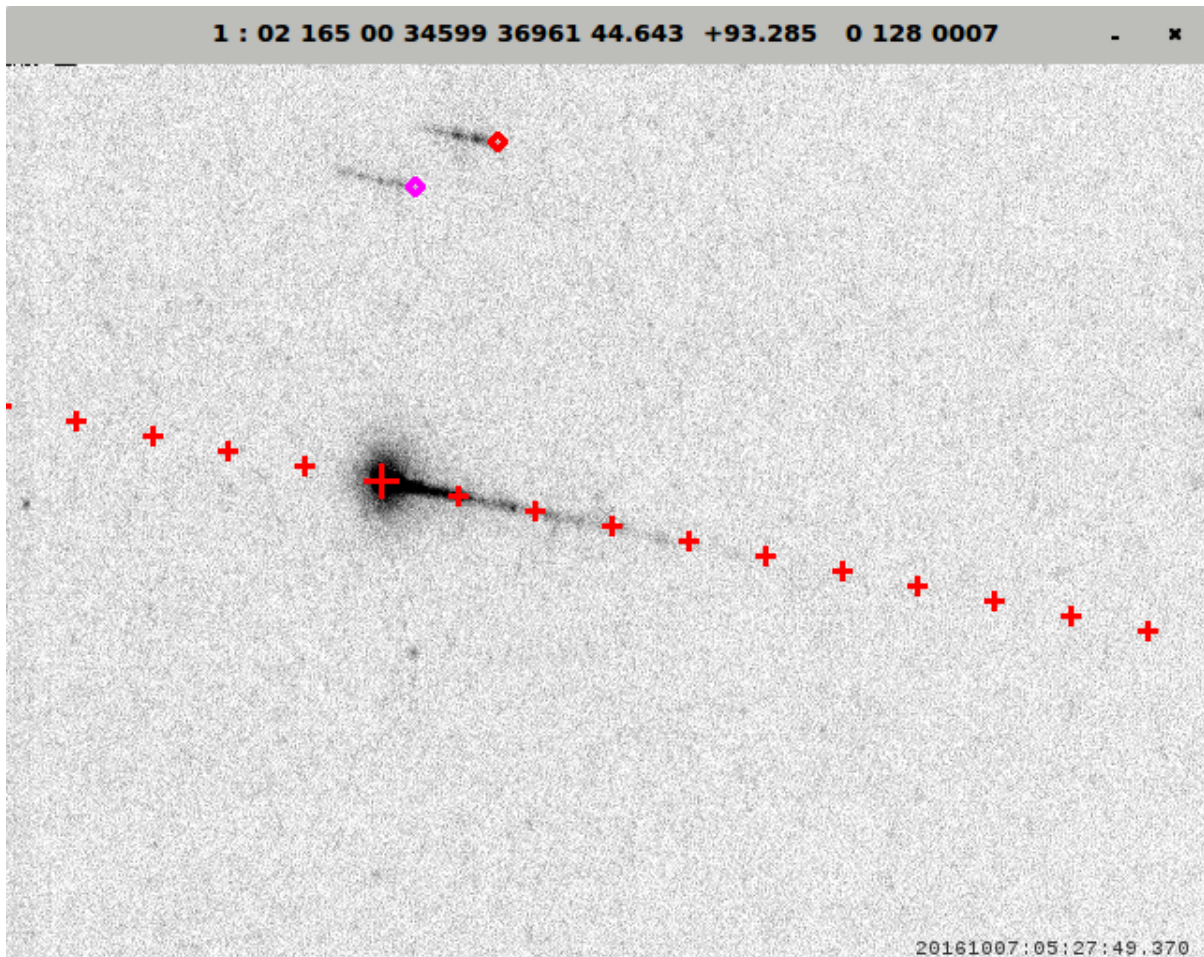
Figure 6.7: `mirfit` graphical user interface. A video frame with a meteor is shown, and the centroid pick for the current frame is marked with a large red plus sign, while astrometric picks on previous and subsequent video frames are marked with smaller red plus signs. Two diamonds mark the predicted positions of stars in the image, which become trailed as the mirrors track the meteor. The diamonds are the exact plate estimates of the two catalog star positions, and are at the end of each trail due to the camera timestamping each video frame at the end of the exposure.
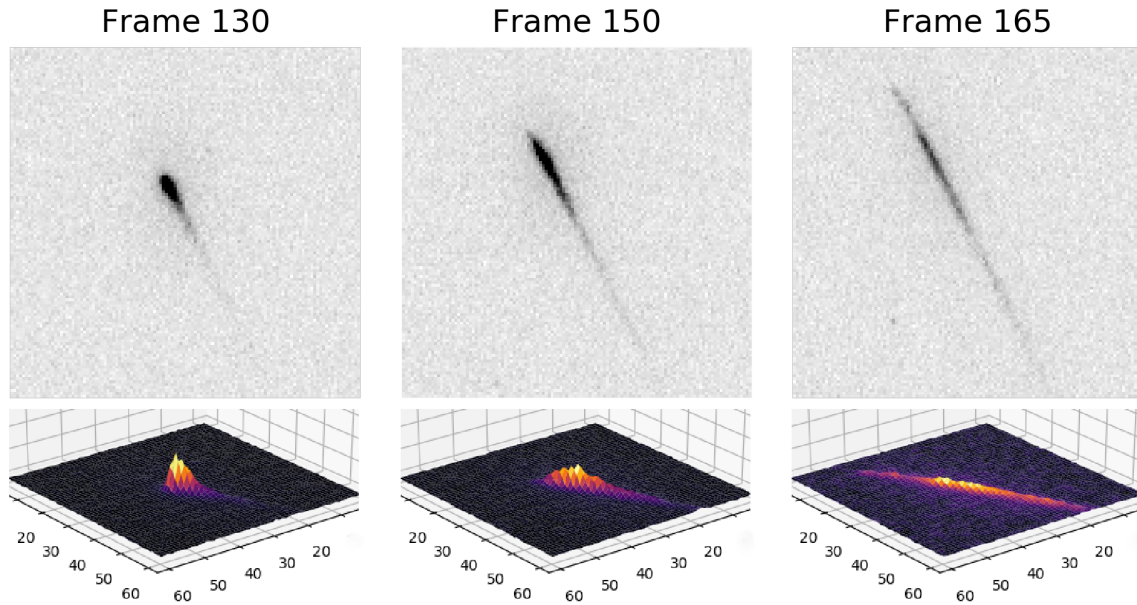
Figure 6.8: Three video frames from a meteor observed on May 17, 2017 at 04:54:26 UTC. The top plots show cropped video frames around the meteor, while the bottom plots shows their respective 3D intensity profiles.

several steps. Figure 6.9 shows a diagram of the procedure. First, assuming picks of meteor positions with coordinates n_x, n_y were done on a particular narrow-field video frame, offsets $\Delta n_x, \Delta n_y$ from the narrow-field image center are computed. $\Delta n_x, \Delta n_y$ are then mapped into offsets in mirror units, $\Delta h_x, \Delta h_y$ using the `scale` plate. $\Delta h_x, \Delta h_y$ indicate the mirror encoder position offset required to centre the meteor in the narrow field. On average, a change of 3 mirror units will shift the narrow-field image by 1 pixel.

As the narrow-field camera's frame rate is not phase synchronized with mirror position updates, the equivalent mirror pointing coordinates h_x, h_y at the time the video frame was recorded are computed by linearly interpolating the recorded mirror positions in time. The offset in mirror units $(\Delta h_x, \Delta h_y)$ is added to the actual mirror positions (h_x, h_y) at the frame time. Using the `exact` plate, the resulting mirror units are mapped onto the celestial sphere. One pixel in the narrow-field image roughly corresponds to 6 arc seconds on the sky (3 m resolution at 100 km range), and thus 1 mirror unit corresponds to about 2 arc seconds on the sky.

The narrow-field photometry is not used operationally because a meteor is usually spread
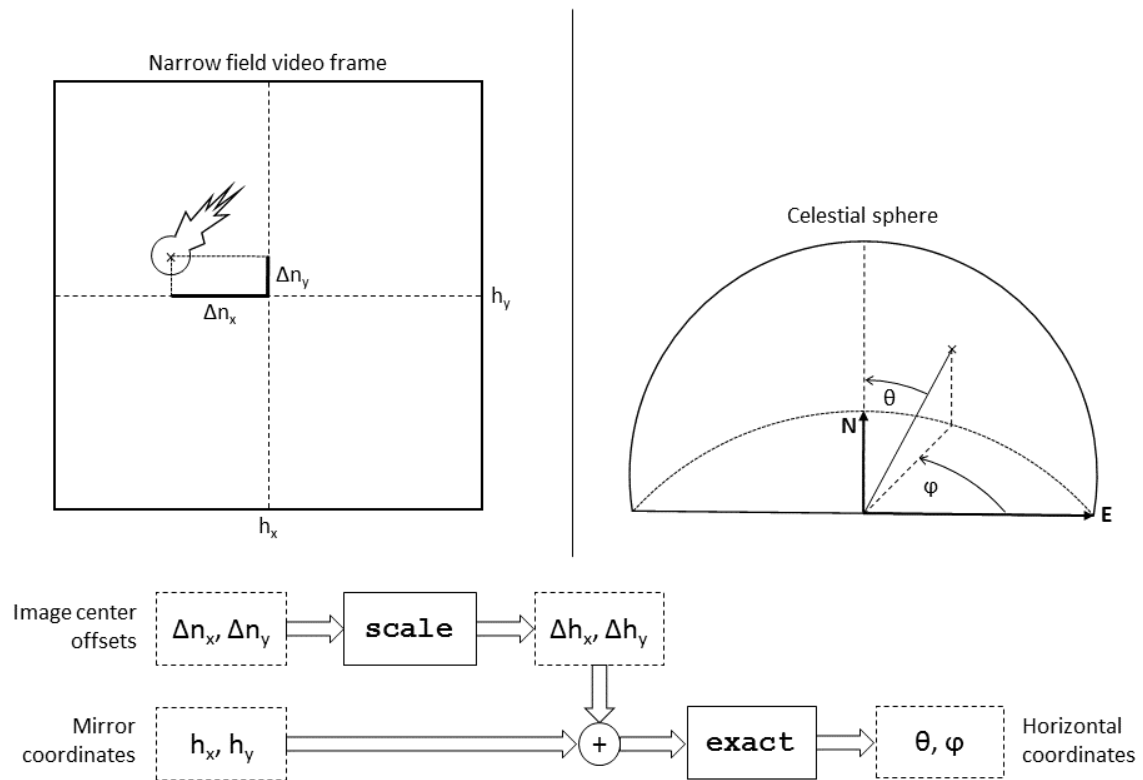
Figure 6.9: Schematic showing how the computation of narrow-field astrometry is performed.

over a large number of pixels in the image, which significantly reduces its signal to noise ratio, especially for fainter wakes. Also, there is a factor of 2 variation in sensitivity across the mirror field of regard, as the total mirror overlap is less on the edges of the field of regard. Nevertheless, photometry can be manually measured for individual events.

Once the narrow-field astrometric reduction is done from both sites, the meteor trajectory is computed using the Monte Carlo trajectory solver (Vida et al., 2019b). This algorithm computes the radiant, heliocentric orbital elements, and associated uncertainties using the variance in the measured look angles as estimators for the precision of the measurements.

6.5   Examples of reduced meteors

In this section, we show three representative examples of ultra-high precision meteor trajectory solutions computed from CAMO narrow-field data and comment on their radiant and velocity accuracy. We show that the accuracy is mainly limited by meteor morphology; the three examples cover meteors having the most to the least favourable morphology.

6.5.1   Morphologies allowing for high precision measurements

Figure 6.10 shows a composite image of a sporadic meteor observed by the CAMO tracking system on October 7, 2016, with the meteor being well tracked from both sites. As seen in the figure, the spatial fit residuals are below one meter (the corresponding angular residuals are ~ 1 arc second), and the point-to-point velocities are very compact and show obvious smooth deceleration. The lag, defined as the "distance that the meteoroid falls behind an object with a constant velocity that is equal to the initial meteoroid velocity" (Subasinghe et al., 2017), matches well between both stations, an indication of a good trajectory solution (Vida et al., 2019b). The meteor showed only continuous fragmentation and no gross fragmentation; this favourable morphology contributed to the quality of the trajectory solution.

In Table 6.2 we give the radiant and osculating orbital elements computed using the Monte
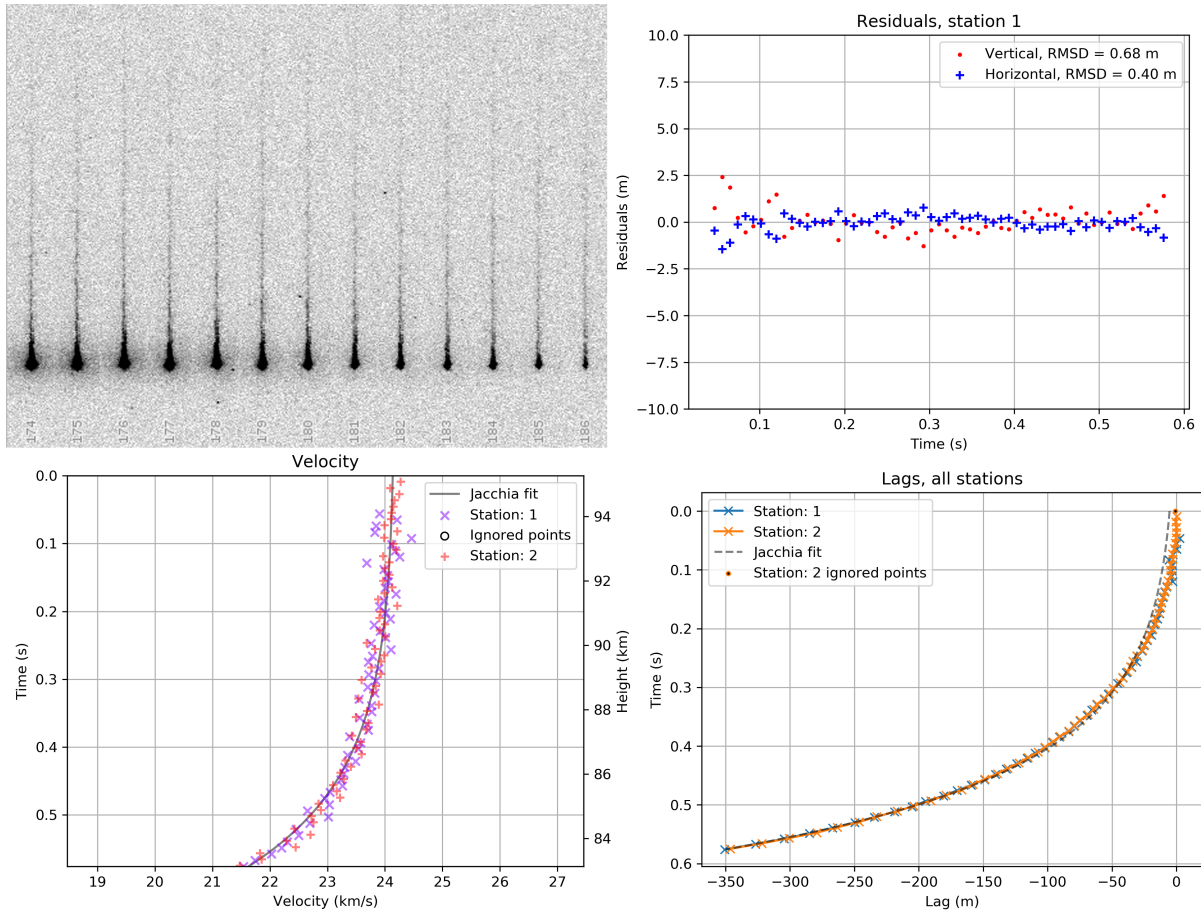
Figure 6.10: Reduction of a meteor observed on October 7, 2016 at 05:27:49 UTC. Upper left: A composite image of the last 13 narrow-field video frames rotated and cropped so that the leading edge is aligned in every frame. The time progresses from left to right at 10 ms increments. Upper right: Spatial fit residuals from the Tavistock site. Lower left: Point-to-point velocities. Lower right: Lag of the leading edge compared to a fixed velocity model. The "Jacchia fit" shows a fitted exponential deceleration model given in equation 6.2.

Carlo trajectory solver (Vida et al., 2019b). The stated uncertainties are small, but there are several caveats. First, the compensation for deceleration prior to detection was not done, thus the initial velocity may be underestimated as much as $500 \, \mathrm{m\,s^{-1}}$ (Vida et al., 2018b). Consequently, the stated velocity measurement uncertainty gives the precision, not the accuracy. Second, Vida et al. (2019a) have shown that radiant uncertainties for CAMO are usually underestimated by a factor of 3 to 4 with this solver based on comparison with simulations. Thus the real radiant accuracy is probably $\sim 0.025°$, well within the minimum precision of $0.1°$ necessary to measure the true physical dispersions of meteor showers (Vida et al., 2019a).

6.5.2   Morphologies with deteriorating measurement precision

Figure 6.11 shows a Southern δ Aquariid meteor observed on August 10, 2019 at 06:09:57 UTC. This meteor had a sudden change in morphology halfway through the observation caused by an increase in the rate of continuous ablation. Prior to the change, the meteor had compact morphology with a short wake. The whole meteor was centroided prior to the morphology change during the manual reduction, excluding the short wake, which produced robust astrometry picks and well-matched velocities from both sites. After the morphology change, the wake became longer and the meteoroid morphology became elongated, showing a leading fragment at the front. At that point the leading fragment was followed, but due to the lower signal to noise ratio and interference from released grains and the wake, the picks were less consistent, which caused a large spread in point-to-point velocities. The change can be seen in the lag as a sudden shift back towards the zero lag line, as the reference point moved forward to the leading fragment by a fixed amount. However, this change did not influence the trajectory fit residuals as the leading fragment did not have a transverse velocity component, though this is not always the case (e.g. Stokan & Campbell-Brown, 2014). Table 6.2 provides the orbital elements and uncertainties for this event. The uncertainties in the radiant and the orbital elements are larger than for the previous event, mainly due to the larger pick scatter in the second half of the meteor trajectory. In contrast, the geocentric velocity uncertainty remained low because the initial velocity used for orbital computation is found using data from the first part of the meteor, in this case prior to the morphology change.

6.5.3   Morphologies which severely limit measurement precision

As a final end-member example, Figure 6.12 shows a meteor on an asteroidal orbit with a probable higher bulk density than the earlier cases, judging from the height range and small deceleration. It exhibited complex morphology (no leading fragment, extended meteor luminosity mostly consisting of a wake), and as a consequence, it was difficult to make consistent position picks. This is reflected in the higher scatter of spatial residuals, velocity, and lag. In
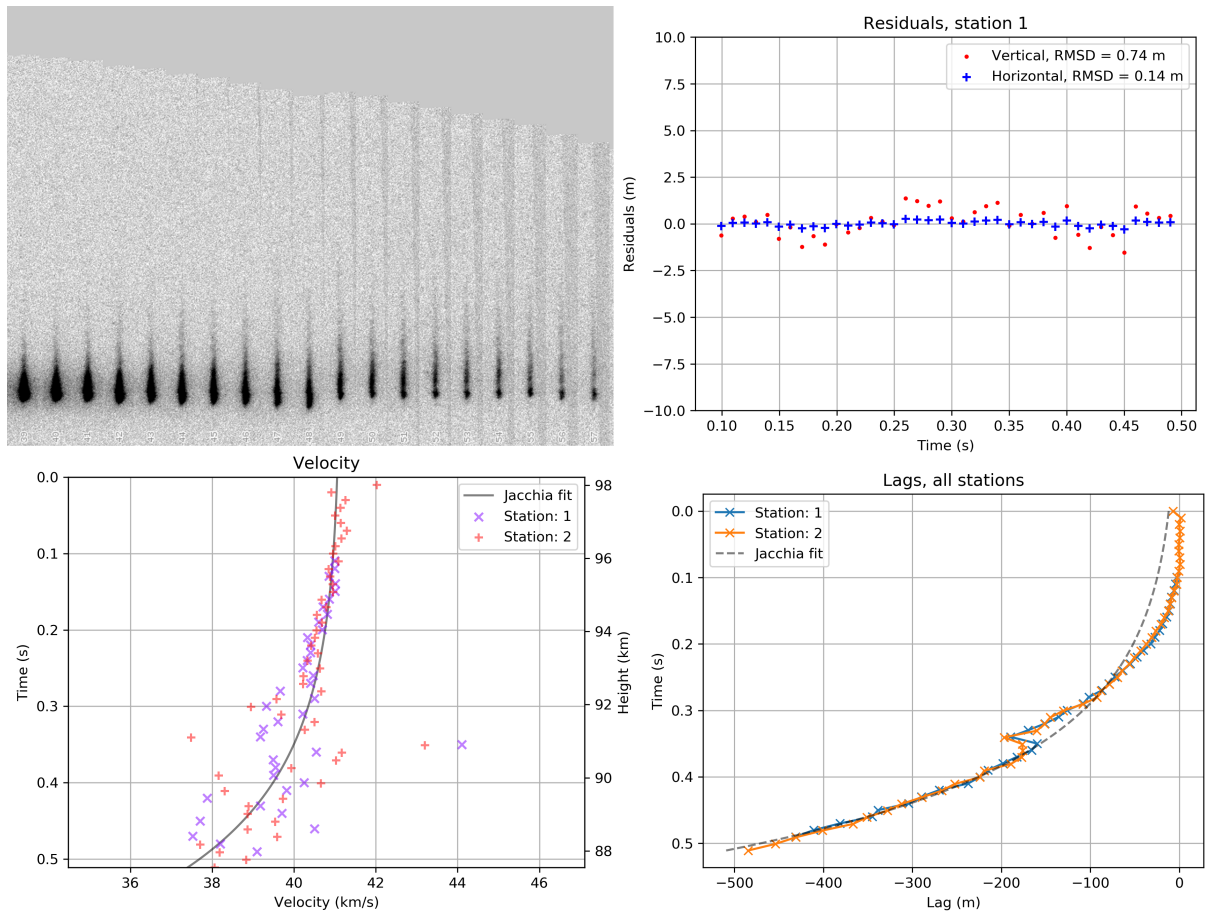
Figure 6.11: Reduction of a meteor observed on August 10, 2019 at 06:19:57 UTC. Upper left: A composite image of the middle 19 narrow-field video frames rotated and cropped so that the leading edge is aligned in every frame. The morphology change occurs halfway though the shown frames. The time progresses from left to right. Upper right: Spatial fit residuals from the Tavistock site. Lower left: Point-to-point velocities. Lower right: Lag with an inflection corresponding to the change in morphology which is visible from both stations.
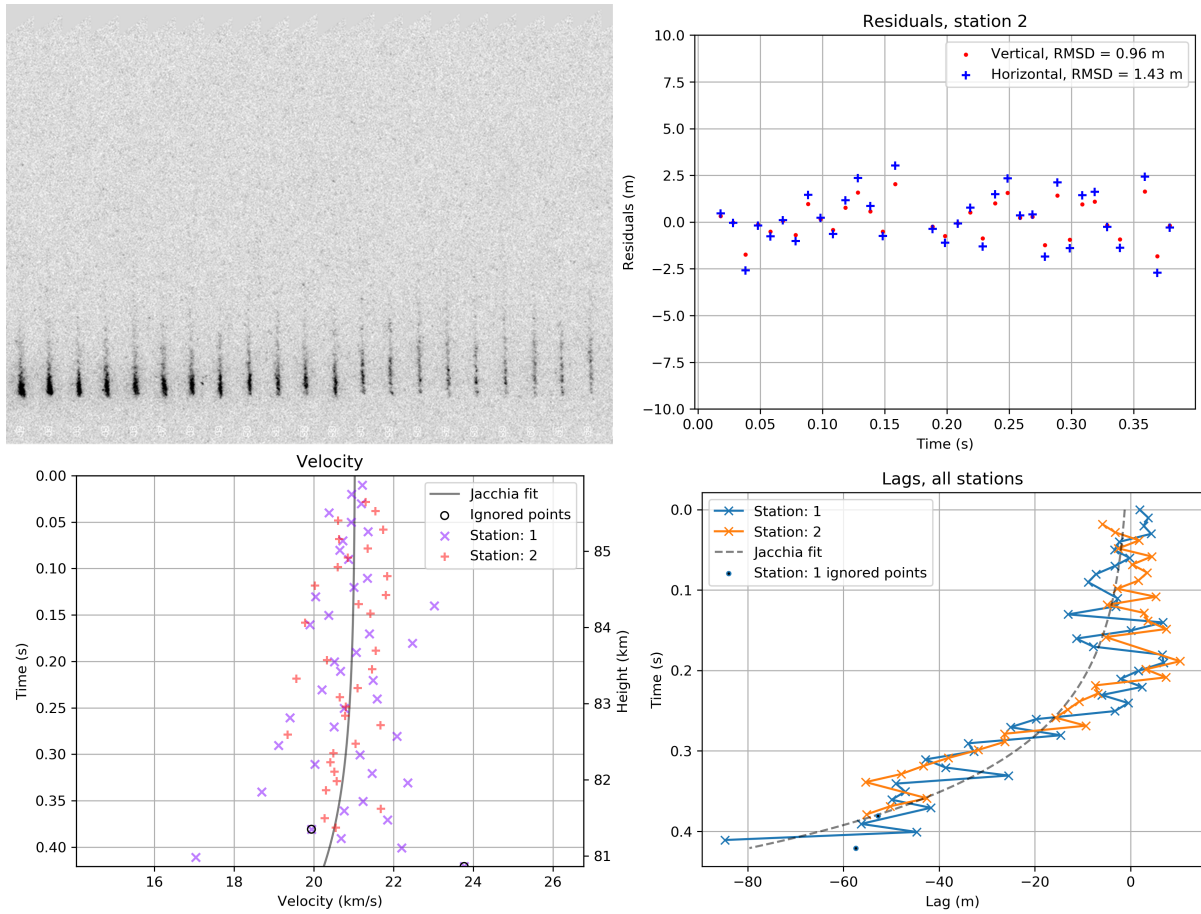
Figure 6.12: Reduction of a meteor observed on August 31, 2019 at 09:12:42 UTC. Upper left: A composite image of 21 selected narrow-field video frames rotated and cropped so that the leading edge is aligned in every frame. The time progresses from left to right. Upper right: Spatial fit residuals from the Tavistock site. Lower left: Point-to-point velocities. Lower right: Lag in distance relative to a constant velocity.

this particular case, the meteor morphology was the limiting factor in achieving better astrometric precision. The radiant and the orbital elements are given in Table 6.2. All uncertainties are larger than for the two previous events due to the larger scatter in astrometric picks. Assuming that the radiant uncertainty was underestimated by a factor of 4, the true total radiant uncertainty is ~0.2°, which may not be sufficiently accurate to measure true physical radiant dispersions of compact meteor showers.

Table 6.2: The geocentric radiant in J2000 and corresponding heliocentric orbital elements of example meteor events. The stated uncertainties are one sigma errors.

	October 7, 2016 meteor	August 10, 2019 meteor	August 31, 2019 meteor
α_g (deg)	11.476 14 ±0.0015	348.615 55 ±0.0033	337.233 62 ±0.0086
δ_g (deg)	15.991 38 ±0.0057	−14.049 97 ±0.0068	12.020 91 ±0.0450
v_g (km/s)	21.474 53 ±0.0010	39.488 92 ±0.0008	17.805 44 ±0.0181
a (AU)	1.915 483 ±0.0001	2.555 910 ±0.0005	1.338 224 ±0.0005
q (AU)	0.556 308 ± < 0.0001	0.100 421 ± < 0.0001	0.593 527 ±0.0003
e	0.709 573 ± < 0.0001	0.960 710 ± < 0.0001	0.556 482 ±0.0004
i (deg)	7.502 682 ±0.0044	26.368 226 ±0.0204	12.390 136 ±0.0373
ω (deg)	273.906 34 ±0.0032	147.014 49 ±0.0070	278.774 75 ±0.0286
Ω (deg)	194.156 40 ± < 0.0001	317.090 80 ± < 0.0001	157.436 69 ± < 0.0001

6.6   Meteoroid compressive strengths derived from direct observations of gross fragmentation

In contrast to optical meteor systems used for previous estimates of meteoroid compressive strengths (see the summary in Section 6.1.3), CAMO can directly observe gross fragmentation of meteoroids. Earlier we described the CAMO data calibration and reduction tools, and demonstrated how meteor morphology limits the ultimate trajectory accuracy. In this section, we discuss those CAMO meteors which show gross fragmentation of the main meteoroid body into several discrete fragments, a process which we assume results from structural failure of the meteoroid under the action of atmospheric dynamic pressure. Meteors with this morphology make up about 5% of all observed meteors with CAMO, and this morphology is not correlated with orbital type (Subasinghe et al., 2016).

These events often have the least accurately defined astrometry because there is no single consistent point of reference that can be tracked. Frequently at the beginning of the luminous track the meteor may resemble a single object, but the amount of continuous fragmentation is usually high and any further consistent astrometric picks become impossible once gross fragmentation occurs. Thus, we only use the wide-field data to compute the reference trajectory, and we project the narrow-field astrometric picks of individual fragments onto it to determine

their dynamics. High-precision measurement of fragment deceleration allows us to compute precise values of the aerodynamic ram pressure as we know the height and speed at each frame. By observing when fragmentation occurs in the narrow field imagery, we can estimate precise values of meteoroid compressive strength.

6.6.1 Sensitivity analysis

First we examine the uncertainty of individual parameters used to compute the dynamic pressure from equation 6.1. For the drag coefficient, we use $\Gamma = 1$, a value appropriate for a sphere, which is a common assumption for meteoroid ablation in free molecular flow (Fisher et al., 2000; Campbell-Brown & Koschny, 2004; Borovička et al., 2007; Vida et al., 2018b). In fact, many works even exclude the drag coefficient from the equation, implicitly assuming it is unity (e.g. Blum et al., 2014; Trigo-Rodríguez & Llorca, 2006).

Observations of the morphology of cometary dust particles by Hilchenbach et al. (2016) indicate that meteoroid components are oblate spheroids, although we are not aware of any works showing detailed shape analysis. If the axial ratios of spheroid meteoroid components were to vary from 0.5 to 1.0, drag coefficients may also vary within a factor of two (List et al., 1973). If that was the case, and the meteoroids were not rotating, we would expect to see a comparable variation in dynamic pressures at points of fragmentation among fragments of one meteoroid, assuming a fixed velocity, atmospheric mass density, and homogeneous strength.

In section 6.6.2 we further discuss the possibility of drag coefficient variation using direct observations of fragments of one meteoroid. Γ also varies with the Reynolds number, but Thomas & Whipple (1951) show that spherical meteoroids moving in a highly rarefied gas and at hypersonic speeds have $\Gamma \sim 1$, thus in this work we fix it to unity.

For our events, uncertainty in P_{dyn} is not driven by the uncertainty in the velocity measurement. Vida et al. (2019a) have shown that initial velocities can be reliably measured to within $0.5\,\mathrm{km\,s^{-1}}$. Even if one assumes a low initial velocity of only $10\,\mathrm{km\,s^{-1}}$, the maximum error in dynamic pressure is only 10%.

The last term required to compute the dynamic pressure is atmospheric mass density. The most sophisticated atmosphere mass density model available to date is the NRLMSISE-00 model (Picone et al., 2002) which gives the atmosphere mass density as a function of geographical location, time, and solar activity. The time component takes the influence of seasonal changes into account. The solar activity is modelled by using the 10.7 cm solar flux $F_{10.7}$ which slowly changes with the 11 year solar cycle, although it can change dramatically on shorter time scales due to the evolution of active regions and solar flares (Tapping, 2013). Picone et al. (2002) show that the influence of changes in $F_{10.7}$ can cause the air mass density in the upper atmosphere (>600 km altitude) to change with an amplitude of half an order of magnitude.

Comprehensive models like The Whole Atmosphere Community Climate Model (WACCM) (Qian et al., 2013) or the Spectral Mesosphere/Lower Thermosphere Model (SMLTM) (Akmaev et al., 2006) provide some insight into the mass density changes over time due to greenhouse gas cooling in the mesosphere or solar effects. Recently, these trend studies were updated using WACCM-X (Solomon et al., 2019), echoing the previously reported density changes at the Mesosphere and Lower Thermosphere (MLT). It was found that changes in mass density in the MLT are larger as compared to the altitudes below and directly above the MLT (150 – 200 km).

From meteor radar observations with the co-located CMOR (Canadian Meteor Orbit Radar) a neutral air density change of approx. 6% per decade was obtained (Stober et al., 2014), which corresponds well to the WACCM and SMLTM results. Additionally, a solar cycle duration response of 2-3% in the neutral air density was estimated. Other meteor radar studies using the meteor ablation altitude (Jacobi et al., 2011; Lima et al., 2015; Liu et al., 2017) or from vertical profiles of the ambipolar diffusion measurements (Yi et al., 2019) have also estimated the seasonal variability of the neutral air density.

However, it is the short term variability of the neutral air density induced by atmospheric waves that is most germane for uncertainty analysis for compressive strength estimation from

CAMO. Stober et al. (2012) explored the magnitude of the neutral air density at heights of interest for CAMO and showed that they can vary due to planetary waves during the winter season 2009/2010 using three meteor radars across Europe.

We investigated the short term variability of the neutral air density using meteorological fields from the NAVGEM-HA (Navy Global Environmental Model- High Altitude) numerical weather prediction system (Hogan et al., 2014; McCormack et al., 2017; Eckermann et al., 2018). NAVGEM-HA combines a global forecast model of the atmosphere with a 4DVAR hybrid data assimilation scheme (Kuhl et al., 2013) to produce global atmospheric specifications for a given time period extending from the surface to ~116 km altitude. NAVGEM-HA assimilates a over 3 million ground-based and satellite-based observations every 6 hours. In the altitude region from $20-100$ km the primary observation sources are temperature, ozone, and water vapor retrievals from the Microwave Limb Sounder (MLS) on board the Aura satellite and temperature retrievals from the SABER instrument on board TIMED. The NAVGEM-HA output used in this study consists of global 6-hourly wind, temperature, and geopotential height fields on a 1° latitude/longitude grid over 74 vertical levels from 1 January to 31 December 2010. At the upper two model levels (above ~95 km altitude), enhanced horizontal diffusion (i.e., a "sponge layer") is applied to reduce wave reflection (McCormack et al., 2015). A validation of the NAVGEM-HA fields at the CAMO Tavistock site can be found in Stober et al. (2019).

The annual mass density variation at the Tavistock site based on NAVGEM-HA is shown in Figure 6.13. The upper panel shows the absolute density values as contour plot with logarithmic scaling, and the lower panel shows the relative variability in percent. We computed a median density value for each geopotential altitude for the whole year of 2010 and used it to normalize all values. Hence, the variability plot not only contains the seasonal variability but also the atmospheric waves. From the plots, it is apparent that the mass density at meteor heights can vary by up to ±25% on short time scales. It is therefore the main driver of the uncertainty in the dynamic pressure. We adopt this ±25% value as representative of the air mass

Absolute mass density

Mass density variation from the mean
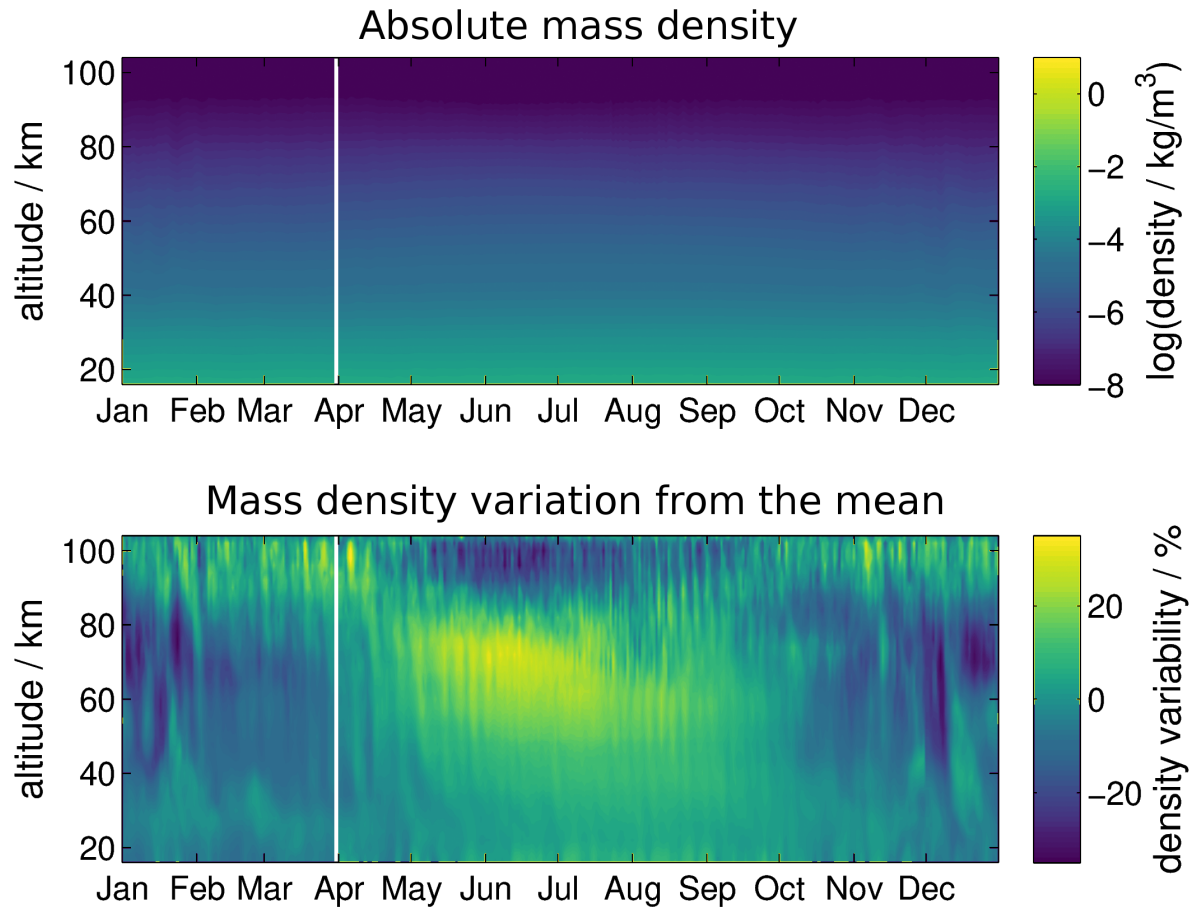
Figure 6.13: Measurement of atmosphere mass density using NAVGEM-HA above the CAMO Tavistock site. The upper panel shows absolute values of the mass density as daily mean values for the year 2010. The lower panel visualizes the relative density variation from the mean.

density uncertainty and use it in what follows to estimate all dynamic pressure measurement uncertainties.

6.6.2 July 21, 2017 event

We begin with a specific case study of an unusual fragmenting meteoroid observed on July 21, 2017. It had a very shallow entry angle of $8°$ degrees and was observed for almost 4 seconds and shows a clear double-peaked lightcurve. It was observed by the wide-field cameras from both sites almost in its entirety, but was only well tracked by the Tavistock narrow-field camera - the tracking parameters were not well estimated from Elginfield (possibly due to the long

wake) where it was only tracked for a few frames before it exited the field of view. Figure 6.14 shows the co-added video frames captured by the wide-field cameras from both sites.

Morphology

The tracking at Tavistock started 0.45 seconds after it was initially observed in the wide-field camera, as the meteor was below the automated detection threshold before that time. Figure 6.15 is a mosaic of 24 narrow-field video frames from Tavistock which shows the morphological evolution. When the tracking started, an extended wake could be seen in the wide-field video. For the complete narrow-field video, see the supplementary materials or `http://meteor.uwo.ca/~dvida/IMC2017/20170721_tavis_narrow.gif`.

The narrow-field video showed that the wake consisted of unresolvable grains (or dust) lagging behind several fragments - the fragments themselves were also enveloped in the dust. Starting 1.4 seconds after the tracking began, the dust was completely gone, leaving 12 discrete fragments visible. During this time, the fragments noticeably decelerated and some showed transverse motion. Several fragments with lower deceleration, which were always brighter and presumably more massive, overtook fainter fragments. During this period devoid of wake, the wide-field video shows a significant dip in the brightness of the meteor as a whole, as shown in Figure 6.16.

After one more second, the fragments developed short wakes and themselves disintegrated, and the total brightness increased again. At this point, the measurements from the wide-field camera show that the bulk of the meteoroid started to rapidly decelerate, as shown in Figure 6.17 (around 2.5 seconds), and that this disintegration produced a second peak in the light curve. Meteors with double peaked light curves were investigated by Roberts et al. (2014) and Subasinghe & Campbell-Brown (2019). However, the observed behaviour of this event does not match any of their proposed meteoroid ablation or fragmentation mechanisms.
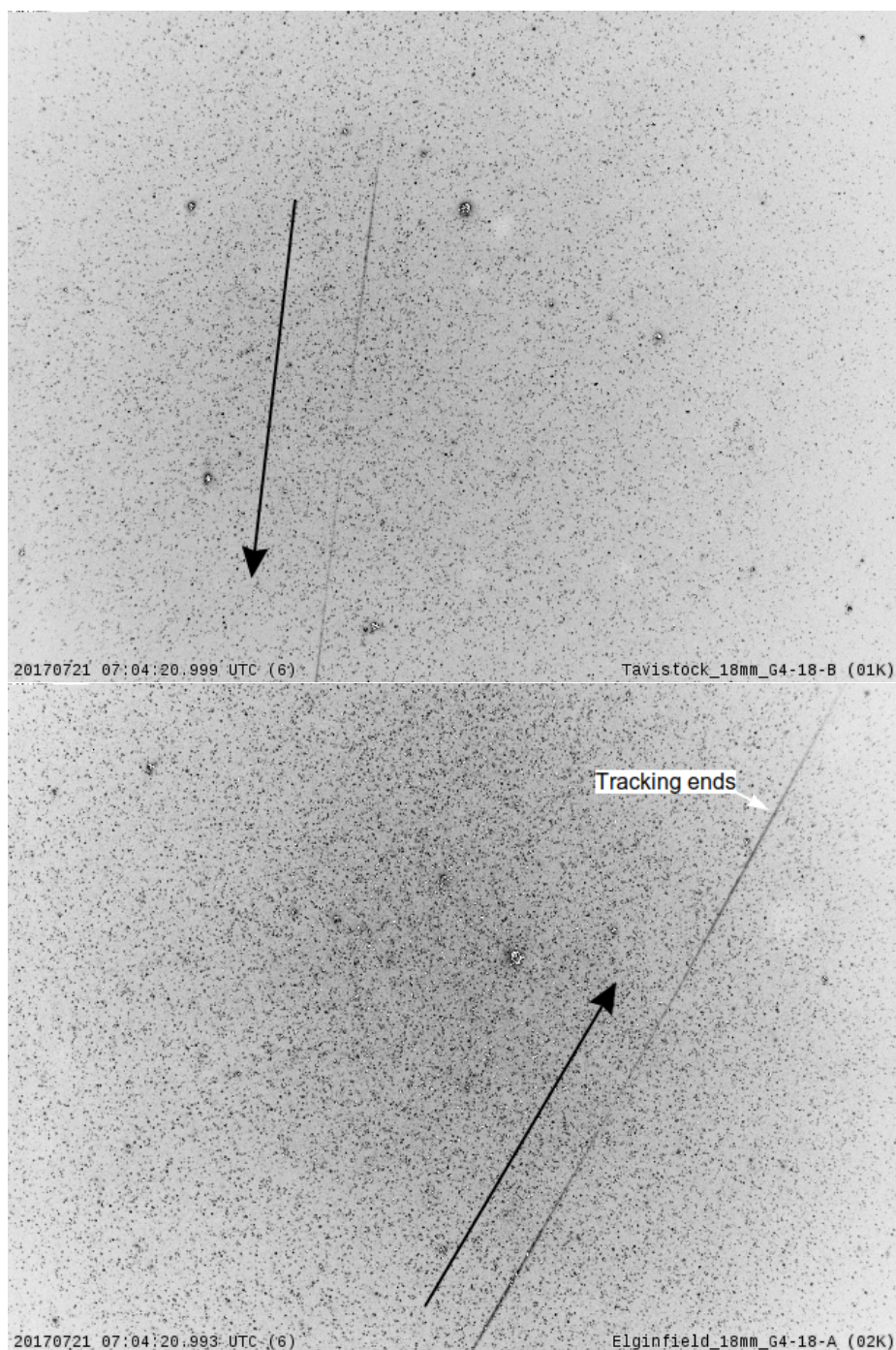
Figure 6.14: Grey-inverted co-added video frames of the July 21, 2017 event. The images are heavily speckled by intensifier shot noise due to co-adding; individual video frames have a much better signal to noise ratio. Top: Tavistock wide-field camera. Bottom: Elginfield wide-field camera. The black arrow indicates the direction of flight, and the white arrow indicates the point on the trajectory where the tracking from the Tavistock site ended.
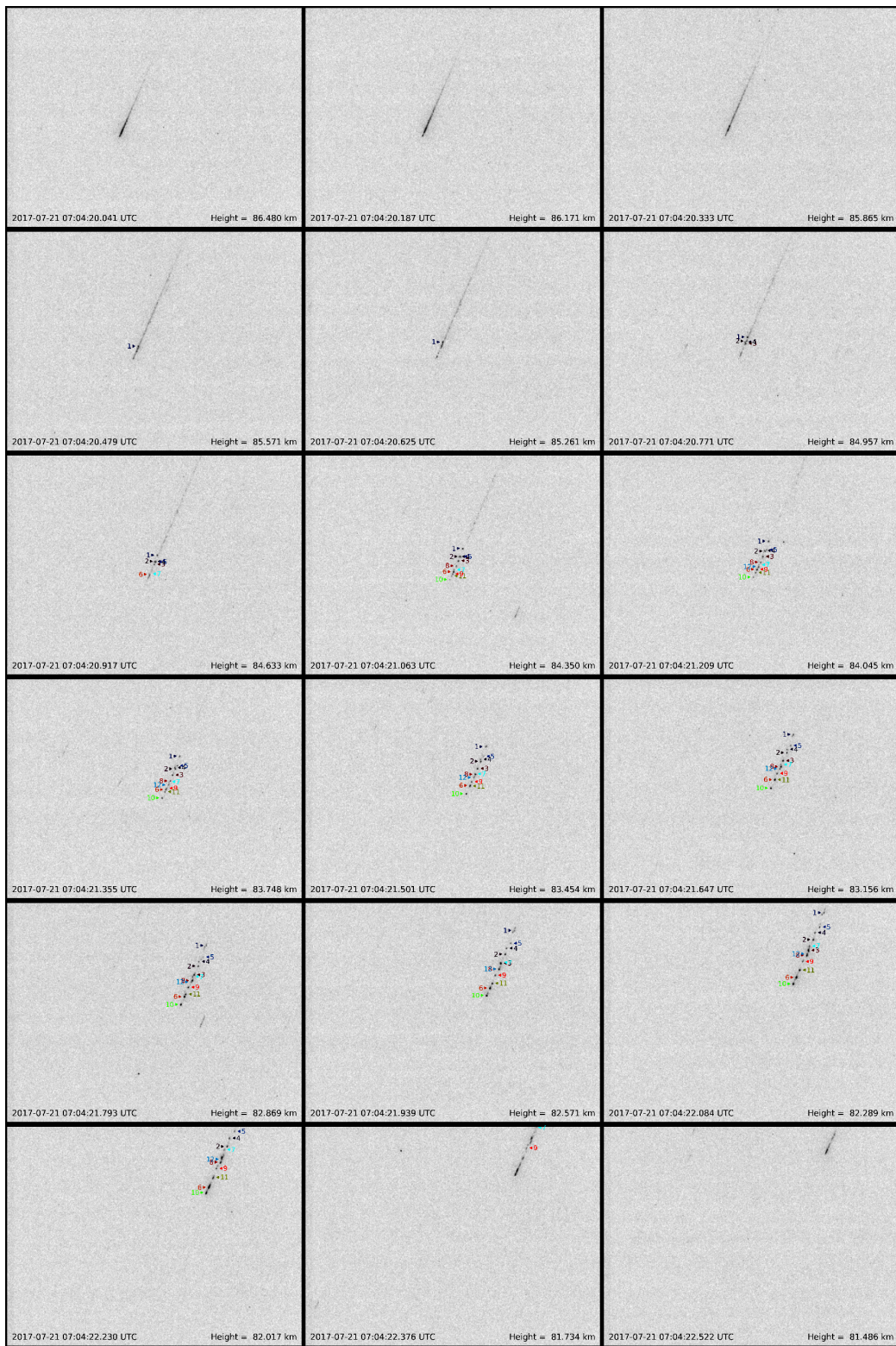
Figure 6.15: Mosaic of 24 narrow-field video frames from the Tavistock site for the July 21, 2017 meteor. Each discrete fragment has been tracked and labeled with a unique number.
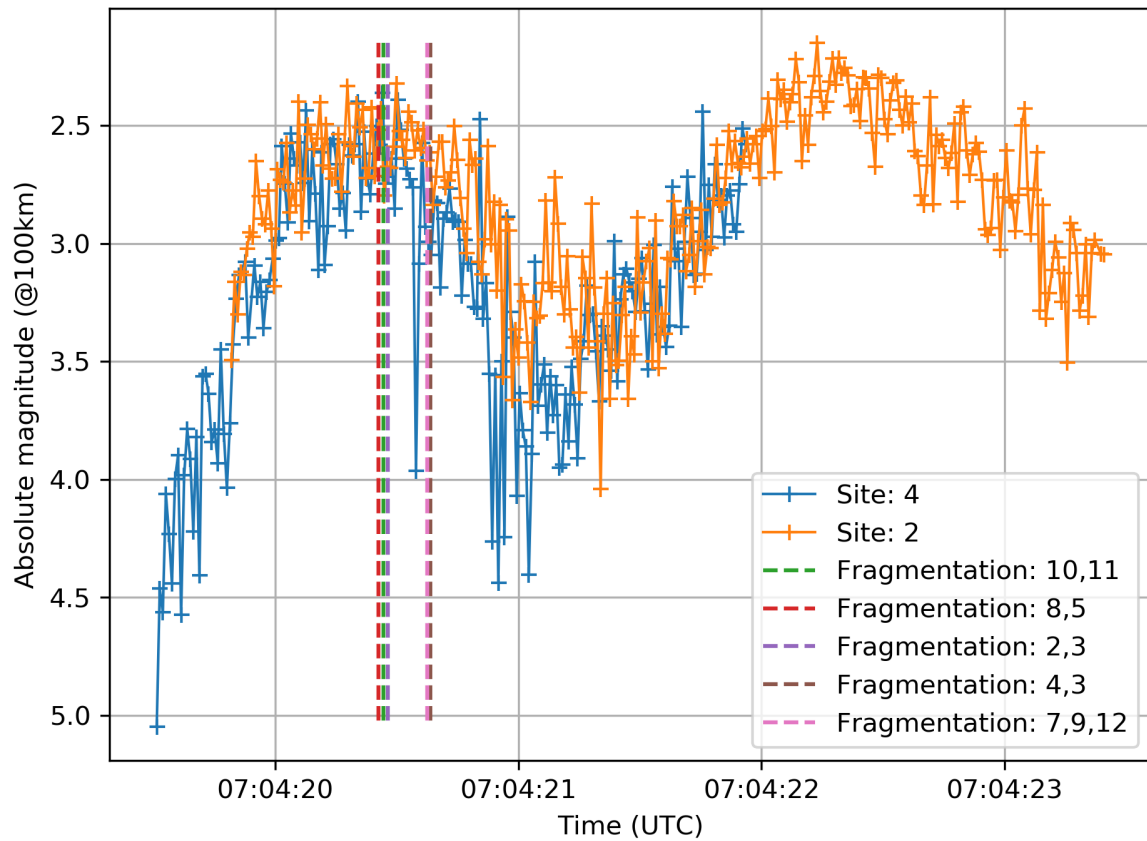
Figure 6.16: Wide-field light curve of the July 21 fragmenting event. Station 2 is Elginfield, station 4 is Tavistock. Vertical lines show the moments of gross fragmentation visible in the narrow field imagery.
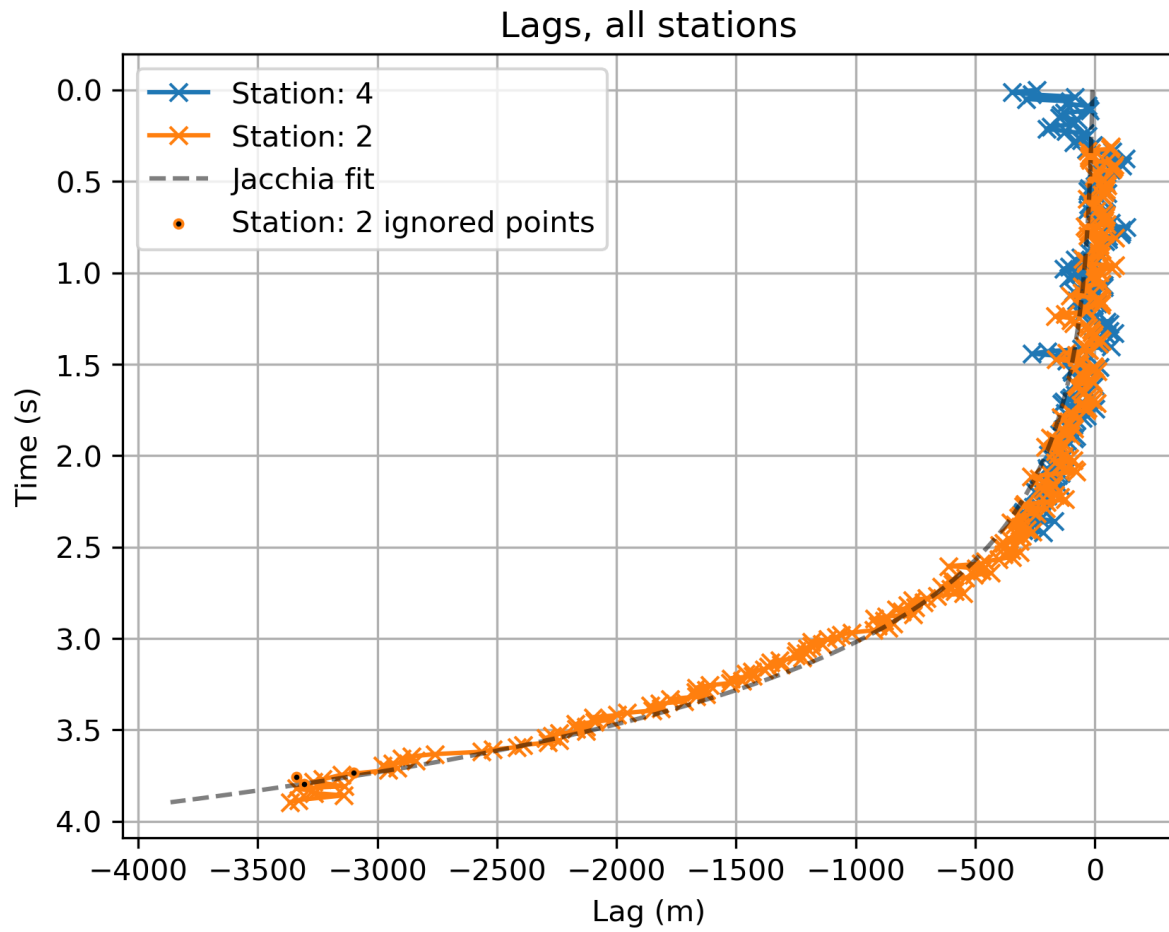
Figure 6.17: Wide-field lag for the leading edge of the visible meteor. Station 2 is Elginfield, station 4 is Tavistock.

Radiant and orbit

Because narrow-field data was only available from the Tavistock site, we used wide-field data from both sites for trajectory and orbit calculation. Due to its long duration, the meteor experienced significant bending of the trajectory from a straight line due to gravity. This is taken into account using the Vida et al. (2019b) meteor trajectory estimation method which we use here.

Figure 6.18 shows the total trajectory fit residuals computed with respect to the radiant line, showing how significant the deviation from the straight line approximation is in this case. The average trajectory fit residuals from both sites were around 25 m, which translates to about 1 arc minute.

From the wide field imagery light curve, we computed a photometric mass of $m = 0.27$ g using the bolometric power of a zero-magnitude meteor $P_{0m} = 840$ W (Weryk & Brown, 2013) and a dimensionless luminous efficiency $\tau = 0.7\%$ (Campbell-Brown et al., 2013) in the red bandpass. Because the end of the meteor was not observed, this mass is a lower limit. Furthermore, due to the uncertainty of the luminous efficiency, the mass uncertainty is at least a factor of 2 (Subasinghe & Campbell-Brown, 2018). Assuming a bulk density of $700 \, \mathrm{kg \, m^{-3}}$, the meteoroid had a diameter of 9(2) mm.

The meteor entered the atmosphere at an angle from the horizontal of only $7.8°$. It was first observed at a height of 87.849 km and it exited the wide camera field of view 3.89 s later at a height of 79.882 km. The velocity at the beginning was $15.9626 \pm 0.0051 \, \mathrm{km \, s^{-1}}$, although it had certainly decelerated from its true pre-atmosphere velocity due to the low entry angle, low velocity, and small size (Vida et al., 2018b).

To quantify the amount of deceleration prior to detection, we used the single-body version of the ablation model of Campbell-Brown & Koschny (2004) to simulate the meteoroid and compute the deceleration from the top of the atmosphere (assumed at 180 km) until it was detected by the wide-field cameras. The simulation roughly reproduces the observed conditions at the point of detection assuming a mass $m = 0.17$ g, bulk density $\rho = 700 \, \mathrm{kg \, m^{-3}}$, heat of ablation $Q = 4600 \, \mathrm{kJ \, kg^{-1}}$, a dimensionless luminous efficiency of 1.4%, and a beginning
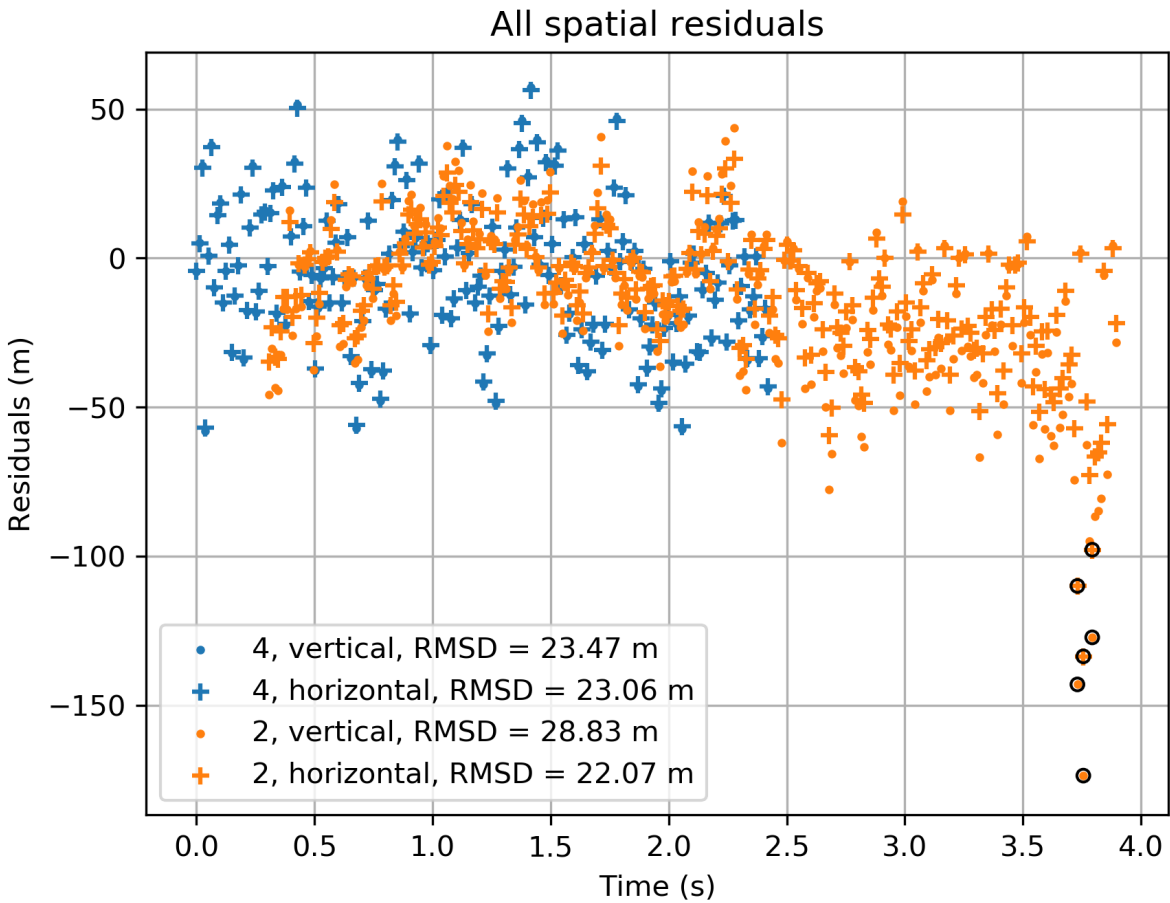
Figure 6.18: Wide-field camera trajectory fit residuals. The bending of the trajectory due to gravity is visible. This should be ~ 50 m for 3.5 seconds of flight. Note that the residuals are computed with respect to a straight line aligned with the radiant, and not a curved trajectory; thus the vertical residuals show an offset near the end. Black circles indicate 3σ outliers which were excluded from the trajectory fit.

Table 6.3: Radiant and orbital elements (in J2000) of the July 21, 2017 fragmenting meteor.

Parameter	Nominal	$v_0 + 400\,\mathrm{m\,s^{-1}}$	Uncertainty*
α_g	253.626	254.399	0.017°
δ_g	-30.216	-29.500	0.103°
v_g	11.839	12.381	$0.007\,\mathrm{km\,s^{-1}}$
$\lambda_\odot$	118.482	118.482	NA
$L_g - \lambda_\odot$	137.292	137.883	0.008°
B_g	-7.583	-6.796	0.032°
a	3.199	3.588	0.005 AU
e	0.703	0.736	0.0005
q	0.952	0.948	0.0001 AU
Q	5.447	6.229	0.010 AU
ω	32.258	32.860	0.010°
i	2.400	2.233	0.033°
π	330.644	331.239	0.094°
T_j	2.742	2.574	0.002

* uncertainties indicate measurement precision, not accuracy

entry angle of 15°, although we emphasize this is not a unique solution.

Note that the entry angle in the simulation is the entry angle relative to the surface of the Earth above the simulation start point, at a height of 180 km. The change in the initial entry angle was caused by the curvature of the Earth as the ground distance between the beginning of the simulation and the first observed point was over 800 km. Here a higher luminous efficiency had to be adopted compared to earlier because no fragmentation was included in the model. To reproduce the measured initial velocity, we had to assume a velocity which was $400\,\mathrm{m\,s^{-1}}$ higher at the beginning of the simulation, indicating that the semi-major axis was ~ 0.4 AU higher than the nominal value.

Table 6.3 lists the meteoroid's radiant and orbital elements, with and without the initial velocity correction. The meteoroid came from the antihelion source and was not associated with any known meteor shower. Its Tisserand's parameter with respect to Jupiter suggests it might have a Jupiter-family comet (JFC) origin. We believe that the ejection from its parent comet happened very recently as it was on a Jupiter crossing orbit, and such orbits have short dynamical lifetimes.

Deceleration, strength, and mass distribution of fragments

Narrow-field video data from Tavistock was reduced in `mirfit` by manually picking the centroids of all discernible fragments. The fragments were labeled from 1 to 12, according to their order of appearance. The celestial coordinates of each fragment were projected onto the trajectory estimated from wide-field observations. As there was no multi-station narrow-field data, only along-track positions of fragments could be precisely determined. Fragments 4 and 7 show a perpendicular offset from the trajectory (a sudden jump at the moment of fragmentation to a position parallel to other fragments), but only lower limits of transverse positions can be computed. Interestingly, these transversely offset fragments show no constant transverse velocity after fragmentation, indicating that they received and immediately lost momentum in the transverse direction. We are unsure what physical process caused this behaviour, but Stokan & Campbell-Brown (2014) give some possible explanations.

The exact moment of fragmentation could not be observed because the fragments were obscured by luminous dust. To extrapolate the motion of fragments shortly before they became observable, we fit a simplistic kinematic model proposed by Jacchia & Whipple (1961) to the along-track distance of every fragment from the beginning of the meteor

$$D(t) = k + v_0 t + a_1 e^{a_2 t}, \qquad (6.2)$$

where t is the relative time since the beginning of the meteor, v_0 is the initial velocity of every fragment at $t = 0$, and a_1 and a_2 are deceleration coefficients. This model is plotted with all lag measurements throughout this work.

We assumed that the v_0 is equal to the meteor's initial velocity estimated from wide-field data. Next, we propagated the positions of fragments back in time using the model fits and identified when the positions intersected, which we took to be the time of a fragmentation event. Candidate fragmentation events were visually confirmed by inspecting the narrow-field video. We found that all fragments, except possibly 1 and 6, emerged from larger fragments. For

fragments 1 and 6 it was not possible to visually confirm any prior points of fragmentation. As a singular point of fragmentation from which all fragments were born could not be determined, we believe that the observed fragments were created by progressive fragmentation; the 12 that were visible had strengths large enough not to fragment further for 1 second.

Figure 6.19 shows the lag of individual fragments, normalized to the first visible fragment which starts at 0 s and has a lag of 0 m. Because all other fragments are in front of fragment 1, they all have a more positive lag. Fragment 10 was leading the "fragment train". The deceleration of fragments was not uniform, which caused fragments to overtake one another, indicative of an underlying mass distribution.

Fragment 6 became visible in the middle of the "fragment train", but it overtook fragments 7, 12, 9, and 11 (in that order). It had the largest mass/area ratio and presumably had the largest mass, thus the smallest deceleration, indicating that there was no sorting by mass along the trajectory prior to fragmentation. A similar behaviour showing fragments overtaking one another has also been observed for fragmenting fireballs (Borovička & Kalenda, 2003). All fragments were sufficiently separated in the transverse direction from one another as to not collide.

The dynamic pressure for every fragment is shown in Figure 6.20. The figure shows that the dynamic pressure at the moment of fragmentation was around 2.0(5) kPa. The fragments themselves started to disintegrate at a height of 82.5 km, which corresponds to a dynamic pressure of around 3 kPa. This suggests that the upper limit of the compressive strength of more compact parts of fresh JFC material is in the range of 2 – 3 kPa.

If the dust seen at the beginning of narrow-field observations is the eroding matrix in which these fragments were embedded it would indicate that the upper limit of its overall global strength is 1 kPa, possibly on the order of several hundreds of pascals for cm-sized JFC meteoroids. Note that the erosion might have also been caused by thermal effects (Borovička et al., 2007). In Figure 6.16 we superimpose the estimated moments of fragmentation onto the wide-field light curve. The figure shows that the moments of fragmentation coincide with the first
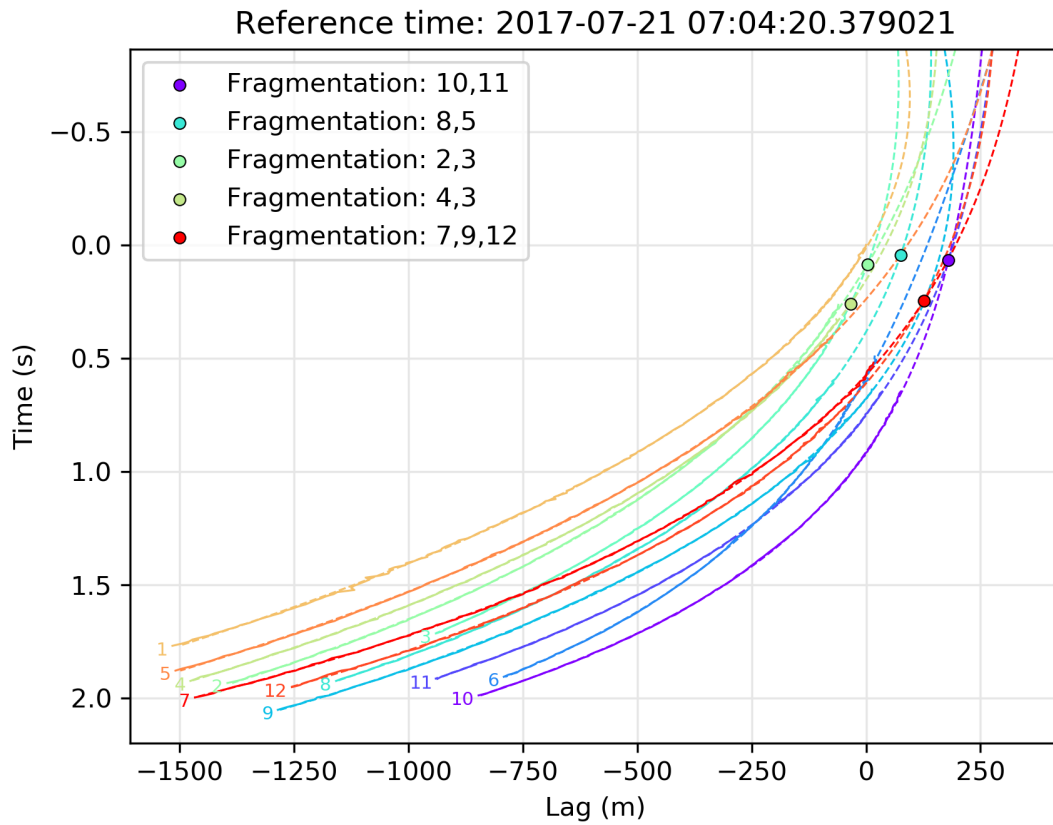
Figure 6.19: Lags of individual fragments. Solid lines show the observed lag, the dashed lines show the extrapolated lag using the exponential function fit (equation 6.2). Solid circles show the estimated points of fragmentation.
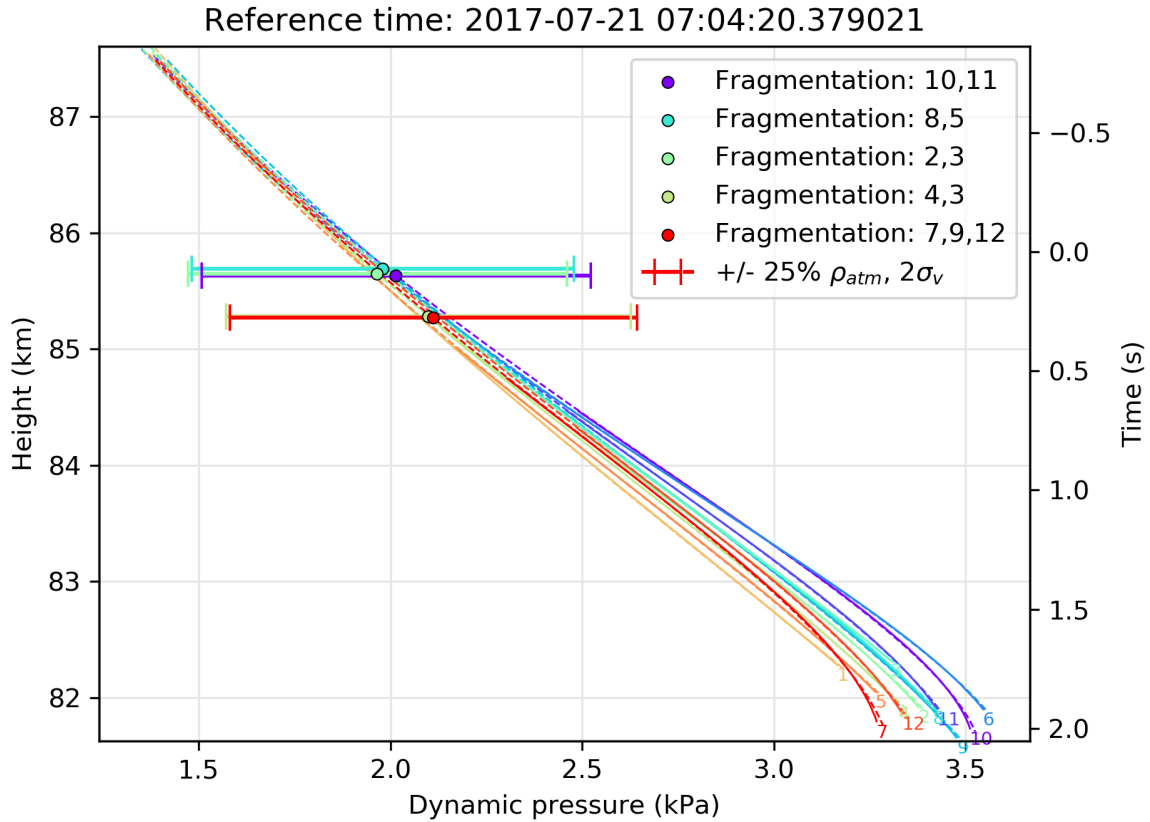
Figure 6.20: Dynamic pressures of individual fragments. Solid circles mark the moments of fragmentation. The horizontal uncertainty bars show the spread in dynamic pressure at the fragmentation point due to the expected variance of the neutral atmosphere mass density.

peak in the light curve, and that the fragments themselves started visibly disintegrating into their constituent grains at the beginning of the second peak.

These results are in accord with the in-situ measurements by the Philae lander (Biele et al., 2015) which estimated the surface strength of 67P to be $1-3$ kPa, a result similar to that found for individual particles by the COSIMA instrument (Hornung et al., 2016). Because all fragments appear to fragment at the same time and dynamic pressure, it appears that they have a similar drag coefficient, i.e. similar axial ratio or rapid rotation. We also note that the strength of the fragments themselves is only marginally larger than the strength at initial fragmentation. The fine separation of fragment strengths in this unusual case was made possible by the low entry angle of the meteoroid which caused a very gradual increase in the dynamic pressure.

Mass and size distribution of fragments

We also attempted to measure the fragment mass distribution. The dynamic mass was computed by using the velocity from the exponential deceleration fit, due to which it was rapidly decreasing, indicating that the fragments themselves were eroding, although that did not become visibly obvious until they developed wakes at the end of luminous flight. The complete photometric mass of fragments was equally challenging to compute because the fragments were either very close to each other or enveloped in dust.

We were able to estimate lower limits to the photometric mass per fragment by measuring the brightness of fragments in one common interval when they were all clearly visible and distinct. Figure 6.21 shows the magnitude of every fragment; vertical lines mark the time range used for computing the mass, when all were visible. Table 6.4 lists the computed masses using the same τ and P_{0m} as used for the wide-field photometric mass, and diameters computed using a bulk density of $\rho = 3000 \, \text{kg m}^{-3}$. Although these masses are half or less of their original value, their relative values to each other should be valid if we assume that they all started ablating at the same time and they ablated with a similar and constant ablation coefficient.

We note that photometric masses of some fragments do not correspond to their dynamical behaviour. For example, fragment 5 was decelerating more than fragment 4, despite having three times larger photometric mass. This may indicate that these fragments had either different shapes, densities, or composition. Alternatively, some fragments may have been an unresolved group of smaller fragments.

Figure 6.22 shows the cumulative distribution of fragment masses. We estimated the mass index using two separate approaches. First, we performed a simplistic least squares (LSQ) line fit to the approximately linear part in the cumulative histogram. The measured mass index is $s = 2.84 \pm 0.21$, with the uncertainty only indicating the line fit uncertainty to those select points (red dots in the plot). This is not a robust approach of fitting power-law distributions to data (Clauset et al., 2009), so we performed a separate fit using maximum likelihood estimation (MLE) and obtained a value of $s = 2.80$, which is close to the line fit value.

Following the procedure of Alstott et al. (2014), we compared the goodness of fit between the power-law and the exponential distribution and found neither distribution is a significantly stronger fit (p-value = 0.29). The Kolmogotov-Smirnov D statistic (Ivezić et al., 2014) was 0.19 for the power-law, and 0.13 for the exponential distribution, indicating that the latter is a slightly better fit. This indicates that either the fragment mass distribution was not a power-law, or that the power-law distribution quickly tapered off due to small number statistics. Thus, we believe that these s values are lower limits.

Using the MLE approach, we also fitted a power-law to the distribution of fragment radii. The sizes changed with $\alpha_s = 6.4$, and the exponent is insensitive to the choice of bulk density. This is consistent with theoretical transformations where the size index exponent is equal to $\alpha_s = 3s - 2$ (Appendix C in Vaubaillon et al., 2005). This is a very large exponent value compared to Rosetta measurements where they measured $\alpha_s = 1.8, s = 1.27$ for particles $>150\,\mu$m, and $\alpha_s = 2.9, s = 1.63$ for particles in the $30 - 150\,\mu$m range (Merouane et al., 2016). This steepness, and the fact that all observed fragments could not be tracked to a single fragmentation event, might indicate that the fragments we measured are daughter-fragments of progressive fragmentation, and that the observed fragments were not pre-existing in the meteoroid. Note that Merouane et al. (2016) give a cumulative size index α_{sc} which relates to the size index α_s used here as $\alpha_s = \alpha_{sc} + 1$.

6.6.3 Identification and analysis of a larger population of fragmenting meteors

Having established and presented our analysis methodology in detail for this first case study, we expand our analysis to additional events. We identified 19 more events which showed gross fragmentation with measurable fragments, and list their details in Table 6.5. These events were not as favourable as the July 21 event because they had steeper entry angles and consequently shorter trajectories (resulting in fewer data points), and had fewer measurable fragments (usually only 2-3). The error in the initial height was not estimated because all moments of frag-
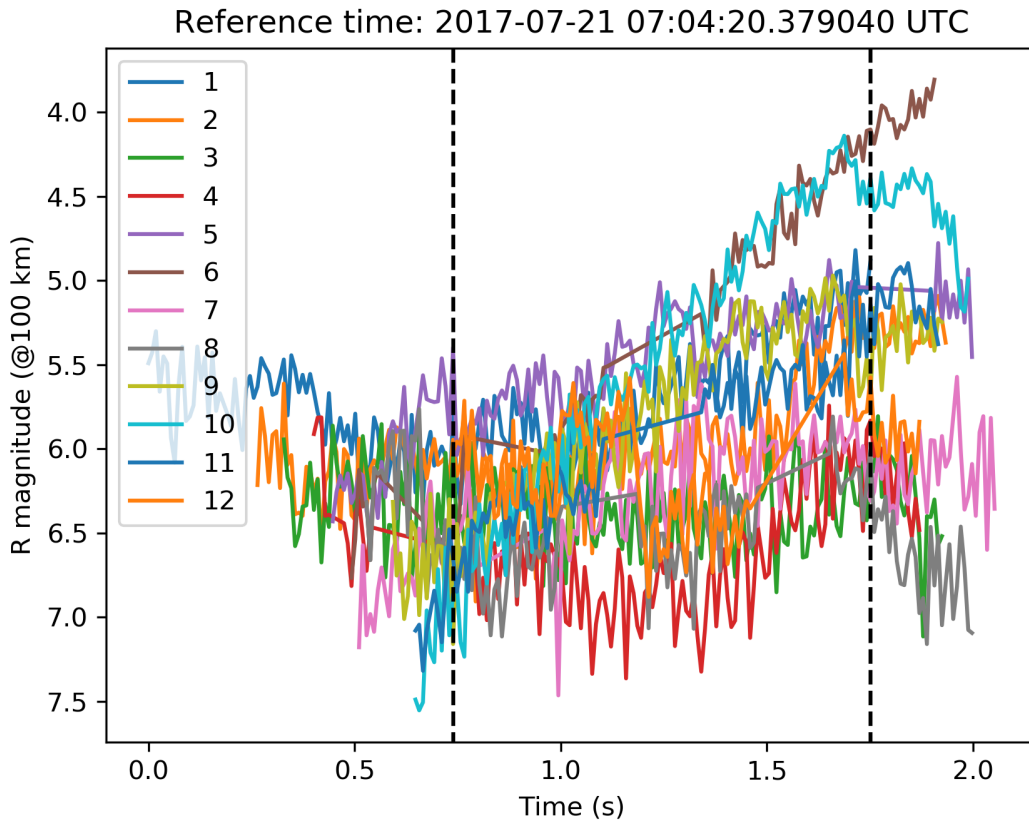
Figure 6.21: Light curve of individual fragments. Vertical lines indicate the portion of time when all fragments were visible, and this was used to compute the partial fragment mass. Not all fragments were visible all the time, so we linearly interpolated the magnitudes in the gaps.

Table 6.4: Estimated partial fragment masses and diameters, sorted by increasing value. The diameters of spherical particles were computed using a bulk density of $3000 \, \mathrm{kg \, m^{-3}}$.

Fragment No.	Mass (kg)	Diameter (mm)
4	1.96×10^{-6}	2.31
8	2.53×10^{-6}	2.52
3	2.62×10^{-6}	2.54
7	3.06×10^{-6}	2.68
12	3.53×10^{-6}	2.81
2	3.98×10^{-6}	2.92
11	4.10×10^{-6}	2.95
9	5.02×10^{-6}	3.16
1	5.33×10^{-6}	3.22
5	5.99×10^{-6}	3.35
10	7.92×10^{-6}	3.68
6	8.28×10^{-6}	3.73
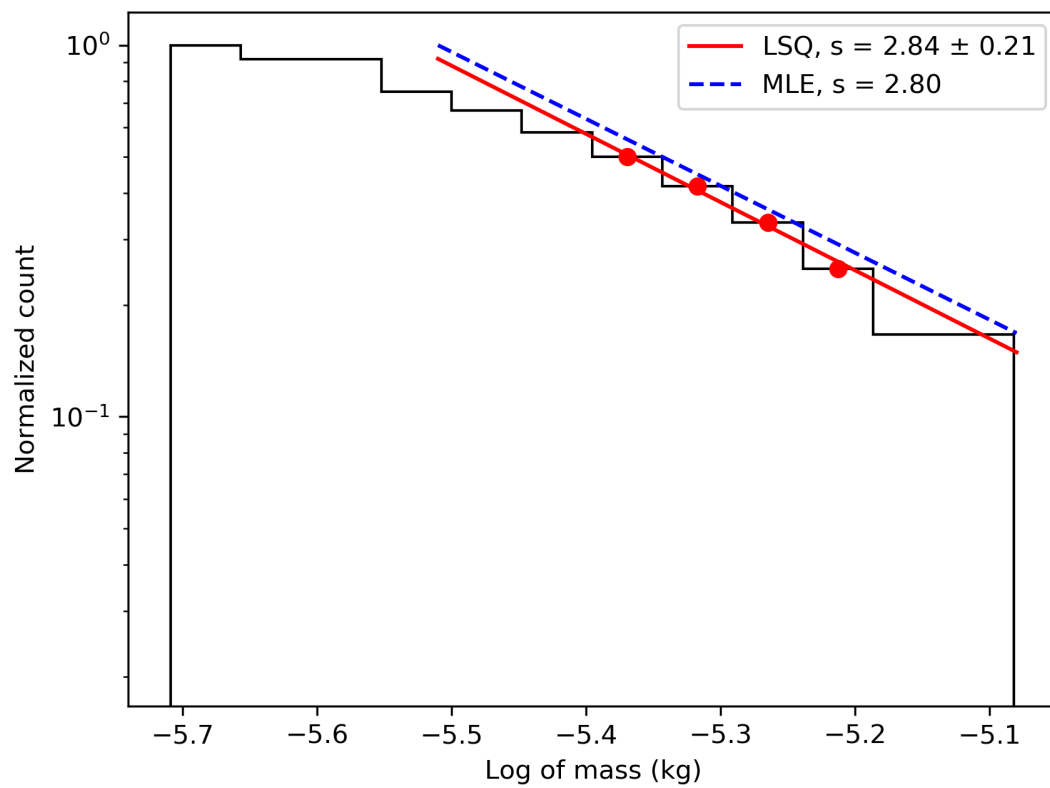
Figure 6.22: Cumulative distribution of fragment masses. The least squares fit (LSQ) on the selected range of masses (red dots) is shown in red, and the maximum likelihood estimation (MLE) fit is shown in blue.

mentation were visually confirmed in the video, thus it was only perhaps off by one or two video frames.

The observed events span a range of velocities and orbital types, indicating that gross fragmentation is not restricted to any one orbital type (a result also previously found by Subasinghe et al., 2016). We emphasize that these events comprise only 5% of all observed meteors; thus this sample should not be considered an unbiased survey of the entire meteoroid population. According to Subasinghe et al. (2016), 95% of all meteors observed by the CAMO tracking system show no discernible fragments, and most (> 85%) have a distinct wake, likely caused by erosion of the meteoroid into constituent grains in the $1 - 100\,\mu$m size range, a process not triggered by mechanical failure (Borovička et al., 2007).

Figure 6.23 shows the measured compressive strengths based on the fragmentation height as function of initial meteoroid speed. The shaded zone represents the $2 - 3$ kPa strength range measured for 67P by the Philae lander (Biele et al., 2015). The nominal strengths of most meteoroids lie in the range of $1 - 5$ kPa, in excellent accord with results reported by other authors discussed in sections 6.1.2 and 6.1.3. Figure 6.24 shows the measured compressive strengths versus the Tisserand's parameter with respect to Jupiter. There is no trend in strength with orbital type. All measurements, except one, are within the measurement uncertainty of the Philae in-situ measured upper strength limits.
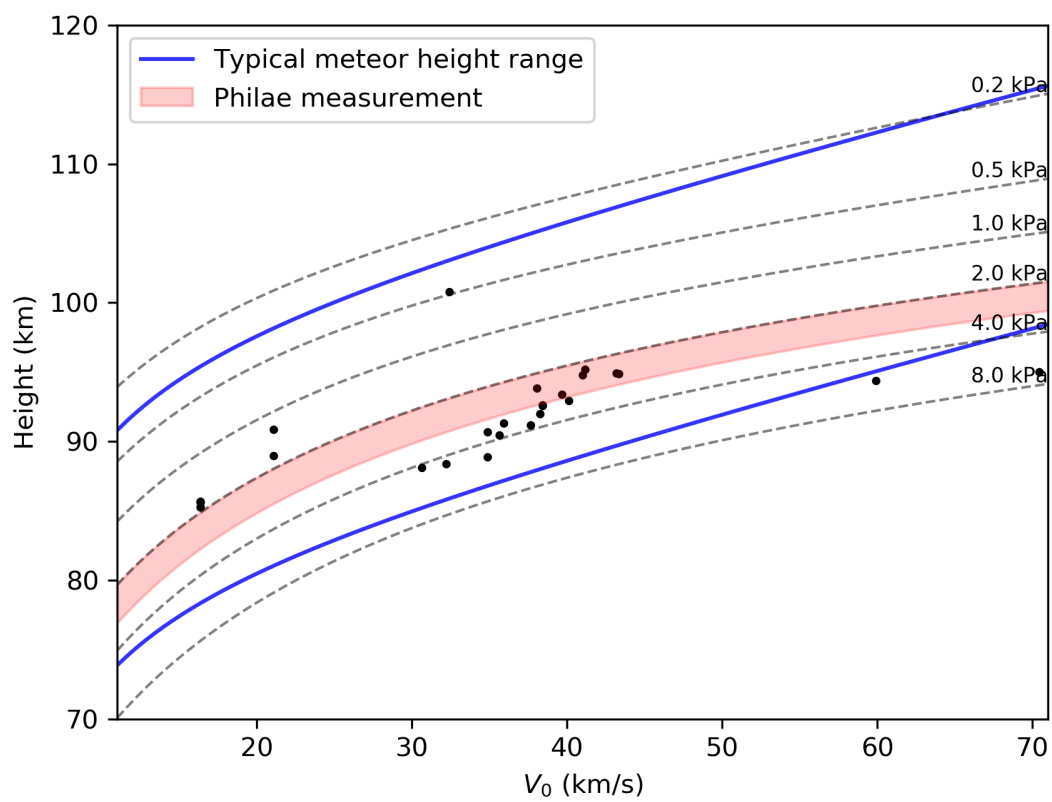
Figure 6.23: Height vs. initial velocity of measured meteors. Dashed lines indicate contours of dynamic pressures at the given height and speed.
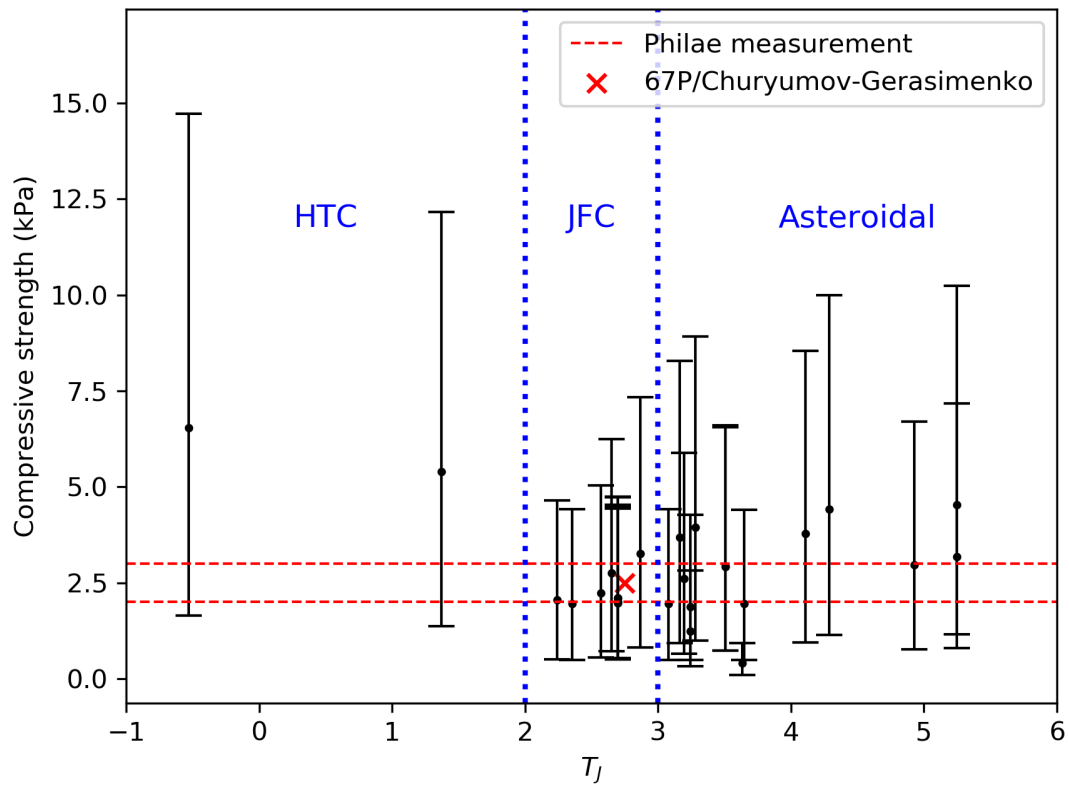
Figure 6.24: Measured compressive strengths vs. Tisserand's parameter with respect to Jupiter. The error bars indicate the uncertainty range in dynamic pressure corresponding to an atmospheric mass density variance of ±25%.

Table 6.5: Radiants, orbits, and compressive strengths of measured meteoroids.

Date and time (UTC)	$\lambda_\odot$ deg	α_g deg	δ_g deg	v_g km s^{-1}	a AU	e	q AU	ω deg	i deg	π deg	P_{dyn} kPa
2017-07-21 07:04:19	118.4821	253.866	-30.059	11.995	3.299	0.7119	0.9505	32.44	2.37	330.83	2.03
		0.019	0.084	0.009	0.007	0.0007	0.00007	0.01	0.03	0.01	
2018-05-21 06:27:59	59.9221	318.411	16.967	58.748	2.298	0.5620	1.0065	190.02	124.07	249.94	5.40
		0.210	0.730	0.064	0.176	0.0307	0.00101	1.06	1.02	1.06	
2018-07-03 03:08:39	100.9155	311.625	-6.031	41.826	2.256	0.9654	0.0780	331.58	46.57	72.50	2.23
		0.022	0.107	0.033	0.010	0.0003	0.00068	0.14	0.34	0.14	
2018-07-07 03:52:46	104.7580	311.131	-4.558	33.827	1.396	0.8869	0.1580	322.83	28.51	67.60	3.79
		0.044	0.296	0.013	0.005	0.0012	0.00124	0.14	0.56	0.14	
2018-07-07 04:45:01	104.7926	312.437	-4.826	38.075	1.834	0.9351	0.1191	325.79	35.65	70.59	2.61
		0.039	0.085	0.006	0.004	0.0003	0.00075	0.12	0.18	0.12	
2018-07-07 05:05:52	104.8064	312.009	-4.428	36.768	1.663	0.9206	0.1321	324.59	33.89	69.41	2.92
		0.031	0.103	0.006	0.003	0.0004	0.00075	0.11	0.20	0.11	
2018-07-07 06:18:01	104.8541	320.981	-26.329	39.515	1.882	0.9535	0.0875	150.75	36.55	75.60	1.96
		0.019	0.073	0.015	0.006	0.0001	0.00051	0.10	0.19	0.10	
2018-07-07 06:31:33	104.8631	275.387	-19.770	17.874	2.277	0.6816	0.7250	252.88	1.97	357.88	1.56

Table 6.5: continued.

Date and time (UTC)	$\lambda_\odot$ deg	α_g deg	δ_g deg	v_g km s^{-1}	a AU	e	q AU	ω deg	i deg	π deg	P_{dyn} kPa
		0.097	0.178	0.098	0.021	0.0035	0.00177	0.15	0.09	0.15	
2018-07-07 08:12:14	104.9298	316.019	2.403	34.192	1.124	0.8687	0.1476	327.02	44.33	71.95	2.97
		0.091	0.129	0.061	0.004	0.0014	0.00181	0.25	0.17	0.25	
2018-07-10 07:45:55	107.7733	323.502	-28.420	36.462	1.593	0.9166	0.1328	144.88	34.33	72.64	1.95
		0.031	0.049	0.019	0.003	0.0002	0.00033	0.05	0.13	0.05	
2018-07-12 03:38:50	109.5174	312.697	-2.902	36.609	2.137	0.9179	0.1754	316.79	31.93	66.31	3.26
		0.022	0.096	0.016	0.006	0.0005	0.00073	0.09	0.15	0.09	
2018-07-16 06:27:18	113.4454	318.755	-1.198	38.760	2.273	0.9383	0.1403	321.31	38.05	74.77	2.76
		0.230	0.533	0.090	0.045	0.0015	0.00467	0.78	1.14	0.78	
2018-07-20 04:33:28	117.1871	320.915	-1.886	35.987	1.890	0.9150	0.1607	319.63	29.20	76.82	3.68
		0.045	0.240	0.012	0.008	0.0006	0.00092	0.12	0.50	0.12	
2018-07-20 07:37:42	117.3092	327.577	5.895	33.230	1.071	0.8645	0.1451	328.06	41.88	85.38	3.86
		0.055	0.163	0.049	0.003	0.0007	0.00108	0.17	0.36	0.17	
2018-08-06 05:37:04	133.4761	346.893	-11.180	41.877	2.571	0.9806	0.0499	157.01	23.95	110.48	2.06
		0.042	0.116	0.006	0.019	0.0002	0.00071	0.19	0.37	0.19	

Table 6.5: continued.

Date and time (UTC)	$\lambda_\odot$ deg	α_g deg	δ_g deg	v_g km s^{-1}	a AU	e	q AU	ω deg	i deg	π deg	P_{dyn} kPa
2018-08-11 03:06:25	138.1700	329.209	29.510	28.636	1.414	0.6464	0.5002	286.86	42.50	65.04	4.42
		0.094	0.303	0.086	0.008	0.0009	0.00383	0.53	0.31	0.53	
2018-08-15 02:45:29	141.9972	347.331	1.497	39.616	2.582	0.9650	0.0903	328.72	20.83	110.73	1.96
		0.031	0.083	0.008	0.005	0.0001	0.00033	0.06	0.26	0.06	
2018-08-15 06:15:57	142.1377	344.188	-11.273	30.427	1.698	0.8581	0.2409	130.59	6.49	92.71	0.41
		0.061	0.168	0.012	0.004	0.0001	0.00058	0.09	0.27	0.09	
2018-09-17 04:13:18	173.9824	8.893	5.885	30.127	1.935	0.8591	0.2727	305.20	2.69	119.22	3.95
		0.095	0.240	0.037	0.010	0.0006	0.00094	0.14	0.36	0.14	
2018-09-19 08:55:05	176.1250	87.333	13.044	69.437	7.693	0.8695	1.0040	357.02	162.08	353.15	6.53
		0.076	0.189	0.047	0.397	0.0063	0.00010	0.25	0.32	0.25	

* uncertainties indicate measurement precision, not accuracy

6.7   Conclusions

We have summarized hardware and software reduction details of the upgraded CAMO mirror tracking system, compared to the original instrument (Weryk et al., 2013). The current CAMO system achieves an effective astrometric precision of 1 arc second, and a temporal resolution of 10 ms.

Using three representative types of meteors observed with CAMO, we have shown that the resolved trail morphology is the limiting factor in precision and ultimately, the obtainable trajectory accuracy. In ideal conditions, CAMO achieves trajectory fit precision of <1 m and initial velocity measurement precision on the order of $1\,\mathrm{m\,s^{-1}}$. Both the radiant and speed of heavily fragmenting and eroding meteors have an order of magnitude higher uncertainty than meteors with short wakes. For highly fragmenting meteors, the radiant precision is similar to what can be achieved with moderate field of view non-tracking systems.

We used direct observations at the instant of gross meteoroid fragmentation to measure the compressive strengths of meteoroids. We used the aerodynamic ram pressure exerted on the meteoroid at the moment of fragmentation as a proxy for the compressive strength. A case study of an unusually long and shallow entry event on July 21, 2017, where narrow-field video showed the exact moment of fragmentation, resulted in 12 distinct fragments whose positions were tracked. A very shallow entry angle of 8° enabled precise determination of the moments of fragmentation, and consequently precise strength measurements. The meteoroid started eroding at dynamic pressures below 1 kPa - this was not observed directly, but it was deduced from the long wake visible at the beginning of narrow-field tracking. We note that the cause of erosion might be thermal and not due to mechanical failure.

Next, the meteoroid visibly fragmented at 2 kPa, and the fragments themselves disintegrated at 3 kPa. We estimated a fragment mass index of $s = 2.8$ but believe this to be a lower limit. This value is much larger than that derived from in-situ measurements by Rosetta of comet 67P's dust, and also larger than the mass indices of major meteor showers. This may indicate that the observed fragments were not pre-existing in the meteoroid matrix, but created

by progressive fragmentation.

Nineteen more meteors showing visible fragments after gross fragmentation were used to survey compressive strengths. The majority had compressive strengths between $1-4\,\text{kPa}$ which were not correlated with orbital type. These measurements are in excellent accordance with the in-situ measurements of comet 67P by the Philae lander (where the maximum strength was between $2-3\,\text{kPa}$) and the Rosetta COSIMA instrument (strength on the order of several kPa), as well as other theoretical and experimental work summarized in Section 6.1.2.

The overall measurement uncertainty of compressive strengths was about $\pm25\%$ due to the uncertainty in the atmosphere mass density. We note that only 5% of all meteors observed by CAMO show gross fragmentation, thus these measurements do not represent all meteoroids, although both cometary and asteroidal orbits are represented in this sample.

Having developed and validated these methods for the analysis of high temporal and spatial resolution meteors observed with CAMO, in the future we aim to accurately measure the orbits of select meteor showers and use the high-precision constraints set by CAMO to improve meteor shower prediction models. The focus of our future work will be on those meteor showers caused by recently ejected meteoroids whose dispersion is solely caused by their ejection velocity from the parent body, as gravitational and non-gravitational forces do not have time to disperse the stream on such short timescales.

Bibliography

Akmaev, R., Fomichev, V., & Zhu, X. 2006, Journal of atmospheric and solar-terrestrial physics, 68, 1879

Alstott, J., Bullmore, E., & Plenz, D. 2014, PloS one, 9, e85777

Asphaug, E., & Benz, W. 1996, Icarus, 121, 225

Baldwin, B., & Sheaffer, Y. 1971, Journal of Geophysical Research, 76, 4653

Bariselli, F., Frezzotti, A., Hubin, A., & Magin, T. E. 2020, Monthly Notices of the Royal Astronomical Society, 492, 2308

Biele, J., Ulamec, S., Richter, L., et al. 2009, Acta Astronautica, 65, 1168

Biele, J., Ulamec, S., Maibaum, M., et al. 2015, Science, 349, aaa9816

Birnstiel, T., Fang, M., & Johansen, A. 2016, Space Science Reviews, 205, 41

Blum, J., Gundlach, B., Mühle, S., & Trigo-Rodriguez, J. M. 2014, Icarus, 235, 156

Blum, J., & Wurm, G. 2000, Icarus, 143, 138

—. 2008, Annu. Rev. Astron. Astrophys., 46, 21

Blum, J., Wurm, G., Kempf, S., et al. 2000, Physical Review Letters, 85, 2426

Blum, J., Gundlach, B., Krause, M., et al. 2017, Monthly Notices of the Royal Astronomical Society, 469, S755

Borovička, J. 1990, Bulletin of the Astronomical Institutes of Czechoslovakia, 41, 391

Borovička, J., Spurnỳ, P., & Koten, P. 2007, Astronomy & Astrophysics, 473, 661

Borovička, J., & Kalenda, P. 2003, Meteoritics & Planetary Science, 38, 1023

Campbell-Brown, M. 2017, Planetary and Space Science, 143, 34

Campbell-Brown, M., Borovička, J., Brown, P., & Stokan, E. 2013, Astronomy & Astrophysics, 557, A41

Campbell-Brown, M., & Koschny, D. 2004, Astronomy & Astrophysics, 418, 751

Čapek, D., Koten, P., Borovička, J., et al. 2019, Astronomy & Astrophysics, 625, A106

Ceplecha, Z., & Revelle, D. O. 2005, Meteoritics & Planetary Science, 40, 35

Clauset, A., Shalizi, C. R., & Newman, M. E. 2009, SIAM review, 51, 661

Davidsson, B. J. 2001, Icarus, 149, 375

Eckermann, S. D., Ma, J., Hoppel, K. W., et al. 2018, Monthly Weather Review, 146, 2639

Elford, W. 1999, in Meteroids 1998, 67

Fisher, A., Hawkes, R., Murray, I., Campbell, M., & LeBlanc, A. 2000, Planetary and Space Science, 48, 911

Gundlach, B., Schmidt, K., Kreuzig, C., et al. 2018, Monthly Notices of the Royal Astronomical Society, 479, 1273

Güttler, C., Krause, M., Geretshauser, R. J., Speith, R., & Blum, J. 2009, The Astrophysical Journal, 701, 130

Hilchenbach, M., Kissel, J., Langevin, Y., et al. 2016, The Astrophysical Journal Letters, 816, L32

Hogan, T. F., Liu, M., Ridout, J. A., et al. 2014, Oceanography, 27, 116

Hornung, K., Merouane, S., Hilchenbach, M., et al. 2016, Planetary and Space Science, 133, 63

Ivezić, Ž., Connolly, A. J., VanderPlas, J. T., & Gray, A. 2014, Statistics, Data Mining, and Machine Learning in Astronomy: A Practical Python Guide for the Analysis of Survey Data (Princeton University Press)

Jacchia, L. G., & Whipple, F. L. 1961, Smithsonian Contributions to Astrophysics

Jacobi, C., Hoffmann, P., Placke, M., & Stober, G. 2011, Advances in Radio Science, 9, 343

Jenniskens, P., Gural, P., Dynneson, L., et al. 2011, Icarus, 216, 40 . `http://www.sciencedirect.com/science/article/pii/S0019103511003290`

Jones, J., & Kaiser, T. 1966, Monthly Notices of the Royal Astronomical Society, 133, 411

Kataoka, A. 2017, in Formation, Evolution, and Dynamics of Young Solar Systems (Springer), 143–159

Kataoka, A., Tanaka, H., Okuzumi, S., & Wada, K. 2013, Astronomy & Astrophysics, 557, L4

Kikwaya, J.-B., Campbell-Brown, M., & Brown, P. 2011, Astronomy & Astrophysics, 530, A113

Koten, P., Rendtel, J., Shrbenỳ, L., et al. 2019, Meteoroids: Sources of Meteors on Earth and Beyond, 90

Krause, M., & Blum, J. 2004, Physical Review Letters, 93, 021103

Kuhl, D., Rosmond, T., Bishop, C., McLay, J., & Baker, N. 2013, Mon. Wea. Rev., 141, 2740

Lima, L., Araújo, L., Alves, E., Batista, P., & Clemesha, B. 2015, Journal of Atmospheric and Solar-Terrestrial Physics, 133, 139

Lisse, C., Fernández, Y., Kundu, A., et al. 1999, Icarus, 140, 189

List, R., Rentsch, U. W., Byram, A. C., & Lozowski, E. P. 1973, Journal of the Atmospheric Sciences, 30, 653

Liu, L., Liu, H., Chen, Y., et al. 2017, Journal of Geophysical Research: Space Physics, 122, 1117

Markkanen, J., & Agarwal, J. 2019, Astronomy & Astrophysics, 631, A164

McCormack, J., Hoppel, K., Kuhl, D., et al. 2017, Journal of Atmospheric and Solar-Terrestrial Physics, 154, 132

McCormack, J. P., Eckermann, S. D., & Hogan, T. F. 2015, Monthly Weather Review, 143, 2121

McNamara, H., Suggs, R., Kauffman, B., et al. 2005, in Modern Meteor Science An Interdisciplinary View (Springer), 123–139

Merouane, S., Zaprudin, B., Stenzel, O., et al. 2016, Astronomy & Astrophysics, 596, A87

Musci, R., Weryk, R., Brown, P. G., Campbell-Brown, M. D., & Wiegert, P. 2012, The Astrophysical Journal, 745, 161. `http://stacks.iop.org/0004-637X/745/i=2/a=161?key=crossref.c0d2a187d081bc242be63bb679ae2977`

Picone, J., Hedin, A., Drob, D. P., & Aikin, A. 2002, Journal of Geophysical Research: Space Physics, 107

Qian, L., Marsh, D., Merkel, A., Solomon, S. C., & Roble, R. G. 2013, Journal of Geophysical Research: Space Physics, 118, 3846

Roberts, I., Hawkes, R., Weryk, R., et al. 2014, in Proceedings of Meteoroids, Poznan, Poland, 26–30 August 2013., 155–162

Sánchez, P., & Scheeres, D. J. 2014, Meteoritics & Planetary Science, 49, 788

Simonenko, A. N. 1968, in IAU Symposium, Vol. 33, Physics and Dynamics of Meteors, ed. L. Kresak & P. M. Millman, 207

Solomon, S. C., Liu, H.-L., Marsh, D. R., et al. 2019, Journal of Geophysical Research: Space Physics, 124, 3799

Stober, G., Baumgarten, K., McCormack, J. P., Brown, P., & Czarnecki, J. 2019, Atmospheric Chemistry and Physics Discussions, 2019, 1

Stober, G., Jacobi, C., Matthias, V., Hoffmann, P., & Gerding, M. 2012, Journal of atmospheric and solar-terrestrial physics, 74, 55

Stober, G., Matthias, V., Brown, P., & Chau, J. L. 2014, Geophysical Research Letters, 41, 6919

Stokan, E., & Campbell-Brown, M. 2014, Icarus, 232, 1

Stokan, E., Campbell-Brown, M., Brown, P., et al. 2013, Monthly Notices of the Royal Astronomical Society, 433, 962

Subasinghe, D., & Campbell-Brown, M. 2018, The Astronomical Journal, 155, 88

—. 2019, Monthly Notices of the Royal Astronomical Society, 485, 1121

Subasinghe, D., Campbell-Brown, M., & Stokan, E. 2017, Planetary and Space Science, 143, 71

Subasinghe, D., Campbell-Brown, M. D., & Stokan, E. 2016, Monthly Notices of the Royal Astronomical Society, 457, 1289

Tapping, K. 2013, Space Weather, 11, 394

Thomas, R. N., & Whipple, F. L. 1951, The Astrophysical Journal, 114, 448

Tóth, J., Kornoš, L., Zigo, P., et al. 2015, Planetary and space science, 118, 102

Trigo-Rodríguez, J. M., & Llorca, J. 2006, Monthly Notices of the Royal Astronomical Society, 372, 655

Vaubaillon, J., Colas, F., & Jorda, L. 2005, Astronomy & Astrophysics, 439, 751

Verniani, F. 1969, Space Science Reviews, 10, 230

Vida, D., Brown, P., Campbell-Brown, M., Gural, P., & Wiegert, P. 2019a, Monthly Notices of
    the Royal Astronomical Society, XXX, ?

—. 2019b, Monthly Notices of the Royal Astronomical Society, XXX, ?

Vida, D., Brown, P., Campbell-Brown, M., & Huggins, S. 2018a, in International Meteor Con-
    ference, Petnica, Serbia, 21-24 September 2017, 18–24

Vida, D., Brown, P. G., & Campbell-Brown, M. 2018b, Monthly Notices of the Royal Astro-
    nomical Society, 479, 4307

Vojáček, V., Borovička, J., Koten, P., Spurnỳ, P., & Štork, R. 2019, Astronomy & Astrophysics,
    621, A68

Weidling, R., Güttler, C., & Blum, J. 2012, Icarus, 218, 688

Weryk, R., Brown, P. G., Domokos, A., et al. 2007, Earth, Moon, and Planets, 102, 241.
    `http://www.springerlink.com/index/10.1007/s11038-007-9183-1`

Weryk, R., Campbell-Brown, M., Wiegert, P., et al. 2013, Icarus, 225, 614

Weryk, R. J., & Brown, P. G. 2012, Planetary and Space Science, 62, 132 . `http://www.`
    `sciencedirect.com/science/article/pii/S0032063311003965`

—. 2013, Planetary and Space Science, 81, 32

Yi, W., Xue, X., Reid, I. M., et al. 2019, Atmospheric Chemistry and Physics, 19, 7567

Chapter 7

Radiant dispersion of the 2019 Orionids measured using the CAMO mirror tracking system

7.1 Introduction

The Orionids are an annual meteor shower that occurs around October 22 and whose parent body is the comet 1P/Halley. The shower is moderately strong with a mean ZHR of around 25 (Jenniskens, 2006), and has a fast geocentric velocity of ~66.5 km s^{-1}. The Orionids have a twin shower, the η Aquariids, which occur in early May each year. These two showers from one parent reflect the fact that both nodes of 1P/Halley are close enough to the Earth that a shower is visible at the ascending node (Orionids) and the descending node (η Aquariids). Each stream's evolution is distinct and complex; the encountered particles have different dynamical histories (Yeomans & Kiang, 1981; McIntosh & Hajduk, 1983). While both showers have mm-sized particles, the Orionids show occasional fireball outbursts (cm-sized objects) while the η Aquariids are particularly rich in small (sub-mm) sized meteoroids (Chau & Galindo, 2008). Observations of the 2006 Orionid fireball outburst have shown that large meteoroids are in a

1:6 resonance with Jupiter (Sato & Watanabe, 2007; Spurnỳ & Shrbenỳ, 2008). Despite the estimated age of the Orionid shower of around 20,000 years (Jones et al., 1989), the 1:6 resonance appears to be impeding the dispersion process, causing stream meteoroids to concentrate and leading to possible future outbursts (Sekhar & Asher, 2014).

Many previous studies investigated the structure of Orionid radiants (e.g. Znojil, 1968; Porubčan, 1973; Hajduk, 1970), but the precision of their measurements was not well defined per observation and was likely on the order of the expected physical dispersion itself. Kresák & Porubčan (1970) measured an Orionid radiant dispersion of 0.84° which they defined as the median offset from the mean radiant. They used high-fidelity multi-station Super-Schmidt data reduced by Jacchia & Whipple (1961), although the data set does not contain any individually determined uncertainties. Spurnỳ & Shrbenỳ (2008) measured the median offset from the mean radiant of the resonant Orionid branch in 2006 to be only 0.12°. Although they also do not report uncertainties, their trajectories are likely more precise than the data used in Kresák & Porubčan (1970) as fireballs usually have more data points for the trajectory fit, despite the higher astrometric uncertainty of individual measurements on all-sky images. For larger meteoroids which are not very affected by non-gravitational forces, tighter radiants are naturally expected if the meteoroids were locked in a resonance, so it is not clear if the true radiant dispersion was resolved by Kresák & Porubčan (1970), or the fireball outburst truly had a tighter spread in radiants.

In this work, we use high-precision observations of the 2019 Orionids collected by the Canadian Automated Meteor Observatory (CAMO) mirror tracking system (see Chapter 6 for hardware details) to characterize the radiant dispersion of the Orionids. In particular, we estimate uncertainties on a per event basis using the Monte Carlo approach described earlier, with estimated measurement errors extracted from the variance in the observed picks from a straight line trajectory. This allows us to sub-select events having the highest measurement precision. Moreover, if the spread in radiant locations exceeds the typical radiant measurement precision we may assume that we are detecting the true physical dispersion of the radiant, not limited by

measurement error.

In Chapter 4 we show that in an ideal case the CAMO mirror tracking system has a radiant precision of ~0.01°, although this is predicated on favourable meteor morphology. As shown in Chapter 6, radiant measurements might be an order of magnitude less precise for highly fragmenting meteors. Nevertheless, we also demonstrated that using our Monte Carlo methodology, the actual measurement uncertainty can be well estimated for CAMO observations. The results suggested that the CAMO system provides the most precise measurements of faint meteor trajectories to date.

7.2   Observations details and data reduction

From October 23 to October 29 2019, the CAMO mirror tracking system observed a total of 15 Orionids that were well tracked from both CAMO sites and had precise trajectories. Five additional Orionids were observed, but had large measurement uncertainties due to either unfavourable geometry or poor morphology, or were not well tracked. For these reasons they were rejected from further analysis. We also manually rejected 6 meteors that the automated shower association algorithm misclassified as Orionids (all meteors within 5° of the mean Orionid radiant and with geocentric velocities within 30% of the nominal value) - their radiants were significantly more scattered than the 15 used in this analysis.

The observations were manually reduced following the procedure described in Chapter 6. As a reminder, astrometric picks were done by manually centroiding meteor positions using narrow-field data, and wide-field data were used for photometry measurements. Radiants and orbits of all 15 Orionids are given in Table 7.1. The velocity correction discussed in Chapter 2 was not applied because it does not take into account the delay between meteor detection and the beginning of narrow-field tracking, which leads to further underestimation of the initial velocity. In the future, we will fit a meteor ablation model to observations to invert pre-atmosphere velocity and an updated list of Orionid orbits will be published.
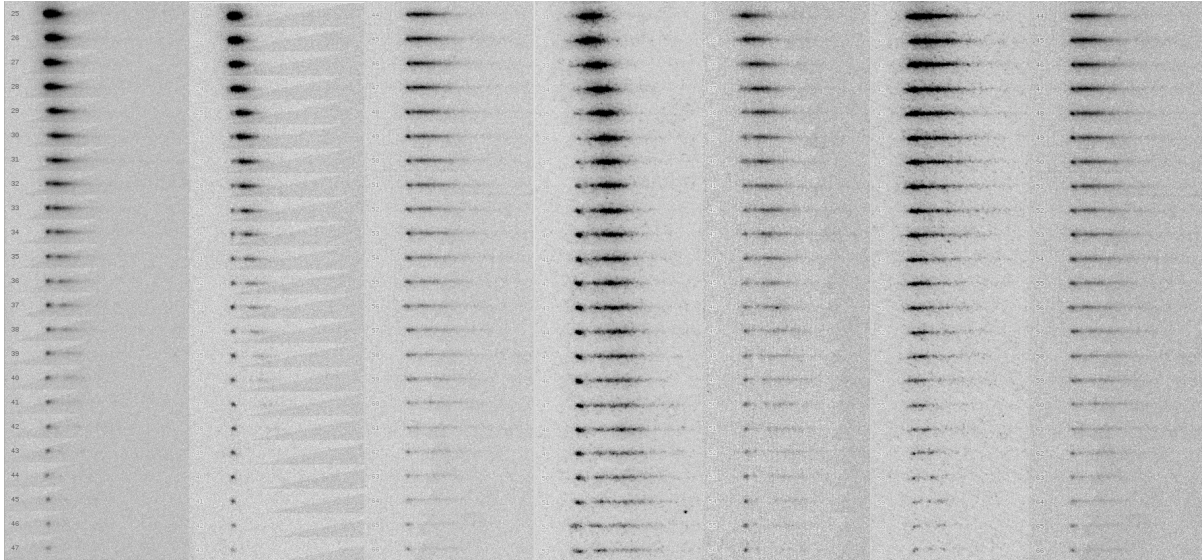
Figure 7.1: Composite gray-inverted image of seven Orionids recorded using CAMO narrow-field camera. The frame number increases from top to bottom. All meteors show the leading fragment morphology type.

A particularly unusual qualitative observation we noted is that all 15 Orionids had the same "leading fragment" fragmentation morphology (Subasinghe & Campbell-Brown, 2018). An example is shown in Figure 7.1. It is notable that examination of more than 1000 CAMO tracked events showed leading fragments present in only about 3% of cases.

At the beginning of their visible trajectory, leading fragment meteors usually exhibit a wake caused by continuous fragmentation. After some time one apparently single-body fragment emerges at the front of the meteor, showing no further fragmentation nor wake and ultimately dimming as a star-like point-spread function below the noise floor. One simple interpretation is that this might indicate that the dust of 1P/Halley is refractory inclusion-rich, although we cannot even speculate on the composition of these inclusions without spectral data.

Further confirmation of these observations can be done by analyzing η Aquariid meteors using the same approach. If these really are refractory inclusions, similar to those found in the dust of comet 81P/Wild 2 (Simon et al., 2008), this would further support the notion of large scale radial mixing between reservoirs of solids in the inner and outer solar nebula during the formation of the Solar System.

The leading fragment morphology is favourable for achieving a high trajectory accuracy because there is a consistent leading reference point with high signal to noise ratio that can be picked. The top inset of Figure 7.2 shows an example of such event, demonstrating the high precision achievable. Nevertheless, due to a different perspective from the two sites it was sometimes difficult to pick the same features in both videos during manual data reduction. Hence, the observed lags from both sites do not match in some cases.

The middle inset of Figure 7.2 shows one such case where the spatial fit residuals are good, reflecting consistent picks along the meteor straight line trajectory. However, as the same meteor features were not able to be located from both sites, there is an offset in the lag of several to tens of meters (1 to 10 pixels in the image), reflecting poor along-track pick consistency.

Finally, the bottom inset of Figure 7.2 shows an event which did not have a constant point of reference. In this case, the transition happened during the moment of separation between the dust and the leading fragment, so the lags show a discontinuous break. Nevertheless, the initial velocity could still be computed with reasonable precision (note the near vertical lag over the first 0.1 sec of the measurement).

As the lags between stations were sometimes inconsistent, in these cases the meteor trajectory was computed using our implementation of the lines of sight method (Borovička, 1990) and uncertainties were computed using the Monte Carlo method of Vida et al. (2020), described in Chapter 3.

7.3   Radiant dispersion

Figure 7.3 shows the radiant and associated uncertainty for the 15 observed Orionid in Sun-centred ecliptic (SCE) coordinates; the solar longitude is colour coded. As detailed modelling of the Orionid radiant structure has not been published to date, we have no theoretical reference to compare our observations. Hence, we can only speculate on the nature and groupings of the
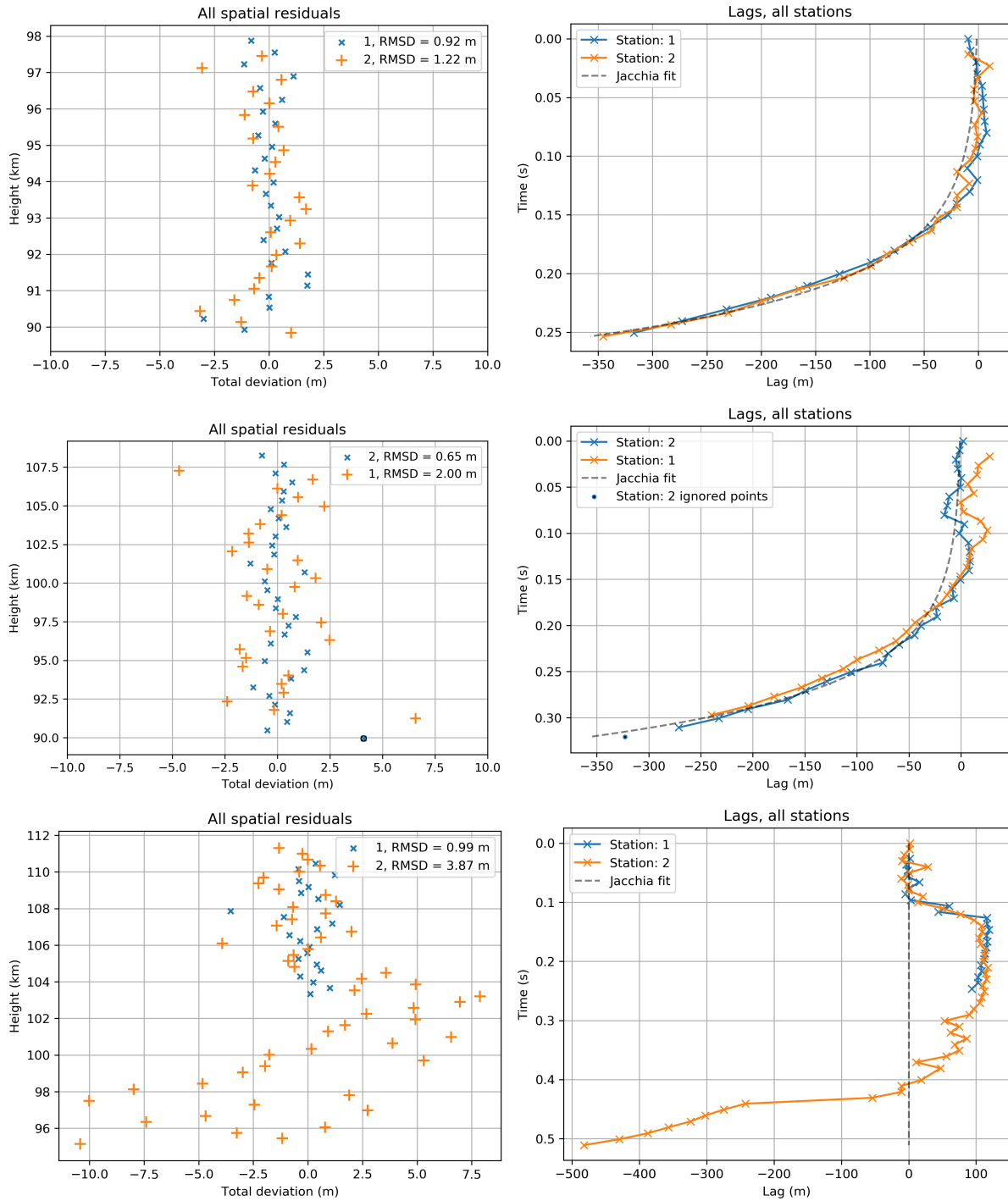
Figure 7.2: Orionids observed on: Top - October 28, 2019, at 05:16:22 UTC. Middle - October 23, 2019, at 08:45:02 UTC. Bottom - October 28, 2019, at 05:18:34 UTC. Left column: Spatial fit residuals from a straight line. Right column: Distance along the trajectory lag relative to an assumed constant velocity model.
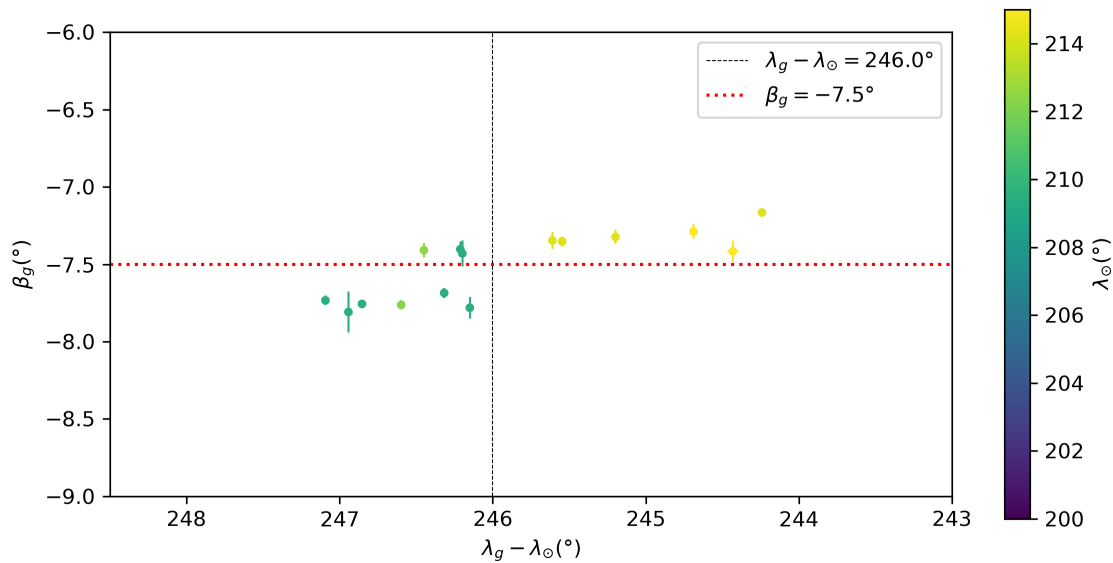
Figure 7.3: Radiants of Orionids observed by CAMO show in in Sun-centered ecliptic coordinates. Here the uncertainty bars represent the one standard deviation in the Monte Carlo estimated radiant location per event. Note the very different range in the x and y scales. The cuts at $(\lambda_g - \lambda_\odot) = 246°$ and $\beta_g = -7.5°$ are shown as well.

observed radiant structure.

The data show a distinct radiant structure and one interpretation is that there are several groups of radiants. One possible way to group them is in the following two groups: a group of radiants with ecliptic latitudes $\beta_g < -7.5°$ which occur near the peak (solar longitude of $\lambda \approx 210°$), and a second group with higher ecliptic latitudes which shows a larger spread in SCE longitudes. The radiants of the second group appear to be drifting with the increasing solar longitude, from λ of $210°$ to $215°$.

Alternatively, the radiants can perhaps be separated into a bulk of radiants with the SCE longitude $(\lambda_g - \lambda_\odot) > 246°$ near the peak of activity, and a second group (a "tail") extending along $\beta_g \approx -7.4°$ after the peak. Due to unfavourable weather conditions CAMO did not observe the activity before the peak. Suggested cuts for both ways of separating the groups are shown in Figure 7.3.

Table 7.2 lists positions of theoretical radiants computed by varying the argument of perihelion and inclination (method H by Neslušan et al., 1998) of the past orbital elements of
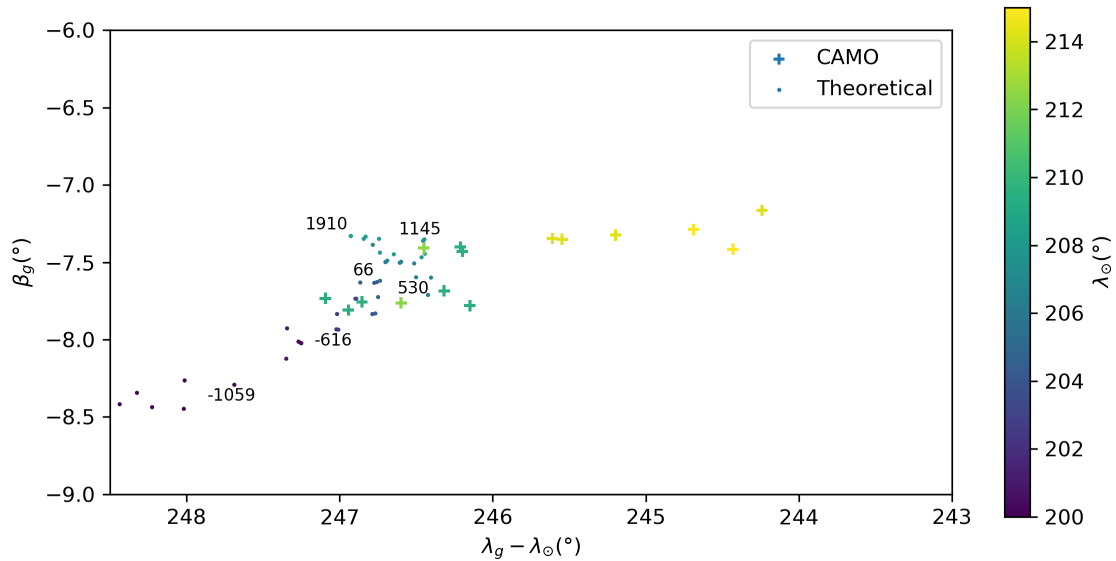
Figure 7.4: Radiants of the Orionids observed by CAMO compared to theoretical radiants. Theoretical radiants are computed from the osculating orbit of 1P/Halley at a particular epoch (Yeomans & Kiang, 1981) and are colour coded by the solar longitude of the closest intersection between the Earth's and the comet's orbit. The year of the comet's perihelion passage is marked for a selection of radiants.

comet 1P/Halley taken from Yeomans & Kiang (1981). This provides a basic framework for interpreting the radiant structure, but more robust modelling looking at evolution of individual trails ejected from the comet and integrating these particles forward to the present epoch are highly desirable.

Theoretical radiants are compared with observations in Figure 7.4. This simplistic approach shows that the radiants observed close to the peak of activity correspond well to theoretical radiants computed using the comets orbital elements from about 0 to 1000 CE. The observed off-peak branch with $(\lambda_g - \lambda_\odot) \leq 246°$ is far from these theoretical radiants and may either be the result of dynamical interactions not modelled in this work or much older ejecta. We also note that theoretical radiants derived from older perihelion passages extend south and roughly follow the beginning of the "Orionid tail" (Jenniskens et al., 2016).

We compare the CAMO Orionid observations to Cameras for All-sky Meteor Surveillance

(CAMS)[1] and Global Meteor Network (GMN)[2] data. These systems observe a similar meteoroid mass range to CAMO. CAMS observations were collected in 2010-2013 using low-light Watec 902H2U CCD cameras operated at 30 frames per second (FPS) and 12 mm f/1.2 lenses, which gave a plate scale of 2.57 arcminutes per pixel and a limiting stellar magnitude of $+5.5^M$ (Jenniskens et al., 2011, 2016). The GMN data was collected in 2019 using IMX291 CMOS cameras operated at 25 FPS and 16 mm f/1.0 lenses corresponding to a plate scale of 0.94 arcminutes per pixel and a limiting stellar magnitude of $+9.0^M$. Note that GMN trajectory analysis and measurement uncertainty were performed using the same methodology as CAMO. Radiants from both data sets with convergence angles $Q_c < 15°$ and velocity errors larger than 15% were rejected. All solutions having radiant errors larger than 0.5° for CAMS (following Jenniskens et al., 2016) and 0.075° for GMN data were rejected. The difference in the radiant error threshold is a reflection of the stated uncertainties in the data sets themselves. After filtering, the median radiant error for Orionids recorded with CAMS was 0.297°, for GMN data 0.043°, and for CAMO data 0.050°. Figure 7.5 shows a comparison of Orionid radiants from all three systems - CAMO and GMN seem to follow the same pattern while CAMS data do not seem to be precise enough to resolve the structure observed by the other two systems.

Figure 7.6 shows observed CAMO and GMN Orionid radiants with the solar longitude colour coded. Both data sets show the same radiant motion over time, although the presence of the two branches is not as clearly visible in the GMN data set. We conclude that the independent GMN observations broadly support the radiant structure, dispersion, and the radiant position dependence on the solar longitude that is present in the CAMO data set.

Taking the whole of CAMO data together, we model the radiant drift as a linear offset in SCE coordinates over time (i.e. solar longitude) as

---

[1] CAMS data can be obtained at: `http://cams.seti.org/`
[2] GMN data can be obtained at: `https://globalmeteornetwork.org/`
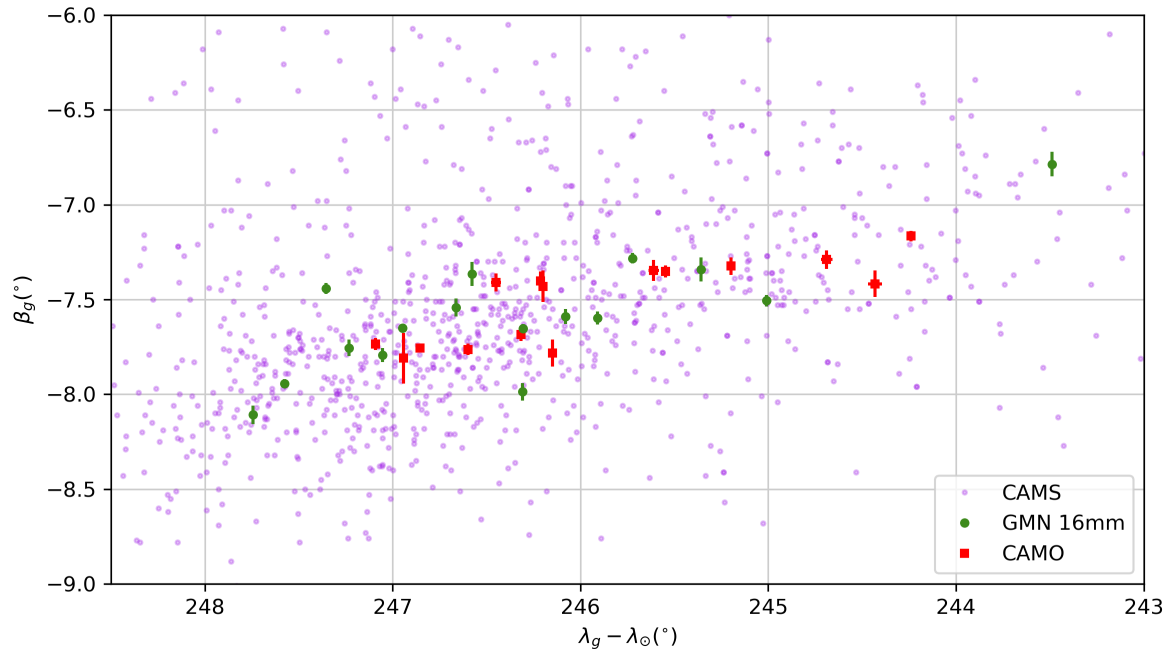
Figure 7.5: Comparison of Orionid radiants captured using CAMS, GMN, and CAMO systems. The error bars for CAMS data were not plotted to reduce visual clutter, but they are on average 6 times larger than for the other two data sets.
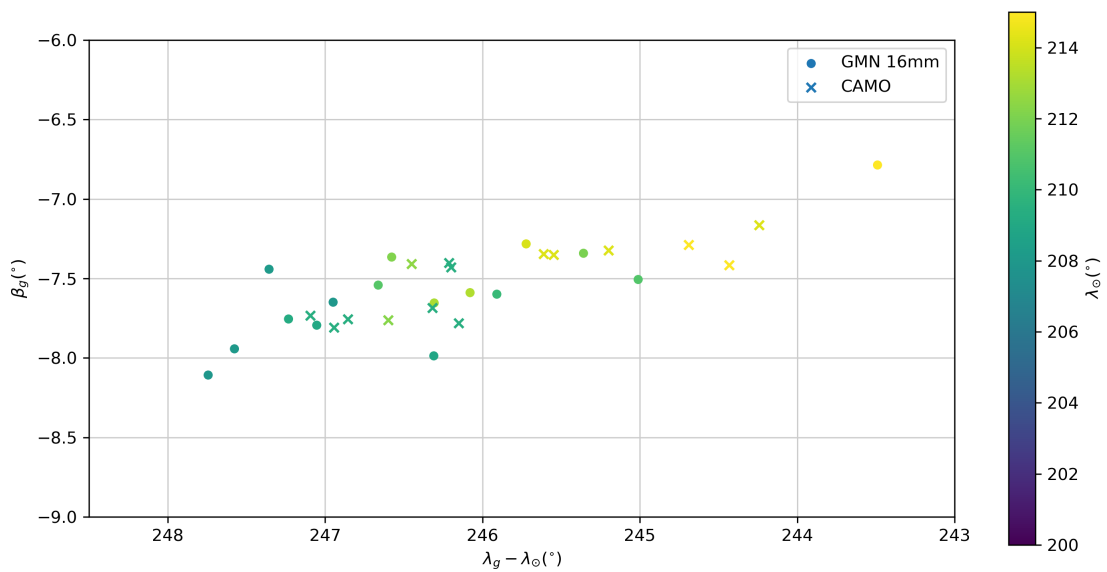
Figure 7.6: Comparison of radiants and solar longitudes of GMN and CAMO Orionids.
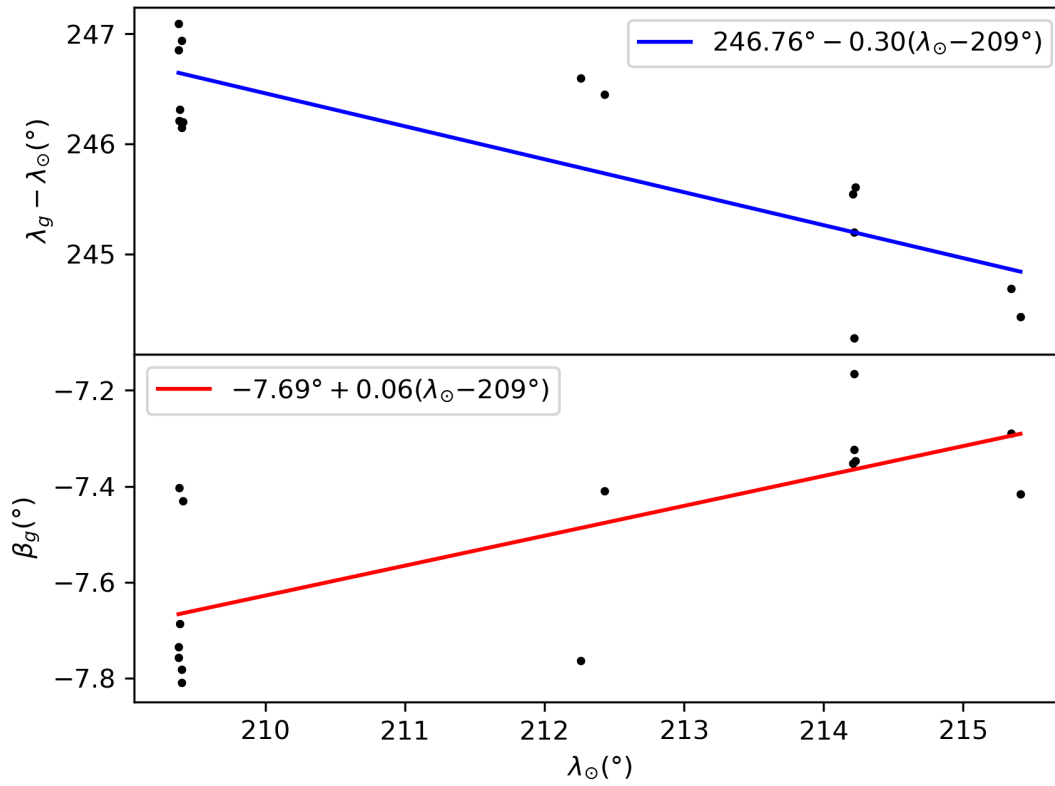
Figure 7.7: Drift in Sun-centred ecliptic longitudes and latitudes for the 2019 Orionids observed by CAMO.

$$(\lambda_g - \lambda_\odot)' = 246.76° - 0.30\,(\lambda_\odot - 209°)\,, \tag{7.1}$$

$$\beta_g' = -7.69° + 0.06\,(\lambda_\odot - 209°)\,, \tag{7.2}$$

and Figure 7.7 shows the radiant drift in both the SCE longitude and latitude. Figure 7.8 shows the radiant positions after the drift correction. The median offset from the mean radiant is 0.43°, but this is entirely due to the scatter in the drift-corrected SCE longitude of 0.41°, compared to the median offset in the latitude of only 0.09°.

Splitting the radiants into two groups by SCE latitude at $\beta_g = -7.5°$ provides only a marginal decrease in the dispersion. The point with the smallest value of the SCE longitude (the
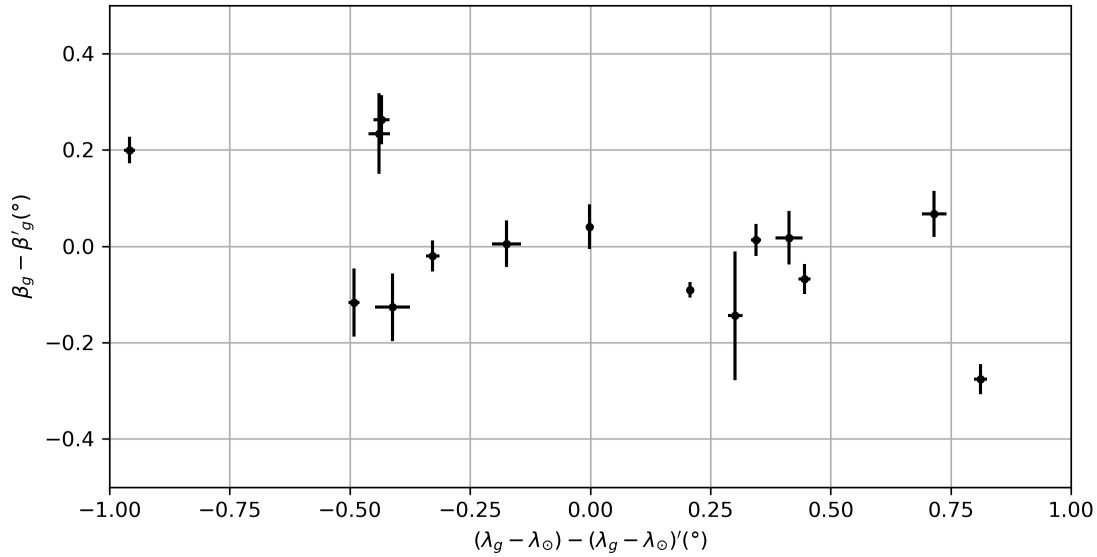
Figure 7.8: Drift corrected CAMO Orionid radiants.

rightmost point in Figure 7.3) appears as an outlier which substantially deviates from the fitted drift of all other points, thus is was removed from the fit. The upper branch with $\beta_g > -7.5°$ has a median offset from the mean radiant of 0.29° which is again entirely driven by the dispersion in the SCE longitude (0.29° vs 0.02° in the latitude). The lower branch with $\beta_g \leq -7.5°$ has a similar median offset from the mean radiant of 0.32° (the longitude/latitude split is 0.31° vs 0.02°). Figure 7.9 shows the drift corrected radiants from the mean of every group.

If the split is done by the SCE longitude $(\lambda_g - \lambda_\odot) = 246°$, and with the outlier removed as described above, one of the branches shows a significant decrease in dispersion. The branch with SCE longitude > 246° still has a similar median offset from the mean radiant than before, around 0.40° (0.33° vs 0.15° longitude/latitude split). On the other hand, the branch with SCE longitude $\leq$ 246° has a dispersion of only 0.12° (0.11° vs 0.02° longitude/latitude split), as seen in Figure 7.10. We note that there are only five radiants in the tighter branch, thus no hard conclusions can be made about the structure due to low number statistics, but the data are suggestive.

It has been suggested in the past that different branches of the Orionids may have different masses (Znojil et al., 1987), hence we also computed observed meteoroid masses. Photometric
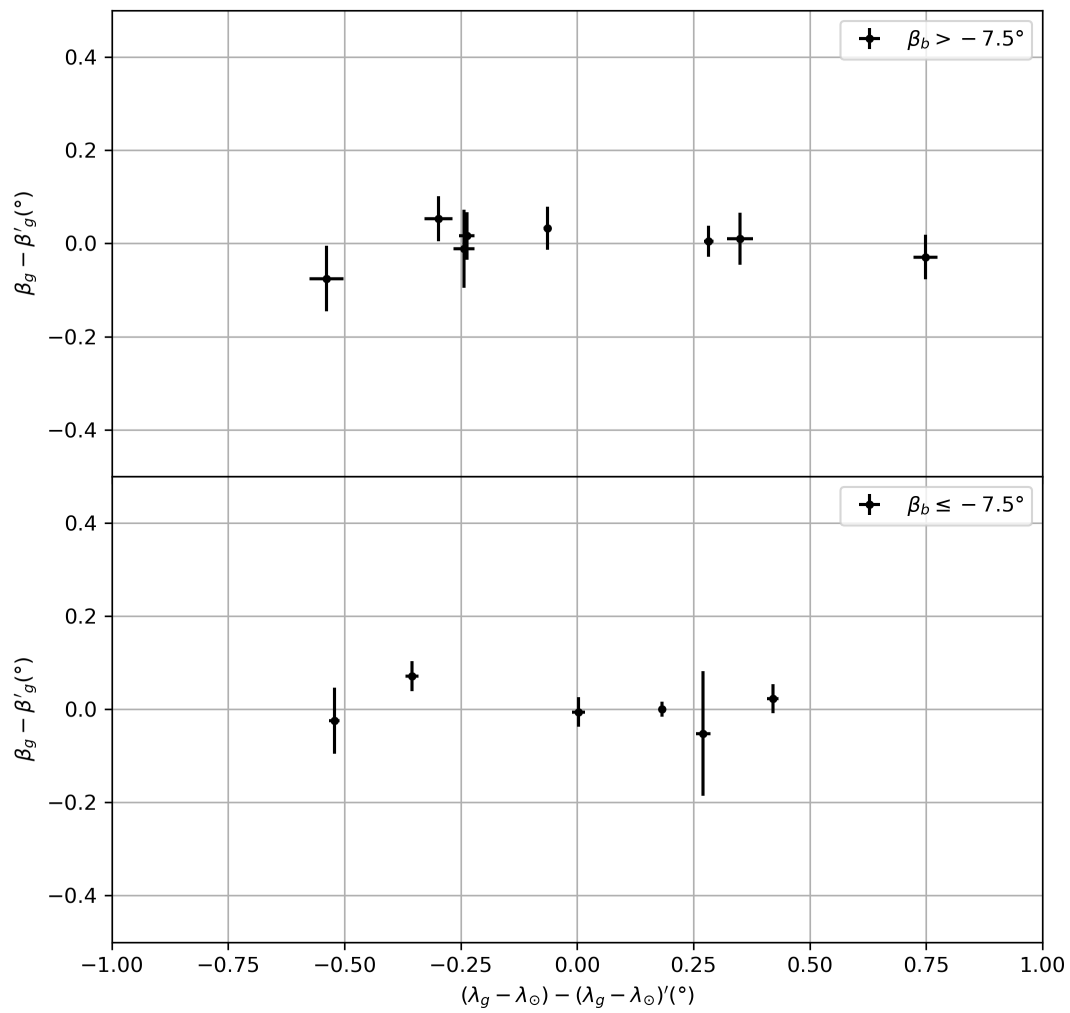
Figure 7.9: Drift corrected CAMO Orionid radiants split into two branches at $\beta_g = -7.5°$.
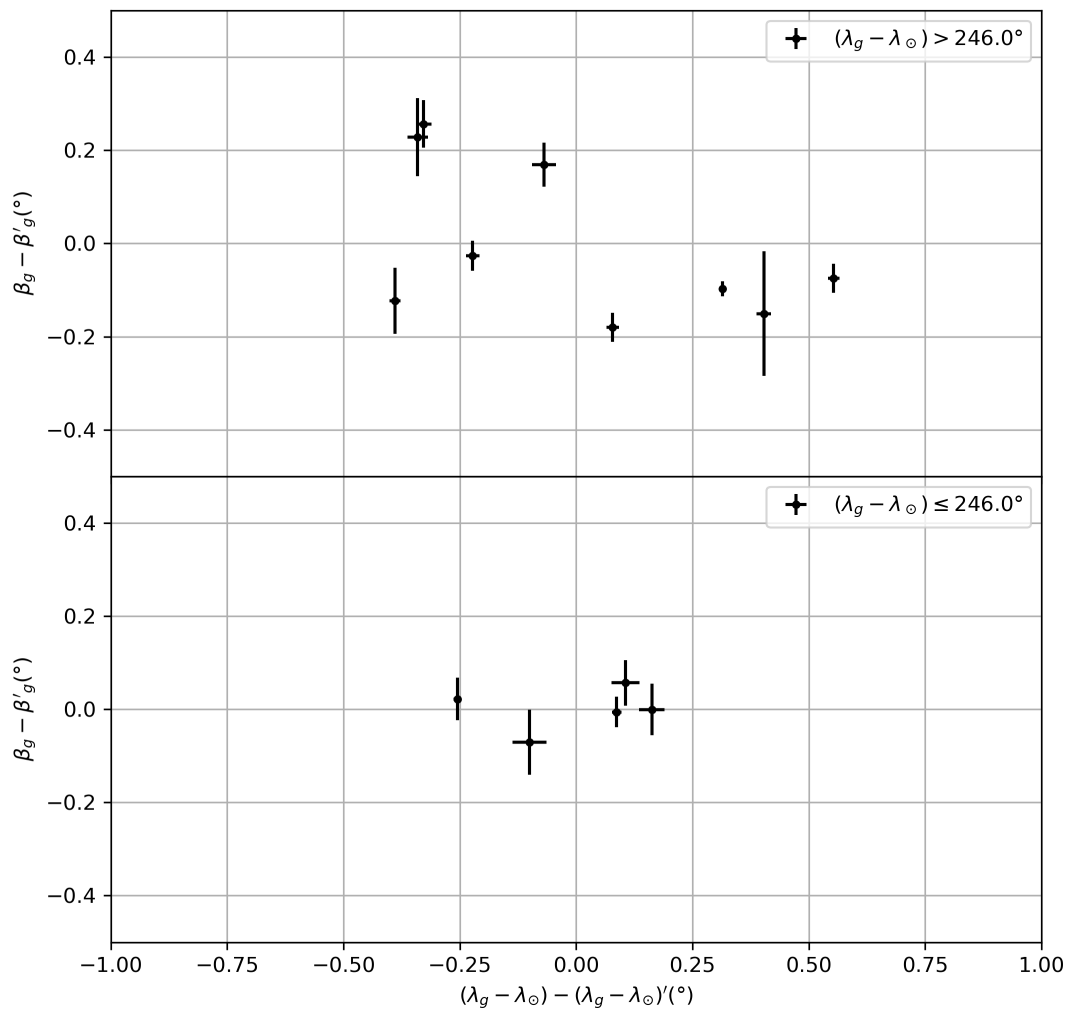
Figure 7.10: Drift corrected CAMO Orionid radiants split into two branches at $(\lambda_g - \lambda_\odot) = 246°$.
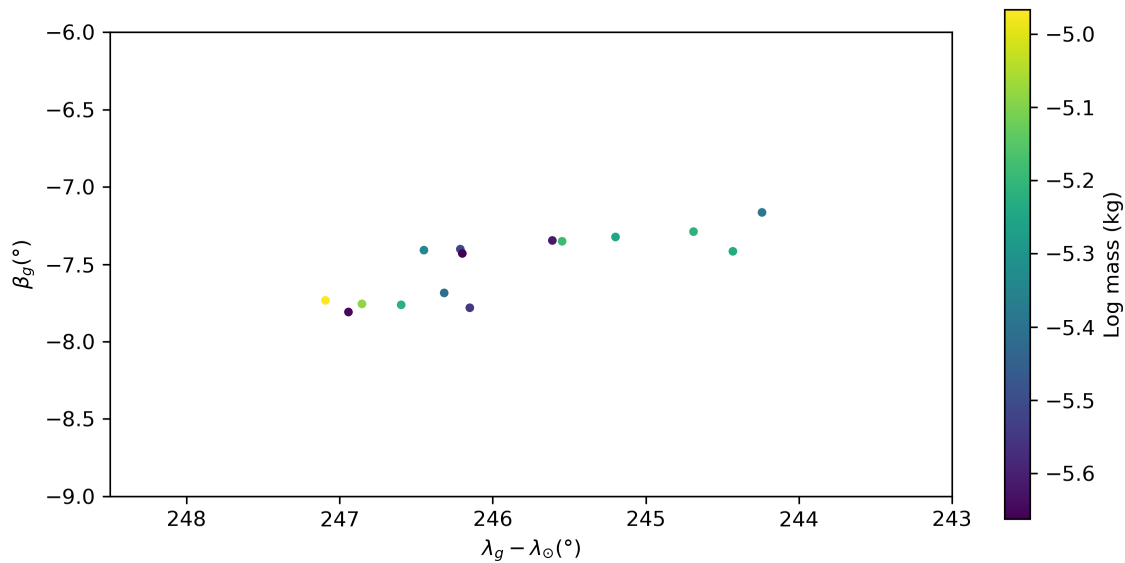
Figure 7.11: Orionid radiants in SCE coordinates with the photometric mass colour coded.

masses were computed from CAMO wide-field light curves using equation 5.16 (in Chapter 5) and a fixed dimensionless luminous efficiency of $\tau = 0.7\%$ and $P_{0M} = 840\,\text{W}$. Figure 7.11 shows the radiant plot with the logarithm of masses colour coded. All observed meteoroids had masses in the $2-10\,\mu\text{g}$ range. There is no strong grouping by radiant position, although the first four meteoroids from the right (excluding the rightmost outlier) have a similar mass of $\sim 6\,\mu\text{g}$.

Finally, we plot the radiants in equatorial coordinates and give them in Figures 7.12 and 7.13. As it can be seen, there is a strong radiant drift in right ascension which may obscure the structure. For this reason, we recommend using Sun-centered ecliptic coordinates.
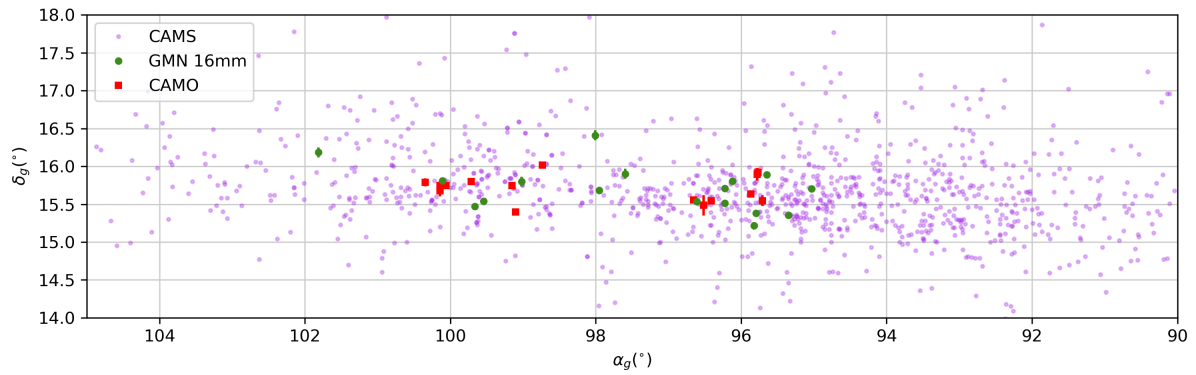
Figure 7.12: Orionid radiants in equatorial coordinates - comparison between CAMS, GMN, and CAMO observations.
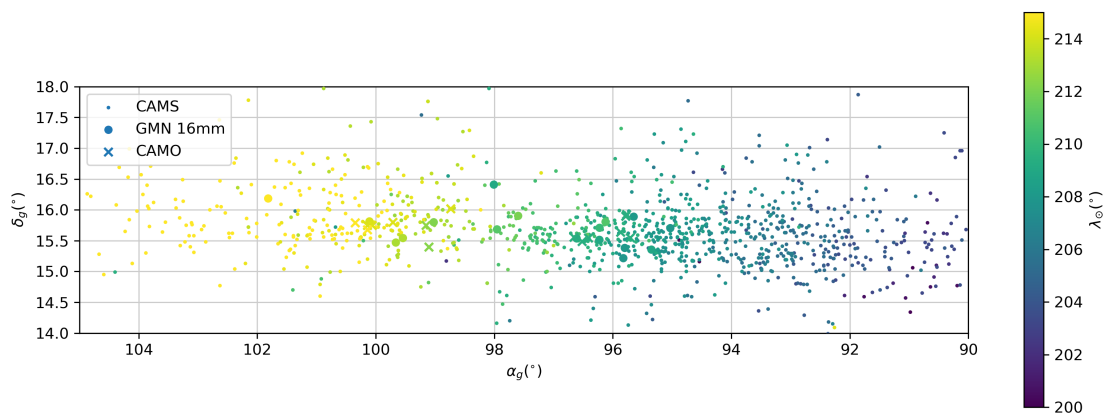
Figure 7.13: Orionid radiants in equatorial coordinates colour coded by solar longitude - comparison between CAMS, GMN, and CAMO observations.

Table 7.1: Radiants, orbits, and masses of the Orionids observed by CAMO. Rows below every entry list 1σ uncertainties. The uncertainties only state the measurement precision and not the total accuracy, the geocentric velocity is surely underestimated due to deceleration prior to detection.

Date and time (UTC)	$\lambda_\odot$ (deg)	α_g (deg)	δ_g (deg)	v_g (km s^{-1})	a (AU)	e	q (AU)	ω (deg)	i (deg)	π (deg)	Log mass (kg)
2019-10-23 08:42:14	209.3762	96.655	15.554	66.397	10.745	0.9455	0.5854	81.20	163.76	110.58	-4.97
		0.011	0.032	0.007	0.082	0.0004	0.00030	0.02	0.06	0.02	
2019-10-23 08:45:02	209.3781	96.410	15.543	66.828	21.291	0.9724	0.5881	80.18	163.76	109.56	-5.09
		0.006	0.017	0.015	0.651	0.0008	0.00013	0.03	0.03	0.03	
2019-10-23 08:49:16	209.3811	95.768	15.923	67.138	604.957	0.9990	0.5779	80.73	164.41	110.11	-5.52
		0.015	0.052	0.026	1640.671	0.0014	0.00023	0.03	0.11	0.03	
2019-10-23 08:54:37	209.3848	95.868	15.636	66.200	11.574	0.9512	0.5646	83.53	163.64	112.92	-5.42
		0.013	0.033	0.008	0.113	0.0005	0.00033	0.03	0.07	0.03	
2019-10-23 09:12:25	209.3971	96.518	15.485	66.510	12.876	0.9546	0.5846	81.06	163.60	110.46	-5.65
		0.012	0.134	0.046	0.542	0.0019	0.00024	0.04	0.28	0.04	
2019-10-23 09:13:10	209.3976	95.705	15.546	66.422	16.561	0.9658	0.5656	83.02	163.45	112.41	-5.55
		0.010	0.071	0.029	0.575	0.0013	0.00033	0.05	0.15	0.05	
2019-10-23 09:29:14	209.4087	95.782	15.895	66.640	21.799	0.9739	0.5688	82.43	164.24	111.83	-5.66
		0.020	0.084	0.029	1.252	0.0015	0.00037	0.01	0.18	0.01	

Table 7.1: continued.

Date and time (UTC)	$\lambda_\odot$ (deg)	α_g (deg)	δ_g (deg)	v_g (km s^{-1})	a (AU)	e	q (AU)	ω (deg)	i (deg)	π (deg)	Log mass (kg)
2019-10-26 06:06:16	212.2575	99.103	15.396	66.351	11.768	0.9513	0.5726	82.52	163.56	114.78	-5.22
		0.012	0.032	0.007	0.107	0.0005	0.00033	0.03	0.06	0.03	
2019-10-26 10:16:08	212.4306	99.151	15.747	66.445	13.251	0.9570	0.5692	82.77	164.28	115.20	-5.34
		0.023	0.049	0.042	0.612	0.0022	0.00075	0.12	0.10	0.12	
2019-10-28 05:06:17	214.2116	100.058	15.746	66.031	11.736	0.9539	0.5409	86.18	164.09	120.39	-5.19
		0.008	0.034	0.020	0.306	0.0009	0.00062	0.09	0.07	0.09	
2019-10-28 05:16:22	214.2186	98.735	16.017	64.993	7.475	0.9342	0.4921	92.59	163.91	126.80	-5.39
		0.010	0.028	0.009	0.051	0.0005	0.00024	0.02	0.06	0.02	
2019-10-28 05:18:34	214.2201	99.711	15.797	65.872	11.374	0.9534	0.5303	87.45	164.02	121.67	-5.25
		0.005	0.046	0.023	0.267	0.0010	0.00036	0.06	0.10	0.06	
2019-10-28 05:28:06	214.2267	100.140	15.746	65.813	9.380	0.9426	0.5381	86.84	164.06	121.07	-5.62
		0.025	0.057	0.096	1.069	0.0046	0.00122	0.27	0.13	0.27	
2019-10-29 08:21:22	215.3456	100.347	15.789	66.244	25.490	0.9794	0.5258	87.21	164.05	122.55	-5.22
		0.027	0.051	0.025	1.971	0.0015	0.00060	0.06	0.10	0.06	
2019-10-29 09:55:41	215.4110	100.140	15.675	65.741	13.508	0.9621	0.5116	89.38	163.59	124.79	-5.24

Table 7.1: continued.

Date and time (UTC)	$\lambda_\odot$ (deg)	α_g (deg)	δ_g (deg)	v_g (km s^{-1})	a (AU)	e	q (AU)	ω (deg)	i (deg)	π (deg)	Log mass (kg)
		0.033	0.072	0.032	0.645	0.0018	0.00059	0.04	0.15	0.04	

Table 7.2: Theoretical radiants of the Orionids computed using the method H of Neslušan et al. (1998) and orbital elements of the comet 1P/Halley given in Yeomans & Kiang (1981) precessed to J2000. The solar longitude $\lambda_\odot$ marks the point of closest approach to Earth, and D_{SH} is the value of the Southworth & Hawkins (1963) D criterion between the nominal orbit and the adjusted orbit that is closest to the Earth.

Apparition year	$\lambda_\odot$ (deg)	α_g (deg)	δ_g (deg)	v_g (km s^{-1})	D_{SH}	q AU	e	i (deg)	ω (deg)	Ω (deg)	Perihelion Julian date
1910	208.5	95.6	16.0	66.78	0.159	0.587	0.967	162.218	111.736	58.563	2418781.678
1835	208.5	95.6	16.0	66.77	0.153	0.587	0.967	162.258	110.705	57.519	2391598.939
1759	208.5	95.5	16.0	66.75	0.151	0.584	0.968	162.372	110.709	57.245	2363592.561
1682	208.5	95.4	15.9	66.70	0.144	0.583	0.968	162.269	109.224	55.568	2335655.781
1607	208.1	95.1	16.0	66.73	0.132	0.584	0.967	162.905	107.550	53.770	2308304.041
1531	208.2	95.1	16.0	66.70	0.128	0.581	0.968	162.917	106.976	53.057	2280492.738
1456	208.3	95.1	15.9	66.67	0.122	0.580	0.968	162.890	105.835	51.866	2253022.133
1378	208.4	95.0	16.0	66.64	0.116	0.576	0.968	163.113	105.295	51.020	2224686.187
1301	208.6	95.2	15.9	66.60	0.111	0.573	0.969	163.076	104.500	50.152	2196546.082
1222	208.2	94.8	16.0	66.61	0.108	0.574	0.969	163.192	103.849	49.304	2167664.323
1145	208.1	94.7	16.0	66.62	0.107	0.575	0.969	163.224	103.704	49.054	2139377.061
1066	207.9	94.5	15.9	66.60	0.102	0.574	0.969	163.112	102.473	47.624	2110493.434
989	206.9	93.8	16.0	66.68	0.100	0.582	0.968	163.399	101.484	46.561	2082538.188

Table 7.2: continued.

Apparition year	$\lambda_\odot$ (deg)	α_g (deg)	δ_g (deg)	v_g (km s^{-1})	D_{SH}	q AU	e	i (deg)	ω (deg)	Ω (deg)	Perihelion Julian date
912	206.9	93.7	15.9	66.65	0.096	0.580	0.968	163.311	100.777	45.646	2054365.174
837	206.6	93.4	15.9	66.67	0.093	0.582	0.968	163.447	100.102	44.930	2026830.770
760	206.5	93.3	15.9	66.67	0.092	0.582	0.968	163.443	99.998	44.687	1998788.171
684	206.7	93.4	15.9	66.63	0.087	0.580	0.968	163.418	99.149	43.800	1971164.267
607	206.4	93.1	15.9	66.65	0.086	0.581	0.968	163.476	98.799	43.261	1942837.976
530	206.8	93.4	15.8	66.58	0.078	0.576	0.969	163.394	97.582	41.974	1914909.630
451	206.8	93.3	15.8	66.56	0.074	0.574	0.969	163.479	97.028	41.210	1885963.749
374	206.3	92.9	15.9	66.60	0.073	0.577	0.969	163.542	96.511	40.579	1857707.842
295	206.2	92.7	15.7	66.56	0.066	0.576	0.969	163.367	95.242	39.111	1828915.898
218	205.4	92.2	15.8	66.62	0.063	0.581	0.968	163.574	94.147	37.908	1800819.223
141	205.0	91.8	15.7	66.63	0.063	0.583	0.968	163.437	93.694	37.219	1772638.934
66	204.7	91.5	15.8	66.65	0.058	0.585	0.968	163.576	92.652	36.129	1745189.460
-10	204.3	91.2	15.8	66.66	0.059	0.587	0.967	163.589	92.559	35.904	1717323.349
-87	204.4	91.2	15.6	66.63	0.050	0.586	0.968	163.340	90.778	34.018	1689863.962
-164	204.1	90.9	15.8	66.63	0.040	0.585	0.968	163.705	89.113	32.063	1661838.066

Table 7.2: continued.

Apparition year	$\lambda_\odot$ (deg)	α_g (deg)	δ_g (deg)	v_g (km s^{-1})	D_{SH}	q AU	e	i (deg)	ω (deg)	Ω (deg)	Perihelion Julian date
-240	203.7	90.5	15.6	66.61	0.036	0.585	0.968	163.467	88.113	30.809	1633907.618
-315	203.4	90.3	15.7	66.64	0.031	0.587	0.967	163.600	86.883	29.543	1606620.024
-391	203.2	90.1	15.7	66.64	0.031	0.588	0.967	163.605	86.813	29.323	1578866.869
-466	202.7	89.7	15.5	66.63	0.025	0.590	0.967	163.264	85.247	27.579	1551414.739
-540	202.4	89.4	15.6	66.66	0.018	0.592	0.967	163.485	83.590	25.842	1524318.327
-616	202.2	89.2	15.5	66.66	0.017	0.593	0.967	163.470	83.316	25.393	1496638.003
-690	201.1	88.4	15.5	66.72	0.018	0.600	0.966	163.381	82.714	24.577	1469421.779
-763	200.8	88.1	15.3	66.71	0.008	0.602	0.966	163.106	80.552	22.381	1442954.030
-836	200.9	88.1	15.4	66.69	0.003	0.599	0.966	163.298	78.565	20.261	1416202.807
-911	200.7	87.9	15.4	66.69	0.006	0.598	0.966	163.253	78.167	19.659	1388819.720
-986	200.2	87.4	15.4	66.71	0.006	0.602	0.966	163.251	77.724	19.044	1361622.064
-1059	198.8	86.4	15.1	66.78	0.006	0.612	0.965	162.940	76.662	17.738	1334960.164
-1129	197.5	85.4	15.1	66.86	0.008	0.622	0.964	162.950	75.003	15.955	1309149.345
-1198	196.6	84.8	15.0	66.92	0.007	0.629	0.963	162.966	74.477	15.367	1283983.733
-1266	195.8	84.1	14.9	66.95	0.006	0.634	0.962	162.850	74.041	14.731	1259263.896

Table 7.2: continued.

Apparition year	$\lambda_\odot$ (deg)	α_g (deg)	δ_g (deg)	v_g (km s^{-1})	D_{SH}	q AU	e	i (deg)	ω (deg)	Ω (deg)	Perihelion Julian date
-1334	196.5	84.6	14.9	66.88	0.015	0.627	0.963	162.805	73.231	13.792	1234416.006
-1404	197.0	84.9	14.9	66.81	0.025	0.620	0.964	162.501	71.947	12.420	1208900.181

7.4 Conclusions

Multi-station observations of the Orionid meteor shower were performed using the CAMO mirror tracking system in October 2019. The narrow field data was manually reduced and high-precision trajectories were computed. The median radiant error for individual Orionids detected by CAMO was 0.05°.

All observed Orionids show a leading fragment morphology, permitting high trajectory precision. Although spectral observations and ablation modelling is required to derive physical properties of these leading fragments, their non-fragmenting nature and lower deceleration would be consistent with refractory inclusions. If so, this would mean that these thermally processed particles were mixed into 1P/Halley, which presumably formed in the outer Solar System.

The Orionid radiant spread shows an elongated structure which is also visible in the high-precision Global Meteor Network data set. The radiant dispersion was measured as the median offset from the mean drift-corrected radiant. Including all observations, the dispersion is 0.41°, but almost entirely in the Sun-centred ecliptic longitude direction - the median spread in the ecliptic latitude is only ~0.1°. This dispersion is considerably larger than our median measurement precision and is about half the the dispersion measured by Kresák & Porubčan (1970). It represents our best estimate of the physical radiant dispersion of the Orionid shower near the time of its maximum appropriate to $1 - 10 \, \mu$g masses.

A significant decrease in the dispersion can achieved if the radiants are split into two groups of SCE longitude at $(\lambda_g - \lambda_\odot) = 246°$. The group with $\leq 246°$ has a dispersion of only 0.12°, but only five radiants are a part of this group. Four out of five radiants in this group had photometric masses around to $6 \, \mu$g, while masses of the whole data set were uniformly distributed in the $2 - 10 \, \mu$g range. This may indicate that only meteoroids in this specific mass range were scattered into the branch after a close encounter with a planet. However, the small number statistics make this breakdown into groupings uncertain; more high precision measurements of the Orionids are needed to see if this structure remains.

We have demonstrated that the CAMO mirror tracking system can resolve the true physical dispersion of the Orionids, which we find to be about an order of magnitude larger than the measurement precision. Nevertheless, more high-precision observations of the Orionids are needed to confidently deduce its radiant structure. Numerical modelling of the Orionid meteoroid stream is necessary to understand its dynamical evolution, and these observations can be used to constrain the model parameters.

Bibliography

Borovička, J. 1990, Bulletin of the Astronomical Institutes of Czechoslovakia, 41, 391

Chau, J., & Galindo, F. 2008, Icarus, 194, 23. `http://linkinghub.elsevier.com/retrieve/pii/S001910350700471X`

Hajduk, A. 1970, Bulletin of the Astronomical Institutes of Czechoslovakia, 21, 37

Jacchia, L. G., & Whipple, F. L. 1961, Smithsonian Contributions to Astrophysics

Jenniskens, P. 2006, Meteor showers and their parent comets (Cambridge University Press)

Jenniskens, P., Gural, P., Dynneson, L., et al. 2011, Icarus, 216, 40

Jenniskens, P., Nénon, Q., Albers, J., et al. 2016, Icarus, 266, 331

Jones, J., McIntosh, B., & Hawkes, R. 1989, Monthly Notices of the Royal Astronomical Society, 238, 179

Kresák, L., & Porubčan, V. 1970, Bulletin of the Astronomical Institutes of Czechoslovakia, 21, 153

McIntosh, B., & Hajduk, A. 1983, Monthly Notices of the Royal Astronomical Society, 205, 931

Neslušan, L., Svoreň, J., & Porubčan, V. 1998, Astronomy and Astrophysics, 331, 411

Porubčan, V. 1973, Bulletin of the Astronomical Institutes of Czechoslovakia, 24, 1

Sato, M., & Watanabe, J.-i. 2007, Publications of the Astronomical Society of Japan, 59, L21

Sekhar, A., & Asher, D. J. 2014, Meteoritics & Planetary Science, 49, 52

Simon, S. B., Joswiak, D., Ishii, H., et al. 2008, Meteoritics & Planetary Science, 43, 1861

Southworth, R., & Hawkins, G. 1963, Smithsonian Contributions to Astrophysics, 7, 261

Spurnỳ, P., & Shrbenỳ, L. 2008, Earth, Moon, and Planets, 102, 141

Subasinghe, D., & Campbell-Brown, M. 2018, The Astronomical Journal, 155, 88

Vida, D., Gural, P. S., Brown, P. G., Campbell-Brown, M., & Wiegert, P. 2020, Monthly Notices of the Royal Astronomical Society, 491, 2688

Yeomans, D. K., & Kiang, T. 1981, Monthly Notices of the Royal Astronomical Society, 197, 633

Znojil, V. 1968, Bulletin of the Astronomical Institutes of Czechoslovakia, 19, 306

Znojil, V., Hollan, J., & Hajduk, A. 1987, Bulletin of the Astronomical Institutes of Czechoslovakia, 38, 372

Chapter 8

Conclusion

8.1   Thesis summary

The main goal of this work is to improve understanding of meteor trajectory and orbit accuracy as a means specifically to measure the physical dispersion of radiants within meteor showers. As discussed in Chapter 1, the current understanding of methods, uncertainty estimation, and the total accuracy of measuring meteor trajectories is insufficient to claim that physical meteor shower radiant dispersions can be resolved. It has been suggested in the past that measured radiant dispersions are dominated by measurement error for all but the oldest and most disperse showers. This suggests that radiant dispersions derived through dynamic modelling of meteoroids ejected from their parent comets might be an order of magnitude smaller than observed dispersions. Measuring the real physical dispersion of young meteor shower radiants, before non-gravitational forces and stochastic processes significantly influence the meteoroid stream, may make it possible to directly derive ejection velocities of meteoroids from their parent bodies (comets and asteroids). As meteor orbits are computed from two distinct measurements, the meteor radiant and the meteoroid pre-atmosphere velocity, we investigated the orbital accuracy one may expect to achieve using state-of-the-art optical meteor observation systems and methods.

In Chapter 2, numerical models of meteor ablation were used to demonstrate that small meteors decelerate up to $750\,\mathrm{m\,s^{-1}}$ (up to 5%) prior to becoming visible by common optical observation systems. The total amount of deceleration prior to detection depends on meteoroid size (smaller ones decelerate more), compositional type (asteroidal decelerate more than cometary), and zenith angle (meteors with steeper entry angles decelerate less). This work demonstrates that despite being able to precisely measure velocities of meteors at the point where they first become visible, the ultimate accuracy of the pre-atmosphere (no deceleration) velocity is model-dependent. Thus, the main limitation to measured orbital accuracy is the fidelity of meteor ablation models and the quality of fit to data.

In Chapters 3 and 4 a novel meteor trajectory simulator and a novel method of meteor trajectory estimation are developed and tested. It was demonstrated that the novel trajectory estimation method is superior to previous methods, especially for data with high-precision measurements where meteor deceleration is visible. Critically, the novel method uses the observed dynamics of meteors to constrain the trajectory, but without forcing meteor kinematic models. Furthermore, through dynamical meteoroid stream modelling of the 2011 Draconid outburst, it was shown that a minimum radiant measurement accuracy of 0.1° is needed to resolve the physical dispersion of structure of the tightest (i.e. the youngest) meteor showers. This radiant measurement accuracy can be achieved by moderate field of view systems, as well as the Canadian Automated Meteor Observatory's mirror tracking system (which has an accuracy approaching 0.01°).

In Chapter 5 a novel method of estimating mass indices of meteor populations based on the maximum likelihood estimation method was developed. The method was applied to the 2018 outburst of the Draconid meteor shower. Multi-station observations of the shower were conducted using sensitive EMCCD cameras, and radiants and orbits of observed meteors were computed. Critically for this thesis, the measured dispersion of the shower was 0.25° (median offset from the mean radiant), which is in good agreement with previous high-precision observations and simulations.

Chapter 6 presents hardware and data reduction pipeline details of the CAMO mirror tracking system. It was shown that the meteor trajectory measurement precision is not only dependent on the optical resolving power but for such a high optical resolution system the meteor morphology becomes a limiting factor. Compact and non-fragmenting meteors have the best radiant precision, approaching the theoretical value of 0.01° for CAMO, while highly fragmenting meteors have a significantly worse precision which is on par with non-tracking moderate field of view systems. As a by-product of this work, the compressive strength of 20 highly fragmenting meteors was measured. The dynamic pressure at the moment of directly observed fragmentation was used as a proxy for meteoroid bulk compressive strength. It was found that the measured values of $1 - 4\,\mathrm{kPa}$ are in excellent accordance with in-situ measurements by Rosetta.

Finally, in Chapter 7 the physical dispersion of the 2019 Orionid meteor shower was measured. Taking all radiants together, the dispersion (measured as the median offset from the drift-corrected radiant) was ~0.4°. Dividing the radiant into branches by Sun-centred ecliptic longitude, a further reduction of the dispersion can be achieved to about 0.1°, but more observations are needed to confidently deduce the true structure. The median radiant measurement error of 0.05° was a factor of two to an order of magnitude smaller than the observed dispersion. It was also noticed through high-resolution CAMO observations that all Orionids show the leading fragment morphology, which has implications to the understanding of Solar System formation.

8.2 Future Work

Future work using the CAMO mirror tracking system to gather high quality radiants to measure dispersion is contingent on favourable observing conditions during the activity of meteor showers of interest. To continue the study described in Chapter 7, more observations of the Orionids need to be collected. The ultimate goal would be to measure physical dispersions of

all major meteor showers to characterize their age, such as the Lyrids, η Aquariids, southern δ Aquariids, Perseids, Draconids, Leonids and Geminids. While the physical spread for young streams is a proxy for ejection speed, the dispersion of older streams is useful as a direct proxy for age; thus the true radiant spread of a shower may give an independent estimate for stream age. The usefulness of low-cost systems used by the Global Meteor Network for dispersion measurements should be investigated, as they may also provide high-quality data. The morphology of all shower meteors observed by the CAMO mirror tracking system will be analyzed to infer their physical properties and dynamical histories.

In the future, meteoroid ablation models may be used to fit Orionid light curves, deceleration profiles, and wakes in an attempt to infer physical properties of Orionid meteoroids and leading fragments. Such detailed models yield as a side-product accurate meteoroid pre-atmosphere velocities, which may help to constrain the orbital parameter space populated by the Orionids and in turn inform their dynamical history.

Finally, an ablation model fit to high-fidelity observations of the 2018 Draconid outburst to infer meteoroid grain size distribution and density would be useful in constraining radiant dispersion. As the Draconids are the youngest observed shower, they are the best candidate for constraining the ejection speed from the parent comet through dynamical meteoroid stream modelling.

Ablation models are complex due to different possible modes of fragmentation and the number of free parameters, hence they are usually fit manually to data. A machine learning approach might be useful to automate the process and facilitate parameter estimation for a larger number of meteor events.

Appendix A

Equations and transformations for trajectory and orbit computation

A.1 Bending of the trajectory due to gravity

The straight line approximation for trajectories breaks down in the case of long (> 4 s) meteors, when they will show vertical curvature that should be visible even with less precise systems. At a height of 100 km the gravitational acceleration is $g = $ ~9.5 m s^{-2}, although it changes as the meteor descends through the atmosphere with the classical relation

$$g(r) = \frac{GM_E}{r^2} \, , \tag{A.1}$$

where M_E is the mass of the Earth and r is the distance of the meteor from the centre of the Earth. To compute the changing value of the gravitational acceleration, we assume that at the begin point, the downward vertical component of the meteor's velocity v_z is equal to the vertical component of the initial velocity

$$v_z = -v_0 \cos z_c \, , \tag{A.2}$$

315

where v_0 is the initial velocity and z_c the apparent zenith angle. Thus, the gravitational acceleration at a relative time t after the beginning of the meteor is

$$g(t) = \frac{GM_E}{(r_0 + v_z t)^2} ,$$
(A.3)

where M_E is the mass of the Earth and r_0 is the distance from the centre of the Earth to the beginning height of the meteor. The total drop of the meteor due to gravity after time T is then

$$\Delta h(T) = \int_0^T g(t)t \, dt .$$
(A.4)

After integration we obtain the following relation:

$$\Delta h(T) = \frac{GM_E}{v_z^2} \left(\frac{r_0}{r_0 + v_z T} + \ln \frac{r_0 + v_z T}{r_0} - 1 \right) .$$
(A.5)

To avoid domain issues when $v_z \approx 0$ we only use this expanded equation if $|v_z| > 100 \, \mathrm{m\,s^{-1}}$, otherwise we use equation A.1 with $r = r_0$ to compute g and the classical way of computing the additional drop in height due to gravity

$$\Delta h(T) = \frac{1}{2} g T^2 .$$
(A.6)

Applying Δh to the vertical component of the meteor at every point in time effectively simulates the curvature of the meteor's trajectory due to gravity.

A.2   Distance between lines in 3D space

Let vector $\vec{P}$ be the position of the observer in an arbitrary rectangular coordinate system, and $\vec{U}$ be the direction vector of the line of sight emanating from the observer. Let $\vec{S}$ be the position of the state vector, and $\vec{R}$ be the radiant vector. The closest points of approach can be calculated as

$$\vec{w} = \vec{P} - \vec{S},$$

$$a = \vec{U} \cdot \vec{U},$$

$$b = \vec{U} \cdot \vec{R},$$

$$c = \vec{R} \cdot \vec{R},$$

$$d = \vec{U} \cdot \vec{w},$$

$$e = \vec{R} \cdot \vec{w}, \qquad (A.7)$$

$$Q_C = \frac{be - cd}{ac - b^2},$$

$$T_C = \frac{ae - bd}{ac - b^2},$$

$$\vec{Q} = \vec{P} + Q_C\vec{U},$$

$$\vec{T} = \vec{S} + T_C\vec{R},$$

$$d = |\vec{Q} - \vec{T}|,$$

where $\vec{Q}$ is the point on the observer's line of sight closest to the radiant line, and $\vec{T}$ is the point on the radiant line closest to the line of sight of the observer. d is the distance between those two points. The equations are taken from Eberly (2006) in a modified form.

A.3   Orbit computation

The orbit is computed from 4 parameters: The apparent radiant unit vector $\hat{R}$, the initial velocity v_0, the ECI coordinates of the state vector $\vec{S}$, and the reference Julian date of the beginning of the meteor JD_{ref}. The equations below assume that the radiant and the state vector are given in the epoch of date, not J2000. Furthermore, we assume that the location of the state vector is at the beginning of the meteor, not at an average point on the trajectory. The state vector $\vec{S}$ should be in meters and the initial velocity v_0 in $\mathrm{m\,s^{-1}}$ to be consistent with constants and parameter units used herein.

First, the geocentric latitude of the state vector is calculated as

$$\varphi' = \text{atan2}\left(S_z, \sqrt{S_x^2 + S_y^2}\right).$$ (A.8)

Next, care must taken to use the Barycentric Dynamical Time TDB in calculations where necessary. For epochs in 1972 and later the dynamical time is simply calculated as the Julian date with the added leap seconds Δt up to the given JD, plus a constant of 32.184 s (Clark, 2010). The number of leap seconds can be obtained from the United States Naval observatory FTP site[1]. For example, Δt for a meteor observed between 2006 and 2009 is 33 s, while for a meteor observed after January 1, 2017 (until a future leap second is added) is 37 s.

$$TDB = JD_{ref} + \frac{\Delta t + 32.184}{86400}$$ (A.9)

Next, the geodetic latitude φ and the longitude λ of the beginning point of the meteor projected onto the Earth's surface are calculated from the ECI coordinates of the state vector using the method described in A.4.2.

A.3.1   Correcting the apparent radiant and the velocity for Earth's rotation

If the trajectory was estimated with the intersecting planes method, or if the stations were kept fixed, one needs to correct the radiant for Earth's rotation. Please note the important fact that the correction described in this section must not be applied if the ECI coordinates of the stations were moving in time in the trajectory estimation procedure. Thus, if the station coordinates were moving during the meteor event, the velocity vector is simply calculated as

$$\vec{v_0} = v_0 \hat{R},$$ (A.10)

and the rest of the equations in this subsection A.3.1 can be skipped. Otherwise, the procedure

---

[1]USNO leap seconds file, `ftp://maia.usno.navy.mil/ser7/tai-utc.dat`, (Accessed February 18, 2018)

described below must be followed.

The rotation velocity of the Earth (in m s^{-1}) at the height of the state vector can be calculated as

$$v_e = \frac{2\pi |\vec{S}| \cos \varphi'}{86164.09053} \, , \tag{A.11}$$

where the number in the denominator is the duration of the sidereal day in seconds.

Next, as the direction of the Earth's rotation vector is always towards the east, we can calculate the components of the velocity vector of the meteor $\vec{v_0}$ as

$$v_{0x} = v_0 \hat{R}_x - v_e \cos \alpha_e \, ,$$
$$v_{0y} = v_0 \hat{R}_y - v_e \sin \alpha_e \, , \tag{A.12}$$
$$v_{0z} = v_0 \hat{R}_z \, ,$$

where α_e is the right ascension of the direction of the rotation of the Earth. This can be calculated using the equations given in Appendix A.6 if we take the azimuth to be $A = \frac{\pi}{2}$ (i.e. due East) and elevation $a = 0$.

It is very important to note that this correction only influences the direction of the radiant, but not the initial velocity itself. This is only true if ECI coordinates are used throughout, regardless of keeping the stations fixed or not. This arises from the way the velocity is computed in this work, which is always done with the time in mind, and using moving stations. Once the trajectory is computed, we can estimate the time offsets easily and compute the rotation-corrected velocity. But as we have used a fixed radiant to do that, we only have to correct it, and not the velocity.

A.3.2 Geocentric radiant

First, we calculate equatorial coordinates of the apparent radiant following Ceplecha (1987) as

$$\hat{v}_0 = \frac{\overrightarrow{v_0}}{|\overrightarrow{v_0}|} \, ,$$

$$\alpha = \text{atan2}\left(\hat{v}_{0y}, \hat{v}_{0x}\right) \, , \tag{A.13}$$

$$\delta = \arcsin \hat{v}_{0z} \, .$$

The geocentric velocity is calculated as

$$v_g = \sqrt{v_0^2 - \frac{2 * 6.67408 * 5.9722 * 10^{13}}{|\overrightarrow{S}|}} \, , \tag{A.14}$$

where the second term under the square root is the square of the escape velocity $\left(\frac{2GM_E}{r}\right)$ at the height of the state vector. Next, the zenith attraction correction is applied using the Schiaparelli method (Gural, 2001):

$$z_c = \arccos\left(\sin\delta \sin\varphi' + \cos\delta \cos\varphi' \cos\left(\theta' - \alpha\right)\right) \, ,$$

$$\Delta z_c = 2\,\text{atan2}\left((v_0 - v_g)\tan\frac{z_c}{2}, v_0 + v_g\right) \, , \tag{A.15}$$

$$z_g = z_c + |\Delta z_c| \, ,$$

where z_c is the apparent zenith angle, θ' is the apparent local sidereal time (see Appendix A.5), Δz_c the zenith attraction correction, and z_g the zenith angle of the geocentric radiant.

The azimuth A_c of the radiant (possibly corrected for Earth's rotation) is calculated using the equations given in Appendix A.7. The apparent α and δ should be used, and care must be taken to use the geocentric latitude φ' instead of the geodetic latitude. The geocentric radiant in equatorial coordinates (α_g, δ_g) is then calculated using the equations given in Appendix A.6, where the azimuth is $A = A_c$, the elevation is $a = \frac{\pi}{2} - z_g$, and the geocentric latitude φ' must be used as well.

Next, the radiant is precessed from the epoch of date (JD_{ref}) to J2000 using the equations given in Appendix A.8. The geocentric ecliptic longitude λ_g and latitude β_g are calculated with equations given in Appendix A.9; care must be taken to use the Julian date of J2000 $(JD = 2451545)$ when computing ecliptic coordinates, not JD_{ref}.

A.3.3 Precessing ECI coordinates to J2000

As the ECI coordinates of the meteor are in the epoch of date, they have to be precessed to J2000. This can easily be done by converting them to spherical coordinates

$$
r_{ECI} = |\vec{S}| ,
$$

$$
\alpha_{ECI} = \text{atan2}\left(S_y, S_x\right) , \tag{A.16}
$$

$$
\delta_{ECI} = \arccos \frac{S_z}{r_{ECI}} ,
$$

were r_{ECI} is the distance from the center of the Earth to the reference position of the meteor, and α_{ECI} and δ_{ECI} are angular components. α_{ECI} and δ_{ECI} are precessed to J2000 from JD_{ref} using equations given in Appendix A.8, after which α'_{ECI} and δ'_{ECI} are obtained. Finally, these coordinates can be converted back to rectangular ECI coordinates in J2000

$$
S'_x = r_{ECI} \sin \delta'_{ECI} \cos \alpha'_{ECI} ,
$$

$$
S'_y = r_{ECI} \sin \delta'_{ECI} \sin \alpha'_{ECI} , \tag{A.17}
$$

$$
S'_z = r_{ECI} \cos \delta'_{ECI} .
$$

A.3.4 Position and the velocity of the Earth

JPL DE430 ephemerids (Folkner et al., 2014) are used for computing Cartesian heliocentric ecliptic coordinates and the velocity of the Earth at the reference dynamical time TDB. As the implementation of the ephemerids does not allow the calculation of the heliocentric ecliptic coordinates of the Earth directly, the following procedure was adopted:

1. The position $\overrightarrow{R_{EMB}}$ and the velocity $\overrightarrow{V_{EMB}}$ of the Earth-Moon barycentre with respect to the Solar System Barycentre is obtained from the model in heliocentric equatorial coordinates (kilometers).

2. The position $\overrightarrow{R_{SB}}$ and the velocity $\overrightarrow{V_{SB}}$ of the centre of the Sun with respect to the So-lar System barycentre is obtained from the model in heliocentric equatorial coordinates

(kilometers).

3. The position $\overrightarrow{R_{EEM}}$ and the velocity $\overrightarrow{V_{EEM}}$ of the centre of the Earth with repect to the the Earth-Moon barycentre is obtained from the model in heliocentric equatorial coordinates (kilometers).

The heliocentric position and the velocity of the centre of the Earth in equatorial coordinates is then computed as

$$\overrightarrow{R_{EH}} = \overrightarrow{R_{EMB}} - \overrightarrow{R_{SB}} + \overrightarrow{R_{EEM}} ,$$
$$\overrightarrow{V_{EH}} = \overrightarrow{V_{EMB}} - \overrightarrow{V_{SB}} + \overrightarrow{V_{EEM}} ,$$

(A.18)

where $\overrightarrow{R_{EH}}$ and $\overrightarrow{V_{EH}}$ are in km and $\mathrm{km\,s^{-1}}$, respectively.

A.3.5 Heliocentric coordinates of the meteor

Coordinates of the meteor in heliocentric equatorial coordinates can be calculated by simply adding the position of the Earth in heliocentric equatorial coordinates to the ECI coordinates of the meteor in J2000

$$\vec{M} = \overrightarrow{R_{EH}} + \frac{\vec{S'}}{1000} .$$

(A.19)

Care must be taken to match the units, as the ECI coordinates were given in meters, while $\vec{M}$ should be in kilometers. Both the coordinates of the meteor $\vec{M}$ and the velocity of the Earth $\overrightarrow{V_{EH}}$ have to be converted to the ecliptic reference frame by rotating them on the X axis by the negative value of the mean obliquity of the Earth at J2000, $\epsilon_{J2000} = 23.439\,291\,111\,1°$

$$\begin{bmatrix} x_{ecliptic} \\ y_{ecliptic} \\ z_{ecliptic} \end{bmatrix} = \begin{bmatrix} 1 & 0 & 0 \\ 0 & \cos(-\epsilon_{J2000}) & \sin(-\epsilon_{J2000}) \\ 0 & -\sin(-\epsilon_{J2000}) & \cos(-\epsilon_{J2000}) \end{bmatrix} \begin{bmatrix} x_{equatorial} \\ y_{equatorial} \\ z_{equatorial} \end{bmatrix} ,$$

(A.20)

after which $\overrightarrow{M'}$ and $\overrightarrow{V'_{EH}}$ in heliocentric ecliptic coordinates are obtained.

The heliocentric velocity vector of the meteor is calculated by adding the geocentric veloc-ity of the meteor to the velocity of the Earth. As $\overrightarrow{V'_{EH}}$ is in heliocentric ecliptic coordinates, we convert the geocentric velocity into an ecliptic velocity vector (λ_g and β_g can be computed using equations in Appendix A.9):

$$v_{gEx} = -v_g \cos \lambda_g \cos \beta_g \,,$$
$$v_{gEy} = -v_g \sin \lambda_g \cos \beta_g \,, \qquad \text{(A.21)}$$
$$v_{gEz} = -v_g \sin \beta_g \,,$$

and add it to the velocity of the Earth around the Sun to obtain the heliocentric velocity vector $\overrightarrow{v_H}$:

$$\overrightarrow{v_H} = \overrightarrow{V'_{EH}} + \frac{\overrightarrow{v_{gE}}}{1000} \,, \qquad \text{(A.22)}$$

where $\overrightarrow{v_H}$ and $\overrightarrow{V'_{EH}}$ are km s^{-1}, and $\overrightarrow{v_{gE}}$ is in m s^{-1}.

A.3.6   Heliocentric ecliptic radiants

Tsuchiya et al. (2017) have shown that low-velocity meteor showers suffer from large disper-sion in geocentric equatorial coordinates due to the component of Earth's velocity. They pro-pose calculating radiants in heliocentric ecliptic coordinates, as slower meteor showers show significantly lower dispersions in that coordinate system. For completeness, we give the equa-tions below.

The unit heliocentric velocity vector of the meteoroid is calculated as

$$\hat{V}_c = \frac{\overrightarrow{v_H}}{|\overrightarrow{v_H}|} \,, \qquad \text{(A.23)}$$

and the radiant in heliocentric ecliptic coordinates is then calculated as

$$\lambda_h = \text{atan2}\left(\hat{V}_{cy}, \hat{V}_{cx}\right) + \pi,$$

$$\beta_h = -\arcsin \hat{V}_{cz}.$$

(A.24)

A.3.7   Keplerian orbital elements

The solar longitude $\lambda_\odot$ can be calculated from the ecliptic heliocentric position of the Earth $\overrightarrow{R'_{EH}}$, which can be computed by rotating the equatorial heliocentric position $\overrightarrow{R_{EH}}$ using equation A.20.

$$\lambda_\odot = \text{atan2}\left(R'_{EHy}, R'_{EHx}\right) + \pi$$

(A.25)

The specific orbital energy ϵ can be calculated as

$$\epsilon = \frac{|\overrightarrow{v_H}|^2}{2} - \frac{\mu_\odot}{|\overrightarrow{M'}|},$$

(A.26)

where $\overrightarrow{v_H}$ is the heliocentric ecliptic velocity vector of the meteor, $\mu_\odot = 1.327\,124\,400\,18 \times 10^{11}\,\text{km}^3\,\text{s}^{-2}$ is the gravitational constant of the Sun, and $\overrightarrow{M'}$ is the heliocentric ecliptic position vector of the meteoroid.

The semi-major axis in AU is

$$a = \frac{-\mu_\odot}{2\epsilon r_{AU}},$$

(A.27)

where $r_{AU} = 149\,597\,870.7\,\text{km}$ is one astronomical unit in kilometers. Mean motion in radians per day can be calculated as

$$n = 86400\sqrt{\frac{GM_\odot}{(1000|a|r_{AU})^3}},$$

(A.28)

where $G = 6.673\,84 \times 10^{-11}\,\text{m}^3\,\text{kg}^{-1}\,\text{s}^{-2}$ is the gravitational constant, and $M_\odot = 1.988\,55 \times 10^{30}\,\text{kg}$ is the mass of the Sun. The orbital period in years is

$$T = \frac{2\pi}{86400 Y_S} \sqrt{\frac{(r_{AU}a)^3}{\mu_\odot}}, \tag{A.29}$$

where $Y_S = 365.256363004$ is the sidereal year in days. Next, we calculate the orbital angular momentum vector

$$\vec{h} = \vec{M'} \times \vec{v_H}; \tag{A.30}$$

the inclination is then simply

$$i = \arccos \frac{h_z}{|\vec{h}|}, \tag{A.31}$$

and the eccentricity is then the magnitude of the eccentricity vector

$$\vec{e} = \frac{\vec{v_H} \times \vec{h}}{\mu_\odot} - \frac{\vec{M'}}{|\vec{M'}|}, \tag{A.32}$$

$$e = |\vec{e}|.$$

We follow Jenniskens et al. (2011) on calculating the perihelion distance:

$$q = \begin{cases} \frac{|\vec{M'}| + \vec{e} \cdot \vec{M'}}{1 + |\vec{e}|}, & e = 1 \\ a(1 - e), & \text{otherwise} \end{cases}; \tag{A.33}$$

the aphelion distance is then simply

$$Q = a(1 + e). \tag{A.34}$$

The ascending node Ω is calculated following Clark (2010) as

$$\vec{k} = [0, 0, 1],$$
$$\vec{n} = \vec{k} \times \vec{h}, \tag{A.35}$$

$$\Omega = \begin{cases} 0, & |\vec{n}| = 0 \\ \text{atan2}\left(n_y, n_x\right), & \text{otherwise} \end{cases}, \tag{A.36}$$

where $\vec{n}$ is a vector pointing from the Sun to the ascending node. Please note that the ascending node loses meaning for inclinations close to $0°$, thus we keep the node at $0°$ when the magnitude of the $\vec{n}$ vector is 0.

If $|\vec{n}| \neq 0$, the argument of perihelion ω is calculated as

$$\omega = \arccos \frac{\vec{n} \cdot \vec{e}}{|\vec{n}||\vec{e}|}, \tag{A.37}$$

and if $e_z < 0$ then $\omega = 2\pi - \omega$. If on the other hand $|\vec{n}| = 0$, then

$$\omega = \arccos \frac{e_x}{|\vec{e}|}. \tag{A.38}$$

The longitude of perihelion ϖ is simply

$$\varpi = \Omega + \omega. \tag{A.39}$$

True anomaly v is calculated as

$$v = \arccos \frac{\vec{e} \cdot \vec{M'}}{|\vec{e}||\vec{M'}|}, \tag{A.40}$$

and if $\vec{M'} \cdot \vec{v_H} < 0$ then $v = 2\pi - v$.

The eccentric anomaly E is

$$E = \text{atan2}\left(\sqrt{1 - e^2} \sin v, e + \cos v \right), \tag{A.41}$$

from which the mean anomaly M can be calculated as

$$M = E - e \sin E. \tag{A.42}$$

The time in days since the last perihelion passage, reference to TDB, is

$$\Delta t_\varpi = \frac{Ma^{3/2}}{k}\,, \tag{A.43}$$

where $k = 0.01720209895(\text{AU})^{3/2}(\text{day})^{-1}(\text{solar mass})^{-1/2}$ is the Gaussian gravitational constant.

Finally, we calculate the Tisserand parameter with respect to Jupiter as

$$T_J = \frac{a_J}{a} + 2\sqrt{(1 - e^2)\frac{a}{a_J}}\cos i\,, \tag{A.44}$$

where $a_J = 5.204267\text{AU}$ is the semi-major axis of Jupiter.

A.4   Earth-centered inertial coordinates

The Earth-centered inertial (ECI) coordinates are a Cartesian coordinate system where the X-Y plane coincides with the equatorial plane of the Earth, and the X axis passes through the equinox of the given epoch. The Z axis passes through the Earth's North pole. As the coordinate system is permanently fixed to the celestial sphere, a fixed point on the surface of the Earth will have changing coordinates in time. As we assume that the observations are given in the epoch of date, we keep the ECI coordinates in the epoch of date as well. The equations in this chapter are reproduced from Chatfield (1997) and Archinal (1992) in a modified form.

Let the distance from the centre of the Earth to the position given by geographical coordinates in the WGS84 system be calculated as follows:

$$N = \frac{r_e}{\sqrt{1 - e_e^2 \sin^2 \varphi}}\,, \tag{A.45}$$

where r_e is the equatorial radius of the Earth as defined by the WGS84 system, $r_e = 6\,378\,137.0\,\text{m}$, and e_e is the equatorial ellipticity of an oblate Earth

$$e_e = \sqrt{1 - \frac{r_p^2}{r_e^2}}, \qquad \text{(A.46)}$$

where r_p is the polar radius of the Earth, $r_p = 6\,356\,752.314\,245$ m. The polar ellipticity is

$$e_p = \sqrt{\frac{r_e^2 - r_p^2}{r_p^2}}. \qquad \text{(A.47)}$$

A.4.1   Converting geographical coordinates to ECI

Let φ be the geodetic latitude, λ the longitude, h the height above a WGS84 model for Earth, and θ' the apparent local sidereal time (LST). Note that the height is not the same as the Mean Sea Level (MSL) height reported by Google Earth and some GPS devices. If the MSL height is used, it has to be first converted to WGS84 height (Pavlis et al., 2012). The apparent LST θ' can be calculated using the procedure described in Meeus (1998) page 88 and Clark (2010), see Appendix A.5 for equations.

First, the coordinates are transformed into Earth-Centred Earth-Fixed (ECEF) coordinates

$$\begin{aligned} x_{ECEF} &= (N + h)\cos\varphi \cos\lambda, \\ y_{ECEF} &= (N + h)\cos\varphi \sin\lambda, \\ z_{ECEF} &= \left((1 - e_e^2)N + h\right)\sin\varphi. \end{aligned} \qquad \text{(A.48)}$$

The radius of the Earth at the given geodetic latitude is then

$$R_h = \sqrt{x_{ECEF}^2 + y_{ECEF}^2 + z_{ECEF}^2}. \qquad \text{(A.49)}$$

Using the geocentric latitude φ'

$$\varphi' = \text{atan2}\left(z_{ECEF}, \sqrt{x_{ECEF}^2 + y_{ECEF}^2}\right), \qquad \text{(A.50)}$$

the ECI coordinates in the epoch of date are then calculated as

$$x_{ECI} = R_h \cos \varphi' \cos \theta' ,$$

$$y_{ECI} = R_h \cos \varphi' \sin \theta' , \qquad \text{(A.51)}$$

$$z_{ECI} = R_h \sin \varphi' .$$

A.4.2 ECI to geographical coordinates

Given the apparent sidereal time at Greenwich θ'_0 (see equation A.60), the longitude can be calculated as

$$\lambda = \text{atan2} \left(y_{ECI}, x_{ECI} \right) - \theta'_0 . \qquad \text{(A.52)}$$

The geodetic latitude φ is calculated as

$$p = \sqrt{x_{ECI}^2 + y_{ECI}^2} ,$$

$$\vartheta = \text{atan2} \left(z_{ECI} r_e, p r_p \right) , \qquad \text{(A.53)}$$

$$\varphi = \text{atan2} \left(z_{ECI} + e_p^2 r_p \sin^3 \vartheta, p - e_e^2 r_e \cos^3 \vartheta \right) .$$

Care must be taken when calculating the height near exact poles due to numerical instabilities. If the coordinates are near the poles, and we take this as being within $1000\,\text{m}$ from the poles, which can be determined by testing if both conditions $|x_{ECI}| < 1000$ and $|y_{ECI}| < 1000$ are true, the height is calculated as

$$h = |z_{ECI}| - r_p , \qquad \text{(A.54)}$$

otherwise, the height above a WGS84 ellipsoid is calculated as

$$N = \frac{r_e}{\sqrt{1 - e_e^2 \sin^2 \varphi}} ,$$

$$h = \frac{p}{\cos \varphi} - N . \qquad \text{(A.55)}$$

This height is given in the WGS84 convention, if the height above mean sea level (MSL) is

desired, a correction described in Pavlis et al. (2012) has to be applied.

A.5   Local apparent sidereal time

First, we calculate the nutation components $\Delta\psi$ and $\Delta\epsilon$ in equation A.57 as given in Meeus (1998), chapter 22. We use the set of equations which give around $0.5''$ precision, which we deem sufficient for needs of meteoroid orbits. The dynamical time TDB is used. Ω is the longitude of the ascending node of the Moon's mean orbit on the ecliptic measured from the mean equinox of the date, L is the mean longitude of the Sun, and L' is the mean longitude of the Moon. The values are in degrees.

$$T = \frac{TDB - 2451545}{36525},$$
$$\Omega = 125.04452 - 1934.136261T,$$
$$L = 280.4665 + 36000.7698T,$$
$$L' = 218.3165 + 481267.8813T.$$

(A.56)

The nutation in longitude $\Delta\psi$ and the nutation in obliquity $\Delta\epsilon$ are calculated in arc seconds as

$$\Delta\psi = -17.2\sin\Omega - 1.32\sin 2L - 0.23\sin 2L' + 0.21\sin 2\Omega,$$
$$\Delta\epsilon = 9.2\cos\Omega + 0.57\cos 2L + 0.1\cos 2L' - 0.09\cos 2\Omega.$$

(A.57)

Next, we calculate the mean sidereal time of the Earth (Greenwich Sidereal Time) in degrees. Note that the time used here is not dynamical.

$$t = \frac{JD - 2451545}{36525},$$
$$\theta_0 = 280.46061837 + 360.98564736629(JD - 2451545)$$
$$+0.000387933t^2 - \frac{t^3}{38710000}.$$

(A.58)

The mean obliquity of the Earth in arc seconds ϵ_0 is calculated using U, which is the time

measured in units of 10000 Julian years from J2000 (note that the dynamical time is used)

$$U = \frac{TDB - 2451545}{3652500},$$

$$\epsilon_0 = 84381.448 - 4680.93U$$

$$-1.55U^2$$

$$+1999.25U^3$$

$$-51.38U^4$$

$$-249.67U^5 \qquad \text{(A.59)}$$

$$-39.05U^6$$

$$+7.12U^7$$

$$+27.87U^8$$

$$+5.79U^9$$

$$+2.45U^{10}.$$

The apparent sidereal time at Greenwich in degrees is calculated as

$$\theta_0' = \theta_0 + \frac{\Delta\psi}{3600}\cos\frac{\epsilon_0 + \Delta\epsilon}{3600}. \qquad \text{(A.60)}$$

After converting to radians, care must be taken to wrap the computed value inside the $[0, 2\pi]$ range using modulus operator

$$\theta_0' = \theta_0' \bmod 2\pi. \qquad \text{(A.61)}$$

Finally, the apparent local sidereal time θ' can be calculated as

$$\theta' = (\theta_0' + \lambda + 2\pi) \bmod 2\pi, \qquad \text{(A.62)}$$

where λ is the geodetic longitude of the observer.

A.6   Horizontal to equatorial coordinate conversion

Right ascension α and declination δ are calculated from azimuth A, altitude a, Julian date JD, and geographical coordinates of the observer, longitude λ and latitude φ, as

$$H = \operatorname{atan2}\left(-\sin A, \tan a \cos \varphi - \cos A \sin \varphi\right),$$

$$\alpha = \theta' - H, \tag{A.63}$$

$$\delta = \arcsin\left(\sin \varphi \sin a + \cos \varphi \cos a \cos A\right),$$

where H is the local hour angle and θ' is the apparent local sidereal time (see Appendix A.5).

A.7   Equatorial to horizontal coordinate conversion

The azimuth A and altitude a are calculated from right ascension α, declination δ Julian date JD, and geographical coordinates of the observer, longitude λ and latitude φ, as

$$H = \theta' - \alpha,$$

$$A = \pi + \operatorname{atan2}\left(\sin H, \cos H \sin \varphi - \tan \delta \cos \varphi\right), \tag{A.64}$$

$$a = \arcsin\left(\sin \varphi \sin \delta + \cos \varphi \cos \delta \cos H\right),$$

where H is the local hour angle and θ' is the apparent local sidereal time (see A.5).

A.8   Precessing equatorial coordinates

We follow the rigorous method of Meeus (1998), pages 134 - 135, for precessing the right ascension α and declination δ from epoch JD_0 to epoch JD. The beginning of each epoch is defined by their respective Julian dates. Please note that ζ, z and θ are given in degrees.

$$T = \frac{JD_0 - 2451545}{36525},$$

$$t = \frac{JD - JD_0}{36525},$$

$$\zeta = \frac{1}{3600}\Big[(2306.2181 + 1.39656T - 0.000139T^2)t$$

$$+(0.30188 - 0.000344T)t^2 + 0.017998t^3\Big],$$

$$z = \frac{1}{3600}\Big[(2306.2181 + 1.39656T - 0.000139T^2)t$$

$$+(1.09468 + 0.000066T)t^2 + 0.018203t^3\Big],$$

$$\theta = \frac{1}{3600}\Big[(2004.3109 - 0.85330T - 0.000217T^2)t \tag{A.65}$$

$$-(0.42665 + 0.000217T)t^2 - 0.041833t^3\Big],$$

$$A = \cos\delta\sin(\alpha + \zeta),$$

$$B = \cos\theta\cos\delta\cos(\alpha + \zeta) - \sin\theta\sin\delta,$$

$$C = \sin\theta\cos\delta\cos(\alpha + \zeta) + \cos\theta\sin\delta,$$

$$\alpha' = \text{atan2}(A, B) + z,$$

$$\delta' = \arcsin C,$$

where α' and δ' are precessed coordinates. If the declination is close to the celestial poles (which we define this as less than 0.5° from the poles), it is calculated differently due to numerical instabilities. If $(90° - |\delta|) < 0.5°$ is true, the declination should be calculated as

$$\delta' = \arccos\sqrt{A^2 + B^2}. \tag{A.66}$$

A.9 Ecliptic coordinates

The geocentric right ascension α_g and declination δ_g at the given epoch (the epoch defined by a Julian date JD, usually at J2000, thus $JD = 2451545$) can be converted to geocentric ecliptic longitude λ_g and latitude β_g with the procedure described below. First, a precise obliquity of

the Earth at the JD of the epoch has to be calculated; $\Delta\epsilon$ can be calculated using equation A.57 and the mean obliquity ϵ_0 using equation A.59. The true obliquity of the Earth in degrees is then simply

$$\epsilon = \frac{\epsilon_0 + \Delta\epsilon}{3600} .$$ (A.67)

The ecliptic longitude and latitude are then

$$\lambda_g = \text{atan2}\left(\sin\epsilon\sin\delta_g + \sin\alpha_g\cos\delta_g\cos\epsilon, \cos\alpha_g\cos\delta_g\right) ,$$

$$\beta_g = \arcsin\left(\cos\epsilon\sin\delta_g - \sin\alpha_g\cos\delta_g\sin\epsilon\right) .$$ (A.68)

Bibliography

Archinal, B. 1992, Explanatory Supplement to the Astronomical Almanac, Chapter 4 Terestrial coordinates and the rotation of the Earth, University Science Books, Mill Valley, California, USA

Ceplecha, Z. 1987, Bulletin of the Astronomical Institutes of Czechoslovakia, 38, 222

Chatfield, A. B. 1997, Fundamentals of high accuracy inertial navigation (American Institute of Aeronautics and Astronautics)

Clark, D. L. 2010, Master's thesis, The University of Western Ontario, London, Ontario, Canada

Eberly, D. H. 2006, 3D game engine design: a practical approach to real-time computer graphics (CRC Press)

Folkner, W. M., Williams, J. G., Boggs, D. H., Park, R. S., & Kuchynka, P. 2014, Interplanet. Netw. Prog. Rep 196, C1

Gural, P. 2001, WGN, Journal of the International Meteor Organization, 29, 134

Jenniskens, P., Gural, P., Dynneson, L., et al. 2011, Icarus, 216, 40

Meeus, J. H. 1998, Astronomical algorithms, 2nd edn. (Willmann-Bell, Incorporated)

Pavlis, N. K., Holmes, S. A., Kenyon, S. C., & Factor, J. K. 2012, Journal of geophysical research: solid earth, 117

Tsuchiya, C., Sato, M., Watanabe, J.-i., et al. 2017, Planetary and Space Science, 143, 142

Appendix B

Table of EMCCD Draconids

B.1   Table of EMCCD Draconids

Table B.1: Radiants, orbits, magnitudes and mass proxies for the observed EMCCD Draconids. Rows below every entry list 1σ uncertainties.

Date and time (UTC)	$\lambda_\odot$ (deg)	α_g (deg)	δ_g (deg)	v_g (km s^{-1})	a (AU)	e	q (AU)	ω (deg)	i (deg)	π (deg)	Mag	$\log_{10} I^*$
2018-10-09 00:06:37	195.4007	261.148	55.909	18.733	2.393	0.5840	0.9954	171.91	29.37	7.31	4.19	-2.20
		0.043	0.025	0.064	0.020	0.0035	0.00004	0.04	0.07	0.04		
2018-10-09 00:07:52	195.4016	262.200	56.273	20.328	2.993	0.6673	0.9960	172.85	31.30	8.26	4.05	-2.15
		0.025	0.036	0.044	0.016	0.0020	0.00002	0.03	0.06	0.03		
2018-10-09 00:08:31	195.4020	262.814	55.988	21.698	4.069	0.7552	0.9961	173.24	32.69	8.65	4.73	-2.31
		0.152	0.034	0.667	0.444	0.0394	0.00001	0.12	0.73	0.12		
2018-10-09 00:10:08	195.4031	262.062	56.168	19.090	2.501	0.6018	0.9960	172.68	29.84	8.08	3.32	-1.86
		0.018	0.016	0.043	0.014	0.0022	0.00001	0.01	0.05	0.01		
2018-10-09 00:10:20	195.4033	260.831	55.913	20.383	3.024	0.6710	0.9949	171.75	31.31	7.16	3.84	-1.96
		0.107	0.010	0.046	0.029	0.0030	0.00007	0.08	0.05	0.08		
2018-10-09 00:10:47	195.4036	262.436	55.955	20.823	3.356	0.7032	0.9959	172.94	31.74	8.35	0.94	-0.82
		0.015	0.012	0.008	0.003	0.0002	0.00001	0.01	0.01	0.01		
2018-10-09 00:12:51	195.4050	261.350	55.779	19.598	2.715	0.6334	0.9953	172.06	30.34	7.46	5.04	-2.36
		0.018	0.022	0.032	0.011	0.0014	0.00001	0.02	0.04	0.02		

Table B.1: continued.

Date and time (UTC)	$\lambda_\odot$ (deg)	α_g (deg)	δ_g (deg)	v_g (km s^{-1})	a (AU)	e	q (AU)	ω (deg)	i (deg)	π (deg)	Mag	$\log_{10} I^*$
2018-10-09 00:14:00	195.4058	261.414	56.034	19.739	2.735	0.6361	0.9955	172.19	30.59	7.59	5.41	-2.51
		0.025	0.008	0.021	0.010	0.0013	0.00002	0.02	0.02	0.02		
2018-10-09 00:14:36	195.4062	262.067	55.961	19.702	2.758	0.6389	0.9959	172.64	30.49	8.05	5.56	-2.72
		0.045	0.023	0.077	0.034	0.0048	0.00002	0.03	0.08	0.03		
2018-10-09 00:14:54	195.4064	262.214	55.958	21.019	3.472	0.7132	0.9958	172.79	31.97	8.20	2.77	-1.62
		0.015	0.024	0.023	0.010	0.0008	0.00001	0.02	0.03	0.02		
2018-10-09 00:17:38	195.4083	262.062	56.143	20.165	2.932	0.6604	0.9958	172.71	31.08	8.12	3.24	-1.86
		0.026	0.015	0.112	0.062	0.0067	0.00001	0.02	0.12	0.02		
2018-10-09 00:17:52	195.4084	262.133	55.744	21.280	3.724	0.7326	0.9956	172.68	32.19	8.09	5.98	-2.83
		0.139	0.047	0.398	0.250	0.0238	0.00003	0.10	0.43	0.10		
2018-10-09 00:17:54	195.4084	261.603	56.081	19.933	2.817	0.6466	0.9956	172.35	30.82	7.76	5.12	-2.36
		0.042	0.007	0.031	0.015	0.0019	0.00002	0.03	0.04	0.03		
2018-10-09 00:18:22	195.4088	262.639	55.737	19.682	2.808	0.6453	0.9961	172.99	30.37	8.40	1.99	-1.23
		0.348	0.130	0.316	0.168	0.0191	0.00025	0.28	0.34	0.28		
2018-10-09 00:18:25	195.4088	261.974	56.042	19.818	2.789	0.6430	0.9958	172.60	30.65	8.01	5.21	-2.47

Table B.1: continued.

Date and time (UTC)	$\lambda_\odot$ (deg)	α_g (deg)	δ_g (deg)	v_g (km s^{-1})	a (AU)	e	q (AU)	ω (deg)	i (deg)	π (deg)	Mag	$\log_{10} I^*$
		0.013	0.008	0.026	0.013	0.0016	0.00001	0.01	0.03	0.01		
2018-10-09 00:18:44	195.4090	262.370	55.669	19.780	2.851	0.6507	0.9959	172.78	30.47	8.19	3.58	-1.95
		0.013	0.026	0.029	0.009	0.0011	0.00001	0.02	0.04	0.02		
2018-10-09 00:19:46	195.4097	262.432	55.913	21.927	4.300	0.7684	0.9958	172.96	32.93	8.37	1.56	-1.05
		0.128	0.066	0.040	0.025	0.0013	0.00010	0.10	0.06	0.10		
2018-10-09 00:19:54	195.4098	260.962	56.355	19.669	2.642	0.6233	0.9953	171.95	30.63	7.36	5.49	-2.76
		0.105	0.064	0.184	0.062	0.0093	0.00009	0.10	0.23	0.10		
2018-10-09 00:19:56	195.4098	260.852	55.758	19.673	2.729	0.6354	0.9950	171.69	30.44	7.10	5.64	-2.57
		0.388	0.141	0.040	0.013	0.0017	0.00030	0.33	0.07	0.33		
2018-10-09 00:20:13	195.4100	261.106	55.483	21.299	3.739	0.7339	0.9948	171.87	32.17	7.28	3.59	-1.91
		0.093	0.034	0.022	0.019	0.0013	0.00007	0.08	0.02	0.08		
2018-10-09 00:24:15	195.4128	261.709	56.185	19.394	2.592	0.6159	0.9957	172.43	30.22	7.85	5.50	-2.72
		0.041	0.041	0.134	0.058	0.0081	0.00003	0.03	0.14	0.03		
2018-10-09 00:24:52	195.4132	261.638	55.836	20.452	3.118	0.6807	0.9954	172.32	31.32	7.73	5.54	-2.55
		0.018	0.024	0.045	0.022	0.0023	0.00001	0.02	0.05	0.02		

Table B.1: continued.

Date and time (UTC)	$\lambda_\odot$ (deg)	α_g (deg)	δ_g (deg)	v_g (km s⁻¹)	a (AU)	e	q (AU)	ω (deg)	i (deg)	π (deg)	Mag	$\log_{10} I^*$
2018-10-09 00:25:23	195.4136	262.628	56.100	21.198	3.589	0.7225	0.9961	173.13	32.20	8.55	3.09	-1.68
		0.034	0.004	0.023	0.019	0.0015	0.00002	0.03	0.02	0.03		
2018-10-09 00:25:59	195.4140	262.163	56.083	20.088	2.911	0.6579	0.9959	172.76	30.97	8.17	3.32	-1.83
		0.009	0.014	0.017	0.006	0.0007	0.00001	0.01	0.02	0.01		
2018-10-09 00:26:48	195.4145	262.170	56.165	19.224	2.550	0.6095	0.9960	172.76	29.99	8.18	5.53	-2.67
		0.017	0.019	0.038	0.010	0.0016	0.00001	0.02	0.05	0.02		
2018-10-09 00:29:09	195.4162	262.108	56.096	19.895	2.819	0.6467	0.9959	172.72	30.76	8.13	2.31	-1.37
		0.012	0.010	0.009	0.003	0.0003	0.00001	0.01	0.01	0.01		
2018-10-09 00:30:10	195.4169	262.123	55.988	20.920	3.391	0.7064	0.9957	172.73	31.88	8.15	2.50	-1.26
		0.014	0.007	0.051	0.035	0.0031	0.00001	0.01	0.05	0.01		
2018-10-09 00:30:24	195.4170	262.482	55.895	20.043	2.938	0.6610	0.9960	172.93	30.84	8.35	4.51	-2.34
		0.125	0.086	0.096	0.034	0.0038	0.00010	0.11	0.13	0.11		
2018-10-09 00:30:45	195.4173	262.300	56.127	19.325	2.596	0.6162	0.9961	172.85	30.10	8.27	4.33	-2.33
		0.015	0.032	0.029	0.006	0.0009	0.00001	0.02	0.04	0.02		
2018-10-09 00:30:57	195.4174	263.270	55.346	19.881	2.997	0.6676	0.9964	173.34	30.45	8.76	4.93	-2.47

Table B.1: continued.

Date and time (UTC)	λ☉ (deg)	α_g (deg)	δ_g (deg)	v_g (km s⁻¹)	a (AU)	e	q (AU)	ω (deg)	i (deg)	π (deg)	Mag	$\log_{10} I^*$
		0.232	0.136	0.109	0.035	0.0034	0.00017	0.18	0.16	0.18		
2018-10-09 00:33:05	195.4189	262.340	55.534	20.073	3.015	0.6697	0.9958	172.72	30.77	8.14	3.04	-1.46
		0.014	0.053	0.065	0.026	0.0028	0.00001	0.02	0.09	0.02		
2018-10-09 00:33:54	195.4194	261.699	56.214	19.620	2.672	0.6273	0.9957	172.44	30.49	7.86	3.68	-1.94
		0.014	0.018	0.033	0.011	0.0016	0.00001	0.01	0.04	0.01		
2018-10-09 00:34:12	195.4196	261.985	55.767	20.477	3.165	0.6854	0.9956	172.55	31.31	7.97	2.88	-1.61
		0.021	0.029	0.036	0.017	0.0017	0.00001	0.01	0.05	0.01		
2018-10-09 00:34:35	195.4199	261.820	55.782	20.460	3.143	0.6832	0.9955	172.43	31.31	7.85	4.71	-2.49
		0.025	0.091	0.080	0.025	0.0025	0.00002	0.03	0.12	0.03		
2018-10-09 00:34:57	195.4201	261.592	56.010	18.759	2.401	0.5854	0.9957	172.27	29.42	7.69	5.19	-2.52
		0.018	0.034	0.036	0.008	0.0014	0.00002	0.02	0.05	0.02		
2018-10-09 00:40:00	195.4236	262.710	54.921	17.099	2.105	0.5266	0.9963	172.76	27.04	8.18	5.63	-2.83
		0.193	0.127	0.370	0.102	0.0183	0.00012	0.15	0.46	0.15		
2018-10-09 00:40:02	195.4236	262.162	56.212	20.711	3.210	0.6897	0.9959	172.82	31.72	8.24	4.69	-2.35
		0.041	0.011	0.027	0.017	0.0016	0.00002	0.03	0.03	0.03		

Table B.1: continued.

Date and time (UTC)	$\lambda_\odot$ (deg)	α_g (deg)	δ_g (deg)	v_g (km s^{-1})	a (AU)	e	q (AU)	ω (deg)	i (deg)	π	Mag	$\log_{10} I^*$
2018-10-09 00:42:09	195.4251	261.976	55.944	19.376	2.629	0.6211	0.9958	172.55	30.11	7.98	4.78	-2.45
		0.262	0.136	0.059	0.010	0.0016	0.00020	0.22	0.10	0.22		
2018-10-09 00:42:24	195.4252	261.600	55.887	19.625	2.719	0.6339	0.9955	172.27	30.40	7.70	4.43	-2.30
		0.010	0.013	0.022	0.007	0.0010	0.00001	0.01	0.03	0.01		
2018-10-09 00:43:13	195.4258	261.918	56.138	20.173	2.930	0.6601	0.9957	172.60	31.10	8.03	4.36	-2.05
		0.014	0.019	0.020	0.006	0.0006	0.00001	0.01	0.03	0.01		
2018-10-09 00:44:30	195.4267	262.635	56.235	21.228	3.572	0.7211	0.9961	173.18	32.28	8.60	2.06	-1.33
		0.281	0.125	0.017	0.023	0.0018	0.00022	0.24	0.04	0.24		
2018-10-09 00:45:10	195.4272	261.695	56.232	21.624	3.816	0.7391	0.9954	172.52	32.76	7.95	3.65	-1.80
		0.032	0.043	0.058	0.035	0.0026	0.00003	0.04	0.08	0.04		
2018-10-09 00:46:20	195.4280	262.032	56.029	20.632	3.198	0.6886	0.9957	172.66	31.57	8.09	4.19	-2.12
		0.030	0.030	0.038	0.015	0.0014	0.00002	0.02	0.05	0.02		
2018-10-09 00:48:59	195.4298	262.503	56.053	20.324	3.048	0.6733	0.9961	173.00	31.21	8.43	4.49	-2.09
		0.143	0.068	0.016	0.009	0.0010	0.00011	0.12	0.03	0.12		
2018-10-09 00:49:03	195.4298	262.424	56.205	22.928	5.589	0.8218	0.9958	173.07	34.10	8.50	3.45	-1.57

Table B.1: continued.

Date and time (UTC)	$\lambda_\odot$ (deg)	α_g (deg)	δ_g (deg)	v_g (km s^{-1})	a (AU)	e	q (AU)	ω (deg)	i (deg)	π (deg)	Mag	$\log_{10} I^*$
		0.034	0.008	0.105	0.173	0.0067	0.00001	0.03	0.11	0.03		
2018-10-09 00:50:26	195.4308	260.164	56.377	18.070	2.146	0.5364	0.9950	171.25	28.75	6.69	6.31	-3.11
		0.089	0.040	0.102	0.031	0.0062	0.00005	0.07	0.11	0.07		
2018-10-09 00:50:30	195.4308	261.233	56.480	18.889	2.376	0.5810	0.9956	172.14	29.73	7.57	4.02	-2.12
		0.016	0.013	0.013	0.003	0.0005	0.00001	0.01	0.02	0.01		
2018-10-09 00:53:49	195.4331	262.207	56.102	20.183	2.954	0.6629	0.9959	172.80	31.08	8.23	4.53	-2.20
		0.026	0.007	0.017	0.010	0.0011	0.00001	0.02	0.02	0.02		
2018-10-09 00:54:02	195.4332	262.175	56.064	19.528	2.676	0.6278	0.9960	172.74	30.32	8.17	6.61	-3.38
		0.010	0.020	0.020	0.005	0.0006	0.00001	0.01	0.03	0.01		
2018-10-09 00:54:33	195.4336	262.130	55.991	18.750	2.416	0.5878	0.9960	172.66	29.38	8.09	3.32	-1.72
		0.010	0.019	0.015	0.002	0.0004	0.00001	0.01	0.02	0.01		
2018-10-09 00:59:05	195.4367	262.004	56.005	21.422	3.746	0.7342	0.9956	172.66	32.44	8.10	1.05	-0.76
		0.029	0.008	0.041	0.036	0.0024	0.00002	0.02	0.04	0.02		
2018-10-09 00:59:12	195.4368	261.853	56.040	19.636	2.710	0.6325	0.9957	172.50	30.45	7.94	5.94	-2.86
		0.054	0.068	0.070	0.019	0.0026	0.00005	0.06	0.10	0.06		

Table B.1: continued.

Date and time (UTC)	$\lambda_\odot$ (deg)	α_g (deg)	δ_g (deg)	v_g (km s^{-1})	a (AU)	e	q (AU)	ω (deg)	i (deg)	π (deg)	Mag	$\log_{10} I^*$
2018-10-09 00:59:30	195.4370	260.516	55.773	18.862	2.428	0.5902	0.9949	171.39	29.51	6.83	6.04	-2.94
		0.069	0.014	0.024	0.009	0.0015	0.00005	0.06	0.03	0.06		
2018-10-09 00:59:35	195.4370	261.633	56.017	19.653	2.712	0.6328	0.9956	172.33	30.47	7.77	3.46	-1.62
		0.009	0.010	0.013	0.004	0.0005	0.00001	0.01	0.02	0.01		
2018-10-09 00:59:50	195.4372	261.715	55.772	19.379	2.644	0.6235	0.9956	172.31	30.07	7.75	2.37	-1.28
		0.014	0.019	0.015	0.003	0.0005	0.00001	0.01	0.02	0.01		
2018-10-09 01:01:43	195.4385	261.983	56.221	20.594	3.132	0.6820	0.9958	172.68	31.60	8.12	6.04	-2.97
		0.117	0.047	0.077	0.039	0.0049	0.00008	0.10	0.08	0.10		
2018-10-09 01:08:52	195.4434	262.068	55.950	20.164	2.967	0.6643	0.9958	172.65	31.02	8.09	5.31	-2.59
		0.174	0.042	0.501	0.331	0.0298	0.00004	0.13	0.54	0.13		
2018-10-09 01:10:16	195.4444	263.413	56.213	21.256	3.654	0.7273	0.9965	173.71	32.27	9.16	4.22	-2.13
		0.088	0.017	0.047	0.033	0.0028	0.00005	0.07	0.05	0.07		
2018-10-09 01:12:26	195.4458	261.633	55.913	19.390	2.625	0.6208	0.9956	172.29	30.13	7.74	4.80	-2.38
		0.043	0.012	0.022	0.009	0.0013	0.00003	0.04	0.03	0.04		
2018-10-09 01:13:18	195.4464	261.579	55.956	19.086	2.511	0.6035	0.9956	172.25	29.79	7.70	5.14	-2.54

Table B.1: continued.

Date and time (UTC)	$\lambda_\odot$ (deg)	α_g (deg)	δ_g (deg)	v_g (km s^{-1})	a (AU)	e	q (AU)	ω (deg)	i (deg)	π (deg)	Mag	$\log_{10} I^*$
		0.261	0.155	0.102	0.040	0.0062	0.00023	0.24	0.12	0.24		
2018-10-09 01:14:12	195.4471	261.196	56.256	19.152	2.483	0.5990	0.9955	172.06	29.98	7.50	4.57	-2.28
		0.019	0.021	0.013	0.002	0.0004	0.00001	0.02	0.02	0.02		
2018-10-09 01:14:40	195.4474	261.443	56.452	20.109	2.823	0.6474	0.9956	172.34	31.15	7.79	5.30	-2.63
		0.080	0.060	0.039	0.011	0.0014	0.00007	0.07	0.06	0.07		
2018-10-09 01:15:32	195.4480	261.452	55.902	20.320	3.024	0.6709	0.9953	172.19	31.21	7.64	3.44	-1.92
		0.139	0.086	0.009	0.012	0.0013	0.00013	0.13	0.02	0.13		
2018-10-09 01:17:31	195.4493	261.989	56.232	20.535	3.097	0.6785	0.9958	172.69	31.54	8.14	4.19	-1.99
		0.106	0.062	0.018	0.013	0.0013	0.00009	0.10	0.03	0.10		
2018-10-09 01:21:22	195.4520	261.745	55.998	19.711	2.742	0.6369	0.9956	172.41	30.53	7.86	4.64	-2.35
		0.101	0.062	0.017	0.010	0.0013	0.00009	0.09	0.02	0.09		
2018-10-09 01:21:30	195.4521	262.764	56.139	20.150	2.956	0.6630	0.9963	173.20	31.03	8.66	5.20	-2.69
		0.145	0.021	0.168	0.066	0.0094	0.00008	0.12	0.19	0.12		
2018-10-09 01:23:21	195.4533	262.104	55.876	20.780	3.327	0.7007	0.9957	172.67	31.69	8.12	1.82	-1.19
		0.026	0.004	0.014	0.009	0.0008	0.00002	0.02	0.02	0.02		

Table B.1: continued.

Date and time (UTC)	$\lambda_\odot$ (deg)	α_g (deg)	δ_g (deg)	v_g (km s^{-1})	a (AU)	e	q (AU)	ω (deg)	i (deg)	π (deg)	Mag	$\log_{10} I^*$
2018-10-09 01:27:34	195.4562	261.840	55.849	20.001	2.897	0.6563	0.9956	172.44	30.81	7.90	4.11	-2.25
		0.057	0.083	0.121	0.061	0.0077	0.00003	0.04	0.13	0.04		

Appendix C

CAMO plate formats

C.1   AST plate

The AST (ASTrometry) plate is a type of plate mapping developed in Weryk & Brown (2012) for use with the ASGARD system. It maps any cartesian (x, y) pair (e.g. image or mirror coordinates) into celestial horizontal coordinates (θ, φ), where θ is the zenith distance and φ is the azimuth (+N of due E). To avoid the discontinuity at the azimuth branch cut (where $\varphi = \pm 180$), the angles on a hemisphere (assuming that only $\theta < 90°$ angles are observable) are projected onto a plane. The vertical axis of the projection, defined by angles (θ_0, φ_0), is chosen to correspond close to the image centre. Thus, we can define the rotation matrix of the projection as

$$M = \begin{bmatrix} -\sin\varphi_0 & -\cos\theta_0\cos\varphi_0 & \sin\theta_0\cos\varphi_0 \\ \cos\varphi_0 & -\cos\theta_0\sin\varphi_0 & \sin\theta_0\sin\varphi_0 \\ 0 & \sin\theta_0 & \cos\theta_0 \end{bmatrix}. \tag{C.1}$$

The columns of matrix M define an orthogonal basis set. Star positions (θ, φ) are rotated using M' (the inverse of M) to obtain (β, γ) pairs

$$\begin{bmatrix} \sin\beta\cos\gamma \\ \sin\beta\sin\gamma \\ \cos\beta \end{bmatrix} = M' \begin{bmatrix} \sin\theta\cos\varphi \\ \sin\theta\sin\varphi \\ \cos\theta \end{bmatrix}, \tag{C.2}$$

which are relative to (θ_0, φ_0). The positions are then projected onto the p, q plane

$$p = \sin\beta\cos\gamma, \tag{C.3}$$
$$q = \sin\beta\sin\gamma.$$

The (x, y) image centroids are then fitted to the (p, q) values for each star using third order polynomials

$$p = a_0 + a_1 x + a_2 x^2 + a_3 x^3 + a_4 y + a_5 y^2$$
$$+a_6 y^3 + a_7 xy + a_8 x^2 y + a_9 xy^2,$$
$$q = b_0 + b_1 x + b_2 x^2 + b_3 x^3 + b_4 y + b_5 y^2 \tag{C.4}$$
$$+b_6 y^3 + b_7 xy + b_8 x^2 y + b_9 xy^2.$$

The reverse mapping polynomials are fit separately, enabling the conversion from (p, q) to (x, y). As discussed in Weryk et al. (2013), this method is advantageous in comparison to a typical gnomonic projection for larger fields of view, by producing smaller fit residuals.

C.2   AFF plate

The AFF plate represents an affine transform, which is a combination of translation, scaling, rotation and mirroring, described by the following equation:

$$\begin{bmatrix} x' \\ y' \end{bmatrix} = \begin{bmatrix} M_{11} & M12 & M_{13} \\ M_{21} & M_{22} & M_{23} \end{bmatrix} \begin{bmatrix} x \\ y \\ 1 \end{bmatrix}. \tag{C.5}$$

The *M* coefficients are the fit parameters. In this implementation, x' and y' are orthogonal, meaning that there is no shearing.

Bibliography

Weryk, R., Campbell-Brown, M., Wiegert, P., et al. 2013, Icarus, 225, 614

Weryk, R. J., & Brown, P. G. 2012, Planetary and Space Science, 62, 132 . `http://www.sciencedirect.com/science/article/pii/S0032063311003965`

Appendix D

Copyright Permissions

Paris, February 3, 2020

Reprint Permission

Material:
Figs. 2&11 in Segon et al. 2017, A&A, 598, A15

To be used in:
PhD thesis entitled "Physical dispersions of meteor showers through high precision optical observations",
The University of Western Ontario

Permission granted to:
Denis Vida

I hold copyright on the material referred to above, and hereby grant permission for its use as requested
herewith. Credit should be given as follows:
Credit: Author, A&A, vol, page, year, reproduced with permission © ESO.

Thierry Forveille
A&A Editor-in-Chief

Standard Licence

Further Information

acknowledge the Journal as the original place of publication with the correct citation details given.

signed this licence on 2018-07-10 14:32:14 GMT.

Standard Licence

You hereby grant to Oxford University Press an exclusive licence for the full period of copyright throughout the world:

- to publish the final version of the Article in the above Journal, and to distribute it and/or to communicate it to the public, either within the Journal, on its own, or with other related material throughout the world, in printed, electronic or any other format or medium whether now known or hereafter devised;
- to make translations and abstracts of the Article and to distribute them to the public;
- to authorize or grant licences to third parties to do any of the above;
- to deposit copies of the Article in online archives maintained by OUP or by third parties authorized by OUP.

You authorize us to act on your behalf to defend the copyright in the Article if anyone should infringe it and to register the copyright of the Article in the US and other countries, if necessary.

In the case of a multi authored article, you confirm that you are authorized by your co-authors to enter the licence on their behalf.

You confirm to OUP that the Article

- is your original work;
- has not previously been published (in print or electronic format), is not currently under consideration by another journal, or if it has already been submitted to other journal, it will be immediately withdrawn;
- will not be submitted for publication to any other journal following acceptance in the above Journal; and
- OUP will be the first publisher of the Article.

You warrant to OUP that

- no part of the Article is copied from any other work,
- you have obtained ALL the permissions required (for print and electronic use) for any material you have used from other copyrighted publications in the Article; and
- you have exercised reasonable care to ensure that the Article is accurate and does not contain anything which is libellous, or obscene, or infringes on anyone's copyright, right of privacy, or other rights.

Further Information

(Full details of OUP's publication rights policies, including author rights can be found at
https://academic.oup.com/journals/pages/access_purchase/rights_and_permissions/publication_rights)

Author Self-Archiving Policy

On publication of your Article in the Journal you are not required to remove any previously posted ORIGINAL VERSIONS from your own personal website or that of your employer or free public servers of articles in your subject area, provided (1) you include a link (url) to the VERSION OF RECORD on the Journalâ s website; AND (2) the Journal is attributed as the original place of publication with the correct citation details given.

You may post the ACCEPTED MANUSCRIPT or the VERSION OF RECORD onto your own website, your institutionâ s website and in institutional or subject-based repositories upon publication, provided that: (1) you include a link (url) to the VERSION OF RECORD on the Journalâ s website; (2) the Journal is attributed as the original place of publication with the correct citation details given.

Free Link to Published Article

On publication of your article, you will receive a URL, giving you access to the published article on the Journal website, and information on use ofthis link.

Educational Use

You may use the Article within your employer's institution or company for educational or research purposes only, including use in course-packs, as long as: (1) you do not use it for commercial purposes or re-distribution outside of the institution/company; (2) you

acknowledge the Journal as the original place of publication with the correct citation details given.

signed this licence on 2019-11-12 17:20:30 GMT.

Standard Licence

Further Information

Author Self-Archiving Policy

Free Link to Published Article

Educational Use

acknowledge the Journal as the original place of publication with the correct citation details given.

edp sciences

Copyright Agreement

To be filled if you did NOT select the open access option

I hereby grant and assign the entire copyright in the article entitled:

A new method for measuring the meteor mass index: application to the 2018 Draconid meteor shower outburst . . . .

and authored by: Denis Vida, M. Campbell-Brown, P. G. Brown, A. Egal, M. J. Mazur . . . .

to ESO.

Date: 17 MARCH 2020

Signature:

4

Curriculum Vitae

Denis Vida
Department of Earth Sciences
1151 Richmond Street
London, Ontario, Canada
N6A 3K7

Education
Doctor of Philosophy (Geophysics & Planetary Science)
University of Western Ontario
London, Ontario, Canada
2017 - 2020

Master of Science (Geophysics & Planetary Science)
Transferred to PhD
University of Western Ontario
London, Ontario, Canada
2016 - 2017

Master of Science (Computer Engineering)
Faculty of Electrical Engineering Osijek
Osijek, Croatia
2014 - 2016

Bachelor of Science (Computer Engineering)
Faculty of Electrical Engineering Osijek
Osijek, Croatia
2011 - 2014

Honours and Awards
Fallona Family Interdisciplinary Research Showcase First Prize - April 2018
Dean's award, Faculty of Electrical Engineering Osijek - May 2016

Rector's award, J. J. Strossmayer University in Osijek - May 2015

Related Work Experience
Teaching Assistant, Earth Sciences, The University of Western Ontario 2016 - 2018

Publications

1. **Vida, D.**, Brown, P.G., Campbell-Brown, M., Weryk, R.J., Stober, G., and McCormack, J.P. 2020. "High precision meteor observations with the Canadian Automated Meteor Observatory: Data reduction pipeline and meteoroid mechanical strength measurements". *Icarus*, submitted

2. **Vida, D.**, Campbell-Brown, M. D., Brown, P. G., Egal, A., and Mazur, M. 2020, "A new method for measuring the meteor mass index: application to the 2018 Draconid meteor shower outburst." *Astronomy & Astrophysics*, submmitted.

3. **Vida, D.**, Brown, P.G., Campbell-Brown, M., Wiegert, P., and Gural, P.S. 2020. "Estimating trajectories of meteors: an observational Monte Carlo approach – II. Results". *Monthly Notices of the Royal Astronomical Society*, 491, 3996.

4. **Vida, D.**, Gural, P.S., Brown, P.G., Campbell-Brown, M., and Wiegert, P. 2020. "Estimating trajectories of meteors: an observational Monte Carlo approach – I. Theory." *Monthly Notices of the Royal Astronomical Society*, 491, 2688.

5. Brown, P. G., **Vida, D.**, Moser, D. E., Granvik, M., Koshak, W. J., Chu, D., Steckloff, J., Licata, A., Hariri, S., Mason, J., Mazur, M., Cooke, W., and Krzeminski, Z. 2019. "The Hamburg meteorite fall: Fireball trajectory, orbit, and dynamics". *Meteoritics & Planetary Science*, 54, 2027.

6. **Vida, D.**, Brown, P.G., and Campbell-Brown, M. 2018. "Modelling the measurement accuracy of pre-atmosphere velocities of meteoroids." *Monthly Notices of the Royal Astronomical Society*, 479, 4307.

7. **Vida, D.**, Brown, P. G., and Campbell-Brown, M. 2017. "Generating realistic synthetic meteoroid orbits". *Icarus*, 296, 197.

8. Šegon, D., Vaubaillon, J., Gural, P. S., **Vida, D.**, Andreić, Ž., Korlević, K., and Skokić, I. 2017. "Dynamical modeling validation of parent bodies associated with newly discovered CMN meteor showers". *Astronomy & Astrophysics*, 598, A15.

9. Borovička J., Spurný P., Šegon D., Andreić Ž., Kac J., Korlević K., Atanackov J., Kladnik G., Mucke H., **Vida, D.**, and Novoselnik F. 2015. "The instrumentally recorded fall of the Križevci meteorite, Croatia, February 4, 2011". *Meteoritics & Planetary Science*, 50, 1244.

10. Šegon D., Andreić, Ž., Gural P. S., Korlević K., **Vida, D.**, Novoselnik F., and Skokić, I. 2014 "Draconids 2011: Outburst Observations by the Croatian Meteor Network", *Earth Moon and Planets*, 112, 1.